Imperial College
London

IMPERIAL COLLEGE LONDON

Department of Civil and Environmental Engineering

# Modelling land-use and climate change impacts on hydrology: the Upper Ganges river basin

Georgia-Marina Tsarouchi

A thesis submitted for the degree of Doctor of Philosophy

December 2014

# Declaration

I confirm that this submission is my own work and the use of all material from other sources has been properly and fully acknowledged.

Several chapters of this dissertation are based on the following publications:

1. Tsarouchi, G., Mijic, A., Moulds, S., Buytaert, W., 2014. Historical and future land-cover changes in the Upper Ganges basin of India. *International Journal of Remote Sensing*, 35: 3150-3176

2. Tsarouchi, G., Buytaert, W., Mijic, A., 2014. Coupling a land-surface model with a crop growth model to improve ET flux estimations in the Upper Ganges basin, India. *Hydrology and Earth System Sciences*, 18, 4223-4238.

Georgia-Marina Tsarouchi

# Abstract

This thesis explores the effects that large-scale land-use/cover change (LUCC) and climate change pose to the terrestrial water cycle, by developing a case study in the Upper Ganges (UG) river basin, in India.

In an area experiencing rapid rates of LUCC and changes in irrigation practices, historic land-use maps are developed, based on satellite images, to investigate historical trends of LUCC. Future projection scenarios of LUCC for years up to 2035 are derived from Markov chain analysis. To explore the impacts of those changes in hydrology, the generated maps are used to force the Land Surface Model (LSM) JULES.

JULES is found to be reasonably skilful in terms of its ability to reproduce observed streamflow. However, the results indicate that there is much room left for improved estimates of evapotranspiration (ET) fluxes, which JULES is found to over-predict. By dynamically coupling JULES with the crop model InfoCrop, the simulated ET fluxes are improved, compared to the original JULES model. The difference in mean annual ET between the two models (coupled and original) is approximately 150 mm/yr and indicates the potential error in ET flux estimations of an LSM without dynamic vegetation.

The impact of LUCC and climate change on the hydrological response of the UG basin is quantified, by calculating variations in hydrological components (streamflow, ET and soil moisture) during the period 2000–2035. Severe increases in the high extremes of flows (+40% in the multi-model mean) are being projected for the nearby future (2030–2035). The changes in all examined hydrological components are greater in the combined land-use and climate change scenario, whilst climate change is the main driver of those changes. These results provide the necessary evidence-base to support regional land-use planning, advanced irrigation practices and develop future-proof water resource management strategies under a water-limited environment.

To my parents

# Acknowledgements

I would like to express my sincere gratitude to my supervisor Dr Wouter Buytaert, who supported me throughout the course of my PhD. Thank you for encouraging my research, for providing aspiring guidance, ideas and constructive criticism over the past 3 years. Many thanks also go to Prof. Neil McIntyre, who offered his time and useful guidance that shaped the direction of this thesis during the first year of my PhD .

I would have not followed this path without the unconditional love and support of my family. There are not enough words to express my gratitude for all the sacrifices that my parents made on my behalf. Thank you for being there for me along this journey and for always believing in me.

To all my friends and colleagues at the Environmental and Water Resources Engineering section, thank you for the stimulating discussions and memorable good moments throughout these years. Special thanks go to Zed Zulkafli, Ana Mijic, Simon Moulds, Jimmy O'Keeffe, Christina Bakopoulou and Claudia Vitolo, for our insightful discussions and collaborations.

Last but not least, I would like to express my sincere gratitude to my beloved Andy, who was always there for me, to advise me, and to offer his ideas and constructive feedback. Thank you for your support and for always making me smile even after a very long day.

This research was co-funded by the Academy of Athens (Greece) and the Grantham Institute for Climate Change (Imperial College). I would like to thank both organisations for their generous support.

# Contents

# List of Figures

# List of Tables

# List of Acronyms

| | |
|---|---|
| **AOGCM** | Atmosphere-Ocean General Circulation Model |
| **APHRODITE** | Asian Precipitation Highly Resolved Observational Data Integration Towards the Evaluation of water resources |
| **CAPRI** | Common Agricultural Policy Regionalised Impact |
| **CA** | Cellular Automata |
| **CF** | change factor |
| **CLUE** | Conversion of Land Use and its Effects |
| **CMIP5** | Coupled Model Intercomparison Project Phase 5 |
| **ECV** | Essential Climate Variable |
| **D8** | eight-direction |
| **DN** | digital number |
| **DEM** | Digital Elevation Model |
| **DOS** | Dark Object Subtraction |
| **EF** | Environmental Flows |
| **ER** | Electromagnetic Radiation |
| **ETM+** | Enhanced Thematic Mapper Plus |
| **ENSO** | El Niño and Southern Oscillation |
| **ET** | evapotranspiration |
| **ESA** | European Space Agency |
| **GCM** | General Circulation Model |
| **GDAP** | GEWEX Data and Assessment Panel |
| **GHG** | Greenhouse Gas |

| | |
|---|---|
| **GLACE** | Global Land-Atmosphere Coupling Experiment |
| **GMAO** | Global Modelling and Assimilation Office |
| **GPCC** | Global Precipitation Climatology Centre |
| **GTAP** | Global Trade Analysis Project |
| **HWSD** | Harmonised World Soil Database |
| **IMAGE** | Integrated Model to Assess the Global Environment |
| **IMD** | Indian Meteorological Department |
| **IPCC** | Intergovernmental Panel on Climate Change |
| **IQR** | Inter-Quartile Range |
| **JULES** | Joint UK Land Environment Simulator |
| **LAI** | Leaf Area Index |
| **LUCC** | Land-Use/Cover Change |
| **LSM** | Land Surface Model |
| **LAPSUS** | LandscApe ProcesS modelling at mUlti-dimensions and Scales |
| **LIA** | Little Ice Age |
| **ME** | Mean Error |
| **MMM** | Multi-Model Mean |
| **MOSES** | Met Office Surface Exchange System |
| **NCEP** | National Center of Environmental Predictions |
| **NDVI** | Normalized Difference Vegetation Index |
| **NSE** | Nash-Sutcliffe Efficiency |
| **PDM** | Probability Distributed Model |
| **PET** | potential evapotranspiration |
| **PBIAS** | Percent Bias |
| **PFT** | Plant Functional Type |
| **RMSE** | Root Mean Square Error |

| | |
|---|---|
| **RUE** | Radiation Use Efficiency |
| **SM** | Soil Moisture |
| **TM** | Thematic Mapper |
| **TRMM** | Tropical Rainfall Measuring Mission |
| **TMPA** | Tropical Multisatellite Precipitation Analysis |
| **UM–CAP** | Unified Model Central Ancillary Program |
| **UG** | Upper Ganges |

# Chapter 1

# Introduction

# Introduction

## 1.1 Motivation - Research background

The fertile soils of the Ganges basin, the world's most densely populated river basin, provide a source of arable land and significant economic opportunities for India.

In recent decades India has undergone substantial environmental change. India's green revolution was initiated by the introduction in the mid-1960s of high yielding varieties of rice and wheat across Latin America and Asia (Singh, 2000; Evenson and Gollin, 2003), with the aim of increasing food security and promoting sustainable economic development (Pinstrup-Andersen and Hazell, 1985). Combined with the expansion of agricultural land area to meet the demand of a rapidly increasing population, the green revolution enabled India to become self-sufficient in food grains (Singh, 2000; Sen Roy *et al.*, 2007). In the initial stages of the green revolution the growth in agricultural area was achieved through widespread deforestation (Rai *et al.*, 1994; Singh, 2000). However, since the beginning of the 1990s India has pursued a policy of afforestation and reforestation combined with conservation of its existing resources (Ravindranath *et al.*, 2008).

Despite its undeniable positive results, India's green revolution, combined with agricultural expansion and increased intensification of groundwater extraction in order to meet irrigation needs, has led to an alarming drop in the water table levels (Briscoe, 2005; World Bank, 2010; GOI, 2010). Even during the 1970s, the dry season flows of the Ganges were barely sufficient to cover regional irrigation needs (Smakhtin, 2013). Since then, the pressure on India's water resources has only mounted and is likely to increase further with forecast population growth (Tenhunen and Saavala, 2012) together with continued economic progress and projected greenhouse warming (IPCC, 2013). To add to the water resources problem, in recent years extreme weather events appear more frequently over India (IPCC, 2007), claiming thousands of lives, and this has been partially attributed to climate change and poor environmental management (Herring *et al.*, 2014). The recent floods (summer 2013) over northern India have raised

concerns about how the regional climate variations and human induced changes in landscape are influencing the temporal dynamics of climate-surface-groundwater interactions. On the one hand, land-cover change is affecting the water resources of northern India in complex ways while several studies have identified a strong feedback mechanism between soil moisture and precipitation (Koster *et al.*, 2004, 2006; Guo *et al.*, 2006; Seneviratne *et al.*, 2006). On the other hand, the potential impacts of a changing climate include changing rainfall patterns, floods, droughts, glacier melt, sea level rise, and food security crisis among others (IPCC, 2014a).

Consequently, in a region characterised by a rapid increase in population which is already facing water stress, it is essential to understand how land-use change and climate change are influencing the spatio-temporal dynamics of hydrological fluxes.

## 1.2 Research aim and objectives

Understanding and monitoring the hydrologic response of watersheds to land-use and climate change is an important element of water resource planning and management. The scientific challenge of this research is to propose a methodology for the assessment of the effects that large-scale land-use changes and climate change pose to the water cycle and flow characteristics and to monitor their representation in macro-scale hydrological modelling, by developing a case study in the river Ganges. The following hypotheses drive the research:

1. **The use of satellite imagery allows for reconstructing historical land-use patterns and projecting them into the future.** Land-use changes and their effects on landscape patterns can impact water supply in a watershed by altering hydrological processes such as evaporation, infiltration, surface runoff, groundwater discharge and stream flow. In order to explore the sensitivity of the catchment's response to land-use changes, remote sensing data are used to reconstruct historical dynamics of land-use change and future projections of change are developed, based on Markov chain analysis. Analysing land-use change is a prerequisite to studying changes in water resources, in regions with intensive agriculture such as the Ganges basin, where irrigation is a dominant driver of change.

2. **Accounting for dynamic crop growth in Land Surface Models (LSMs) significantly improves the representation of soil and land-surface processes in the Ganges basin.** The LSM JULES that is applied in this study, is coupled with the crop model InfoCrop, to develop a system able to dynamically simulate crop growth, development and interactions with the land surface. The coupled model is parametrised for the two main crops of the Upper Ganges (UG) basin (wheat and rice) to capture well the inter-annual variations in land surface processes. Two sets of simulations are run:

    - JULES with the default $C_3$ grass parametrisation adapted to crops, and
    - JULES coupled with InfoCrop, including dynamic crop growth parametrisation.

3. **The combined impacts of land-use and climate change will be greater than the impacts posed by land-use change and climate change individually, on hydrological components.** The quantification of land-use and climate change impacts on hydrological fluxes is a challenge in hydrological science and especially in the data sparse tropical regions. Many studies focus on climate change impacts only and others focus on land-use change impacts only. However, there are just a few studies that consider the combined effects of climate and land-use change by quantitatively integrating both. In this study, those relative impacts are investigated by analysing annual variations of hydrological components (stream flow, evapotranspiration and soil moisture) during the simulation period, under different land-use and climate change scenarios.

The general literature behind these hypotheses will be discussed in the next Chapter.

## 1.3 Research Context

This research is associated with a large Changing Water Cycle collaborative project between Indian and UK partners (Hydroflux-India). The aim of this large project is to understand to what extent the large-scale, human-induced land-use changes and groundwater depletion that have taken place in India over the last 50 years, feed back to the hydrological and climate system at a basin scale. This PhD project fits well with ongoing research on land surface modelling and research conducted by other PhD students working on the Hydroflux-India project at the Imperial College hydrology group.

The study area is the Upper Ganges basin (approximately 87,000 $\mathrm{km}^2$). However, the hydrological analysis performed in terms of streamflow estimations is focused in a smaller sub-catchment located in the north of the UG basin, the Bhimgoda catchment (approximately 23,000 $\mathrm{km}^2$). Due to strict policies of the Indian government regarding the sharing of river flow data, this was the only catchment for which the Hydroflux-India project was able to receive streamflow data. All other types of analysis / modelling are applied in the entire UG basin.

## 1.4 Thesis structure

Chapter 2 presents the scientific background in terms of remote sensing analysis techniques, land-use change modelling, coupling schemes of LSMs with crop models, feedbacks of land-use change to the climate, and impacts of climate and/or land-use change on water resources. Chapter 3 provides a description of the study area in terms of geography, land use, geology, hydrology, climate, water management and data availability. Chapter 4 describes the data used, methods applied and results derived by the historic modelling of land-use change and the application of Markov chain analysis for the development of future land-use change scenarios. Chapter 5 presents a critical analysis of the JULES LSM, which is evaluated in terms of its robustness, under a sensitivity and uncertainty analysis framework. This Chapter also includes a section on precipitation data uncertainties. Chapter 6 describes the methodology followed to couple JULES with InfoCrop, the modelling experiments and results of this new proposed scheme. Chapter 7 offers a comparison between land-use change and climate change as drivers of hydrological change. The future land-use scenarios developed in Chapter 4 are used in combination with future climate change scenarios in a series of modelling experiments. Finally, Chapter 8 revisits the three hypotheses that drove this research, summarizes the main outcomes, highlights the research limitations and suggests future directions of work.

# Chapter 2

# Scientific background

# Scientific Background

The following sections provide an overview of the current state of knowledge in science relevant to the hypotheses that drive this research. The purpose is to develop an understanding of the complete and current state of research in the relevant to the study fields of land-use, hydrology and climate science, with a particular focus on India.

## 2.1 Remote sensing analysis of land use / land cover

One of the most essential applications of remote sensing techniques is recording land-use/cover changes (LUCC) through time (Christensen *et al.*, 1988). The Landsat program, one of NASA's major Earth observation initiatives, has been almost continuously recording global land-cover change since it originated in 1972 (Cohen and Goward, 2004). Landsat Thematic Mapper (TM) was a sensor flying on Landsat 4 and 5 satellites. Landsat 4 was launched in 1982 and ended image acquisition in 1993, while Landsat 5 was launched in 1984 and ended image acquisition in 2013. U.S. Geological Survey (USGS) decided to decommission the satellite, leaving the orbit open for the new Landsat 8. Landsat 5 had a remote sensing system that was geared towards providing increased spectral discrimination of different types of vegetation, soils, water and rocks among others, by monitoring the Earth's surface through 7 different spectral bands known as multi-spectral design. Six of the bands were covering the visible and near infrared wavelengths, and one was covering the thermal infrared wavelengths. The Landsat Enhanced Thematic Mapper Plus (ETM+) was introduced with Landsat 7 in 1999 and continues operation until today. ETM+ data include new features that facilitate their usage in land-cover monitoring and change studies. The main new characteristics on Landsat 7 include a panchromatic band with 15-meter spatial resolution, on-board radiometric calibration and a thermal infrared channel with 60-meter spatial resolution

The fixed acquisition schedule Landsat sensors follow (the satellite revisits the same spot on the earth every 16 days) has provided a long-term record, representing the longest and one of the most consistent available datasets in remote sensing history. Its use has extended knowledge of land surface

processes and enhanced scientific research (Cohen and Goward, 2004). Satellite images are widely used today in land-cover classification and change detection analysis (Ehlers *et al.*, 1990; Westmoreland and Stow, 1992; Yeh and Li, 1999). However, as a result of management decisions and operational errors, the availability of Landsat images for northern India is poor (Goward *et al.*, 2006). Furthermore, heavy cloud cover during the monsoon period (June-September) means that satellite images for this season frequently cannot be used (Thenkabail *et al.*, 2005; Goward *et al.*, 2006). Because of these shortcomings, the dynamics of land-cover changes over the Indian subcontinent remain poorly studied. To overcome this challenge we mainly focus on the study of annual scale land-cover changes.

Recently published regional land-use mapping studies tend to focus on cities of central and southern India. They use statistical classification approaches in high resolution satellite images acquired by Landsat and/or the Indian Remote Sensing (IRS) sensor to study urbanization patterns (e.g., for Ajmer city, Jat *et al.* 2008; for Kolkata, Bhatta 2009; for Mumbai, Moghadam and Helbich 2013). Several other recent studies (Sheeja *et al.*, 2011; Bhagyanagar *et al.*, 2012; Rahman *et al.*, 2012; Raja *et al.*, 2013) that focus on India are mainly investigating LUCC of small scale systems. Therefore, investigating the dynamics of LUCC in a large scale system, such as the UG basin, is a challenge for this study.

### 2.1.1 Pre-processing of satellite images

The accuracy of land-use maps generated from satellite images is highly dependent on the quality of the interpreted satellite data. Before the analysis and comparison of multi-temporal images, a primary pre-processing task is required, in which radiometric and atmospheric corrections are applied to each image.

Digital sensors acquire the intensity of electromagnetic radiation (ER) from each spot viewed on the Earth's surface and store this information as an 8-bit satellite quantized calibrated digital number (DN) for each spectral band. The DN values are affected by parameters such as meteorological conditions at the moment the image was taken, the Sun's position, and the viewing geometry of the satellite. (Chavez, 1996). Additionally, solar radiation after its reflection from the land surface interacts with the atmosphere and is therefore modified. This modification enhanced with absorption and scattering by aerosols, particles and gases while solar radiation travels through the atmosphere, causes reduction in the contrast of the

image. Because of scattering the radiance value recorded for a specific pixel incorporates the scattered radiance value from neighbouring pixels (known as the *adjacency effect*). Therefore, it is essential to apply effective radiometric corrections and remove the atmospheric interferences during the pre-processing analysis of satellite images, in order to make meaningful measures of physical parameters of the Earth's surface and to determine true surface reflectance values. Figure 2.1 describes the steps followed during the radiometric corrections process. These are further described in the following paragraphs.

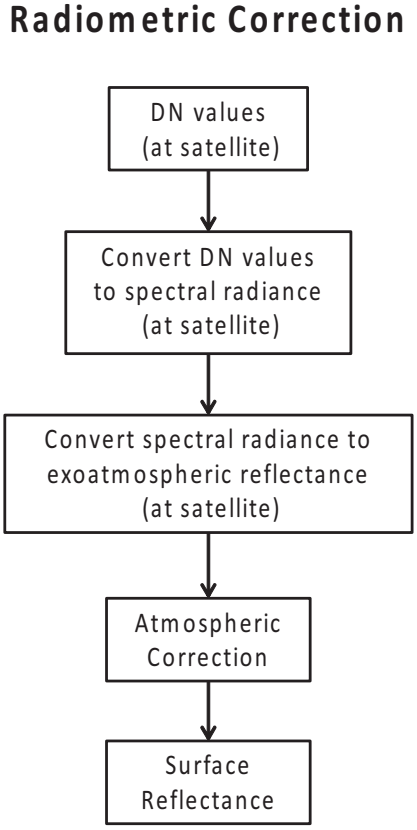


**Figure 2.1:** Radiometric correction process, showing steps followed for converting DN to surface reflectance.

Radiometric correction involves the use of standard equations to convert DN values to at-satellite reflectance. This processing intends to reduce the influence of *noise* in image brightness values and allow the development of a common radiometric scale, which will in turn allow merging multiple images and

comparison with images acquired by different sensors or on different days. The process is completed in the two following steps:

- DN is converted to at-satellite spectral radiance, and
- At-satellite spectral radiance is converted to at-satellite exo-atmospheric reflectance.

Conversion of spectral radiance to at-satellite exo-atmospheric reflectance facilitates better comparison among different scenes, by reducing in-between scene variability for the following three reasons: (a) The cosine effect of varying solar zenith angles of images acquired on different dates/times is removed (Chander and Markham, 2003); (b) Accounts for diverse values of exo-atmospheric solar irradiance due to differences between spectral bands; and (c) Balances the differences in the Earth-Sun distance due to images acquired on different dates (Chander and Markham, 2003).

At-satellite exo-atmospheric reflectance (which combines the surface and atmospheric reflectance seen at the satellite) derived from the previous step does not remove the atmospheric effects. The atmosphere is the primary source of noise preventing accurate measurements of surface reflectance (Song and Woodcock, 2003). Therefore, the key purpose of atmospheric correction is to define the atmosphere's optical properties and to then remove the atmospheric effects from the satellite images (Markham and Barker, 1986; Kaufman, 1989). Various algorithms have been proposed for this aim, including image-based correction algorithms (Chavez, 1988, 1989, 1996; Liang *et al.*, 2001, 2002; Song *et al.*, 2001; Song and Woodcock, 2003), which rely on utilization of information derived exclusively from the image to compensate for atmospheric effects. Further, a number of physically based models that use Radiative Transfer Codes have been proposed, such as 6S and Modtran, which require detailed in-situ field data of the atmosphere's characteristics at the date and time of image acquisition (Kneizys, 1988; de Haan *et al.*, 1991; Rahman and Dedieu, 1994; Vermote *et al.*, 1997; Hu *et al.*, 2001). These data are not available for most parts of the world, and therefore the application of Radiative Transfer Codes for atmospheric corrections is not easy (Lu *et al.*, 2002). Various other simpler methods, based exclusively on the image itself, have been suggested, such as Dark Object Subtraction (DOS) (Chavez, 1989, 1996; Moran *et al.*, 1992), histogram matching (Richter, 1996), invariant object (Hall *et al.*, 1991), path radiance (Wen *et al.*, 1999) and dense dark vegetation (Kaufman and Sendra, 1988; Liang *et al.*, 1997).

DOS is a non-parametric, strictly image-based atmospheric correction method, perhaps the most

widely used, and is suitable for areas with dense vegetation (Spanner *et al.*, 1990; Jakubauskas, 1996; Huguenin *et al.*, 1997). It is relatively simple to use and requires only information derived from the image itself. The method assumes that each image has dark objects with zero or near-zero surface reflectance (e.g. water, dark vegetation, shadowed areas due to topography) (Kaufman and Sendra, 1988). According to this method, the darkest DN value counting at least a thousand pixels (Teillet and Fedosejevs, 1995), is considered as the dark object, in each spectral band. Any signal that the sensor records from those dark objects is only due to atmospheric scattering and is subtracted from all the pixels in each spectral band (Chavez, 1989). The method is further described in Chapter 4, Section 4.3.1.

Studies that compared the accuracy of absolute and relative atmospheric correction algorithms with respect to classification and LUCC detection results, applied on multi-temporal datasets of Landsat-5 TM images, suggest that the simple DOS method produced improved accuracy in classification and change detection than the more complicated atmospheric correction algorithms, when consistency over a common scale is more preferable that accurate surface reflectance measurements (Song *et al.*, 2001; Hadjimitsis *et al.*, 2004; Chrysoulakis *et al.*, 2010). By bringing the multi-date images to a common scale, the spectral distance between images acquired on different dates is minimised. This is more important than precise surface reflectance values when the focus is in classifying the image and detecting changes through time and space (Song *et al.*, 2001). This simple method is preferred when atmospheric or meteorological data are not available (Hadjimitsis *et al.*, 2004) and can provide adequate results when used in applications related to land cover and vegetation (Chrysoulakis *et al.*, 2010).

In the UG basin study, where historical data sets of Landsat images are used to explore LUCC, in situ measurements of atmospheric parameters describing the atmospheric conditions during the image acquisitions are impossible to acquire. Consequently, physically based models cannot be employed for atmospheric correction and therefore the image based DOS method was selected to apply atmospheric corrections. The DOS method used in this study is described as DOS1 in the study by Song *et al.* (2001).

### 2.1.2 Land-use change detection

Change detection methods can be categorized into two types (Lu *et al.*, 2004):

- Those identifying change from non-change without providing any other information about the

nature of the change (using image differencing, vegetation index differencing, image ratioing and principal component analysis), by selecting appropriate threshold values (more detailed discussion in Section 2.1.2.1). Sometimes with these techniques it is not easy to separate between true and detected change as for instance the different phenological characteristics of crops can often be misleading.

- Those identifying detailed change from one land-use type to another (using post-classification change analysis, change vector analysis, and hybrid change detection methods), by providing a complete matrix of change directions after the development of accurate classification images. Change detection based on classification methods requires significant effort to be implemented and to provide accurate results but avoids problems such as the ones mentioned above.

#### 2.1.2.1 Vegetation Index differencing analysis

To identify change from no-change, the method applied in this study is vegetation index differencing analysis. This algebraic method was selected due to its broad usage across the scientific community and its computational efficiency. It helps detect possible changes in the vegetation cover and their significance (Singh, 1989), by highlighting changes in the Earth's surface spectral response and minimizing effects of topography and illumination. Based on relationships between different spectral bands, vegetation indices are more sensitive to the vegetation spectral response than the individual bands. The combination of red (TM Band 3) and near infra-red (TM Band 4) spectral bands allows for distinguishing vegetation from soil, because different vegetation covers demonstrate the same spectral behaviour in relation to other ground features and therefore allow identification of change from no change. Visible radiation in the red band is absorbed by chlorophyll while radiation in the near infrared band is strongly reflected by leaf cellular structures (Bannari *et al.*, 1995).

Vegetation indices produced by remote sensing data are extensively used for monitoring land use (Hadjimitsis *et al.*, 2009, 2010). Based on a literature search of land-cover change studies, the Normalized Difference Vegetation Index (NDVI), proposed by Rouse *et al.* (1974), was chosen for this study, to monitor vegetation dynamics. NDVI is the most well known and commonly used vegetation index and as previously mentioned by Song *et al.* (2001) has been applied in several studies to monitor vegetation

dynamics (Sader, 1987; Lenney *et al.*, 1996; Michener and Houhoulis, 1997). More details about NDVI are presented in Chapter 4, Section 4.3.1. According to Hadjimitsis *et al.* (2010), it is really important to account for atmospheric effects in satellite images before the calculation of any vegetation index, otherwise large inconsistencies might arise.

#### 2.1.2.2 Post-classification change analysis

Image classification of a multi-band raster image refers to the process of pixel categorization into one of several land-use classes. The raster produced from image classification can be used to create thematic maps of land use. There are two broad subdivisions of classification:

- Supervised classification, where the analyst interacts with the computer, identifying examples of the land-use classes in the imagery, referred to as "training areas", each of which is a known surface material that represents a desired spectral class. The computer performs a signature analysis to determine the average spectral pattern for each training class, by using an algorithm, and classifies the remaining pixels at the class they resemble most.

- Unsupervised classification, in which the computer generates its own spectral classes and the only intervention from the analyst is the definition of the number of classes to be produced. Usually, and as in this study, unsupervised classification is used as a preliminary guide for the selection of training sites before supervised classification.

After running the supervised classifications, it is easier to identify individual land-use classes and therefore the analyst is able to detect the main changes occurring in the study area, by overlaying two independent classifications. By applying a cross-tabulation detection method, a change matrix is produced showing different combinations of change that are identified. This method was selected because it is straightforward to implement whilst at the same time provides highly accurate results. Therefore, it is possible to quantify the changes knowing how much of a given land-cover type has changed and into what categories.

### 2.1.3 Accuracy Assessment

One of the most important steps to be followed after the classification of satellite images is the accuracy assessment of the classification. The classification algorithm might sometimes misclassify pixels either due to an analyst's error during the training procedure of the model or due to a spectral overlap between different land-use types.

The most widely used method for accuracy assessment is the error matrix, as it is the only way to effectively compare two maps quantitatively. The matrix consists of a square array of numbers, or cells, (set out in rows and columns), that express the number of sample units assigned to each land-cover type as compared to what is on the ground. Ground truth data is the first and most important step in accuracy assessment since the whole procedure will be pointless if the reference data are not trustworthy. From an error matrix, it is possible to calculate overall accuracy, Kappa coefficient (Eq. 2.1), omission and commission errors (Lu *et al.*, 2004). The Kappa coefficient is calculated from the error matrix as:

$$K = \frac{N \sum_{i=1}^{r} x_{ii} - \sum_{i=1}^{r} (x_{i+} \times x_{+i})}{N^2 - \sum_{i=1}^{r} (x_{i+} \times x_{+i})} \tag{2.1}$$

Where $N$ the grand total of observations, $r$ the number of rows in the matrix , $x_{ii}$ the number of observations in row $i$ and column $i$, $x_{i+}$ the marginal total for row $i$ and $x_{+i}$ the marginal total for column $i$.

Omission error (also known as producer's accuracy) is calculated by dividing the total number of correctly classified pixels in a class, by the total number of pixels of that class in the reference data (column total). The omission error denotes the probability of a reference data pixel being correctly classified. Commission error (also known as user's accuracy) is calculated by dividing the total number of correctly classified pixels in a class by the total number of pixels that were classified in that class (row total). The commission error denotes the probability that a pixel is classified on the map to actually represent the correct class on the ground.

Other methods developed to analyse the accuracy of change detection include accuracy assessment curves (Morisette and Khorram., 2000), and area-based accuracy assessment methods for the analysis

of change maps (Lowell, 2001). The accuracy assessment is not easy to perform due to the difficult collection of reliable ground truth data. In recent years, several accuracy assessment methods have been developed for single-date classified images but nevertheless, the error matrix method is still an important technique for the validation of change detection performance (Lu *et al.*, 2004).

To perform an accuracy assessment it is useful to obtain a set of field-based data that will be compared against the classified image. Alternatively, the use of aerial photography that is converted to a reference raster has the advantage of larger sample sizes and variety in the dates of acquisition. In this study, data from the Geo-Referenced Field Photo Library of the University of Oklahoma were used in the accuracy assessment. This is a data portal for sharing, visualizing and archiving geo-referenced photos from ground survey sites around the world (University of Oklahoma, 2011). GPS-derived coordinates for each of the ground survey sites were used to relate ground land use to the supervised classification results. In addition, validation points for each land-cover map were selected by visual interpretation of high-resolution imagery on Google Earth, along with ground truth data collected after a survey of the study area in 2012. After developing the error matrix, overall accuracy and Kappa Coefficients were calculated for each classification using techniques described in Congalton (1991).

## 2.2 Land-use change modelling approaches

### 2.2.1 Land-use and land-cover change

LUCC models were built to project spatial and temporal LUCC evolution and to define factors that drive land-use changes. As Brown *et al.* (2004) mention, it is important to separate between land-cover change and land-use change models. Land-use change is defined by human activity, while land-cover change might occur without human intervention (e.g., through climate change). The importance of this distinction lies in different data requirements and representation of processes, depending on which of the two types of change is addressed. However, representation of both types is required in order to bring together human actions and ecological processes (Brown *et al.*, 2004). Brown *et al.* (2000) suggest a modelling approach that projects changes in the forested areas as a result of socio-economic changes, by also taking into account human decision-making.

Several different LUCC models that have been used to explore changes have been described and reviewed in the literature. Some of these review studies offer an historical overview of the LUCC study over time, by presenting and evaluating selected theories and models of change and suggesting ideas that will help bridge the gap between policy-makers and LUCC modellers (Briassoulis, 2000; Sohl and Claggett, 2013). Other studies are based on the models' ability to predict specific changes such as land-use intensification, deforestation and dryland degradation (Lambin, 1997; Kaimowitz and Angelsen, 1998; Lambin *et al.*, 2000). There are also review studies that explore the functionality and ability of different models in terms of scale (both spatial and temporal) and complexity, and how well they incorporate time, space and human-induced factors (Agarwal *et al.*, 2002), whilst other studies offer reviews of specific types of modelling systems, such as the studies by Parker *et al.* (2003); Bousquet and Page (2004), for multi-agent models.

### 2.2.2 Model categories

Over the last years, a remarkable increase in the available LUCC modelling tools has been observed (Sohl and Claggett, 2013). Different approaches such as agent-based models and cellular automata models have substantially improved the representation of complex systems, offering different levels of modelling complexity, depending on the input data availability (Sohl and Claggett, 2013). As there is a large diversity of modelling approaches and concepts underlying the models, several studies suggested classification schemes for the different LUCC models (Verburg *et al.*, 2006). According to Lambin *et al.* (2000), four broad categories of LUCC models are distinguished: empirical-statistical, stochastic, optimization and dynamic (process-based) simulation models.

Empirical-statistical models use multiple linear regression techniques to identify the causes of LUCC in empirically-derived rates of change. Therefore, although these regression models fit well in specific regions from where the original data are obtained, they can perform poorly in other regions. In addition, these models are only able to simulate LUCC types that have already existed at some point in the past. Examples of such model applications are the studies by Veldkamp and Fresco (1996); Geoghegan *et al.* (2001).

Stochastic models are based on transition probabilities (i.e. changes from one land-cover category

to another) to describe the states of the system. Similarly to empirical-statistical models, stochastic models can only model transitions that have been observed in the past, which is not always the case. For example, Luijten (2003) presented a spatially explicit stochastic methodology to simulate LUCC without describing relationships between human decision-making, environmental processes, and socio-economic components that affect land-use transitions at the local scale. Another type of stochastic models is the Cellular Automata (CA). These are grid-based models, in which the land-use state of each cell evolves according to transition rules defined by the cell's historic transitions and the state of the neighbouring cells (Sohl and Claggett, 2013). Indicative descriptions of such models can be found in the studies by Clarke *et al.* (1997), White *et al.* (1997) and Wu (1998). CA models can be relatively straightforward to implement, and quite often are combined with other models such as agent-based or Markov chain models in order to minimize their limitations (Sohl and Claggett, 2013).

Optimization models apply optimisation techniques by using linear programming or general equilibrium models. Such models examine how various policies impact the direction of land-use change. Objectives and constraints are subject to criteria representing optimal land-use allocation (such as biodiversity, sediment loss, erosion, greenhouse gas emissions etc.). However, these models have important limitations such as human behaviour, which in reality cannot be optimised. Indicative descriptions of such models can be found in the studies by Kaimowitz and Angelsen (1998) and Fischer and Sun (2001). While the previously mentioned CA models are focused on representing biophysical landscape change and historic transition rules, agent-based models (which belong into the optimisation type of models), such as the one described by Rouchier *et al.* (2001), focus mostly on human actions by describing the decision-making processes and influence of individual agents' behaviour on LUCC (Parker *et al.*, 2003).

Dynamic (process-based) models take into account the feedbacks of biophysical and socio-economic processes into land-cover changes. In recent years several dynamic process-based LUCC models have been developed and described in the literature (Parker *et al.*, 2003; Verburg *et al.*, 2009; Stephenne and Lambin, 2001; Alcamo *et al.*, 1998). Dynamic models are able to represent human decision making, environmental management policies and take into account the processes that are driving LUCC.

Finally, Lambin *et al.* (2000) mention a new approach, the Integrated modelling approach, which is based on combining elements of the above mentioned model categories. Examples of such combined tools are presented in the next Section.

### 2.2.3 Integrated modelling examples

In recent years, an increased number of LULC change modelling tools have been linked with each other, leading to multidisciplinary modelling frameworks.

For instance, Claessens *et al.* (2009) coupled the LUCC model CLUE (Conversion of Land Use and its Effects, Verburg *et al.*, 2002) with the landscape process model LAPSUS (LandscApe ProcesS modelling at mUlti-dimensions and Scales, Schoorl *et al.*, 2002), which simulates water and tillage erosion and sedimentation, to model interactions and feedbacks between LUCC and geomorphic processes.

The CLUE modelling framework (Veldkamp and Fresco, 1996; Verburg *et al.*, 1999) uses empirically calculated relationships between land use and its drivers to dynamically model LUCC. The model allows for simulating multiple land-use classes, which may dynamically interact with each other. A modified approach of the model for regional applications, named CLUE-s (the Conversion of Land Use and its Effects at Small regional extent), has also become available (Verburg *et al.*, 2002).

Over the last years, different versions of the CLUE model have been linked to several other models: Renwick *et al.* (2013) combined the CAPRI[1] (Common Agricultural Policy Regionalised Impact) and Dyna-CLUE (Overmars *et al.*, 2007; Verburg and Overmars, 2009) models to examine impacts related to agricultural land-use conversion and modified trade policies across the EU. Verburg *et al.* (2008) presented a modelling scheme that would assist policy discussions as formed in the Eurialis project (Westhoek *et al.*, 2006). Three models are linked together: an extended version of the global economic model GTAP (Global Trade Analysis Project), the IMAGE (Integrated Model to Assess the Global Environment) model and CLUE-s. Their study provides a useful tool in locating hot-spots of land-use change and in assessing impacts of LULC changes on various environmental indices.

Agent-based models are often linked with other modelling tools, especially CA models, in order to address the complexity associated with spatial heterogeneity and structural hierarchy for which they don't explicitly model (Sohl and Claggett, 2013). According to Parker *et al.* (2003), this linkage is a promising direction for future LUCC model development.

Finally, the IMAGE model (Bouwman *et al.*, 2006; Strengers *et al.*, 2004) is an integrated assessment model which explores the long-term dynamics of global environmental change. It takes into account

[1]The project website www.capri-model.org provides information on the model and a list of its applications.

basic drivers of LUCC such as demographics, economic development, agricultural demand, energy consumption and production, along with trade and production (Bouwman *et al.*, 2006), and links them with biophysical and socio-economic processes.

### 2.2.4 The selected model for the study area

To develop realistic LUCC models it is essential to identify the most important drivers of change (Veldkamp and Lambin, 2001). LUCC is driven by socio-economic and biophysical factors (Lambin *et al.*, 2001). Therefore to make valid predictions about future LUCC it is necessary to understand the causes of historic LUCC. However, the data requirements of the dynamic and integrated models do not allow for their implementation in a data scarce region such as the UG basin. Similarly, due to lack of relevant policy information optimisation models were not possible to apply. Therefore, to overcome this limitation, a stochastic model (Markov chains) was selected. This approach has been extensively applied in studying land-use change in the past and before applying it the method was tested to evaluate its validity for projecting land-cover changes in the study area.

Many studies of land-cover change analysis use Markov's modelling (Drewett, 1969; Lever, 1973; Bell, 1974; Muller and Middleton, 1994; Weng, 2002; Petit *et al.*, 2001; Wu *et al.*, 2006; Rajitha *et al.*, 2010; Moghadam and Helbich, 2013). These studies are mainly focused on small areas and based on data sampled from field work, existing maps or aerial photography. The application of Markovian analysis in large scale systems such as the UG basin, is a challenge for this study. The usage of satellite images is expected to reduce uncertainty and improve the analysis. The method is based on the assumption that the driving forces that produced changes in the past will continue to do so into the future. Future scenarios for the years up to 2035 were generated based on developed historic land-cover maps. These historic maps and future scenarios were subsequently used to drive the LSM JULES and analyse the effects of LUCC on the hydrology of the UG basin.

## 2.3 The dynamics of land surface - atmosphere interactions

### 2.3.1 LUCC feedbacks on water resources and the climate

Understanding the impacts of LUCC on terrestrial hydrology is a prerequisite for optimal management of water resources (Scanlon *et al.*, 2005) because LUCC can significantly influence catchment hydrological processes such as infiltration, groundwater recharge, and runoff (Lin *et al.*, 2007). Spatially distributed hydrological models relate model parameters to observed land-surface properties and therefore provide a framework to investigate and interpret the relationships between climate, hydrology and human decision-making (Legesse *et al.*, 2003; Haverkamp *et al.*, 2005). Lately, hydrological models have been widely used in quantification of the impact of LUCC and different land-use management policies on the hydrologic cycle (Bultot *et al.*, 1990). Regionalised conceptual and physics based models have been applied in different climate regions, for different LUCC scenarios, with the aim of developing a methodology to assess the effects of LUCC on the hydrologic response of a catchment (Wooldridge *et al.*, 2001; Hundecha and Bardossy, 2004; Liu *et al.*, 2009; Kalantari *et al.*, 2014). These effects were found to depend on the spatial distribution of LUCC as well as the size and timing of storm events (Kalantari *et al.*, 2014). Another methodology suggested by Lorup *et al.* (1998), combines common statistical methods with hydrological modelling in order to distinguish between the effects of climate variability and LUCC on catchment runoff, by analysing long hydrological time series.

Several studies have shown that anthropogenic LUCC (e.g. deforestation, agricultural expansion, urbanisation) affects the climate by influencing the land surface properties and the hydrologic cycle (Foley *et al.*, 2005; Kalnay and Cai, 2003). Deforestation was found to have a significant radiative effect on global climate (Matthews *et al.*, 2003) via increased surface albedo that leads to increased reflection of incoming solar radiation and eventually surface cooling. On the other hand, agricultural expansion causes surface warming resulting from increased release of latent heat flux through the process of evapotranspiration. Depending on the location and the season, the relative importance of these two opposite effects may vary. For instance, Bounoua *et al.* (2002) found that conversion from forest and grassland to agricultural areas causes cooling in temperate latitudes and warming in the tropics. When averaged globally, these opposite effects cancel each other out. Therefore, the regional signal of LUCC is impor-

tant (Bounoua *et al.*, 2002). The importance of LUCC signature at regional scales has been highlighted by other authors as well, as often impacts of LUCC in a sub-basin scale cancel each other out at the catchment scale (Wagner *et al.*, 2013).

### 2.3.2 Land surface - atmosphere feedbacks in Northern India

The north Indian plains are amongst the most densely populated and intensively cultivated areas in the world. More than 400 million people depend on monsoon rainfall for their livelihood. Land-cover change may affect the water resources of northern India in complex ways. In early modelling experiments, Meehl (1994) showed that the increase in soil moisture at the land surface due to irrigation influenced the strength of the Asian monsoon. More recently, several studies of the Global Land-Atmosphere Coupling Experiment (GLACE; Koster *et al.*, 2004, 2006; Guo *et al.*, 2006; Seneviratne *et al.*, 2006), based on an ensemble of 12 atmospheric general circulation models, identified a strong feedback mechanism between the land surface (soil moisture) and the atmosphere (precipitation). This arises because the amount of soil moisture at the land surface affects the partitioning between sensible and latent heat: more soil moisture increases the latent heat flux and reduces the amount of energy available to warm the air at the near surface (Pitman, 2003). This, in addition to feedbacks on stomatal conductance in vegetation, alters the properties of the boundary layer.

Further, high evaporation linked to croplands and irrigation systems, causes increased humidity and reduced temperatures near the surface, followed by lower actual and potential evaporation. These changes can lead to local feedbacks in cloud formation and convection. Local feedbacks on convection have already been observed elsewhere in the tropics, e.g. in the Sahel (Taylor and Ellis, 2006) and in West Africa (Lavender *et al.*, 2010). However, feedbacks may apply also on larger spatio-temporal scales. Much evidence already suggests that land-surface conditions in the Indo-Gangetic Plains are coupled to precipitation patterns. A study by Sen Roy *et al.* (2010) linked soil moisture from irrigation to increased precipitation during the dry season. Turner and Annamalai (2012) suggest that the South Asian monsoon is a fully coupled ocean-land-atmosphere system while previous studies found that croplands play an important role in determining the local climate. Yamashima *et al.* (2011) found evidence that the impact of LUCC on the hydroclimate of the *hot spots* (as identified by Koster *et al.*, 2004) is high. Therefore,

the classical theory supporting the claim that the strength of the monsoon systems is a consequence of the land-sea temperature contrast appears to need to be made much more complex.

Agricultural intensification and irrigation increase the latent heat flux and energy distribution in the Indian monsoon region. As previously mentioned, this reduces the surface temperature and consequently alters precipitation patterns over the Indian monsoon region (Douglas *et al.*, 2009). An 11% increase in mean annual vapour fluxes, attributed to irrigation, highlights the impact of irrigated agriculture on land-atmosphere interactions in India (Douglas *et al.*, 2006). In the humid tropical regions, the mean climate was found to be altered by varying crops (Osborne *et al.*, 2009) suggesting a strong feedback of crops on seasonally arid climates. Several other studies have analysed the climatic impacts of anthropogenic LUCC and found similar results which highlight the significant impacts of agricultural expansion in regional temperature and precipitation over India (Zhao *et al.*, 2001; Findell *et al.*, 2007). The conversion of forested areas to agricultural lands and the resulting agricultural intensification from 1700 to 1850 reduced precipitation during the summer months over India (Takata *et al.*, 2009). LUCC was found to be the major source of climate disturbance during that period. The impact of those LUCC on the seasonal cycle of the hydro-climate of India was investigated on a follow-up study by Yamashima *et al.* (2011). The authors found that conversion from forested areas to croplands results in decreased precipitation, evapotranspiration, and soil moisture throughout the year.

The pressure on water resources in India is likely to increase further, with forecast population growth together with continued economic progress (Tenhunen and Saavala, 2012). Consequently it is essential to understand historic trends in LUCC and make valid predictions of future changes in order to understand their effects on water resources and improve water security in the region.

## 2.4 Introducing dynamic vegetation growth in LSMs

LSMs are tools that represent the exchange of energy and water fluxes between land and the atmosphere, the above ground gas transfer and below-ground heat and water transfer. Although much progress has been made in adding detailed physical processes into these models, there is much room left for improved estimates of evapotranspiration (ET) fluxes, by including a more reasonable and accurate representation of crop dynamics. As previously mentioned, recent studies suggest a strong land-surface–atmosphere

coupling over India and since the study area is part of one of the most intensively cultivated areas in the world, the strong impact of crops on the evaporative flux cannot be neglected.

Changes in climate factors affect the vegetation dynamics and vice-versa. Nowadays, it is common practice that LSMs are driven with prescribed vegetation dynamics. Vegetation parameters such as Leaf Area Index (LAI), root depth and canopy height are obtained off-line and they either remain constant throughout the entire simulation period or can vary temporally and/or spatially depending on data availability prior to the simulation. However, such a simplified approach is expected to have a negative impact on the LSM's performance, by affecting the simulated ET fluxes and ultimately obstructing weather and climate predictions and assessment of their impact on water resources.

This is especially the case in the Ganges basin, a region which experiences monsoon flooding almost every year. In that region, the need for better predictions of the water resources regime and understanding of the land-surface–atmosphere interactions is very important.

To overcome this limitation, several recent studies achieved dynamical coupling of LSMs, climate or hydrological models with crop growth models (Boegh *et al.*, 2004; Mo *et al.*, 2005; Pauwels *et al.*, 2007; Osborne *et al.*, 2007; Maruyama and Kuwagata, 2010; Lei *et al.*, 2010; Black *et al.*, 2012; Li *et al.*, 2013). Efforts have also been made to include dynamic vegetation representation in LSMs (Cox *et al.*, 2000; Dai, 2003; Van den Hoof *et al.*, 2011) and hydrologic models (Calvet *et al.*, 1998; Calvet and Soussana, 2001; Li *et al.*, 2011).

Depending on different purposes, these studies achieved the following: (a) improved representation of the two-way interactions between climate and crop growth (Osborne *et al.*, 2007; Pauwels *et al.*, 2007; Lei *et al.*, 2010; Van den Hoof *et al.*, 2011; Black *et al.*, 2012; Li *et al.*, 2013); (b) improved simulated latent heat fluxes (Arora, 2003); (c) investigated the impact of agriculture on the energy budget, carbon and water cycles (Casanova and Judge, 2008; Maruyama and Kuwagata, 2010; Li *et al.*, 2013); (d) represented the yield and phenology of crops, water consumption and water-use efficiency (de Noblet-Ducoudré *et al.*, 2004; Mo *et al.*, 2005); and (e) investigated the feedbacks of soil moisture and evaporative demand on photosynthesis (Garcia-Quijano and Barros, 2005).

In this study the LSM JULES (Best *et al.*, 2011) is applied in order to investigate the impact of inter-seasonal LUCC in the ET fluxes of the UG river basin in India. JULES was developed by the UK Met Office and is based on MOSES (Met Office Surface Exchange System), the LSM used in the

Unified Model of the UK Met Office. It is a combined process-based distributed/lumped parameter model that simulates the exchange of energy, water, and carbon fluxes between land surface and the atmosphere. However, JULES in its current version does not simulate crop growth[2] and $C_3$ grass is often used by the model as proxy for annual crops (Van den Hoof *et al.*, 2011). This simplified approach has a disadvantage: parameters which in reality are constantly evolving, remain constant throughout long periods. Given that the larger part (60%) of the UG basin is occupied by agriculture, such simplification is expected to lead to errors in the model results. In order to overcome this problem and develop a system able to dynamically simulate crop development and its interactions with land surface properties, JULES was coupled with the crop growth model InfoCrop (Aggarwal *et al.*, 2006a). During the growing season, the new coupled system will allow for consistent variation of crop parameters.

The novelty of my approach lies in the combination of the following points: (1) The potential error in ET estimations of LSMs with no dynamic vegetation is quantified, by comparing the pre-coupling and post-coupling modelling results; Most of previous studies did not show modelling results before the coupling. This allows for testing the sensitivity of an LSM with regard to the dynamics of the vegetation cover; (2) The large spatial scale of the application; Most of the past studies are focused on small scales, or even point scales, and validated their results against flux tower sites. The extent of the agricultural areas in the UG basin, and the lack of in situ measurements make it a very challenging research environment; (3) The specific focus on impact on evaporative flux, contrasting to most coupling studies that focus on LAI, crop yield and/or soil moisture fluxes.

The dynamic coupling of an LSM with a crop growth model is expected to improve the modelling of land surface processes and allow further investigations of the two way interactions between crops and the atmosphere, whilst quantifying the potential error in ET fluxes generated by LSMs with no dynamic vegetation.

[2]The most recent version of JULES (v4.1) that was released on November 2014 includes a crop model, but was not available during the course of this research

## 2.5 The future climate of India

India's population depends largely on the summer monsoon rainfall for food and energy production, agricultural activities and industrial development. Over recent years, extreme weather events in South Asia, such as the July 2002 drought over India (Bhat, 2006), the Pakistan floods of July-August 2010 (Lau and Kim, 2011), and the north India floods of July 2013, have claimed thousands of lives and could be attributed to a changing climate and poor environmental management. The World Bank in a recent report (World Bank, 2013) states that an extremely wet Indian summer monsoon which currently occurs once every 100 years, is projected to occur once every 10 years by the end of this century. Several other studies, including the IPCC's Fifth Assessment Report (Intergovernmental Panel on Climate Change (AR5), IPCC, 2014b), are linking climate change to extreme weather events over south Asia. Given the rapid increase in population in that region and the need for water and food security, it is essential to understand how the climate will change in the future and how its change will impact humans and the environment.

In many regions of India, the increased population is already facing water stress (World Bank, 2013). The projected impacts of climate change on the Indian subcontinent vary from extreme heat waves, changing rainfall patterns, droughts, floods, groundwater depletion, glacier melt, sea level rise, to agriculture and food security crisis, energy and water security threats, and human health impacts among others.

Some of the points highlighted by the 5th IPCC report (IPCC, 2013), related to the present and future climate of India are the following:

- "There is medium confidence that in India modern large floods are comparable or surpass historical floods in magnitude and/or frequency."
- "There is medium confidence that overall precipitation associated with the Asian monsoon will increase but with a north-south asymmetry: Indian monsoon rainfall is projected to increase. There is medium confidence in that the Indian summer monsoon circulation weakens, but this is compensated by increased atmospheric moisture content, leading to more rainfall."
- "In India, flood frequencies since 1950 are the largest for the last several hundred years for eight

rivers, interpreted as a strengthening of the monsoon conditions after the Little Ice Age (LIA) between 1450 and 1850 (Kale, 2008)."

- "The Himalayan Glaciers' melting due to climate change is expected to affect water resources in terms of quantity and quality, leading to increased runoff volumes downstream."

IPCC AR4 climate model simulations consistently show that warming over land exceeds warming over sea as a result of greenhouse gas forcing, which is consistent with observations suggesting that surface temperature over land increases faster than surface temperature over the ocean (Sutton *et al.*, 2007).

The CMIP5 (Coupled Model Intercomparison Project Phase 5) model projections for the end of this century suggest an intensification of heavy precipitation events over India under the scenarios with a continuous rise in radiative forcing (Scoccimarro *et al.*, 2013). The average summer rainfall over India will increase by around 5-10%, pointing towards a wetter on average summer season (Turner, 2013). According to these projections, precipitation intensity seems to increase more than mean precipitation under a warmer climate (Scoccimarro *et al.*, 2013; Meehl *et al.*, 2005), which is physically consistent with the fact that warmer air can hold more moisture, leading to more intense rainfall when it does occur (Turner and Annamalai, 2012). Therefore, the suggested increase in the summer monsoon rainfall is directly related to the projected increase of the land-sea thermal contrast but also to the projected temperature increase over the Indian Ocean, which will allow for more moisture to be advected towards India (Hu *et al.*, 2000; May, 2002; Ashrit *et al.*, 2003; May, 2004; Ueda *et al.*, 2006; Turner *et al.*, 2007; Kripalani *et al.*, 2007; Cherchi *et al.*, 2011; Turner and Annamalai, 2012). Besides, the Indian Ocean/western Pacific warm pool region has a nearly monotonous warming trend in the past 50 years (Knutson *et al.*, 2006) and it could potentially allow for an increase in the moisture supply over the Indian continent (Turner and Annamalai, 2012). More rainfall would increase water availability but on the other hand, the larger inter-annual variability in summer rainfall could be associated with more frequent/severe flood and drought events. The spatial patterns of these changes vary from model to model, making it difficult to project how rainfall might change within India (Turner and Slingo, 2009).

In addition, most of the recent studies suggest a weakening of the summer monsoon circulation, due to the warming over the tropics in the middle-to-upper troposphere, which is responsible for the reduction

in the meridional thermal gradient in the Asian region (Ueda *et al.*, 2006).

Another set of studies are considering the effects of aerosol forcing on the Indian summer monsoon (Lau *et al.*, 2006; Meehl *et al.*, 2008; Collier and Zhang, 2009; Wang *et al.*, 2009; Fatima *et al.*, 2010; Ganguly *et al.*, 2012; Bollasina *et al.*, 2013). The observed earlier onset of Indian monsoon, which is responsible for increased June rainfall over India was found to be related to the presence of aerosols (Bollasina *et al.*, 2013). Aerosols are responsible for the reduction of incoming solar radiation at the surface, due to absorption and scattering (Charlson *et al.*, 1992) and therefore the weakening of the SST gradient. It is possible therefore for aerosols to offset the impact of GHG on India's precipitation patterns, by limiting monsoon rainfall. According to Ramanathan *et al.* (2005), aerosols are responsible for 50% masking of the surface warming due to GHGs and the mitigation of both aerosol and GHG impacts could explain the lack of an abrupt transition in the seasonal monsoon precipitation (Turner and Annamalai, 2012).

The future daily patterns of weather over India, such as changes in precipitation intensity, number of dry/wet days, and active-break events, remain still highly uncertain (Turner, 2013). More confidence in the projections of day-to-day and intra-seasonal variability will arise from (a) better understanding of the physical processes going on, (b) improved observations, and (c) better simulations in numerical weather prediction and climate models (Sperber *et al.*, 2013). It is expected that in the near future, high-resolution multi-model regional climate change projections for India will bring more confidence (Chaturvedi *et al.*, 2012).

Apart from changes in precipitation, there are significant feedbacks between the carbon and water cycle under climate change conditions. Increased $CO_2$ concentrations would mean that the photosynthetic carbon fixation rate of the plants would increase, whilst stomatal conductance would decrease. Plants would get sufficient $CO_2$ uptake and would not need their stomata to be as open as under lower $CO_2$ concentrations (Taub, 2010). That essentially means that plants water use efficiency would be improved, leading to reduced rates of transpiration. On the contrary, increased air temperature would lead to higher potential evaporation as warmer air can hold more moisture, counteracting the effects of increased $CO_2$ concentrations on evapotranspiration (IPCC, 2007).

### 2.5.1 Bias correction for climate projections

The CMIP5 precipitation projections are likely to provide unreliable estimates of the mean values and daily variations of precipitation due to inherent limitations of the GCMs (Raty *et al.*, 2014). In addition, biases have also been identified in simulating the present-day observed Indian summer monsoon climatologies (Sengupta and Rajeevan, 2013). To diminish the impacts of GCM biases, several techniques that adjust the climate projections have been developed over the last years and plenty of studies have revised and evaluated these techniques (Fowler *et al.*, 2007; Maraun *et al.*, 2010; Piani *et al.*, 2010; Teutschbein and Seibert, 2012; Raisanen and Raty, 2013; Raty *et al.*, 2014). There are two broad categories of such adjusting techniques: a) Delta-change methods, which apply the ratios between simulated historic and future projections to scale the observed climate, and b) Bias correction methods which adjust the future projections based on differences between the observed and simulated historic climate (Raisanen and Raty, 2013; Raty *et al.*, 2014).

In this study, the delta-change method was applied as it is the simplest approach that can be applied in multi-model ensembles with small computational effort, given the time-constraints of the present work. In addition, it is a method broadly used for transforming coarse resolution GCM outputs into finer scale products suitable for hydrological applications. It calculates the change in time between the control and future GCM simulations of a variable and applies this change in the baseline climate by simply adding or scaling the mean climatic change factor (CF) to each day (Fowler *et al.*, 2007). However, this approach has a number of limitations: a) It assumes a constant GCM bias through time, as it suggests that relative change is better simulated than absolute values; b) It assumes a constant spatial pattern of the climatic variable and ignores changes in variability, as the calculated CFs only scale the mean, max and min values; c) There is no change in the temporal sequence of wet/dry days (Fowler *et al.*, 2007).

### 2.5.2 Impacts of Climate Change on humankind and the environment

A declining trend of the Indian monsoon rainfall since the 1950s has already been observed but the frequency of heavy rainfall events has increased (World Bank, 2013; Turner and Annamalai, 2012; Joseph and Simon, 2005). This change in the variability of monsoon rainfall could be responsible for the biggest impacts on short time scales as it can be associated with increased floods but also more droughts (World

Bank, 2013; Turner and Annamalai, 2012).

The consequences of more frequent droughts in a country whose economy is based on crop production could be severe. According to the World Bank (2013), more than 60% of India's agricultural areas are rain-fed. Drought periods, followed by ground water depletion could have dramatic impacts in the stability of Indian economy and food production for millions of people. Even a small change of 5-10% in the Indian summer monsoon could have impacts on the agricultural production and the stocks and commodities market.

Rivers such as the Brahmaputra and Indus, are mainly glacier-fed rivers and a potential melting of Himalayan glaciers due to temperature rise could lead to higher spring flows during the snow melt season (World Bank, 2013). On the other hand, in the rainfall-runoff-dominated UG basin, flows are expected to increase (at least until 2050) due to a projected increase in precipitation (Lutz *et al.*, 2014). The contribution of glacier melt in the UG basin is small and the future hydrology largely depends on the monsoon precipitation signal (Lutz *et al.*, 2014).

Densely populated coastal cities like Mumbai are under high risk of sea water flooding, due to a potential increase in the sea water levels. The whole India is near the equator and it is expected that it will be much more affected by rising sea levels than other latitude regions (World Bank, 2013).

Hydro-power stations and thermal power plants, which are the dominant power generation mechanisms in India, are under direct threat by a potential water resources depletion. Less regulated river flows along with temperature increase could pose major threats to these power generation sources (World Bank, 2013).

# Chapter 3

# Study Area Description

# Study Area Description

## 3.1 General Characteristics

The river Ganges originates in the southern Himalayan mountains, on the Indian side of the Tibetan border. It flows through the Gangetic plains of Northern India, and following a south-east direction it flows into the Bay of Bengal. It has been declared the national river of India and as a source of water for agriculture, transportation and energy, sustains one of the most densely populated areas of the world. Its religious significance is immense. It is the most sacred river of India, a spiritual entity and symbol of purity for the whole country. Some of the most important cities of India are located along its banks (IIT Kanpur - Gangapedia, 2013).

The study area is the Upper Ganges (UG) basin, which corresponds to the main upper branch of Ganges and covers an area of $87{,}000\,\mathrm{km}^2$. The domain is located in northern India between longitudes $77°$E to $81°$E and latitudes $25°$N to $32°$N. Elevation ranges from $7400$ m in the Himalayan mountain peaks to $90$ m in the plains (Fig. 3.1). The UG basin lies in the states of Uttaranchal and Uttar Pradesh and the main physical subdivisions of the area are the northern mountainous regions (Himalayan foothills) and the Gangetic plains.

In the upstream mountainous regions where the river originates, hydro-power is the main focus of development with mega and micro projects either already operating or currently under construction (Bharati *et al.*, 2011). When the river reaches the plains, it becomes subject to a vast irrigation demand as more than 410 million people are depending on it to cover their daily needs (Verghese, 1993).

The plains are characterised by highly regulated and reduced flows due to the development of numerous water structures (dams, barrages and irrigation canals), as illustrated in Fig. 3.2, which cause impacts on the water quality and availability whilst at the same time affecting the riverine ecosystems (Bharati *et al.*, 2011). The two main dams in the UG basin are Tehri and Ramganga (Fig. 3.2). The three main canal systems are the Upper Ganga canal (starting at Bhimgoda Barrage), the Madhya Ganga

canal and the Lower Ganga canal (starting from Narora barrage), irrigating 2, 0.18 and 0.5 million ha respectively (Bharati *et al.*, 2011). Numerous hydro-power plants constructed on the Upper Ganga canal are using its falls to generate power (Jain *et al.*, 2007). Although there is a rich canal network in the UG basin, the storage capacity of reservoirs (apart from those at Tehri and Ramganga) is not large enough to permit preservation of flows during the monsoon season and dry season flows are not sufficient to maintain ecosystem and other demands (Jain *et al.*, 2007).

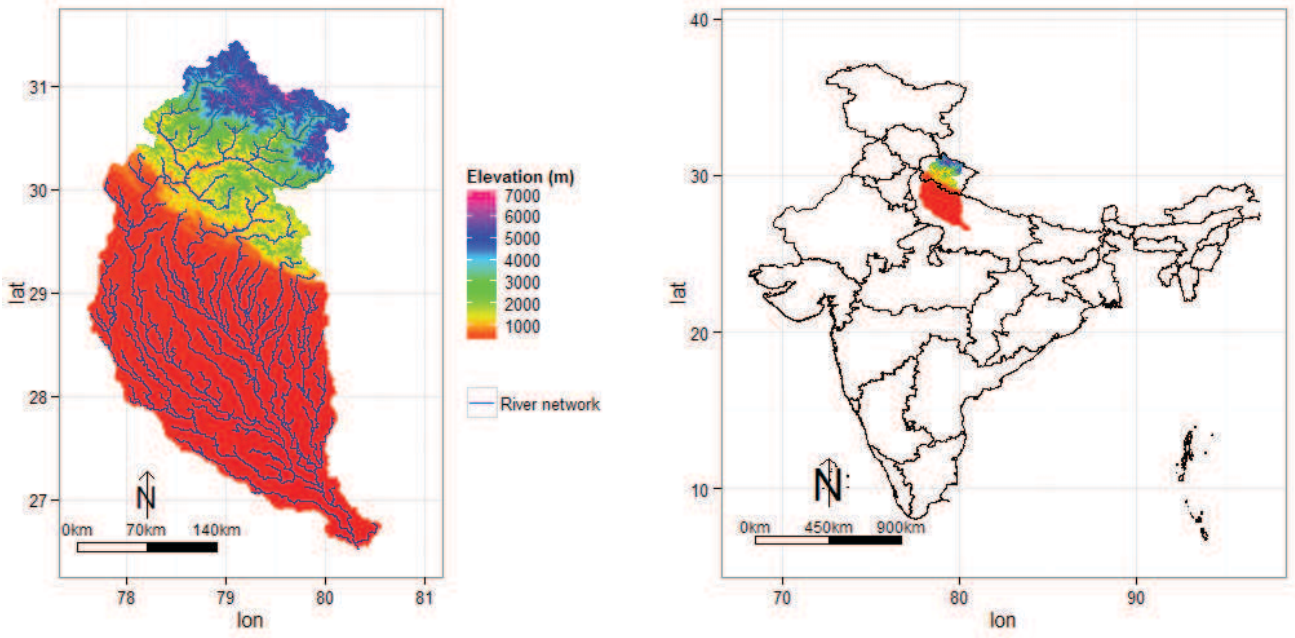


**Figure 3.1:** Location map of the study area in north India and a Digital Elevation Model (DEM) of the UG basin showing the ranges of the elevations (m altitude). The UG basin was delineated using the 90m resolution SRTM digital elevation map and the eight-direction (D8) flow model, following an approach presented in Jenson and Domingue (1988). Kanpur barrage was used as the outlet point.

As shown in Fig. 3.3, areas in the north of the UG basin (Himalayas) are either barren or covered by snow. The central and northern parts of the catchment are dominated by forests (20% of the total catchment area). Around 60% of the basin is occupied by agriculture (main crop types include wheat, rice, maize, sugarcane, bajra and potato). Most of the urban and agricultural areas in the basin are located towards the south, in the plains of the UG basin.

The soils dominating the upper areas of the catchment are classified as Leptosols (Fig. 3.4). They are very shallow and erodible soils, formed usually on continuous hard rocks, allowing minimal development

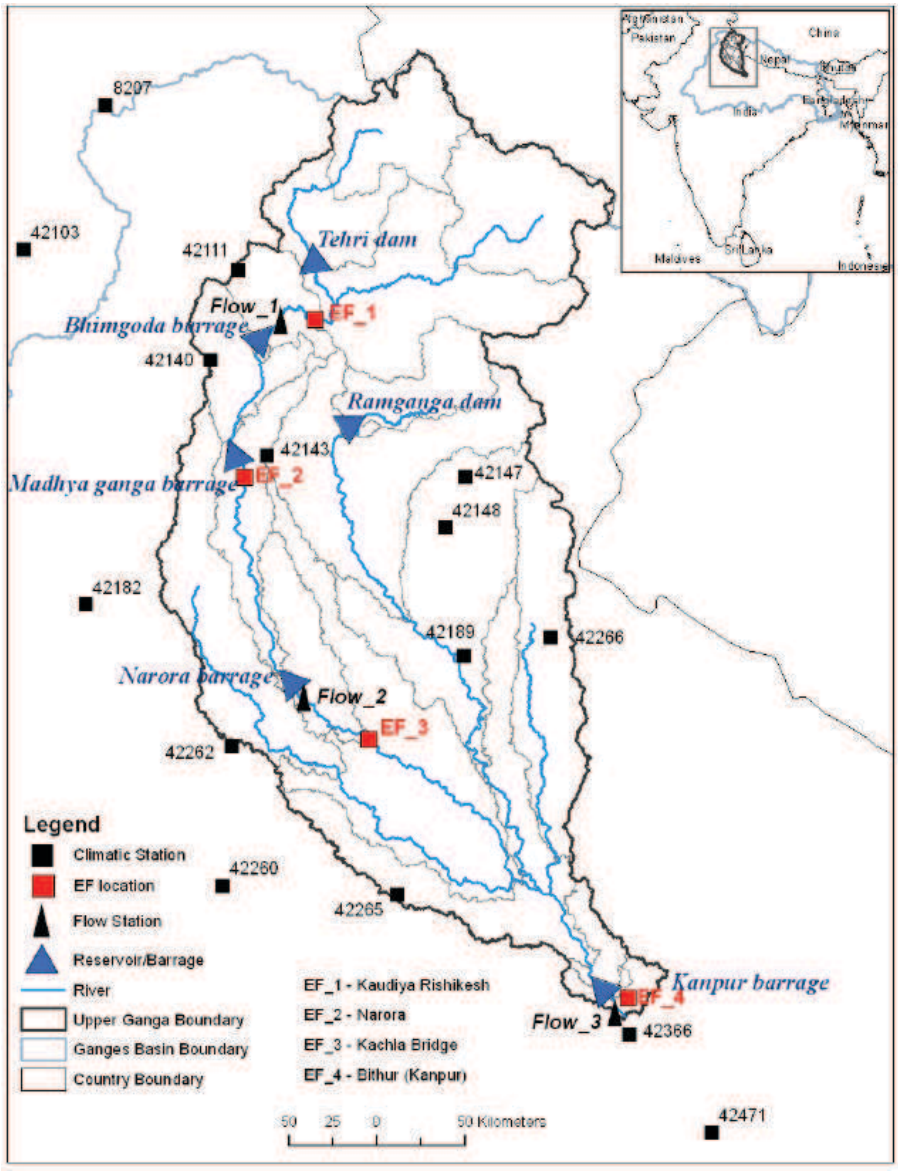


**Figure 3.2:** Locations of barrages, reservoirs, environmental flows (EF) sites, climatic stations and flow measurement stations of the UG basin. From: Bharati *et al.* (2011); Sapkota *et al.* (2013)

(Chesworth, 2008). Thicker, more fertile Cambisols and Fluvisols are found in the lowland areas. Most farms are located in Fluvisol dominated areas because they form easily worked land. These soils are often wet due to the presence of groundwater or river flood water (Chesworth, 2008). Lixisols, located on the west part of the UG basin, are characterised by low levels of nutrients, are greatly affected by water erosion, making agriculture possible only with frequent fertilizer applications. Of alluvial origin is the

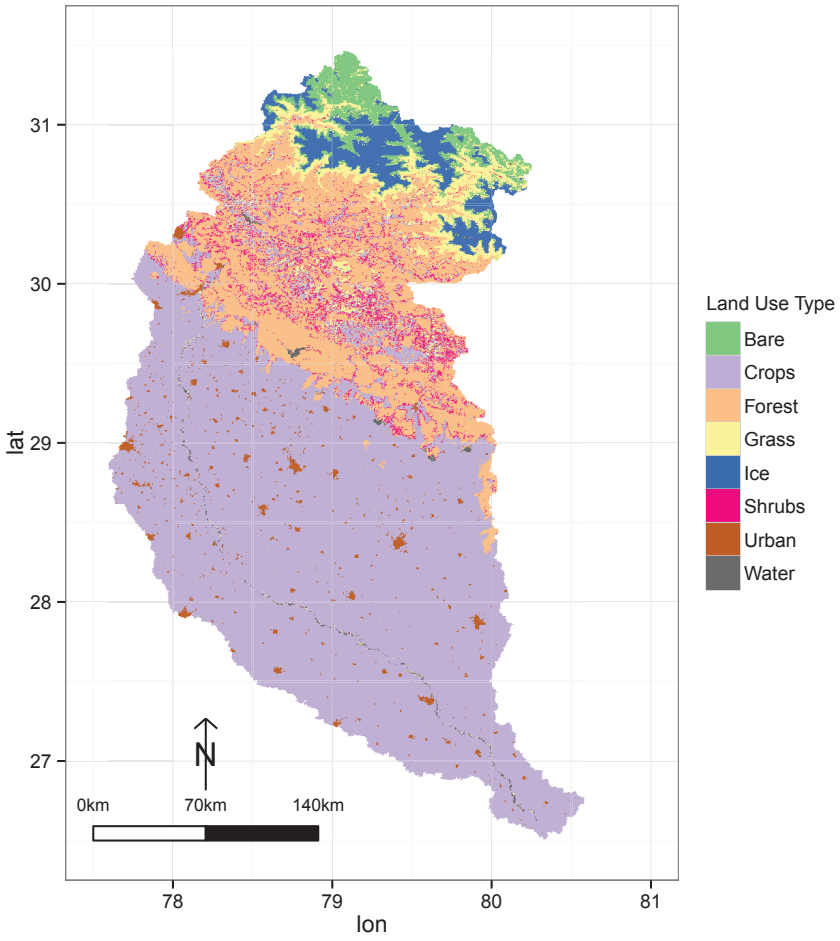


**Figure 3.3:** Land-cover map of the UG basin, for year 2010, as developed by Tsarouchi *et al.* (2014).

shallow, fine-textured band of Regosols located in the mid-north parts of the catchment (Encyclopaedia Britannica inc., 2012a,b). The fertile soils developed on the river's alluvial deposits are making it a highly productive agricultural area.

The two main crops grown in that region are wheat and rice. In Uttar Pradesh, rice is predominantly rain fed and depends largely on the monsoon season rains from June to September (USDA-I, 2013). However, the intensive wheat/rice crop rotation in the area is responsible for soil degradation and causes drops in the water table levels (through ground-water extraction for irrigation) in some areas and water-logging in others, when irrigation is applied in areas without adequate drainage (USDA-I, 2013). In

Uttarakhand, around 80% of the population depends on agriculture for its survival. Only 20% of the district's area is flat, the rest 80% is hilly. Further, only 11% of the agricultural area is irrigated and that happens mainly in the hilly areas (Kaushal and Kansal, 2011).

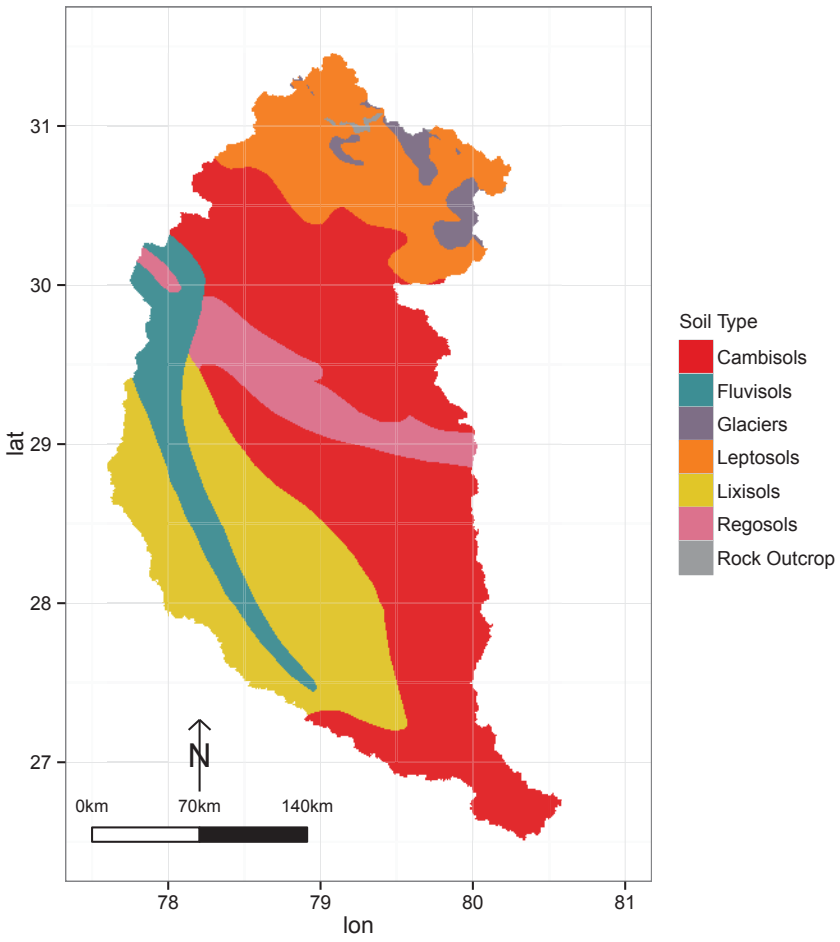


**Figure 3.4:** The dominant soil types in the Upper Ganges basin as derived from the HWSD soil map (FAO, 2009).

## 3.2 Hydrology and Climate of the region

The annual average rainfall in the UG basin ranges between approximately $610\ \mathrm{mm}$ and $1810\ \mathrm{mm}$ (Fig. 3.6). The main source of rainfall is the south-west monsoon, which occurs at this location from July to late September, providing more than 80% of the total annual precipitation (Fig. 3.7, Turner and

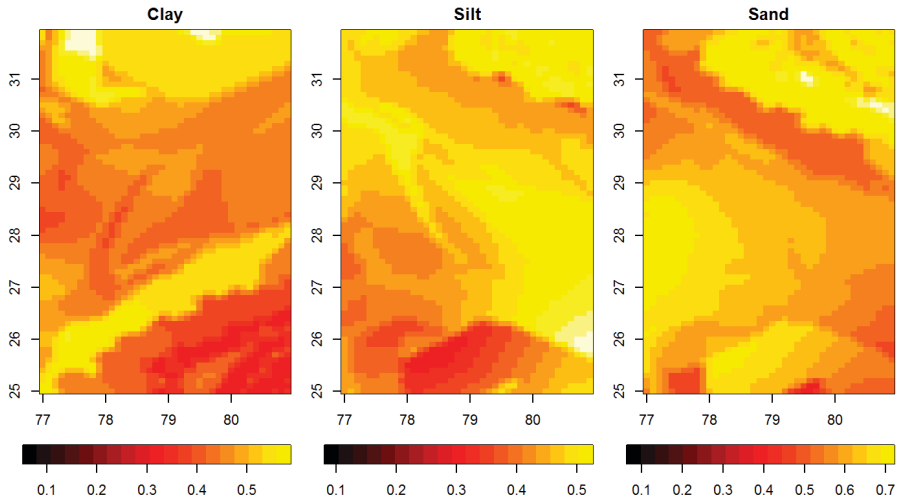


**Figure 3.5:** Soil texture map of the Upper Ganges basin as derived from the HWSD database.

Annamalai, 2012). The runoff regime in the UG basin is rain dominated, due to the monsoon-dominated precipitation regime, and the maximum discharge of the river occurs during the monsoon period (Lutz *et al.*, 2014). However, the fluctuation between monsoon flows and dry period flows is very high and that means that large areas are subjected to floods and/or droughts every year (Jain *et al.*, 2007), resulting in huge loss of life and property (e.g. recent northern India floods in Uttarakhand, June 2013).

The Indian monsoon is part of the larger-scale Asian monsoon which is an annually reversing wind system (Lau *et al.*, 2005). This system is characterised by winds blowing from the south-west direction during the summer months (June–September) and from the north-east during the winter months (December–February). The reversal of the wind direction in May brings a rich amount of moisture from the warm tropical ocean to the Indian continent (Xavier *et al.*, 2002). This reversion is associated with the temperature difference between sea and land surface. South of the equator, the Indian Ocean is cooler than the northern Indian Ocean, the northern India plains and the Tibetan Plateau. Therefore, temperature and pressure gradients are formed from south to north.

The Indian monsoon is characterised by large spatial and intra-seasonal variability. The intra-seasonal variation of monsoonal precipitation is defined by ‘active’ periods of high rainfall and ‘break’ periods with weak or no rainfall over central India and the west coast (Xavier *et al.*, 2002). The monsoon trough, which is a low pressure system that lies over the northern plains of India during the monsoon

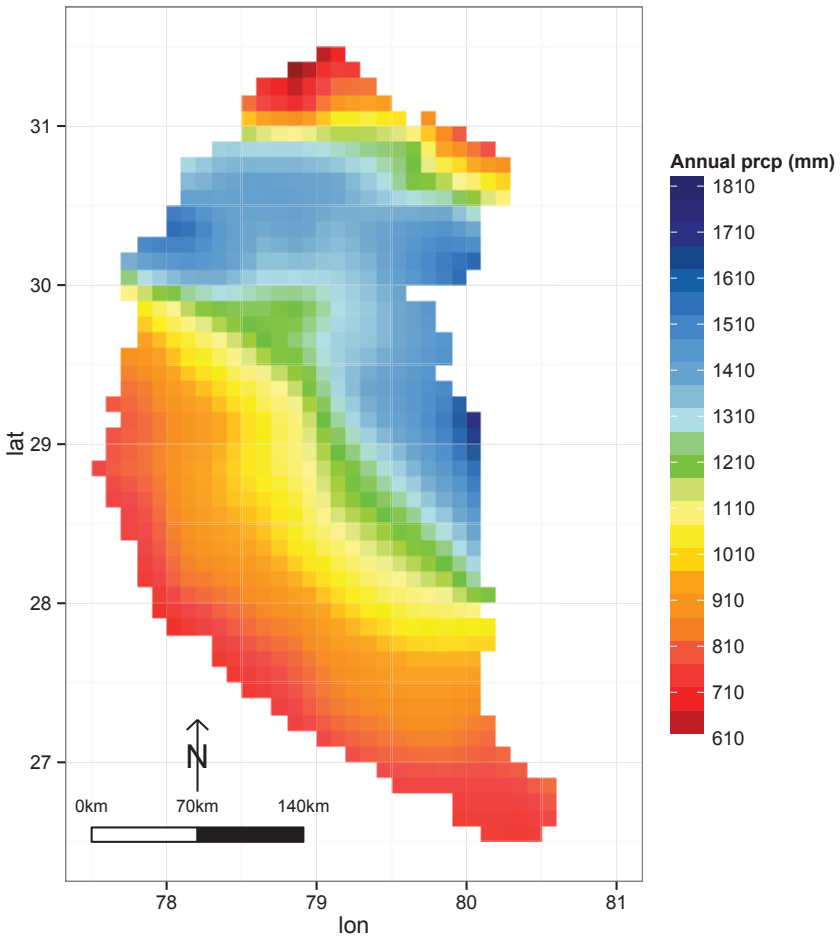


**Figure 3.6:** Annual average precipitation distribution in the study area, based on TRMM 3B42v7A satellite product (years 1998–2011).

season, plays an important role in these variations. When the trough is over the Himalayan foothills, central India and the west coast are under a 'break' period. When the trough is over the northern Indian plains, central India and the west coast are under an 'active' period (Krishnamurthy and Shukla, 2000).

From July to October, the Ganges river water supply depends on the south-westerly monsoonal rains. From April to June (which is the hot season), the river's water supply depends on the snow-melting flows from the Himalayas. The upper parts of the catchment receive a considerable amount of snowfall and some areas in the Himalyian foothills are permanently covered by snow (Fig. 3.3). Apart from the monsoons, precipitation also comes in the form of tropical cyclones originating in the Bay of Bengal during late spring and early autumn. During the winter months, only a small amount of rainfall occurs in

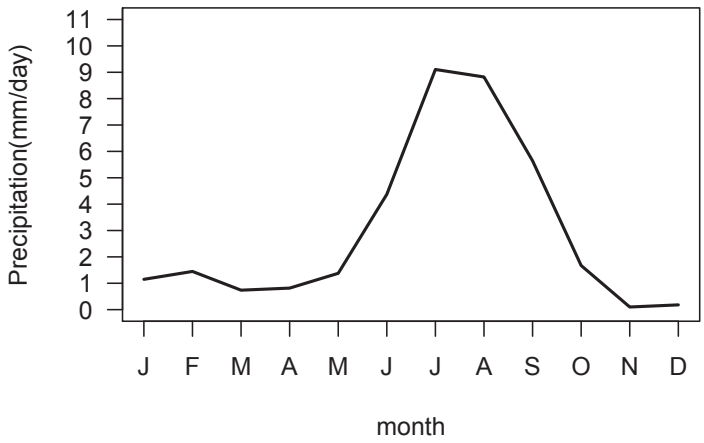


**Figure 3.7:** Precipitation monthly climatology in the UG basin based on Tropical Rainfall Measuring Mission (TRMM) satellite data product 3B42v7A, over the period 1998–2004.

the study area. Temperature in the catchment ranges from $-20°$C during the winter in the northern parts, to $38°$C during the summer in the lowlands.

Since this project is interested in large-scale surface water - climate fluxes and feedbacks, the mountainous headwaters in the north of the basin are not taken into consideration. Although climate change impacts on glaciers and snow melt are of great concern, they are an intensive field of research, but have only limited impact on the water resources of the lower plains (Immerzeel *et al.*, 2010). The large downstream monsoon-dominated system of the Ganges river basin, in combination with limited upstream precipitation and small glaciers are the reasons for this minor contribution of snow and glacier water to the Ganges (Immerzeel *et al.*, 2010).

There is a strong link between the Indian monsoon and the El Niño and Southern Oscillation (ENSO) phenomena through ocean – atmosphere interactions. Ropelewski and Halpert (1996) identified the Ganges basin as one of the regions whose precipitation characteristics are related to the ENSO events. In addition, Whitaker *et al.* (2001) found a significant relationship between the natural variability of the Ganges annual flow and the ENSO index.

Goswami *et al.* (2006) describe north-east India as a region with high mean precipitation and high variability. Local orography has a strong influence on the rainfall and thus, it is difficult to identify trends

in rainfall extremes due to a warming environment. However, while there has been no overall trend in seasonal mean rainfall of the Indian summer monsoon, this masks a complex pattern of reduced frequency of light-to-moderate rain events, and increased frequency and magnitude of heavy rain events (Goswami *et al.*, 2006). Similar trends were found by Rajeevan *et al.* (2008) who suggest that increasing trends of extreme rainfall events could be related to increasing trends of sea surface temperatures and surface latent heat fluxes over the tropical Indian Ocean. This is consistent with the general intensification of the hydrological cycle in the tropics (Trenberth *et al.*, 2003). Increased greenhouse gas concentrations lead to a warmer climate, which means that the water-holding capacity of the atmosphere increases along with the concentrations of water vapour, leading to higher potential evaporation. However in terms of ET, the increased temperature effect offsets the impact of increased $CO_2$ concentrations, which is reduced plant transpiration (as previously mentioned) due to decreased stomatal conductance, resulting in increased plant water use efficiency. Besides, increasing groundwater extractions for irrigation have already strongly decreased groundwater storage (Briscoe, 2005; World Bank, 2010; GOI, 2010) and increased soil moisture and surface-atmosphere fluxes.

## 3.3 Threats to water supply

The Ganges basin is the most densely populated river basin in the world, with an average population density of $520\ \mathrm{persons/km^2}$. Between 1991 and 2001, the urban population of India increased by 32%, and this trend is likely to continue, making the study area subject to rapid land-cover changes (O'Keeffe *et al.*, 2012). According to the Census 2011 (Office of the Registrar General & Census Commissioner, India, 2011), the population of India has increased by more than 181 million from 2001 to 2011, reaching 1.21 billion. Population density in Uttar Pradesh has increased by more than 100% from 1971 to 2001, leading to a sharp increase in water demand (Kaushal and Kansal, 2011). Especially during the dry period, the pressure is high for the canals to maintain the required flow revels and sustain riverine ecology.

Over the past decades, the Indian subcontinent has undergone one of the largest environmental changes in human history. India's green revolution, besides the ubiquitous benefits, has resulted in large-scale changes in land cover and a significant increase in the exploitation of water resources, including the vast groundwater aquifers of the Gangetic plains. From 1960 to 1999, irrigation from tube wells and

other wells grew by more than 400% and currently represents well over half of the country's irrigated area (Scott, 2009). At the same time, groundwater provides 50-80% of domestic water demand (Kumar *et al.*, 2005). Large groundwater irrigated areas increased by 187% from 1970 to 1999 (Zaisheng *et al.*, 2006). The situation is getting worse as in more recent years the increasing demand for better diet led farmers to mainly plant high water intensity crops such as wheat, rice and sugarcane (Kaushal and Kansal, 2011). This has put severe pressure on water resources, whilst groundwater levels show a steady decline (Rodell *et al.*, 2009).

The pressure on water resources is expected to further increase in the near future. By 2030, India's urban population is expected to rise from 286 million (in 2001) to 575 million (Tenhunen and Saavala, 2012). The country eyes double-digit economic growth. At the same time future climate change, and particularly the reliance of water resources on the highly erratic precipitation patterns of the summer monsoon, pose significant risks to water supply. Since 80% of India's rainfall occurs during the summer monsoon, any change in its timing, intensity and duration, affected by increases in greenhouse gas concentrations could be seriously detrimental to water supply. Due to a rapidly growing population, this area is considered at high risk for water shortages in the future. Countrywide evidence cited earlier, supported by localised studies, already suggests decreased frequency of light-to-moderate rainfall events and increases in heavy rainfall events, specifically in the central and north-east region, since the early 1950s (Dash *et al.*, 2009).

Another environmental challenge India has to face is the very poor water quality over large parts of the Ganges river. Although in the mountainous regions the water is clean, as it reaches the plains, the water quality issues that arise are huge as municipal waste and industrial sewage are major contributors to the river's pollution (Jain *et al.*, 2007).

The World Bank (Briscoe, 2005) has warned India that in order to sustain its current economic development and manage its water resources system, severe changes need to take place. Otherwise, the reality of limited water supplies and growing demands could lead to a very serious water crisis.

## 3.4 Data availability

When it comes to data availability for research studies, this region is one of the most data scarce regions in the world. This scarcity arises mainly from political restrictions and to a lesser extent from physical difficulties. The Himalayan mountainous parts of the catchment are not equipped with gauging stations. Nevertheless, further downstream, in the plains, there are several measurement stations but India has very strict data sharing policies due to national security laws. Ganges is a transboundary river and despite the existence of several official two-sided mechanisms and treaties between India and border countries (such as the Joint Rivers Commission between India and Bangladesh, the Ganges Treaty of 1996), there has not been much progress in reforming policies that would allow data sharing, or establishment of organisations with the purpose to assist cooperation, joint operations and management of these transboundary waters. As a result, the lack of data accessible by the scientific community is responsible for a general lack of hydrological and water resources studies in the UG basin area and has been a great challenge for the present research. There has been an ongoing debate regarding the flow data availability but until this issue is resolved, all feature studies will have to deal with this limitation.

# Chapter 4

# Historic and future land use changes

# Historic and Future Land Use Changes

This chapter is an expansion of the work described on the following publication:

Tsarouchi, G., Mijic, A., Moulds, S., Buytaert, W., 2014. Historical and future land-cover changes in the Upper Ganges basin of India. *International Journal of Remote Sensing*, 35: 3150-3176.

## 4.1 Introduction

In this Chapter, trends in land-cover changes are detected and quantified, by developing and analysing historic land-cover maps and by modelling land-cover change in a region that has undergone one of the largest environmental changes in human history over recent decades. India's green revolution, besides its ubiquitous benefits, has resulted in large-scale changes in land cover. Remarkably strong agricultural expansion, development activities, urbanization, and deforestation have caused alterations and modifications in the land-cover status. This is the first study attempting to evaluate and understand the dynamics of land-cover change processes in this region by monitoring and analysing the spatial patterns of change at a high resolution, which allowed detailed descriptions of land-cover transitions over time.

The land-cover changes that took place in northern India over the last decades are affecting water resources in the region in complex ways. The increased demand for irrigation, which follows the agricultural expansion, along with population growth and economic development, are threatening India's water supplies (Rodell *et al.*, 2009). As a result, the study of historic land-cover change trends and the generation of future scenarios of land cover is a step towards a better understanding of the impacts posed by these changes on water resources and towards improved water security in the region.

The large scale of application is a challenge for this study (previous studies have only focused in small-scale systems). The lack of available data for dynamic-based land-cover change models led to the selection of a simple Markov chains model to generate the future scenarios, as previously mentioned.

This Chapter aims to capture historical changes by generating a time-series of land-use maps, after applying supervised classification techniques on historical data sets of satellite images. Subsequently,

future spatio-temporal land-cover scenarios are developed, based on Markov chain analysis. The research methodology is divided into three phases:

1. Image processing of 30m resolution multi-temporal Landsat 5 Thematic Mapper (TM) and Landsat 7 Enhanced Thematic Mapper plus (ETM+) data and land-cover maps preparation.

2. Land-cover change detection and analysis of land-cover changes between 1984 and 2010, by using post-classification change analysis.

3. Stochastic modelling and future projections of land-cover change with Markov modelling, by generating transition probability matrices, which indicate transition potentials from one land-cover class to another.

The results are expected to enhance progress in identifying and understanding the temporal dynamics of climate-surface-groundwater fluxes as a function of land-cover change.

## 4.2 Data description

The Data used to prepare the land-cover maps and detect trends of change include:

1. **Remote sensing data**: Landsat 5 TM and Landsat 7 ETM+ images, 77 in total, for the month October of years 1984, 1990, 1998, 2000, 2002, 2004, 2006, 2008 and 2010 were acquired from the US Geological Survey Global Visualization Viewer. Prior to the analysis, the images were co-registered to the UTM projection zone 44N, WGS 1984 datum and corrected for radiometric and atmospheric effects. Then the images were classified using a Maximum Likelihood classifier method with pixel training data sets, resulting in land-cover maps of eight different classes. Further details are given in the next Section.

2. **Field data**: The total of 400 validation points for each land-cover map were selected by visual interpretation of high resolution imagery on Google Earth, along with ground-truth data collected after a survey of the site in 2012. In addition, online data from the Global Geo-Referenced Field Photo Library (University of Oklahoma, 2011) were used to relate land cover to the supervised

classifications results. The field data were also used in the land-cover change detection analysis to distinguish between areas with and areas without change. All images from Google Earth and from the Global Geo-Referenced Field Photo Library are labelled with their acquisition date. For the validation, images acquired on the same month with the Landsat images were selected. If that was not possible, the images selected were acquired within a month's difference from the satellite image acquisition date.

## 4.3 Description of Methods

### 4.3.1 Image processing and land-cover maps preparation

The work that's been carried out is as follows:

Land-cover maps were produced by applying supervised classification techniques on the Landsat images with a $30\mathrm{m}$ ground resolution. However, the accuracy of the classification is highly dependent on the quality of the satellite data interpreted. Therefore, and especially in cases where multi-temporal images (i.e. not acquired on the same date) are to be analysed and compared, a primary pre-processing task is necessary, in which radiometric and atmospheric corrections are applied to each image.

As previously mentioned, the digital sensors acquire the intensity of electromagnetic radiation (ER) from each spot viewed on the Earth's surface and store this information as an 8-bit satellite quantized calibrated digital number (DN) for each spectral band. Radiometric correction involves the use of standard equations to convert DN values to at-satellite reflectance. DN is converted to at-satellite spectral radiance L$\lambda$ according to the following expression (Chavez, 1996; Chander and Markham, 2003; Chander *et al.*, 2007):

$$L_\lambda = G \times Q_{cal} + B \tag{4.1}$$

where:

$L_\lambda$ = Spectral radiance at the sensor's aperture $[\mathrm{W}/(\mathrm{m}^2\,\mathrm{sr}\,\mu\mathrm{m})]$, where sr is for steradians: units of solid angle (the full sphere has a solid angle of $4\pi$ steradians)

$Q_{cal}$ = Quantized calibrated pixel value [DN],

$G$ = Band-specific rescaling gain factor $[(\mathrm{W}/(\mathrm{m}^2\,\mathrm{sr}\,\mu\mathrm{m}))/\mathrm{DN}]$, and

$B$ = Band-specific rescaling bias factor [W / ($\mathrm{m}^2$ sr $\mu$m)].

The $G$ and $B$ factor values can be found in the header records, per specific band.

After conversion to at-satellite spectral radiance, the six bands of optical - reflective data used in this study (bands 1-5 & 7) have to be converted to at-satellite exo-atmospheric reflectance (which is the combined surface and atmospheric reflectance seen at the satellite). The conversion assumes cloud-free conditions and a uniform Lambertian surface according to the following equation (Chander and Markham, 2003):

$$\rho_p = \frac{\pi \times L_\lambda \times d^2}{(ESUN \times cos(\theta_z))} \tag{4.2}$$

where:

$\rho_p$ = Unitless exo-atmospheric reflectance at the satellite (this takes values of 0-1),

$d^2$= Squared Earth-Sun distance in astronomical units,

*ESUN* = Mean solar exo-atmospheric irradiance $[\mathrm{W}/(\mathrm{m}^2\,\mu\mathrm{m})]$, from Finn *et al.* (2012), and

$\theta_z$ = Solar zenith angle when the scene was recorded.

An image-based dark object subtraction (DOS) method was used (Chavez, 1989, 1996; Moran *et al.*, 1992). This method is the simplest yet most widely used approach, suitable for areas with dense vegetation (Spanner *et al.*, 1990; Huguenin *et al.*, 1997). As previously mentioned, it assumes that objects with near zero reflectance exist in each image (Kaufman and Sendra, 1988). The smaller DN value in each spectral band repeated over at least one thousand pixels ($DN_{min}$) is considered to be the dark object (Teillet and Fedosejevs, 1995). The signal received from those objects is due to atmospheric scattering, also known as path radiance (Eq. 4.3), and is subtracted from all the pixels of the spectral band (Chavez, 1989). Once $DN_{min}$ is determined, path radiance, $L_p$, can be estimated using Eq. 4.3.

$$L_p = G \times DN_{min} + B - \frac{0.01 \times [E_o \times cos(\theta_z) \times T_z + E_{down}] \times T_u}{\pi} \tag{4.3}$$

where:

$L_p$ = Path radiance resulted from the interaction of the electromagnetic radiance with the atmospheric components (molecules and aerosols),

$DN_{min}$ = Darkest DN value in each spectral band with at least one thousand pixels,

$E_o$ = Exo-atmospheric solar constant corrected for solar distance ($E_o = ESUN/d^2$),

$T_z$ = Atmospheric transmittance between the sun and the surface in the illumination direction,

$E_{down}$ = Downwelling diffuse irradiance, and

$T_u$ = Atmospheric transmittance from the target toward the sensor.

The method assumes no atmospheric transmittance loss ($T_z$ and $T_u$ to be unity) and the downwelling diffuse irradiance ($E_{down}$) to be zero (Chavez, 1989).

The DOS model has the following form to calculate the surface reflectance ($\rho$), where path radiance ($L_p$) is subtracted from the at-satellite sensor radiance ($L_\lambda$):

$$\rho = \frac{\pi \times (L_\lambda - L_p)}{T_u \times (E_o \times cos(\theta_z) \times T_z + E_{down})} \tag{4.4}$$

After these corrections, supervised classifications were implemented by using the Maximum Likelihood algorithm. All six optical bands of the TM5 and ETM+ sensors were used (bands 1-5,7). The steps followed for the supervised classifications included: 1) selection of training regions, 2) calculation of region's statistics in order to avoid overlapping between different classes, 3) evaluation of each class and 4) application of the Maximum Likelihood Classifier. A total of 160 training regions, evenly distributed between the land-cover classes, were chosen by means of on-screen selection for each image (i.e. selection of training polygons based on the analyst's judgement, by identifying areas that clearly belong to a certain class), to ensure that all spectral classes are properly represented in the training statistics (Wu *et al.*, 2006). Land-cover classes were defined as water, forest, shrubs, grass, crops, urban, snow and barren.

The Normalized Difference Vegetation Index (NDVI), proposed by Rouse *et al.* (1974), was used as an additional data layer in the classification procedure to enhance detection among various land-cover classes and also to reduce the shadow effect due to the mountainside slopes. Derived from relationships between different spectral bands, as previously mentioned, NDVI is more sensitive to the vegetation spectral response than the individual bands. Corresponding cell values in bands TM3 ($0.63 - 0.69\mu$m) and TM4 ($0.76 - 0.90\mu$m), can be used to produce this vegetation index according to the following

expression:

$$NDVI = \frac{TM4 - TM3}{TM4 + TM3}. \tag{4.5}$$

Calculations of NDVI for a given pixel always result in a range from -1 to +1. Pixel values close to 1 indicate the highest possible density of green vegetation, whereas pixel values below 0.1 are considered as non-vegetated according to Loveland *et al.* (1991). Although it is possible to obtain NDVI values from at satellite exo-atmospheric reflectance values, it is more accurate to first apply the atmospheric corrections and use the surface reflectance values in order to estimate NDVI values.

The classification algorithm might sometimes misclassify pixels, either due to an analyst's error during the training model procedure or due to a spectral overlap between different land-cover types. To determine how accurate the produced maps are, the overall accuracy and Kappa Coefficient were calculated for each classification, using techniques described in Congalton (1991).

The total of 200 samples for each image date is obtained through visual interpretation of the area. This is aided by a combination of direct field observation and Google Maps interpretation. Those 200 samples were split by random sampling into training and validation datasets, making sure that all land-cover types are equally represented in each dataset. The training dataset (160 points, evenly distributed between the land-cover classes) was used to calibrate the model. The validation dataset (40 points, evenly distributed between the land-cover classes) was used to test the model's performance. This cross validation procedure (i.e. repeated random sub-sampling) was carried out 10 times for each image. The final error was estimated as the average of the individual errors. Once the cross validation testing was complete, 400 validation points (see section 4.2) were used to test the performance of the model that gave the best accuracy during cross validation.

As no ground truth data or aerial photographs were available for the 1984 and 1990 classifications, validation relied upon manual expert judgement of the classification in the validation points.

### 4.3.2 Land-cover change detection and analysis

In order to detect and quantify the changes in land-cover patterns from 1984 to 2010, a post-classification change analysis approach was followed, that produces a change matrix where different combinations

of change are identified. This allows quantification of the changes by knowing how much of a given land-cover type has changed and into what categories, as well as to identify trends in land-cover changes that have taken place in the UG basin since 1984. The classified images are compared on a pixel by pixel basis and the quality of the change map is very much dependent on the accuracies of the individual classification maps. Hence, this method requires a very good level of accuracy in both images (Singh, 1989; Lambin and Strahler, 1994). In addition, for the analysis of the location, type and rate of change, a set of images that indicates the gains and losses per land-cover class was produced.

### 4.3.3 Stochastic modelling and future projections of land-cover change

To generate future land-cover scenarios, one of the analytical methods of modelling stochastic processes, Markov chain analysis, was applied. The method is based on the assumption that the driving forces that produced changes in the past will continue to do so into the future. However, this assumption is not always true, especially for long periods. Therefore, the decision was taken to apply the method only for the period from 2000 to 2010, where the frequency of available land-cover maps is high (1 map per 2 years). In theory, a given cell of land may change from any type of land cover to any other.

Before applying the Markovian analysis, the method was tested to evaluate its validity for projecting land-cover changes in the UG basin. The three assumptions tested were: a) Land cover is not statistically independent from land cover at the preceding time period; b) This dependence is a 1st order Markovian dependence and not a 2nd order dependence; and c) The system is stationary, meaning that the driving factors caused changes in the past will continue to do so into the future.

More analytically, the first test was a statistical independence test. The null hypothesis that land cover at one point in time ($t_1$) is statistically independent of land cover at the preceding time period ($t_0$) is being tested (essentially this test is testing for order 0 versus 1st order Markovian dependence). If $M$ is the number of land-cover classes (here $M = 8$), Karl Pearson's $\chi^2$ is calculated with $(M-1)^2$ degrees of freedom:

$$\chi^2 = \sum_i \sum_k \frac{(n_{ik} - m_{ik})^2}{m_{ik}}, \tag{4.6}$$

where $n_{ik}$ the amount of cells that transitioned from class $i$ to $k$ in period $2000 - 2010$ for instance;

and $m_{ik}$ the expected amount of cells that transitioned from class $i$ to $k$ under the null hypothesis of independence, under the constraint that the expected marginal totals are equal to the observed transition matrix ones; $m_{ik}$ is therefore calculated as:

$$m_{ik} = \frac{n_{i*} n_{*k}}{n}, \tag{4.7}$$

where $n_{i*}$,$n_{*k}$ the marginal totals (for row and column respectively) and $n$ the sample size.

The test will be called $K^2$ instead of $\chi^2$, to differentiate from its distribution ($\chi^2$). For $(M-1)^2 = 49$ and a critical region of 0.05, values of $K^2$ less than 66.3 would indicate that the hypothesis of land-cover independence is true.

If the data are proved to be statistically dependent, the second test will show whether the dependence is characterised by a $1^{\text{st}}$ or higher order Markov dependence (Weng, 2002). The test for the $1^{\text{st}}$ order Markov dependence is again a $\chi^2$ goodness of fit test, calculated by the Eq. 4.9. The hypothesis that the data are described by $1^{\text{st}}$ order Markovian dependence is true if for $\mathrm{M}(\mathrm{M}-1)^2$ degrees of freedom:

$$\chi_c^2 < \chi_{1-n, M(M-1)^2}^2 \tag{4.8}$$

where

$$\chi_c^2 = \sum_{ijk} n_{ij} \frac{(\frac{n_{ijk}}{n_{ij}} - \frac{n_{jk}}{n_j})^2}{\frac{n_{jk}}{n_j}}, \tag{4.9}$$

where $n_{ijk}$ is formed similarly to $n_{ij}$.

The third test is a stationarity test. Markov transition probability based models assume that the probability matrix is stationary over time and space. According to this assumption, changes in land cover for all tested periods between 2000 and 2010 come as a result of the same transition mechanism. To test this assumption, the steady state probabilities, which show the equilibrium distributions for these periods, will be calculated. These distributions are calculated by multiplying the transition matrices by themselves (Bell, 1974; Bourne, 1976) until they converge to a matrix with identical rows. The values of the equilibrium matrix represent the amount of each land-cover class at a hypothetical future equilibrium. Furthermore, this shows that the Markovian process is not a simple linear extrapolation because the transition potentials change over time as the various transitions reach an equilibrium state.

The matrices of change produced by the post-classification change analysis show the number of cells that changed from each land-cover class to another class. These numbers are converted to probabilities by dividing each element by its equivalent row total. In this study, the probability for each land-cover class to change to every other class is being represented in a matrix, which (with 8 land-cover classes, and therefore 64 possible different land-cover transitions) is a 64 cell transition matrix for each discrete time period. The rows represent the older land-cover categories and the columns the newer ones. The model applied in this study is a $1^{st}$ order Markov chain, meaning that the dependence of land-use upon the past is entirely captured upon the dependence on the exact previous land-use state. The transition predictions can be determined as functions of current land cover. The mathematical structure of this approach is based on probabilities of transition between each pair of land covers $i$ and $j$. The model has the form of:

$$n_{t_1} = P \times n_{t_0} \tag{4.10}$$

where $n_{t_0}$ and $n_{t_1}$ are vectors representing fractions of each land-cover class at the time $t_0$ and $t_1$, respectively and P is a transition probabilities matrix that indicates the probability of moving from one class $i$ at time $t_0$ to another class $j$ at time $t_1$. For $m$ land-cover classes, $P$ has a dimension of $m \times m$. Each row of the matrix must sum to 1. Once the initial transition probability matrix is calculated, it can be used to project land-cover changes at any time in the future.

The new transition matrix is derived by simply powering the base matrix, if the date to be projected is an even multiple of the training period. If the future projection date is not an even multiple of the training period, it is necessary to produce an annual transition matrix. A linear algebra formula of the power root of matrices has been used in the past to generate this annual matrix but several difficulties arise by this approach as is discussed in the study of Takada *et al.* (2010). Therefore, in the present study, future scenarios are developed based on even multiples of the training periods.

In this study, all 15 available transition matrices of periods between the years 2000 and 2010 were used to develop different scenarios of the future land-cover status for the year 2020. As the trends in different matrices vary, the future predictions generated are not expected to be the same. It is by definition impossible to test the accuracy of a scenario that projects the future; however, to visualize the uncertainty and identify outliers between those 15 future scenarios, box-plots were created, which help identify the

spread and skewness of the future predictions.

## 4.4 Results

### 4.4.1 Image processing and land-cover maps preparation

Land-cover maps were produced after supervised classification techniques were applied to Landsat images for the years 1984, 1990, 1998, 2000, 2002, 2004, 2006, 2008 and 2010 (Fig. 4.1). The error matrix produced by comparing classification results with ground truth data and high resolution images (Table 4.1) indicates a sufficient level of accuracy, which allows for further analysing and studying land-cover change trends in the UG basin. The highest overall accuracy achieved was 93.73% for year 2002. The Kappa coefficient for that year was 0.91, representing a 91% better agreement than if the classification was result of a random assignment. Kappa values greater than 0.80 represent strong agreement (Congalton, 1991) and a widely used, minimum level of acceptable accuracy for land-cover classification is 85% (Anderson *et al.*, 1976).

**Table 4.1:** Classification Accuracy assessment for each classification based on ground truth data and high resolution images. The results were produced by applying techniques described in Congalton (1991).

| Image | Overall | Kappa |
|---|---|---|
| 1984 | 87.03 | 0.86 |
| 1990 | 86.88 | 0.84 |
| 1998 | 87.15 | 0.86 |
| 2000 | 90.57 | 0.88 |
| 2002 | 93.73 | 0.91 |
| 2004 | 93.21 | 0.90 |
| 2006 | 92.90 | 0.90 |
| 2008 | 88.86 | 0.87 |
| 2010 | 91.72 | 0.91 |

### 4.4.2 Land-cover change detection and analysis

According to the 1984 classification (Fig. 4.1), areas in the north of the UG basin (Himalayas) were either barren or covered by snow. The central and northern parts of the catchment were dominated by

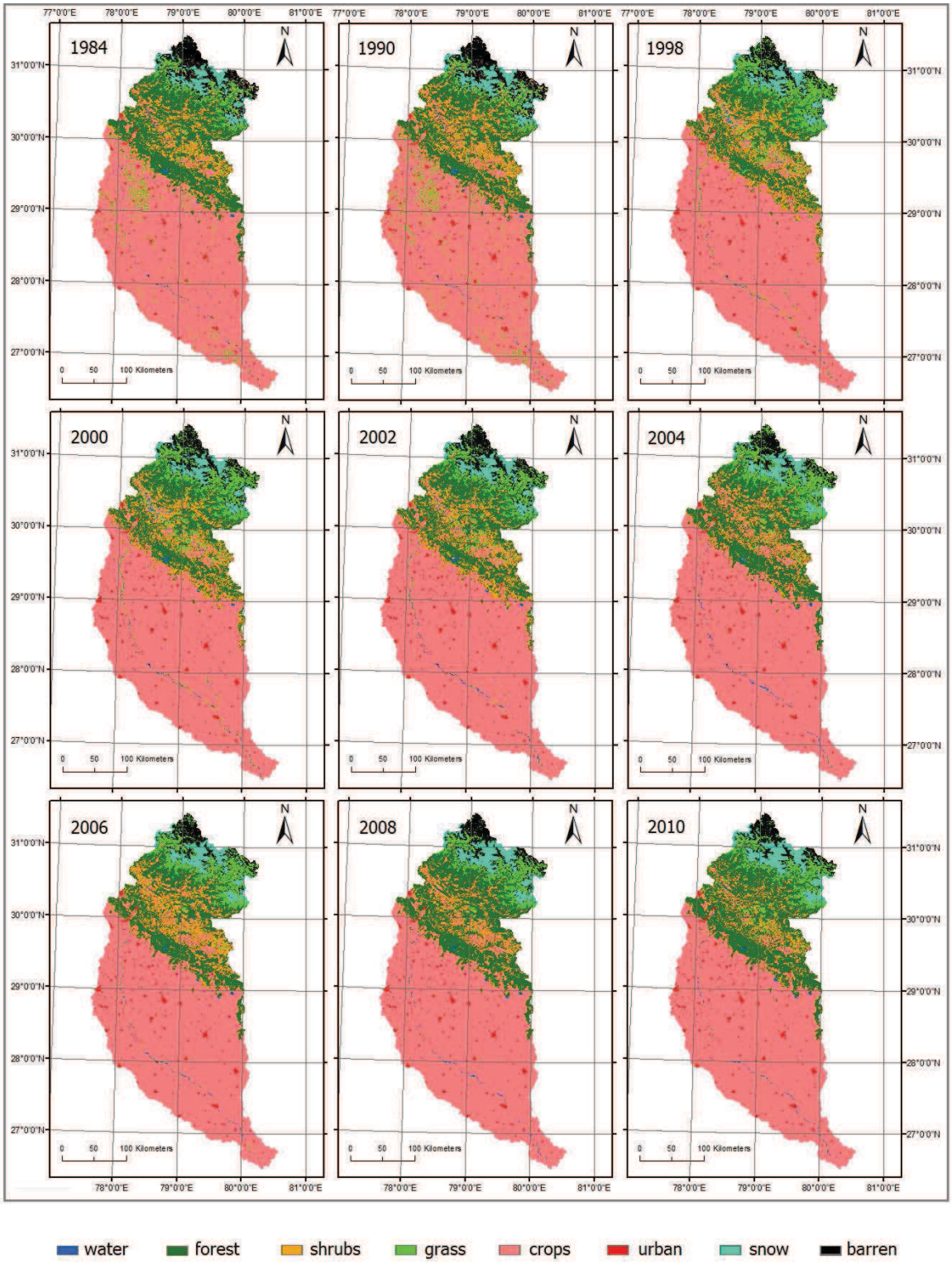


**Figure 4.1:** Image classification results for the examined years. The eight classes identified are: water, forest, shrubs, grass, crops, urban, snow and barren.

forests. In the central areas, a combination of dense vegetation and crops is identified along with barren and grass land. Most of the urban and agricultural areas in the basin are located towards the south, in the plains of the UG basin.

Looking at changes in land-cover proportions over the periods examined (Fig. 4.2 & 4.3), crop area increased from 1984 to 2006 but from 2006 to 2010 it decreased. However, the overall change from 1984 to 2010 is an increase of $1.3\%$. The trends observed in the forest proportion follow the opposite direction: forest area decreased from 1984 to 1998 but from 1998 to 2010 it increased, achieving a total increase of $4.7\%$ from 1984 to 2010. Shrub coverage increases from 1984 to 2000 but from 2000 onwards it decreases and reaches an overall change of $-11.6\%$ from 1984 to 2010. Grass and barren lands do not show a stable trend of increase or decrease in the periods examined between 1984 and 2010. Nevertheless, they have all been reduced from 1984 to 2010 by $9\%$ and $9.5\%$ respectively. Urban coverage is being expanded from 1984 onwards and the total increase during the 1984–2010 period is $5.8\%$.

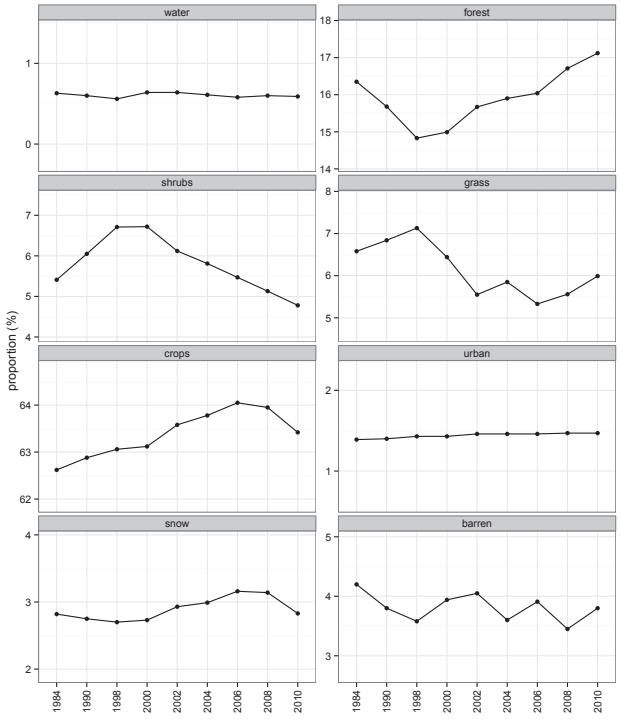


**Figure 4.2:** Land-cover proportions based on the image classification results.

Figure 4.4 shows the contributors to net change from a perspective of land cover. The main con-

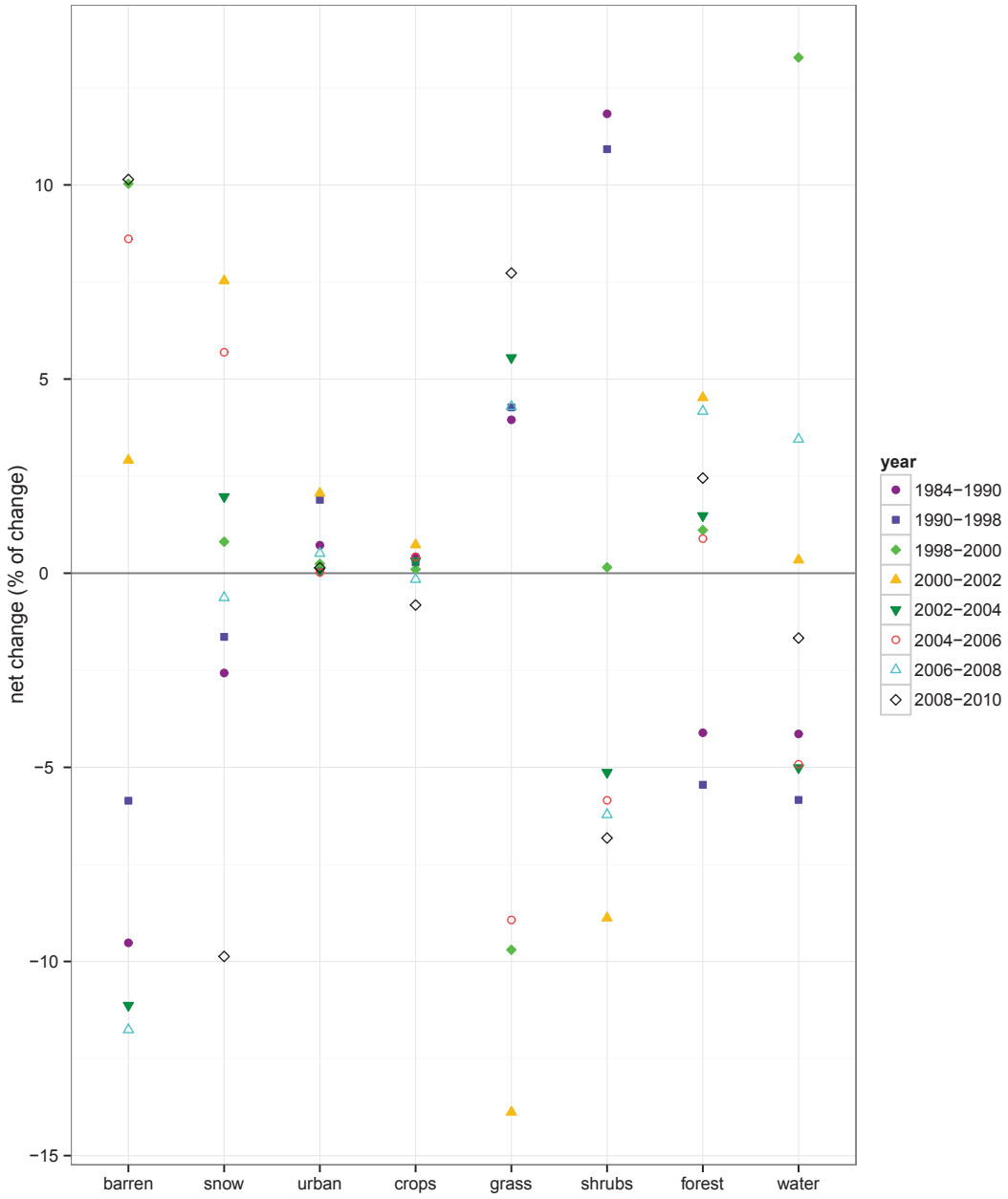


**Figure 4.3:** Changes in land-cover proportions over the periods examined, based on the image classification results.

tributor to the net change in forest area is the conversion to/from shrubs. Barren land is changing due to conversion to/from water, grass and snow. Crop change occurs due to conversion to/from water, shrubs, grass and barren. Grass change is due to conversion to/from water, snow and barren land. The main

contributors to changes in shrubs are forest, snow and barren land-cover classes. Finally, shrubs, grass and barren land are the main contributors to snow coverage change.

The Landsat classifications indicated that share of forested areas decreased by $4.1\%$ from 1984 to 1990 (Fig. 4.3). The same trend was observed by Gulati and Sharma (2000). This forest loss could be explained by the conversion to agricultural and other uses, such as heavy grazing, or by forest fires driven by population growth. During the period 1984–1990 agriculture in the UG basin increased by $0.4\%$, urban by $0.7\%$, grass by $4\%$ and shrubs by $11.8\%$. According to Figure 4.4, the main reason for the forest loss during the 1984–1990 period is conversion to shrubs.

The trends in forested area between 2000 and 2006 show an increase of $7\%$ (Table 4.2). This is consistent with reports that indicate forest growth in India over that period, in the states of Uttar Pradesh and Uttarakhand where the study area belongs to. Specifically, the State of Forest Report by the Forest Survey of India (reports of years 2001 and 2009), showed for the state of Uttar Pradesh an increase of 4.33% from year 2001 to year 2007 and for the state of Uttarakhand an increase of 3.17% from year 2001 to year 2007. In addition, the Global Forest Resources Assessment by FAO (2010), showed an increase of 0.70 % in the forest-cover area of India from 2000 to 2005 and an increase of 0.21% from 2005 to 2010 respectively.

**Table 4.2:** Land-cover proportions for the developed land-cover maps.

| Image | water | forest | shrubs | grass | crops | urban | snow | barren |
|---|---|---|---|---|---|---|---|---|
| 1984 | 0.63 | 16.35 | 5.41 | 6.58 | 62.62 | 1.39 | 2.82 | 4.20 |
| 1990 | 0.60 | 15.68 | 6.05 | 6.84 | 62.88 | 1.40 | 2.75 | 3.80 |
| 1998 | 0.56 | 14.83 | 6.712 | 7.13 | 63.06 | 1.43 | 2.70 | 3.58 |
| 2000 | 0.64 | 14.99 | 6.72 | 6.44 | 63.12 | 1.43 | 2.73 | 3.94 |
| 2002 | 0.64 | 15.67 | 6.12 | 5.55 | 63.58 | 1.46 | 2.93 | 4.05 |
| 2004 | 0.61 | 15.90 | 5.81 | 5.85 | 64.78 | 1.46 | 2.99 | 3.60 |
| 2006 | 0.58 | 16.04 | 5.47 | 5.33 | 64.05 | 1.46 | 3.16 | 3.91 |
| 2008 | 0.60 | 16.71 | 5.13 | 5.56 | 63.95 | 1.47 | 3.14 | 3.45 |
| 2010 | 0.59 | 17.12 | 4.78 | 5.99 | 63.42 | 1.47 | 2.83 | 3.80 |

In order to analyse the location, type and rate of changes, a set of images that indicate the gains and losses per land-cover class was produced. Figure 4.5 shows indicative changes for the land-cover types of forest, snow, grass, crops and shrubs. During the 1984–1998 period, the forest proportion was decreased in the basin mainly in the north parts (Fig. 4.5d). Contradictory, during the period 1998–2010, the forest proportion increased (Fig. 4.5a). The crop proportion increased during the 1984–1990 period

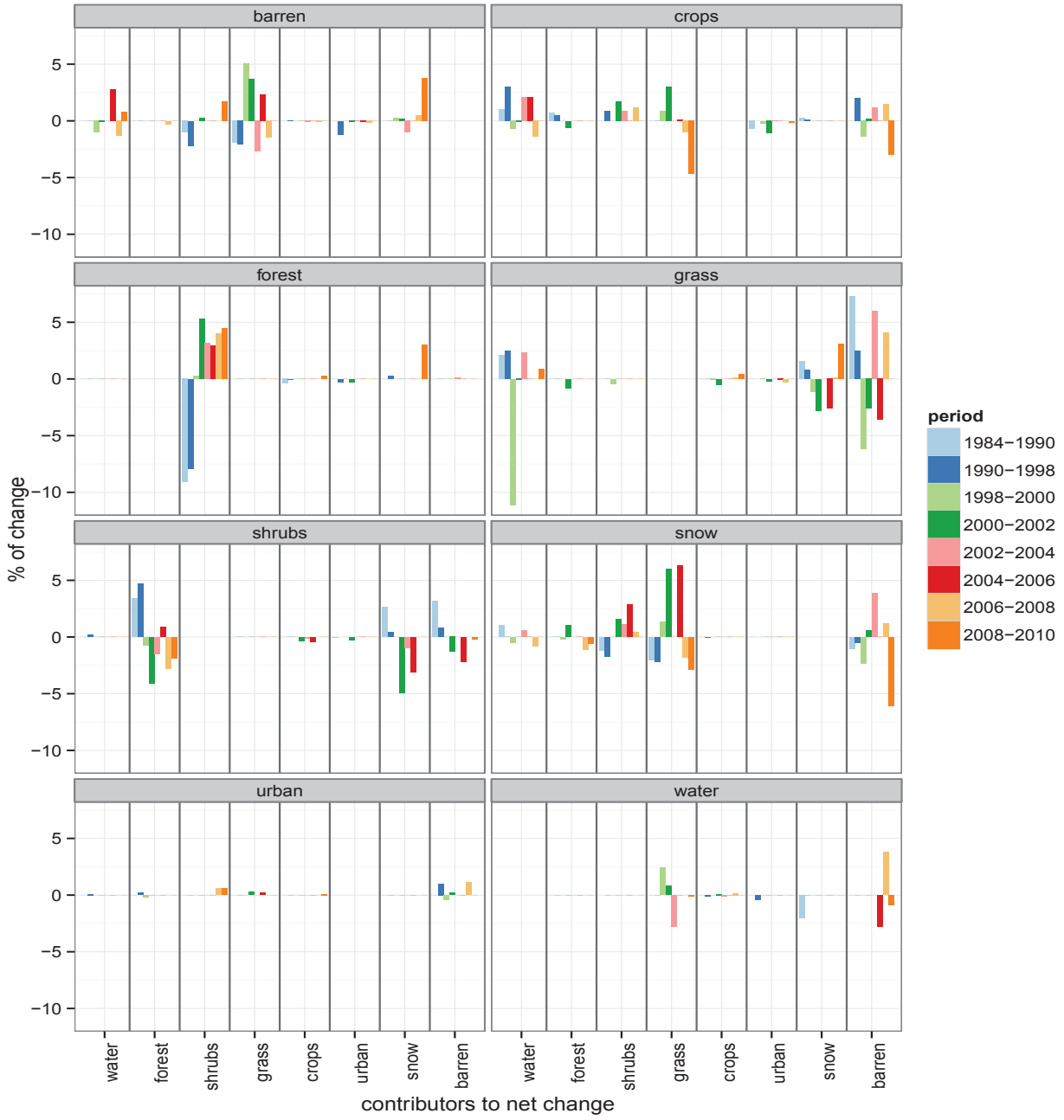


**Figure 4.4:** Bar plots illustrate the contributors to net change from a perspective of land cover. A positive value corresponds to land-cover types that contributed to the increase of the proportion of the particular class during the examined periods. A negative value corresponds to land-cover types to which the particular class was converted to.

in the middle and southern parts of the basin, but was also expanding towards the northern areas near the Himalayan foothills. During the period 2000–2006, the grass coverage was reduced in the northern part of the study area, while during the same period snow cover was increased (Fig. 4.5b & Fig. 4.5c). According to Figure 4.4, the most important contributor to the snow growth observed during that period is conversion from grass land.

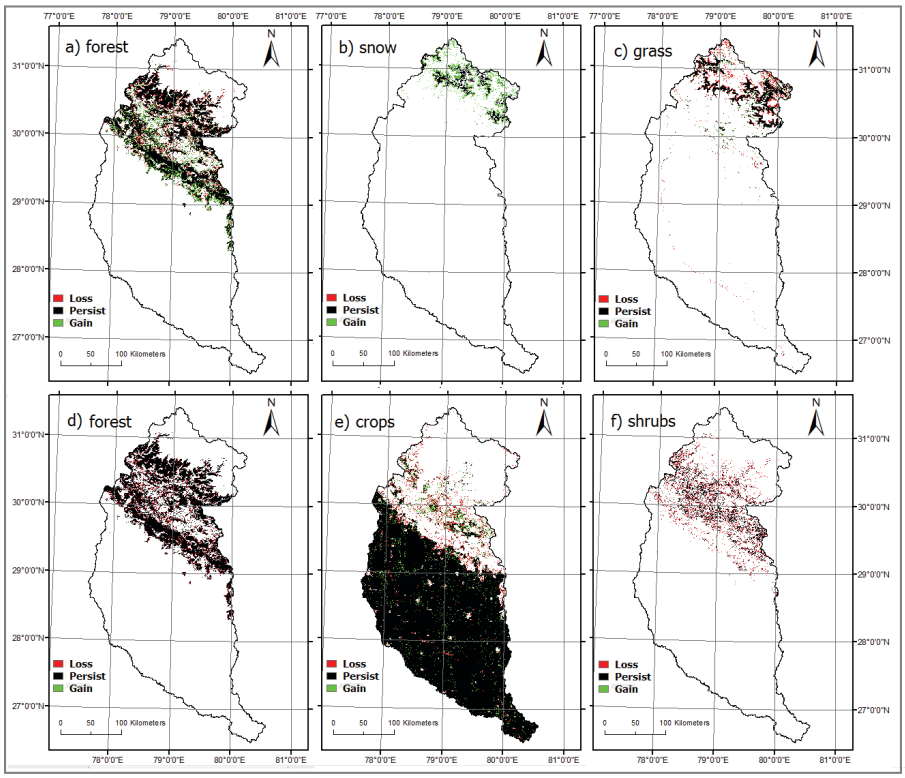


**Figure 4.5:** Indicative gains, losses and areas of land-cover persistence for: a) Forest during the period 1998–2010, b) Snow during the period 2000–2006, c) Grass during the period 2000–2006, d) Forest during the period 1984–1998, e) Crops during the period 1984–1990 and f) Shrubs during the period 1998–2010.

Trends from literature for other locations in India, such as Kerala and Haryana, for the period 1965 to 1996, confirm the intensification and expansion of cultivated land and the decrease in barren land (Indian National Science Academy, 2001). According to Rao and Pant (2001), who studied a small watershed in the mid elevation zone of the central Himalayas (India), between 1986 and 1996 the annual deforestation rate was 0.57%. During this period, intensification of cultivated land and conversion of natural forests and grazing lands to agriculture, as well as a constant thinning of available forest was recorded. Semwal

*et al.* (2004), report increase in agricultural land use by 30% during the 1963–1993 period, at the cost of loss of 5% of forest areas in the Pranmati watershed (Uttar Pradesh, India).

### 4.4.3 Stochastic modelling and future projections of land-cover change

Indicative transition probabilities for the periods 2000–2004, 2000–2010 and 2004–2010 are presented in Tables 4.5-4.7 at the end of this Chapter. Under the Markovian hypothesis, the expected transition probability matrices for different periods between 2000 and 2010 were calculated. All obtained Carl Pearson's $K^2$ values are shown in Table 4.3. Since all values were greater than the critical number 66.3, the null hypothesis that land cover at one point in time ($t_1$) is statistically independent of land cover at the preceding time period ($t_0$) was rejected.

**Table 4.3:** Carl Pearson's $K^2$ values and $\chi^2$ goodness of fit test values.

| | $K^2$ | $\chi^2$ |
|---|---|---|
| 2002-2006 | $1.07 \times 10^5$ | 1.22 |
| 2002-2010 | $1.75 \times 10^5$ | 4.85 |
| 2004-2010 | $1.98 \times 10^5$ | 4.41 |
| 2006-2010 | $1.95 \times 10^5$ | 4.60 |
| 2000-2004 | $0.74 \times 10^5$ | 0.99 |
| 2000-2006 | $1.09 \times 10^5$ | 1.31 |
| 2000-2008 | $1.13 \times 10^5$ | 1.48 |
| 2000-2010 | $1.39 \times 10^5$ | 1.88 |
| 2002-2008 | $1.37 \times 10^5$ | 2.54 |
| 2004-2008 | $0.94 \times 10^5$ | 0.97 |

The $\chi^2$ goodness of fit test for the $1^{st}$ order Markovian dependence gave values of $\chi^2$ as shown in Table 4.3. For 49 degrees of freedom and 5% level of significance, the critical value of $\chi^2$ was equal to 33.93. The dependence was therefore characterised by a $1^{st}$ order Markovian dependence, in all cases.

Table 4.4 and Fig. 4.6 show the equilibrium distributions of land cover for all tested periods, used for analysis of the stationarity of the system. These distributions were calculated by Matrix Powering (Bourne, 1976). According to that method and starting from an initial land-cover distribution $n$, the iteration $n$, $n \times P$, $n \times P^2$, $n \times P^3$,..., converges to a unique stationary distribution. The transition matrices ($P$) are multiplied by themselves (Bell, 1974; Bourne, 1976) until they converge to a matrix with identical rows. The obtained values indicate the amount of each land-cover class at a hypothetical

**Table 4.4:** Steady state probabilities calculated by multiplying the transition matrices by themselves (Matrix Powering, Bourne, 1976) until they converge to a matrix with identical rows. The values represent the proportion of each land-cover class at a hypothetical future equilibrium.

| | Water | Forest | Shrubs | Grass | Crops | Urban | Snow | Barren |
|---|---|---|---|---|---|---|---|---|
| 2000-2002 | 0.0045 | 0.2490 | 0.0466 | 0.0309 | 0.5595 | 0.0210 | 0.0573 | 0.0312 |
| 2002-2004 | 0.0032 | 0.1724 | 0.0319 | 0.0341 | 0.6442 | 0.0909 | 0.0139 | 0.0095 |
| 2004-2006 | 0.0020 | 0.1515 | 0.0863 | 0.0232 | 0.5776 | 0.1218 | 0.0256 | 0.0120 |
| 2006-2008 | 0.0025 | 0.1792 | 0.0160 | 0.0254 | 0.3051 | 0.0952 | 0.3181 | 0.0585 |
| 2008-2010 | 0.0044 | 0.2622 | 0.0458 | 0.0740 | 0.4187 | 0.0109 | 0.1264 | 0.0575 |
| 2002-2006 | 0.0022 | 0.1736 | 0.0632 | 0.0283 | 0.6123 | 0.0953 | 0.0183 | 0.0068 |
| 2002-2010 | 0.0026 | 0.2618 | 0.0363 | 0.0336 | 0.4413 | 0.0130 | 0.1910 | 0.0204 |
| 2004-2010 | 0.0029 | 0.2334 | 0.0354 | 0.0324 | 0.4113 | 0.0122 | 0.2297 | 0.0427 |
| 2006-2010 | 0.0032 | 0.2353 | 0.0279 | 0.0442 | 0.2559 | 0.0071 | 0.3692 | 0.0571 |
| 2000-2004 | 0.0036 | 0.2397 | 0.0379 | 0.0403 | 0.6347 | 0.0133 | 0.0201 | 0.0105 |
| 2000-2006 | 0.0022 | 0.2318 | 0.0712 | 0.0228 | 0.6376 | 0.0133 | 0.0161 | 0.0050 |
| 2000-2008 | 0.0023 | 0.2814 | 0.0328 | 0.0199 | 0.5069 | 0.0108 | 0.1268 | 0.0192 |
| 2000-2010 | 0.0018 | 0.2602 | 0.0310 | 0.0197 | 0.3227 | 0.0914 | 0.2524 | 0.0208 |
| 2002-2008 | 0.0022 | 0.2204 | 0.0278 | 0.0222 | 0.4730 | 0.1238 | 0.1103 | 0.0203 |
| 2004-2008 | 0.0027 | 0.2089 | 0.0320 | 0.0220 | 0.4829 | 0.0900 | 0.1239 | 0.0377 |

future equilibrium. Some of the distributions are quite similar to each other but the results do not provide evidence that the system is stationary since not all of them are similar (Fig. 4.6). As other studies have shown, transitions are often not constant through long periods. Nevertheless, stationarity can be assumed to make scenario-based projections and identify the response of the landscape to management and policy decisions. In the UG basin, the classification results already indicated changes in the land-cover trends in between the periods examined from 1984 to 2010.

An interesting trend is being observed here regarding the 2000–2002 transition matrix: Although from 2000 to 2002 a small increase of 0.73% in the agricultural proportion was identified (Fig. 4.3 & Table 4.2), the equilibrium distributions show a decrease in the agricultural proportion which from 63.58% in 2002 is being reduced to 55.96% (Table 4.4). The bar-plots of Fig. 4.4 illustrate that the only contributors to the crops reduction during the 2000–2002 period are conversion to forests (-0.6%) and urban (-1.1%). Therefore, in this case, the agricultural decrease suggested by the equilibrium distributions can be explained by the forest and urban growth noted at the same period (Table 4.4, 2000–2002 period). The fact that the equilibrium distribution of the 2000–2002 matrix shows an opposite trend in the crop land cover than the one observed during the 2000–2002 period highlights that the Markovian analysis is

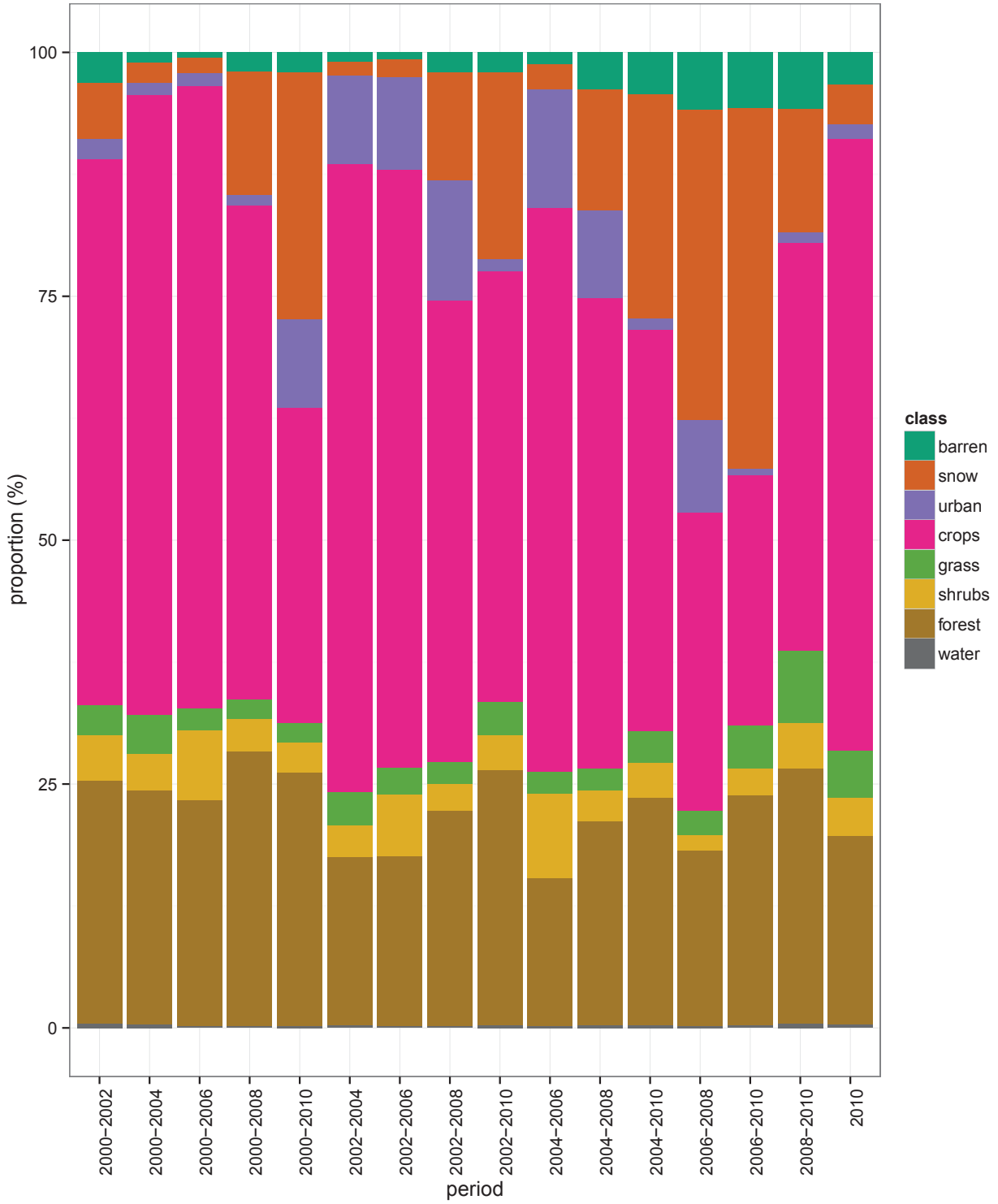


**Figure 4.6:** Equilibrium distributions of land cover as they were projected by all transition probability matrices. The calculated proportions of land cover for year 2010 are shown in the right end for comparison purposes.

not a simple linear extrapolation of trends, as the transition potentials might change over time until the equilibrium state is reached.

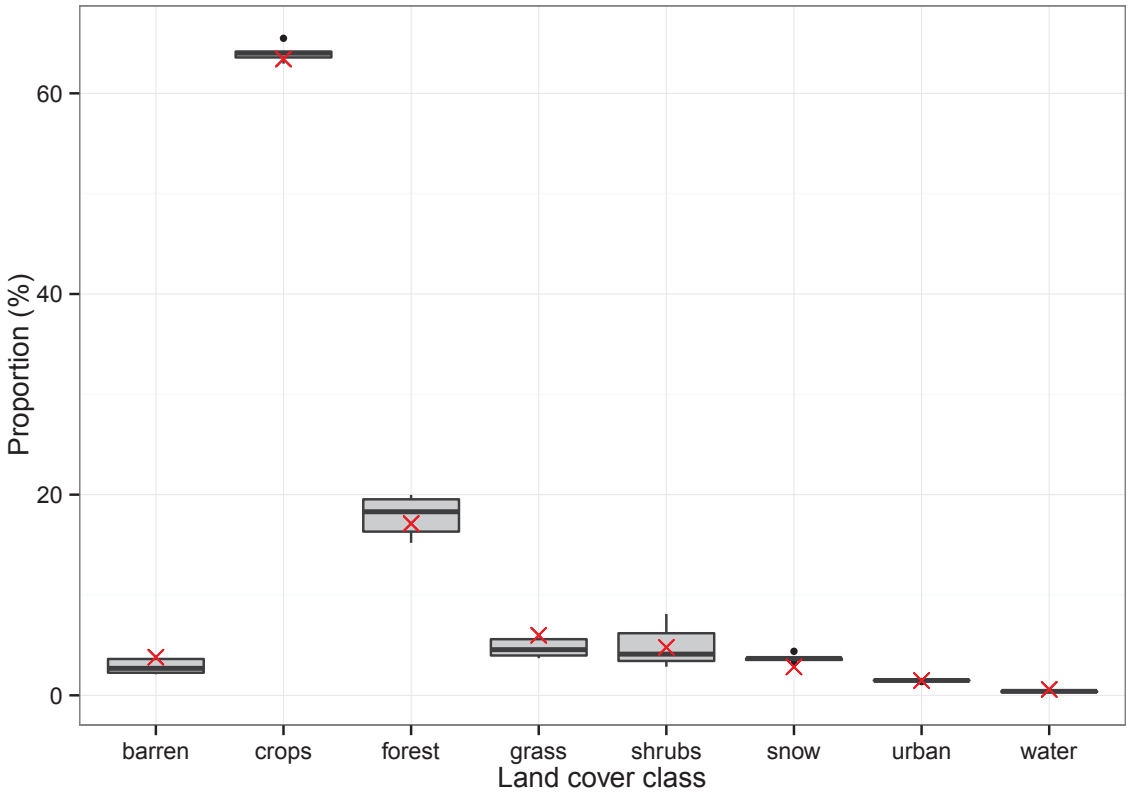


**Figure 4.7:** Box plots indicating land-cover trends with uncertainties for year 2010, as developed by applying Markov chain analysis. The transition probabilities of years previous to 2010 were used to generate a 2010 scenario. With red colour are illustrated the actual land-cover proportions of year 2010, as derived from the Landsat classifications. The middle bar of each box shows the median, while the bottom and top of the box bars show the $25^{\text{th}}$ and $75^{\text{th}}$ percentiles (or first and third quartiles), respectively. The upper and lower whiskers extend to the highest and lowest values that are within $1.5 \times \text{IQR}$ of the box's top and bottom bars, where IQR is the inter-quartile range. Dots show values beyond the end of the whiskers.

Before developing future projections of the land-cover status, the method was tested to examine how accurate it is. As a validation measure of the ability to generate future land-cover scenarios under Markov chain analysis, transition matrices of years previous to 2010 were used, and future scenarios for the year 2010 were generated. These scenarios were compared to the historic land-cover map of 2010 as shown in Fig. 4.7 (with red colour are land-cover proportions of the historic map). The results indicate

that the generated scenarios for 2010 are quite close to the actual historic proportions. Highest overall uncertainties are observed for the land-cover classes forest and shrubs. For instance, the actual proportion of forest in 2010 is 17.12%, while the two most extreme values that were obtained through Markov chain analysis for forest are 19.98% and 15.20% (Fig. 4.7). This increases confidence in developing other near future scenarios by applying the same method.

All possible transition probabilities of periods between the years 2000 and 2010, fifteen in total, were used to generate 15 different scenarios of future projections for the year 2020 (Fig. 4.8). As the trends in different matrices vary, the future predictions generated were not exactly the same. Whenever 2020 was not an even multiple of the training period (see section 4.3.3), a simple interpolation (or extrapolation) was used to calculate the proportions for that year.

Figure 4.9 shows the uncertainty of the projected scenarios. The land-cover types with the higher values of uncertainty are forest and crops, which was expected given that these are the two dominant land-cover types of the study area and the key difference between the transition matrices used for the future scenarios is that some of them are projecting an expansion of forest and/or agricultural areas and others are projecting a loss in these areas.

Figure 4.10 shows the spatial distribution of the predicted future land cover for year 2020 after determining the dominant land-cover types by applying the majority rule in the 15 different scenarios. The main projected trends include forest growth, replacing some of the shrub and grass areas in the mid-north parts of the UG basin and less grass and barren lands in the north, where the snow coverage expands. In addition, agricultural expansion and urbanization are being projected mainly for the southern parts of the study area.

## 4.5 Chapter Summary

In this Chapter, trends in land-cover changes were detected and quantified by classifying satellite imagery and modelling land-cover change in a region that has undergone one of the largest environmental changes in human history over recent decades.

The study focused on a period characterized by dramatic land-cover changes of high complexity. The hypothesis of a stationary system is therefore unreliable and the future land-cover distributions generated

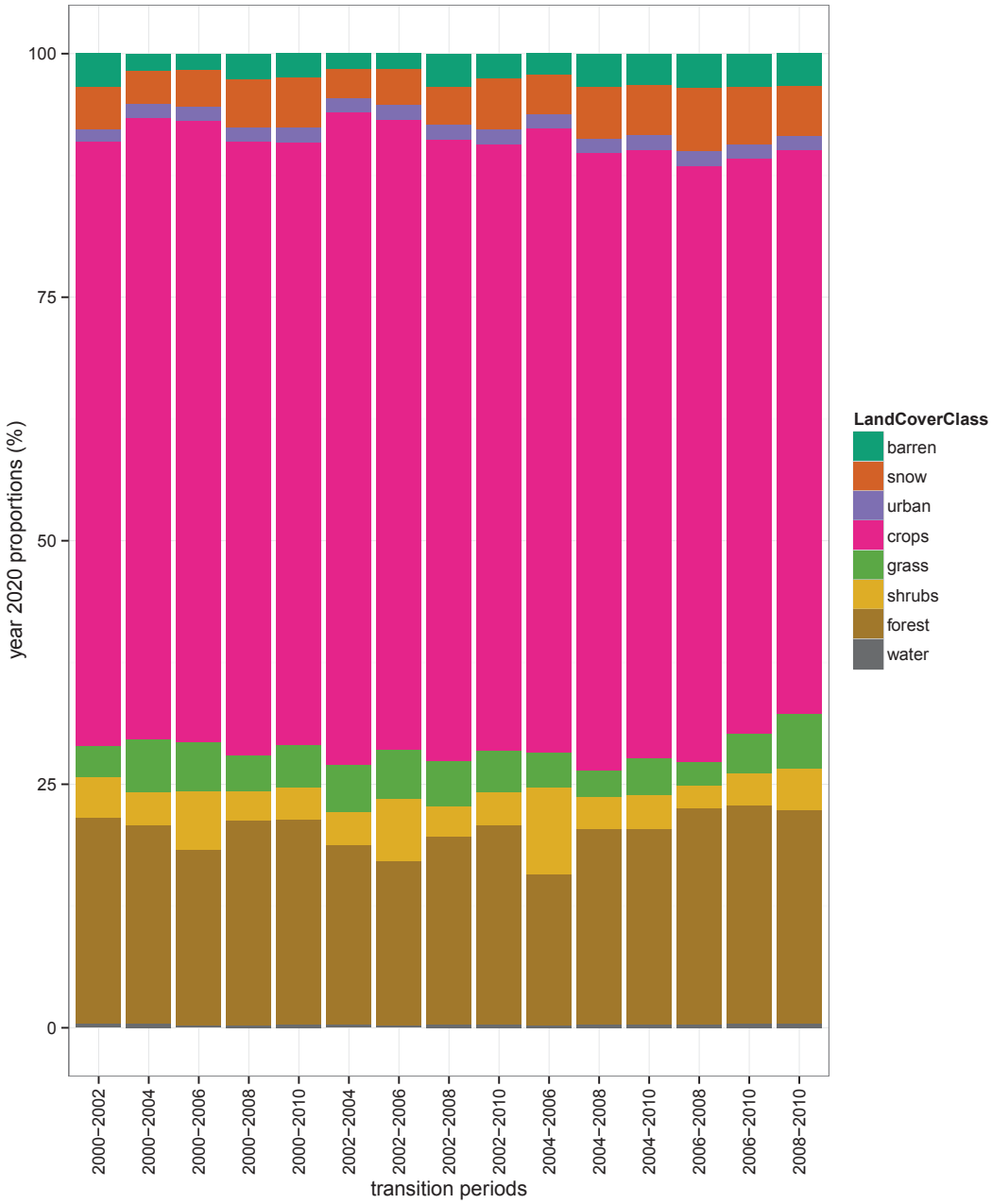


**Figure 4.8:** Projected proportions of land cover for year 2020, based on the 15 scenarios tested as shown in the x axis labels.

by different transition matrices revealed different trends that do not necessarily represent realistic future states for the UG basin. However, the Markov chain analysis is a simple method for projection of trends and regardless of its limitations can indicate potential scales and directions of future changes (Bell 1974).

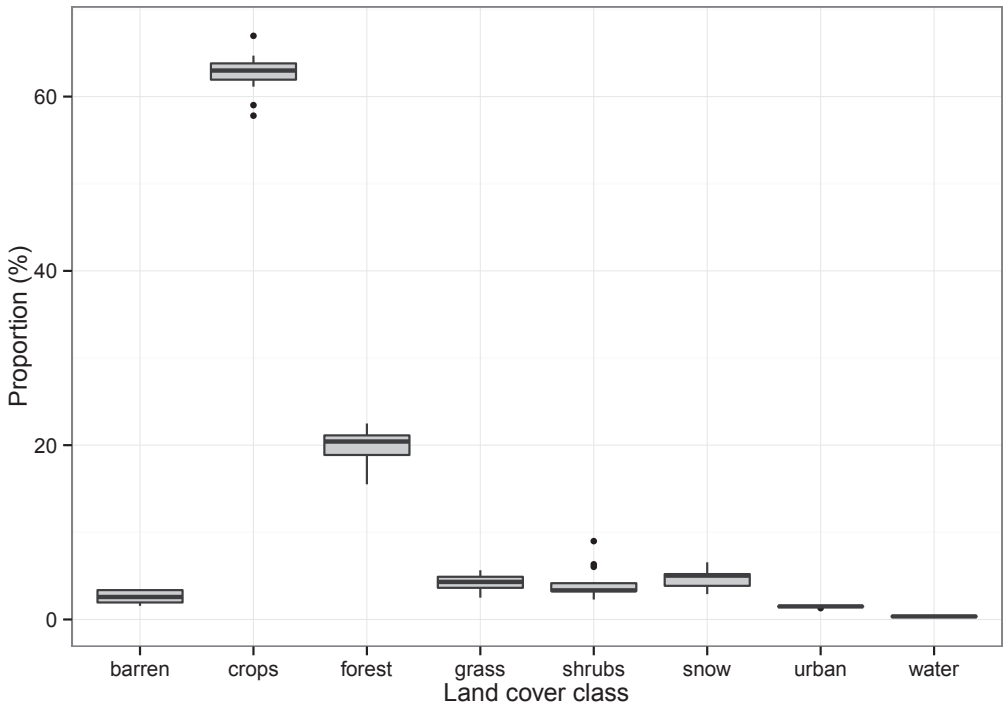


**Figure 4.9:** Box plots indicating future land-cover trends with uncertainties in the future scenarios for year 2020. The middle bar of each box shows the median, while the bottom and top of the box bars show the $25^{\text{th}}$ and $75^{\text{th}}$ percentiles (or first and third quartiles), respectively. The upper and lower whiskers extend to the highest and lowest values that are within $1.5 \times \text{IQR}$ of the box's top and bottom bars, where IQR is the inter-quartile range. Dots show values beyond the end of the whiskers.

The main trends of changes observed in the study region for the period from 1984 to 2010 are increased areas of forest, agricultural land, and urbanization, and loss of barren, shrubs, and grassland.

Potential future directions of land-cover change in the UG basin vary and depend on the historic time period selected by the analyst to project past changes into the future. In this study, 15 different scenarios based on historic land-cover change produced different future projections. The scenario using land-cover maps for 2008 and 2010 projects future expansion of forest, urban, grass, and shrubland, with a decline in agriculture and bare soil. More confidence can be placed in this result as it is based on analysis of the most recent land-cover change. Future work will attempt to improve the prediction of land cover by applying modelling approaches that utilize biophysical and socio-economic datasets that did not become available during the course of the study. This is a possible way to reduce uncertainty and provide more accurate projections for the future status of land cover in the UG basin.

**Table 4.5:** Transition probabilities, 2000–2004

| | Water | Forest | Shrubs | Grass | Crops | Urban | Snow | Barren |
|---|---|---|---|---|---|---|---|---|
| Water | 0.2351 | 0.1813 | 0.0729 | 0.1228 | 0.3367 | 0.0005 | 0.0121 | 0.0386 |
| Forest | 0.0017 | 0.8528 | 0.0910 | 0.0173 | 0.0366 | 0.0001 | 0.0001 | 0.0004 |
| Shrubs | 0.0045 | 0.6175 | 0.2482 | 0.0173 | 0.1115 | 0.0001 | 0.0004 | 0.0005 |
| Grass | 0.0220 | 0.0345 | 0.0132 | 0.7275 | 0.1213 | 0.0001 | 0.0082 | 0.0732 |
| Crops | 0.0019 | 0.0155 | 0.0092 | 0.0033 | 0.9679 | 0.0020 | 0.0001 | 0.0001 |
| Urban | 0.0010 | 0.0016 | 0.0006 | 0.0006 | 0.0945 | 0.9015 | 0.0001 | 0.0001 |
| Snow | 0.0009 | 0.0001 | 0.0001 | 0.0575 | 0.0001 | 0.0001 | 0.8959 | 0.0453 |
| Barren | 0.0051 | 0.0001 | 0.0001 | 0.2385 | 0.0019 | 0.0001 | 0.1539 | 0.6003 |

**Table 4.6:** Transition probabilities, 2000–2010

| | Water | Forest | Shrubs | Grass | Crops | Urban | Snow | Barren |
|---|---|---|---|---|---|---|---|---|
| Water | 0.2069 | 0.2577 | 0.0633 | 0.0586 | 0.3631 | 0.0004 | 0.0209 | 0.0291 |
| Forest | 0.0009 | 0.8955 | 0.0733 | 0.0073 | 0.0225 | 0.0001 | 0.0001 | 0.0003 |
| Shrubs | 0.0053 | 0.6701 | 0.2218 | 0.0089 | 0.0931 | 0.0001 | 0.0002 | 0.0005 |
| Grass | 0.0147 | 0.0451 | 0.0286 | 0.7108 | 0.0849 | 0.0001 | 0.0175 | 0.0983 |
| Crops | 0.0017 | 0.0155 | 0.0134 | 0.0037 | 0.9654 | 0.0001 | 0.0001 | 0.0001 |
| Urban | 0.0001 | 0.0001 | 0.0003 | 0.0001 | 0.0001 | 0.9990 | 0.0002 | 0.0001 |
| Snow | 0.0005 | 0.0001 | 0.0001 | 0.0040 | 0.0001 | 0.0001 | 0.9706 | 0.0245 |
| Barren | 0.0026 | 0.0011 | 0.0003 | 0.0583 | 0.0028 | 0.0001 | 0.3344 | 0.6004 |

**Table 4.7:** Transition probabilities, 2004–2010

| | Water | Forest | Shrubs | Grass | Crops | Urban | Snow | Barren |
|---|---|---|---|---|---|---|---|---|
| Water | 0.3137 | 0.0891 | 0.0096 | 0.1193 | 0.4375 | 0.0032 | 0.0212 | 0.0064 |
| Forest | 0.0017 | 0.8804 | 0.0824 | 0.0047 | 0.0304 | 0.0002 | 0.0001 | 0.0001 |
| Shrubs | 0.0050 | 0.5860 | 0.3015 | 0.0152 | 0.0916 | 0.0003 | 0.0003 | 0.0001 |
| Grass | 0.0092 | 0.0671 | 0.0211 | 0.6163 | 0.0323 | 0.0002 | 0.0892 | 0.1646 |
| Crops | 0.0020 | 0.0111 | 0.0114 | 0.0065 | 0.9665 | 0.0023 | 0.0001 | 0.0001 |
| Urban | 0.0001 | 0.0010 | 0.0008 | 0.0002 | 0.0840 | 0.9137 | 0.0001 | 0.0001 |
| Snow | 0.0009 | 0.0001 | 0.0003 | 0.0133 | 0.0001 | 0.0001 | 0.9533 | 0.0319 |
| Barren | 0.0021 | 0.0029 | 0.0008 | 0.1102 | 0.0018 | 0.0002 | 0.1803 | 0.7017 |

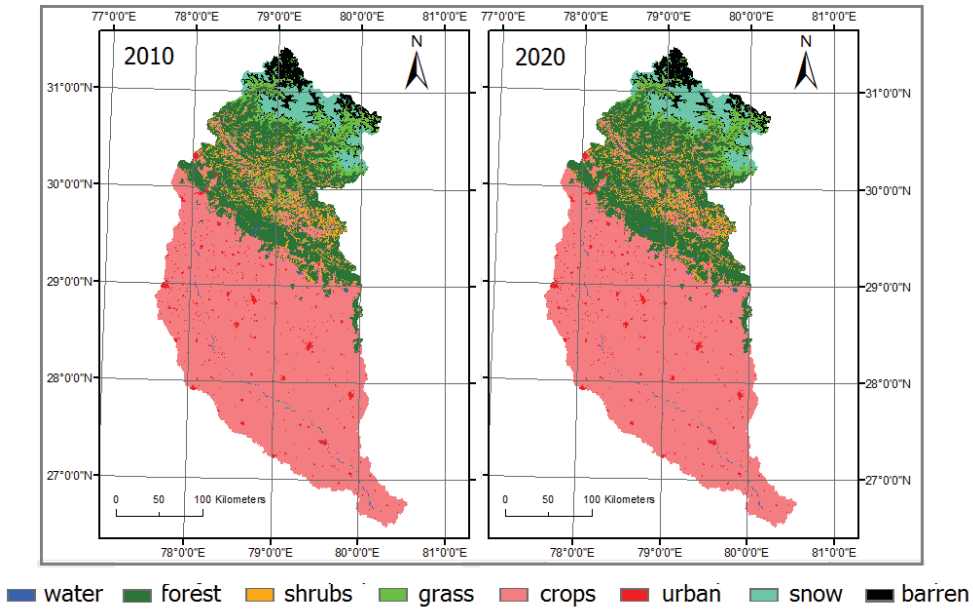


**Figure 4.10:** Land-cover maps of historic year 2010 (on the left) and future scenario for year 2020 (on the right), as calculated after determining the dominant land-cover types by applying the majority rule in the 15 different scenarios. Developed by Markov chain analysis.

# Chapter 5

# A critical analysis of JULES for water resources applications

# A critical analysis of JULES for water resources applications

## 5.1 Introduction

In this Chapter, the Land Surface Model (LSM) JULES (Best *et al.*, 2011) is explored and evaluated, in terms of large scale modelling of the Upper Ganges (UG) hydrologic regime. By performing a sensitivity and uncertainty analysis, I look into the model's robustness and how sensitive it is to different processes.

In the sensitivity analysis Section, the model's sensitivity to precipitation forcing is discussed, as large precipitation data uncertainties arise from the comparison of various datasets. Further, in an attempt to assess and improve the parameterisation of JULES, different model parameters and structural schemes have been perturbed in a series of experiments, the results of which are being presented and discussed.

On the other hand, during the uncertainty analysis I explore whether it is possible to implement JULES as a hydrological model that provides robust predictions, by taking into account input data and parameter uncertainties. The model's potential to bracket observations is explored and quantified, in terms of streamflow, evapotranspiration (ET) and soil moisture fluxes.

Overall the model is found to be reasonably skilful in terms of its ability to reproduce observed hydrological fluxes. However, both the sensitivity and uncertainty analysis show that there is much room left to improve JULES so that it can function as a proper hydrological model for water resources assessments. Potential ways of addressing the model's shortcomings are discussed.

This research, undertaken over a large but understudied catchment of the Ganges river, is expected to provide valuable insights into whether global LSMs and large scale datasets are appropriate for studying and assessing the hydrological behaviour of tropical river basins.

## 5.2 Data

### 5.2.1 Precipitation datasets

The rainfall datasets used for the precipitation uncertainty analysis are summarised in Table 5.1.

The IMD gridded product was obtained from the Indian Meteorological Department's (IMD) archive. The dataset was created by interpolating rain gauge observation data from 1803 stations across India (Rajeevan *et al.*, 2006).

The APHRODITE gridded product was obtained from the Asian Precipitation Highly Resolved Observational Data Integration Towards the Evaluation of water resources (APHRODITE) project archive. The dataset was created by collecting rain gauge observation data across Asia (Yatagai *et al.*, 2009).

NCEP data were obtained from the Princeton Hydrology archive and consist of reanalysis data that have been post-processed and merged with observations (National Center of Environmental Predictions, Kalnay *et al.*, 1996; Sheffield *et al.*, 2006).

The Tropical Rainfall Measuring Mission (TRMM) Multisatellite Precipitation Analysis (TMPA) products, versions 6 and 7, were obtained from the NASA archive [1] (Huffman *et al.*, 2007; Huffman and Bolvin, 2013), and will be hereafter referred to as TRMMv6 and TRMMv7.

Only 5 stations providing ground observations from the IMD national rain gauge network became available during the course of this study. They are not enough for spatial interpolation but can provide useful information when compared to the gridded datasets mentioned above.

### 5.2.2 Land surface modelling datasets

The datasets used to force the LSM JULES are summarised in Table 5.2. Precipitation data that were mentioned above, are not included in the table.

Similar to the NCEP precipitation data, NCEP data for other meteorological variables were obtained from the Princeton Hydrology archive. This product was developed by Sheffield *et al.* (2006), after merging reanalysis with ground truth data.

[1] `ftp://disc2.nascom.nasa.gov/ftp/data/s4pa//TRMM_L3/`

**Table 5.1:** Rainfall datasets used for precipitation uncertainty analysis

| Name | Type | Resolution | Time step | Time domain | Reference |
|---|---|---|---|---|---|
| Kanpur Nagar | rain gauge | | daily | 1989,1991,1996–1999, 2001–2002, 2005–2006 | IMD network |
| Moradabad | rain gauge | | daily | 1980–1982, 1985–2006 | IMD network |
| Haridwar | rain gauge | | daily | 1980–2005 | IMD network |
| Chamoli | rain gauge | | daily | 1990–1992,1996–1999 | IMD network |
| Tehri-Garhwal | rain gauge | | daily | 1980–1981, 2003–2006 | IMD network |
| IMD | gridded | 1° | daily | 1951–2003 | Rajeevan *et al.* (2006) |
| APHRODITE | gridded | 0.25° | daily | 1961–2007 | Yatagai *et al.* (2009) |
| TMPA v6 | gridded | 0.25° | daily | 1997–2011 | Huffman *et al.* (2007) |
| TMPA v7 | gridded | 0.25° | 3-hourly | 1997–2014 | Huffman and Bolvin (2013) |
| NCEP | gridded | 1° | 3-hourly & daily | 1948–2008 | Sheffield *et al.* (2006) |

**Table 5.2:** Datasets used to force the LSM JULES

| Variable | Name | Resolution | Time step | Time domain | Reference |
|---|---|---|---|---|---|
| Radiation | NCEP | 1° | 3-hourly & daily | 1948–2008 | Sheffield *et al.* (2006) |
| Air temperature | NCEP | 1° | 3-hourly & daily | 1948–2008 | Sheffield *et al.* (2006) |
| Surface pressure | NCEP | 1° | 3-hourly & daily | 1948–2008 | Sheffield *et al.* (2006) |
| Specific humidity | NCEP | 1° | 3-hourly & daily | 1948–2008 | Sheffield *et al.* (2006) |
| Wind speed | NCEP | 1° | 3-hourly & daily | 1948–2008 | Sheffield *et al.* (2006) |
| Land cover | | 30 m | 2 years | 1998–2010 | Tsarouchi *et al.* (2014) |
| Soil properties | | 0.1° | | | K. Bovis, UM–CAP |

The land-cover representation is based on high-resolution land-cover maps for northern India, developed by the authors (Tsarouchi *et al.*, 2014) and based on Landsat satellite imagery, as discussed in Chapter 4.

Maps of soil parameters were created by the UK Met Office Unified Model Central Ancillary Program (UM–CAP) at the model resolution, based on soil texture maps from the HWSD (FAO, 2009) and ISRIC[2] databases. This is further discussed in Section 5.3.2.

The datasets used to evaluate the model's performance are summarized in Table 5.3.

**Table 5.3:** Datasets used to evaluate JULES' performance

| Variable | Name | Resolution | Time step | Time domain | Reference |
|---|---|---|---|---|---|
| Evapotranspiration | MODIS | 1 km | daily | 2000–2010 | Mu *et al.* (2011) |
| | LandFlux-EVAL | 1° | monthly | 1989–2005 | Mueller *et al.* (2013) |
| Streamflow | | | daily | 1998–2011 | Hydroflux-India partners |
| Soil moisture | ESV-SM | 0.25° | daily | 1978–2010 | Liu *et al.* (2012); Wagner *et al.* (2012) |

The MODIS global ET dataset was developed as part of the NASA/EOS project to estimate global terrestrial ET by using satellite remote sensing data. It was developed by Mu *et al.* (2011) improved

[2]Observations of soil sand, silt and clay fractions are available from the ISRIC world soil information website: www.isric.org

ET algorithm over a previous Mu *et al.* (2007) paper. The algorithm is based on the Penman-Monteith (Monteith, 1965) approach.

The LandFlux-EVAL dataset was generated as part of the LandFlux-EVAL initiative of the GEWEX Data and Assessment Panel (GDAP). Mueller *et al.* (2013) evaluated and compared existing land ET products and generated global merged benchmark products based on the analysis of the already existing datasets. In this study the 1989–2005 period dataset was used, which is based on 14 data sets in total. ET is derived from satellite products, field observations, LSMs that are forced with observed meteorology or reanalysis models (Mueller *et al.*, 2013).

Daily records of streamflow for the Bhimgoda barrage in the north of the study area were obtained through communication with Indian partners of the Hydroflux-India project. Figure 5.1 shows the location of the Bhimgoda sub-catchment with red colour, relative to the UG basin.

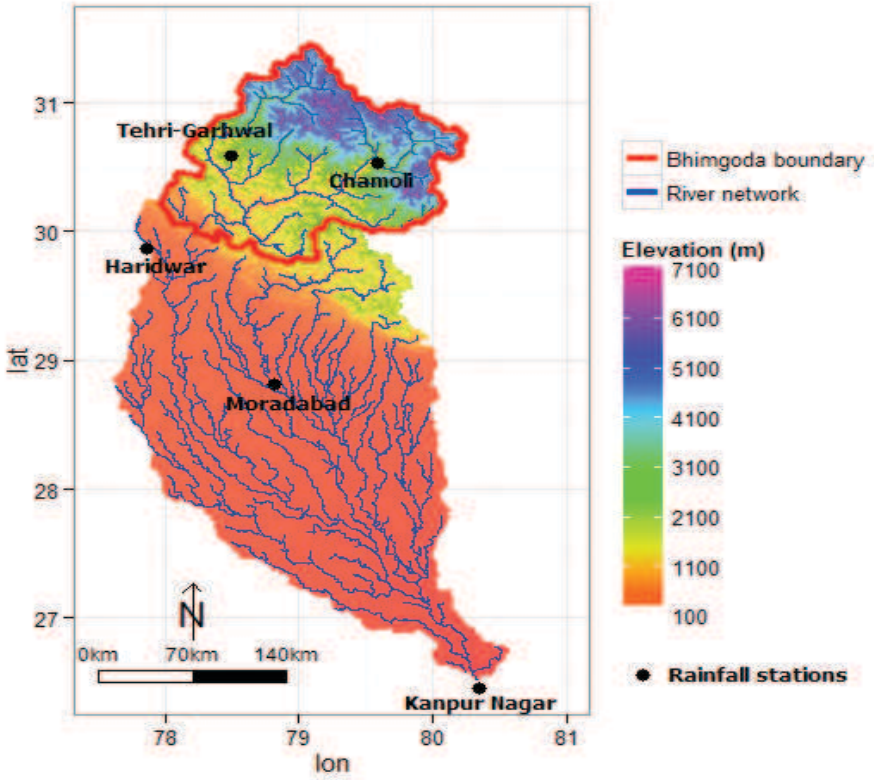


**Figure 5.1:** Location map of Bhimgoda sub-catchment (red line), for which daily river flow data were obtained, and of IMD rainfall stations (black dots) used in this study.

The Essential Climate Variable (ECV) Soil Moisture (SM) dataset was released as part of the Phase

1 of the European Space Agency (ESA) Climate Change Initiative Soil Moisture project. The global merged surface soil moisture product is the output of blending soil moisture products derived from active and passive microwave satellite sensors, at a daily time-step (Liu *et al.*, 2012; Wagner *et al.*, 2012).

All datasets were further spatially disaggregated to $0.1^\circ \times 0.1^\circ$ resolution grids, which is the resolution the model is set up, using the bilinear interpolation method.

## 5.3 Methods

### 5.3.1 Model overview: JULES Land Surface Model

JULES, the Joint UK Land Environment Simulator, (Best *et al.*, 2011; Clark *et al.*, 2011) is a physics-based model, which is used as the land surface scheme of the UK Met Office's Unified Modelling system (Fig. 5.2).

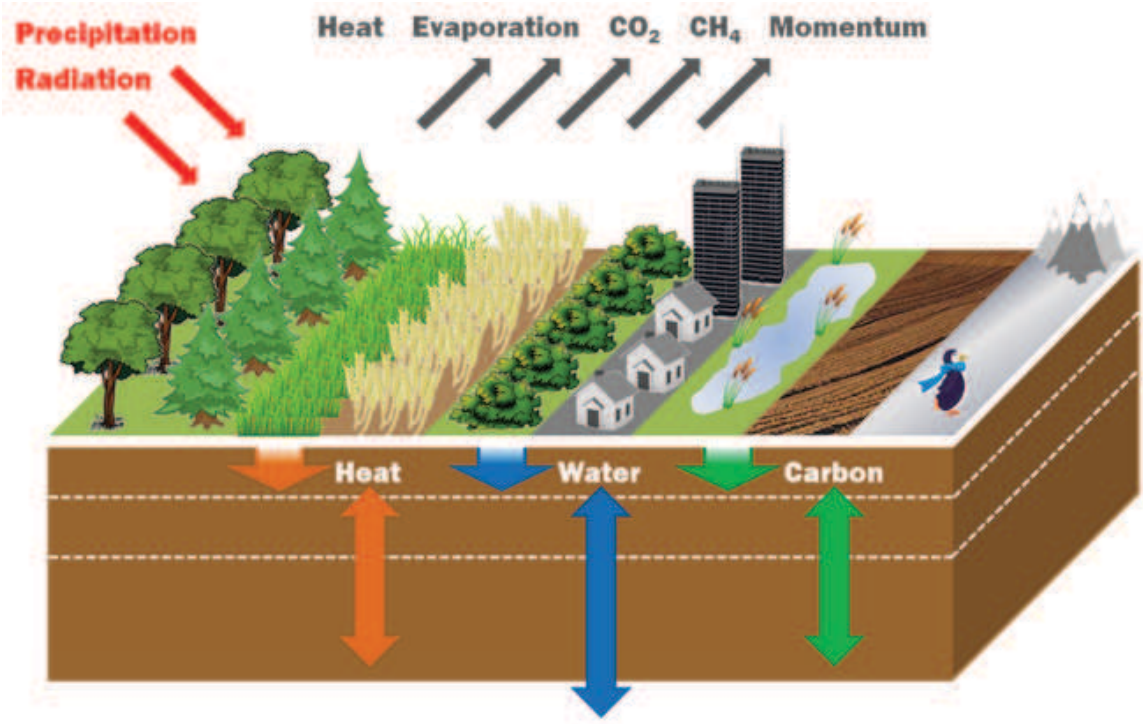


**Figure 5.2:** JULES overview, UK Met Office, 2013

The model partitions precipitation into canopy interception and throughfall. In the default runoff

scheme, surface runoff is generated based on Hortonian Infiltration and there is no representation of saturation-excess runoff generation.

Surface heterogeneity within JULES is represented by the tile approach (Essery *et al.*, 2003). The surface of each grid-box comprises fractions of 9 different surface types; five vegetated - Plant Functional Types (PFTs): broad-leaf trees, needle-leaf trees, $C_3$ grasses, $C_4$ grasses and shrubs, and four non-vegetated: urban, water, bare soils and ice. For each surface type of the grid-box, the energy balance is solved, and a weighted average is calculated from the individual surface fluxes for each grid-box. In the subsurface, the soil column is divided into 4 layers, which have a thickness of 0.1m, 0.25m, 0.65m, and 2m respectively, going from the top to the bottom. The Darcy-Richards equation (Richards, 1931) is solved using finite difference approximation, to calculate water movement through the soil. Subsurface runoff is represented by a free drainage from the deepest soil layer. The soil water retention characteristics (relationship between volumetric water content and soil suction) and the relationship between volumetric water content and hydraulic conductivity follow the relationships of van Genuchten (1980). An alternative option using Brooks and Corey (1964) relationships is also available. A structural limitation of the current JULES version is that there is no subsurface heterogeneity at the sub-grid scale, in contrast to on the surface.

Stomatal conductance, transpiration and vegetation biophysical processes, such as photosynthesis, dynamically interact with hydrological and land-atmosphere energy exchange processes (such as transpiration) through an integrated coupling. Potential evaporation is calculated from an extended version of the Penman-Monteith equation (Monteith, 1965) that includes a model of conductive heat transfer through the soil (Cox *et al.*, 1998) . It is assumed that evaporation from saturated parts of the surface (lakes, wet vegetation canopies and snow) occurs at the potential rate (i.e. subject to an aerodynamic resistance), while plant transpiration from root water uptake from all 4 soil layers (vegetated areas) is restricted by stomatal resistance and bare soil evaporation from the top soil layer is restricted by the soil moisture state (Zulkafli *et al.*, 2013). The stomatal resistance is also responsible for the regulation of $CO_2$ exchange between plants and the atmosphere (Cox *et al.*, 1999).

For each soil layer ($k$), the ability of vegetation to extract water is dependent on a soil moisture stress factor ($\beta_k$) and root density ($r_k$). For transpiration $E$, the flux extracted from each soil layer is $e_k^o E$,

where:

$$e_k^o = \frac{r_k \beta_k}{\sum_k r_k \beta_k} \tag{5.1}$$

where $r_k$ is the fraction of roots extending from depth of soil layer $k-1$ to depth of soil layer $k$. For each soil layer, the soil moisture stress factor is calculated as:

$$\beta_s = \begin{cases} 1 & \theta \geq \theta_c \\ \frac{\theta - \theta_w}{\theta_c - \theta_w} & \theta_c > \theta > \theta_w \\ 0 & \theta \leq \theta_w \end{cases} \tag{5.2}$$

where $\theta$ is the mean unfrozen soil water content of the soil layer and $\theta_c$, $\theta_w$ are the critical and wilting point concentrations of the soil layer, respectively.

According to Eq. 5.2, plant water availability depends on soil water content ($\theta$) and decreases linearly when $\theta$ decreases from its critical point value to its wilting point value, which depends on soil texture and the hydraulic parameterisation scheme (Van Genuchten or Brooks & Corey).

Because the model does not simulate the dynamic growth of vegetation, agricultural areas are processed as natural grass (Van den Hoof *et al.*, 2011). Vegetation parameters such as Leaf Area Index (LAI), root depth and canopy height are obtained off-line and they either remain constant throughout the entire simulation period or can vary temporally and/or spatially (apart from the root depth which cannot vary spatially), depending on data availability prior to the simulation.

The input meteorological data requirements are time-series of incoming short-wave and long-wave radiation, temperature, specific humidity, wind speed, and surface pressure. These are used in a full energy balance equation that includes components of radiation, sensible heat, latent heat, canopy heat, and ground surface heat.

For a more detailed description of the model see Best *et al.* (2011).

### 5.3.2 Model setup

JULES was run in a 0.1°longitude x 0.1°latitude grid resolution, for the period 1999–2008. For each grid point, the full set of input data (model parameters, time-series of meteorological data, land-use and soil map) were prescribed. Before each run of the model, a spin-up run is performed, to initialise the internal states. After each spin-up cycle, the model tests whether soil moisture and soil temperature have changed by more than a specified amount. If the change is greater than this amount, the model repeats the spin-up cycle. If the change is less, the model is considered to have spun-up, and it then proceeds to the main run. The maximum specified change for soil moisture is $1kg/m^2$ and for soil temperature is $1\%$.

The input data used to force the model are described in Section 5.2 and Table 5.2. The watershed boundary for the study basin was delineated based on SRTM 90m resolution digital elevation data (Jarvis *et al.*, 2008).

For the parametrisation of plant functional types and non-vegetated tiles, the default parameters described by Best *et al.* (2011) in Tables 5 & 6, were used.

The soil parameters describing hydraulic characteristics of the soil are based on the van Genuchten (1980) model and listed in Table 5.4. The maps of soil properties are ancillary maps produced by UM–CAP (based on the documentation by Dharssi *et al.*, 2009), at the model resolution. Soil texture maps providing fractions of sand ($F_s$), silt ($F_{st}$), and clay ($F_c$) were produced by blending the HWSD (FAO, 2009) and the ISRIC[3] soils datasets. For simplicity and since HWSD comprises the base and the largest contributor of data, the combined dataset is referred to as HWSD. The van Genuchten parameters were then calculated, using the HWSD soil textural information and the look-up Table 5.5. In addition, soil surface albedo was obtained from MODIS.

Soil thermal properties are calculated independently of the soil hydraulics and are described by two fields: (a) Thermal conductivity, $h_{con}$ $(\mathrm{Jm^{-1}K^{-1}s^{-1}})$, and (b) Dry heat capacity, $h_{cap}$ $(\mathrm{Jm^{-3}K^{-1}})$. Thermal conductivity is derived based on Eq. 5.3, after Farouki (1981).

$$h_{con} = \lambda_{air}{}^{\theta_{sat}} \lambda_c{}^{(1-\theta_{sat})F_c} \lambda_s{}^{(1-\theta_{sat})F_s} \lambda_{st}{}^{(1-\theta_{sat})F_{st}} \tag{5.3}$$

[3]Observations of soil sand, silt and clay fractions were downloaded from the ISRIC world soil information website: www.isric.org

**Table 5.4:** Soil hydraulic parameters in JULES

| Symbol | Description | units |
|---|---|---|
| $1/(n-1)$ | Van Genuchten parameter | no units |
| $1/\alpha$ | Air entry matric potential | m |
| $\theta_{sat}$ | Soil moisture content at saturation | $\mathrm{m^3m^{-3}}$ |
| $\theta_{crit}$ | Soil moisture content at field capacity | $\mathrm{m^3m^{-3}}$ |
| $\theta_{wilt}$ | Soil moisture content at wilting point | $\mathrm{m^3m^{-3}}$ |
| $h_{con}$ | Thermal conductivity | $\mathrm{Jm^{-1}K^{-1}s^{-1}}$ |
| $h_{cap}$ | Dry heat capacity | $\mathrm{Jm^{-3}K^{-1}}$ |
| $K_{sat}$ | Saturated hydraulic conductivity | $\mathrm{Kgm^{-2}s^{-1}}$ |
| $alb$ | Soil albedo | no units |

**Table 5.5:** UM-CAP pedotransfer look-up table, based on Wosten *et al.* (1999) (Keir Bovis, UK Met Office, personal communication 22/07/2013)

| Textural class | Clay ($\mathrm{F_c}$) | Silt ($\mathrm{F_{st}}$) | Sand ($\mathrm{F_s}$) | $\mathrm{K_{sat}}$ ($\mathrm{ms^{-1}}$) | $\theta_{\mathrm{sat}}$ ($\mathrm{m^3m^{-3}}$) | $\theta_{\mathrm{r}}$ ($\mathrm{m^3m^{-3}}$ ) | $\alpha$ ($\mathrm{m^{-1}}$) | n (-) |
|---|---|---|---|---|---|---|---|---|
| Coarse | 0.05 | 0.1 | 0.85 | $1.9454 \times 10^{-5}$ | 0.3824 | 0 | 16.014 | 1.2755 |
| Medium | 0.230 | 0.5 | 0.2700 | $2.773 \times 10^{-6}$ | 0.4581 | 0 | 2.5206 | 1.1508 |
| Medium-Fine | 0.2300 | 0.5000 | 0.2700 | $2.773 \times 10^{-6}$ | 0.4581 | 0 | 2.5206 | 1.1508 |
| Fine | 0.5200 | 0.2700 | 0.2100 | $1.520 \times 10^{-6}$ | 0.4559 | 0 | 3.0860 | 1.0893 |
| Very-Fine | 0.5200 | 0.2700 | 0.2100 | $1.520 \times 10^{-6}$ | 0.4559 | 0 | 3.0860 | 1.0893 |
| Organic | 0.5200 | 0.2700 | 0.2100 | $1.520 \times 10^{-6}$ | 0.4559 | 0 | 3.0860 | 1.0893 |

where:

$$\begin{aligned} &\lambda_{air} \text{ is the conductivity of air} = 0.025\ \mathrm{Jm^{-1}K^{-1}s^{-1}} \\ &\lambda_c \text{ is the conductivity of clay} = 1.16\ \mathrm{Jm^{-1}K^{-1}s^{-1}} \\ &\lambda_s \text{ is the conductivity of sand} = 1.57\ \mathrm{Jm^{-1}K^{-1}s^{-1}} \\ &\lambda_{st} \text{ is the conductivity of silt} = 1.57\ \mathrm{Jm^{-1}K^{-1}s^{-1}} \end{aligned} \tag{5.4}$$

Dry heat capacity is derived based on Eq. 5.5, according to the documentation provided by the UM–CAP[4].

$$h_{cap} = (1 - \theta_{sat})(F_c c_c + F_s c_s + F_{st} c_{st}) \tag{5.5}$$

where:

$$\begin{aligned} &c_c \text{ is the heat capacity of clay} = 2.373 \times 10^6\ \mathrm{Jm^{-3}K^{-1}} \\ &c_s \text{ is the heat capacity of sand} = 2.133 \times 10^6\ \mathrm{Jm^{-3}K^{-1}} \\ &c_{st} \text{ is the heat capacity of silt} = 2.133 \times 10^6\ \mathrm{Jm^{-3}K^{-1}} \end{aligned} \tag{5.6}$$

[4] `http://www.hpsc.csiro.au/users/dix043/cap_doc/AncilDoc_CAP.html`

The van Genuchten equation, used to derive $\theta_{crit}$ and $\theta_{wilt}$ is:

$$\theta = \theta_r + \frac{\theta_s - \theta_r}{(1 + (\alpha h)^n)^{1-1/n}} \tag{5.7}$$

where $\theta_s$ is the soil moisture content at saturation, $\theta_r$ is the residual soil moisture content, $\alpha$ (related to the inverse of air entry matric potential) and $n$ (measure of the pore-size distribution) are van Genuchten parameters, and $h$ is the soil water suction (m) calculated as:

$$h = \frac{\psi}{\rho_w g} \tag{5.8}$$

where $\psi$ is the soil matric potential, $\rho_w$ is the density of water and $g$ is the gravitational acceleration.

Soil moisture content at field capacity, $\theta_{crit}$, and soil moisture content at wilting point, $\theta_{wilt}$, are calculated from Eq.5.7 by using soil matric potential[5] values $\psi = -0.033$ MPa and $\psi = -1.5$ MPa, respectively. The other hydrological parameters are set according to values read in from the look-up Table 5.5, as previously mentioned.

The soil hydraulic conductivity ($K$) is calculated as:

$$K = K_s S_e^L [1 - (1 - S_e^{(}(1/m))^m)]^2 \tag{5.9}$$

where $K_s$ is the saturated hydraulic conductivity, $S_e = (\theta - \theta_r)/(\theta_s - \theta_r)$, $m = 1 - 1/n$ and $L = 0.5$ (Dharssi *et al.*, 2009).

### 5.3.3 Runoff routing

JULES generates surface and subsurface runoff for each grid cell, which has to be translated into streamflow in order to assess the model's performance against observational data. The runoff routing method applied here is a transfer function which assumes that runoff from each grid reaches the catchment's outlet point after a time delay $t_i$ calculated as:

$$t_i = \frac{x_i}{c} \tag{5.10}$$

[5] soil suction is the negative of soil matric potential

where $x_i$ is the distance of the $i$ grid point to the outlet and $c$ the flood wave velocity, which is assumed to be constant.

Following that, the streamflow at the outlet point is calculated as the sum of all contributing local hydrographs in the basin, lagged in time (Zulkafli *et al.*, 2013):

$$Q_t = \sum_{i=1}^{n} Q_{i_1(t-t_{i_1})} + Q_{i_2(t-t_{i_2})} \tag{5.11}$$

where the subscripts 1 and 2 correspond to surface and subsurface runoff respectively.

The surface and subsurface runoff velocities were optimized through a Monte-Carlo simulation. The optimal values were found to be $c_1 = 1.1$ m/s for surface runoff and $c_2 = 0.6$ m/s for subsurface runoff. A map indicating the $x$ distances to the outlet point was generated based on the DEM and flow direction vectors.

### 5.3.4 Precipitation data uncertainty

The different precipitation products explored comprise of interpolated ground observations from gauge networks, GCM reanalysis data and satellite remote–sensing estimates and are summarised in Table 5.1.

During the course of this research, the TRMMv7 product was released, after retrospective reprocessing of the TRMMv6 product. TRMMv7 is assumed to be more accurate over land compared to TRMMv6 as it uses the newer version of rain gauge data provided by the Global Precipitation Climatology Centre (GPCC Prakash *et al.*, 2013). However, over mountainous regions such as the Himalayas, the TRMMv7 product was found to overestimate precipitation compared to its predecessor and to generally provide increased (by 5-9%) precipitation over high precipitation regimes, mainly over the ocean and mountainous regions (Prakash *et al.*, 2013).

### 5.3.5 Sensitivity to parameter perturbation

#### 5.3.5.1 Convective rainfall fraction

The total precipitation in JULES is the summary of convective and large scale precipitation. Convective precipitation is characterised by higher intensity and shorter duration than the large scale precipitation.

Most tropical rainfall is convective and takes place on spatial scales much smaller than the large scale precipitation. To account for the size of convective storms compared to gridsize, the parameter $\epsilon_r$ in the model defines the fraction of the gridbox that receives rainfall when convective precipitation occurs. In the default parameterisation $\epsilon_r$ is set to 0.3, for convective precipitation. However, for large–scale precipitation or condensation and point studies this fraction is set to 1 (Best *et al.*, 2011), meaning that the entire gridbox receives rainfall. In addition, the parameter tForConv is the near-surface air temperature at or above which the precipitation is assumed to be convective in origin. At lower temperatures than tForConv, all the precipitation is assumed to be large scale in origin. In the default parameterisation tForConv is set to be 300 K. The near-surface air temperature at or below which the precipitation is assumed to be snowfall must be less than tForConv, implying that all solid precipitation is large-scale in origin (Clark *et al.*, 2010). Here, the model's sensitivity to the convective rainfall fraction is tested, by flipping between convective and large scale rainfall, which affects the rainfall intensity.

#### 5.3.5.2 Vegetation canopy interception

The canopy capacity, $C_m$ $(kg \times m^{-2})$, is the amount of water that can be held on the canopy by the interception of precipitation and in JULES it is calculated by the following Equation:

$$C_m = A_m + B_m \times LAI \tag{5.12}$$

where $B_m$ is the rate of change of canopy capacity with LAI and $A_m$ is the minimum canopy capacity describing the puddling of water on the soil surface and its interception by leafless plants. The default parameter values used by JULES are $A_m = 0.5$ and $B_m = 0.05$. This suggests that there is not much variance between the interception of a leafless plant and a plant full of leaves because interception is not that much dependent on the LAI.

However, canopy capacity is very important as it is used to calculate the saturated fraction of the vegetated tile, $f_a$, at which the evaporation of intercepted water takes place. Evaporation from saturated surfaces occurs at the potential rate and is only subject to an aerodynamic resistance. In JULES, $f_a$ is

calculated as:

$$f_a = \frac{C}{C_m} \tag{5.13}$$

where $C$ $(kg \times m^{-2})$ is the canopy moisture content and $C_m$ the canopy capacity as already defined.

A literature review by Breuer *et al.* (2003), suggests that for global temperate ecosystems, the mean interception corresponding to $C_m$ for crops is 2.6 mm, for grasses 1.9 mm, for coniferous forests 1.9 mm, for deciduous forests 1.0 mm, and for shrubs 1.1 mm. The mean LAI values suggested by this review are 3.8, 6.2, 6.3, 5.4, and 3.7 respectively. As also mentioned in the study by Van den Hoof *et al.* (2013), in other LSMs such as SiB2 (Sellers *et al.*, 1996) and BATS (Dickinson *et al.*, 1993) the canopy moisture content is described as: $C_m = 0.1 \times LAI$. Based on this information, the existing formula was replaced with the following one that is more in line with the one suggested by Van den Hoof *et al.* (2013) and is expected to increase interception dependence by LAI:

$$C_m = 0.05 + 0.25 \times LAI \tag{5.14}$$

#### 5.3.5.3 Infiltration enhancement factor

Surface runoff (Y) in JULES is calculated as:

$$Y = \begin{cases} R\frac{C}{C_m}exp(-\frac{\epsilon_r K C_m}{RC}) + R(1 - \frac{C}{C_m})exp(-\frac{\epsilon_r C_m}{R\Delta t}), & \text{if } K\Delta t \leq C \\ Rexp(-\frac{\epsilon_r (K\Delta t + C_m - C)}{R\Delta t}), & \text{if } K\Delta t > C \end{cases} \tag{5.15}$$

where $R$ is the rainfall rate that covers $\epsilon_r$ fraction of a grid, $C$ is the canopy moisture content, $C_m$ the canopy capacity and $K$ is the surface infiltration rate, equal to $b_s \times K_s$; Where $K_s$ is the soil saturated hydrological conductivity and $b_s$ an enhancement factor (Best *et al.*, 2011). The default value of $b_s$ in JULES varies dependent on the vegetation type. For trees $b_s$ is 4 and for $C_3$ grass, $C_4$ grass and shrubs it is 2. However, and as also suggested by Van den Hoof *et al.* (2013), no justification can be found for different $b_s$ values between different PFTs, therefore, here I experimented by setting the value of $b_s$ equal to 1 for all PFTs.

### 5.3.6 Sensitivity to structural perturbation

As mentioned earlier, JULES in its default version does not account for sub-grid soil heterogeneities. However, the model offers two alternative runoff generation schemes, the PDM and the TOPMODEL parameterization schemes, that introduce heterogeneity in the soil moisture store depths. TOPMODEL represents heterogeneity throughout the soil column, whereas PDM considers heterogeneity only in the top soil layer (Best *et al.*, 2011).

#### 5.3.6.1 TOPMODEL runoff generation scheme

In JULES-TOPMODEL, a no-flux condition replaces the free drainage lower boundary condition, and sub-surface runoff is represented as a lateral "baseflow", generated from any soil layer below or containing the top of the water table (Best *et al.*, 2011). The spatial variability of soil moisture is parameterized in terms of the spatial distribution of the topographic index $\lambda$, which determines in what fraction of the gridbox the water table is above the surface. An extra soil layer is included below the standard 3m soil column to represent the deep aquifer if the standard total depth is exceeded (Best *et al.*, 2011).

The topographic index $\lambda$, calculated from a Digital Elevation Model (DEM), is relating the area draining through a point from upslope and the point's hillslope inclination:

$$\lambda = ln(a/tan(\beta)), \tag{5.16}$$

where $a$ is the area draining to this location per unit contour length and $tan(\beta)$ is the slope of the land surface. Maps of the mean topographic index and its standard deviation were generated based on the DEM of the study area. The maps were used to force JULES when the TOPMODEL configuration was selected.

In JULES-TOPMODEL, the saturated hydraulic conductivity, $K_s$, is assumed to decrease with depth $(z)$ below the surface:

$$K_s(z) = K_s(0)e^{(-fz)} \tag{5.17}$$

where $K_s(0)$ the saturated conductivity at the soil surface and $f$ a decay parameter. A spatial map of

the decay parameter $f$ was generated and used in JULES-TOPMODEL, based on the following formula suggested by Fan and Miguez-Macho (2011):

$$\begin{aligned} f &= (1 + 150\overline{s})/100 \\ f &= 0.4, \qquad\qquad \text{when} \quad f > 0.4 \end{aligned} \tag{5.18}$$

where $\overline{s}$ is the grid-averaged slope.

#### 5.3.6.2 PDM runoff generation scheme

JULES PDM calculates saturation excess runoff based on the Probability Distributed Model (PDM, Moore, 1985). The model assumes that in each gridbox multiple storages of different capacities exist. The distribution of the soil storage capacity in each gridbox is modelled by a pdf (Clark and Gedney, 2008), allowing for sub-grid variation of storage capacity. A saturated soil store contributes to the fraction of the gridbox that generates surface runoff. The saturated fraction of the gridbox, $f_{sat}$, is calculated as:

$$f_{sat} = 1 - (1 - \frac{\theta}{\theta_{max}})^{\frac{B}{(B+1)}} \tag{5.19}$$

where $\theta$ is the gridbox soil water content, $\theta_{max}$ is the storage at saturation and $B$ is a shape parameter describing the proportion of shallower to deeper stores (Best *et al.*, 2011). The default value of $B$ is 1, which means that there is equal proportion of high to low capacity soil water stores within a gridbox. B values higher than 1 imply higher probability of more low capacity water stores within a gridbox. B values lower than 1 imply higher probability of more high capacity water stores within a gridbox (Moore, 2007).

### 5.3.7 Sensitivity to temporal resolution of input data

A comparison between simulated fluxes under daily and 3-hourly meteorological forcing is informative on the model's sensitivity to sub-daily forcing. JULES initially run at an hourly time-step with daily weather data (TRMMv7 precipitation data and NCEP data for the rest meteorological variables). In an alternative simulation type, JULES run at an hourly time-step but this time the original 3-hourly weather

data were used. It is expected that the 3-hourly data will be able to better capture the diurnal variation of all meteorological fluxes. The diurnal cycle of variables such as temperature, radiation and convective precipitation is very important for the description of land surface physical processes such as the energy and water balance.

### 5.3.8 Uncertainty analysis

Combinations of the above described model input data, parameter sets and structures were tested. An ensemble of model simulations, based on different combinations of (1) precipitation forcing, (2) convective rainfall fraction, (3) vegetation canopy interception, (4) infiltration enhancement factor, (5) runoff generation mechanism, and (6) temporal resolution of input data, was generated. With the aim to construct a model that is robust in its predictions, the impact of uncertainties in input data, along with uncertainties arising from the different parameter combinations is discussed, while the model's potential to bracket the observations is presented.

### 5.3.9 Model validation

Available daily streamflow observations for the Bhimgoda outlet point (period 1999–2008) were used to assess the model's performance. The goodness of fit is based on the following performance scores: Mean Error (ME), Root Mean Square Error (RMSE), Percent Bias (PBIAS), Nash-Sutcliffe Efficiency (NSE), Pearson's correlation coefficient (r).

$$ME = \frac{1}{N}\sum_{i=1}^{N}(S_i - O_i) \tag{5.20}$$

$$RMSE = \sqrt{\frac{1}{N}\sum_{i=1}^{N}(S_i - O_i)^2} \tag{5.21}$$

$$PBIAS = 100 \times \frac{\sum_{i=1}^{N}(S_i - O_i)}{\sum_{i=1}^{N} O_i} \tag{5.22}$$

$$NSE = 1 - \frac{\sum_{i=1}^{N}(S_i - O_i)^2}{\sum_{i=1}^{N}(O_i - \overline{O})^2} \tag{5.23}$$

$$r = \frac{N \times \sum_{i=1}^{N}(S_i \times O_i) - \sum_{i=1}^{N} S_i \sum_{i=1}^{N} O_i}{\sqrt{[N \times \sum_{i=1}^{N}(S_i)^2 - (\sum_{i=1}^{N} S_i)^2][N \times \sum_{i=1}^{N}(O_i)^2 - (\sum_{i=1}^{N} O_i)^2]}} \tag{5.24}$$

In addition, the modelled ET fluxes were validated against the MODIS and LandFlux equivalent products, whilst the modelled top layer soil moisture fluxes were validated against the ESV-SM product.

## 5.4 Results

### 5.4.1 Precipitation data uncertainty

Before performing any kind of hydrological analysis, and because precipitation is one of the most important inputs to an LSM, it was essential to compare different gridded precipitation datasets available for the study area and make sure that there is an agreement in their estimations.

The analysis of different precipitation products reveals surprisingly large variations between them. The comparison between gridded and gauge data highlights large uncertainties in both types of products. As it was not possible to judge the quality of the gridded products, due to the small number of gauge measurements acquired, all 5 gridded datasets were used to force JULES initially, and based on the model's performance scores the most suitable one for the study area was selected.

A comparison between 5 different precipitation datasets (Figs. 5.3 and 5.4) reveals large variations in the mean annual precipitation and the monthly precipitation climatologies, over the period 1998–2004. When compared against the 5 IMD rainfall gauge observation datasets, as shown in Figs.5.6 & 5.5, the gridded products were found to underestimate the high extremes of rainfall in most cases but also to underestimate the number of dry days. This negative bias is the case especially in Haridwar, Moradabad

and Chamoli that are located in the northern parts of the catchment and to a lesser extent in Kanpur Nagar that is located in the most southern part. Although one could argue that the quality of the 5 gauge stations is questionable, further analysis of the water balance and the daily streamflow time-series confirms that the total amount of water that precipitates in the study area is underestimated by all gridded products.

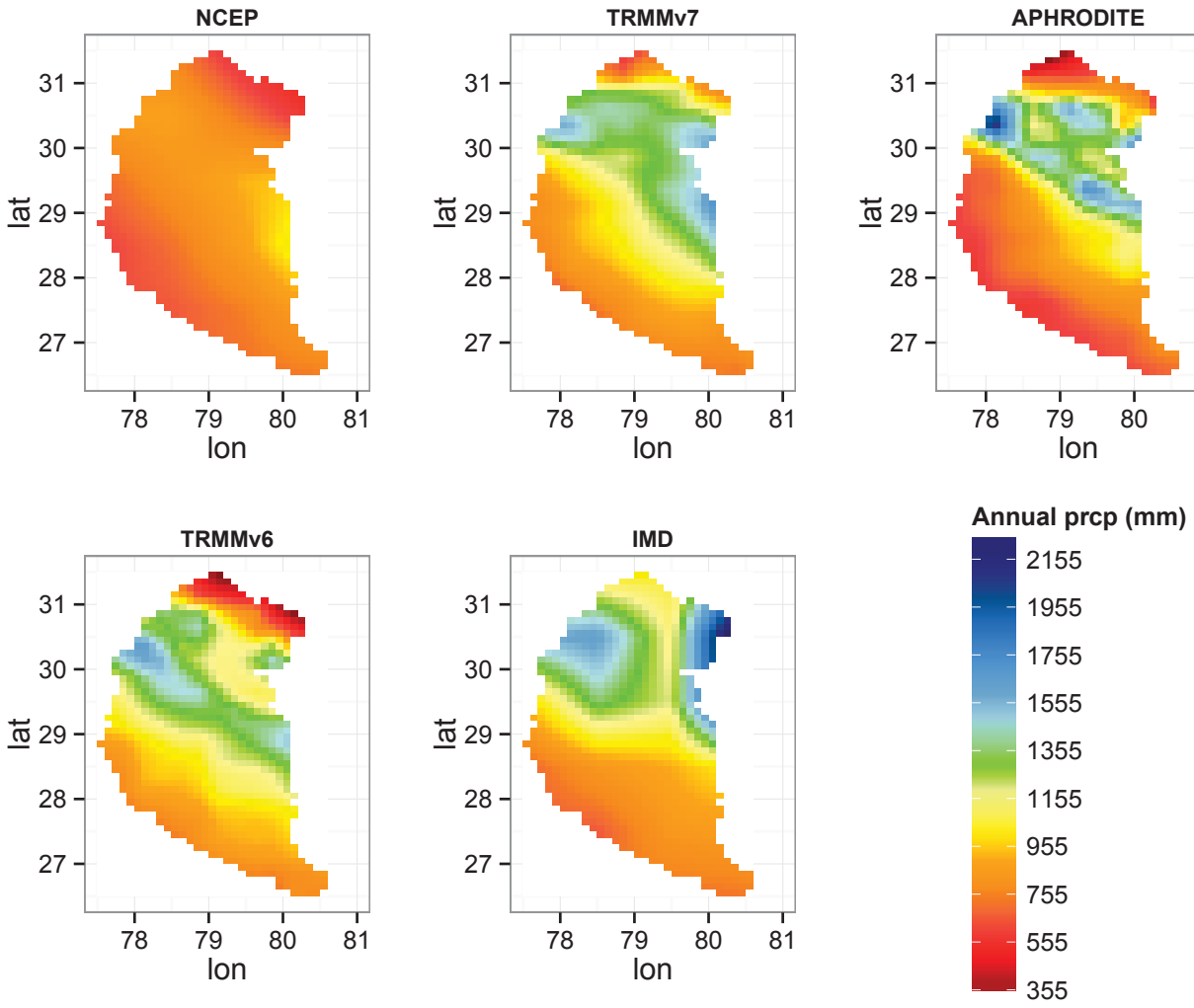


**Figure 5.3:** Spatial variability of the mean annual precipitation between NCEP, APHRODITE, IMD, TRMMv6 and TRMMv7 datasets, over the period 1998-2004.

As shown in Fig. 5.10 the simulated streamflow by JULES is underestimated in the rising limb of the hydrograph and in some cases the peak of the flow, when compared to the observed values available for the Bhimgoda sub-catchment. Another indication of the data uncertainties arises from the calculated

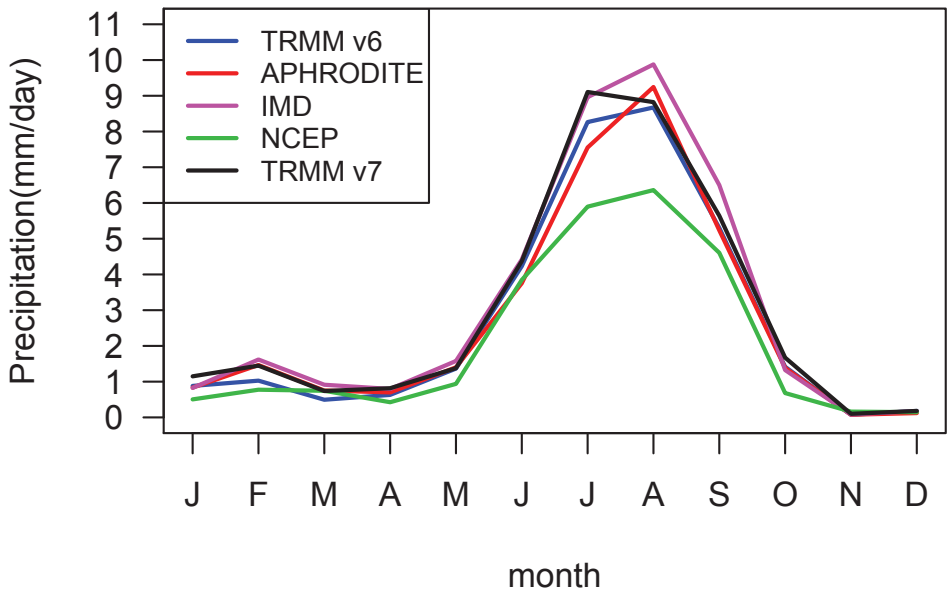


**Figure 5.4:** Monthly precipitation climatologies of the 5 gridded datasets examined, over the period 1998-2004.

runoff ratios as shown in Table 5.8 and Fig. 5.9, which often exceed the value of 0.80, and reach values up to 2.11 (NCEP dataset, year 2004). According to literature, typical mean annual values of runoff coefficients for tropical catchments are in the range of 0.5–0.7 (Manoharan and Murugappan, 2012; Biggs *et al.*, 2007; Campling *et al.*, 2002; Buytaert *et al.*, 2006) and IMD seems to be the dataset better reproducing these values. However, this indicates that apart from the previously discussed uncertainties in the precipitation data, uncertainties might also exist in the daily streamflow measurements.

The spatial comparison between mean annual precipitation of TRMMv6 and TRMMv7, as illustrated in Fig. 5.3, reveals increased precipitation patterns for TRMMv7 in the central and northern mountainous parts of the catchment but at the same time a slight decrease in the precipitation of the most southern areas. Temporally, the monthly climatology of the period 1998–2004 (Fig. 5.4) shows increased precipitation in TRMMv7 compared to TRMMv6 for all months and especially in July. On the other hand, the large differences between IMD and APHRODITE shown in Fig. 5.3 are rather surprising as both products are

based on interpolated rain gauges.

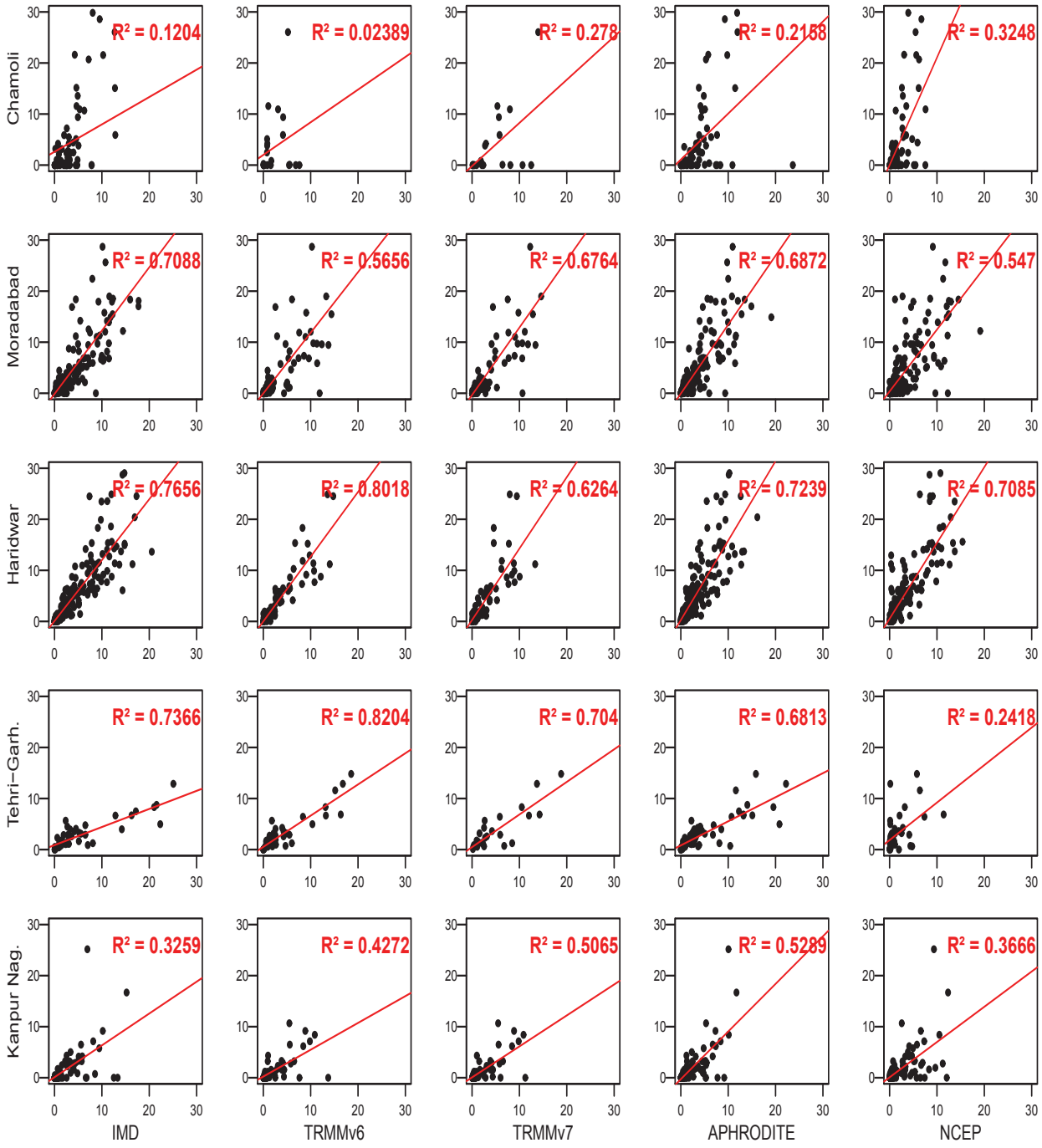


**Figure 5.5:** Scatter-plots comparing the observed monthly averaged gauge precipitation with the equivalent point values of the 5 gridded datasets examined (values in mm/d).

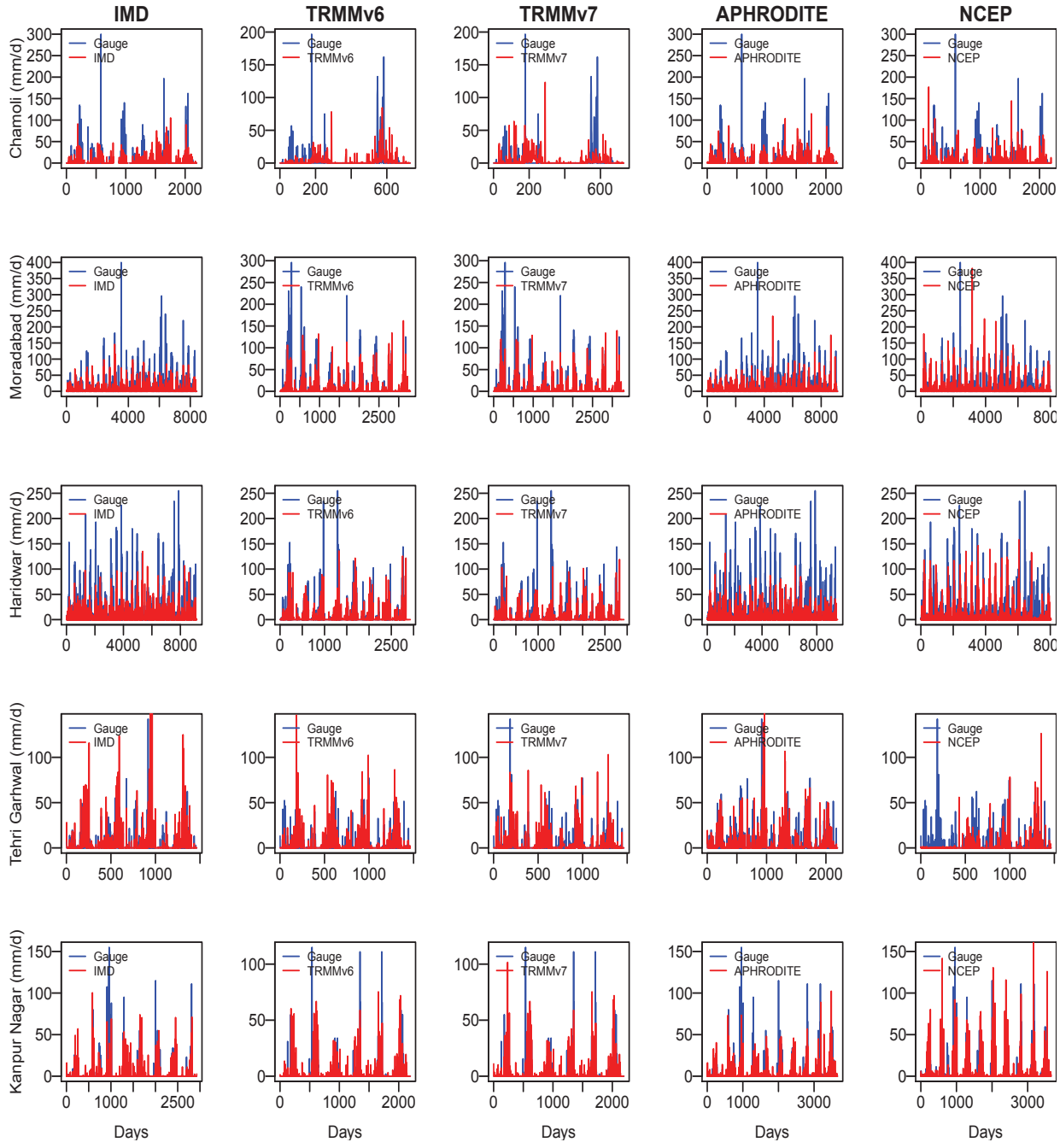


**Figure 5.6:** Precipitation time-series comparing the observed gauge precipitation with the equivalent point values of the 5 gridded datasets examined.

## 5.4.2 Sensitivity analysis

### 5.4.2.1 Streamflow sensitivity to precipitation forcing

After forcing JULES with each one of the 5 gridded datasets, it is evident that the model is very sensitive to precipitation forcing. Performance scores indicate that TRMMv7 and IMD are the best available products to use in the UG basin. The derived NSE values (Fig. 5.7 and Table 5.6) suggest that the best streamflow simulation results are generated when JULES is forced with the TRMMv7 product (a perfect fit gives a value of NSE=1). Looking at other performance indices (Fig. 5.8 and Table 5.7), IMD produces slightly better results than TRMMv7, in terms of ME, PBIAS (%) and r coefficient, in daily, monthly and annual scale. The worst results are generated by the NCEP reanalysis product, which was not constrained by observations during its generation, although afterwards it was post-processed and bias corrected by observations. In addition, the large spatial resolution of this product ($1^\circ \times 1^\circ$) makes it unsuitable for regional scale studies of lower resolution as it cannot capture well the spatial variations of convective precipitation above the mountainous regions of the study area (Fig. 5.3).

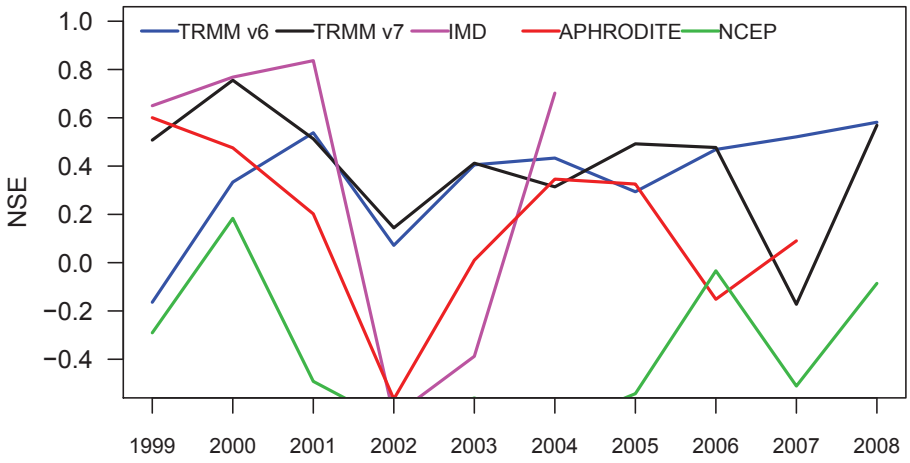


**Figure 5.7:** NSE values of the model run at a daily time-step, calculated per year of simulation, under different precipitation forcing.

**Table 5.6:** NSE values over the total modelling period (1999–2008), derived after forcing JULES with different precipitation datasets.

| Precipitation | NSE |
|---|---|
| TRMM v6 | 0.35 |
| TRMM v7 | 0.44 |
| NCEP | −0.35 |
| IMD | 0.35 |
| APHRODITE | 0.21 |

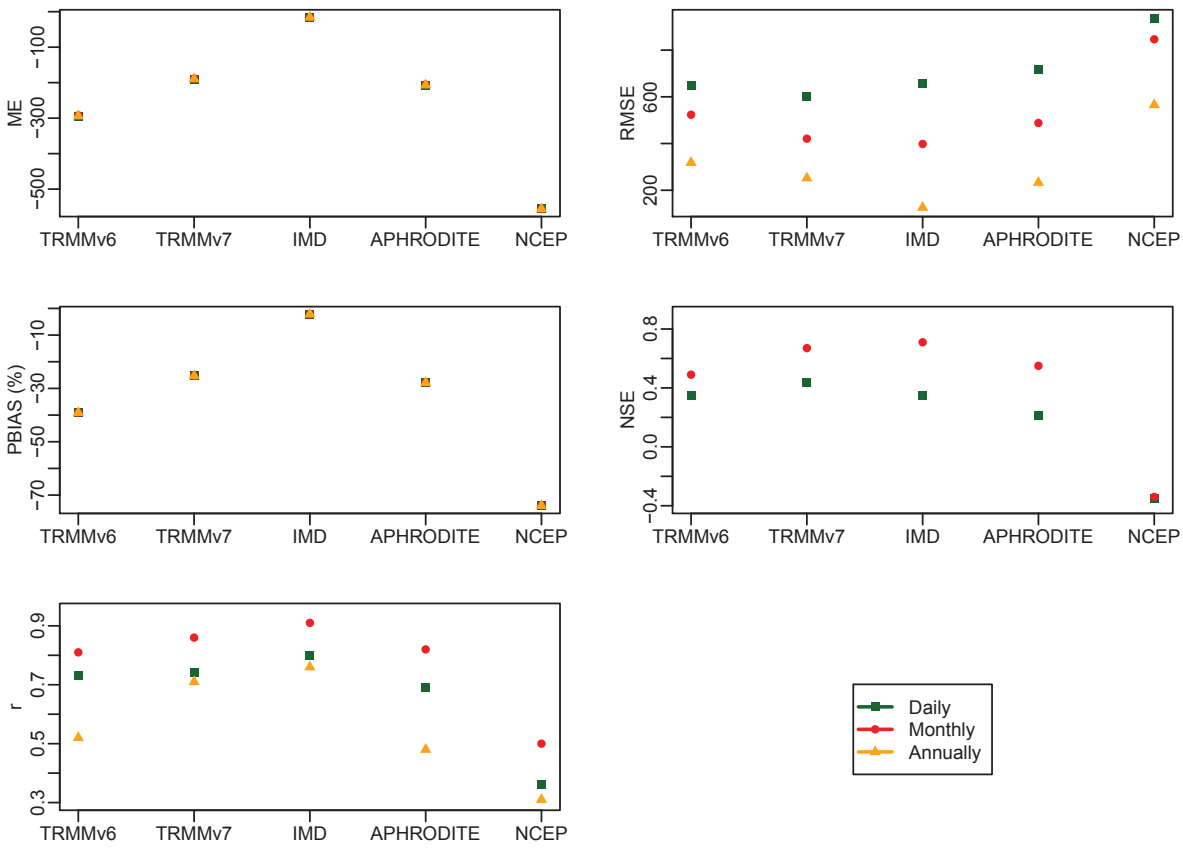


**Figure 5.8:** Performance scores of the model's ability to simulate streamflow in the Bhimgoda catchment

**Table 5.7:** Seasonal Performance scores assessing JULES streamflow-based performance

| Function | TRMMv6 | | | TRMMv7 | | | IMD | | | APHRODITE | | | NCEP | | |
|---|---|---|---|---|---|---|---|---|---|---|---|---|---|---|---|
| | Daily | Month. | Ann. | Daily | Month. | Ann. | Daily | Month. | Ann. | Daily | Month. | Ann. | Daily | Month. | Ann. |
| $ME$ | -294.1 | -291.9 | -294 | -189.9 | -188.1 | 189.8 | -16.2 | -16.1 | -16.2 | -207 | -205.2 | -207 | -555.8 | -551.7 | -555.8 |
| $RMSE$ | 647.5 | 523.3 | 318.1 | 601.7 | 420.6 | 215.9 | 655.6 | 398.1 | 126 | 715.8 | 488.1 | 232.9 | 935.1 | 846.3 | 565.4 |
| $PBIAS$ | -39.1 | -39.1 | -39.1 | -25.3 | -25.2 | -25.3 | -2.2 | -2.2 | -2.2 | -27.9 | -27.8 | -27.9 | -74 | -73.9 | -74 |
| $NSE$ | 0.35 | 0.49 | -12.95 | 0.44 | 0.67 | -5.42 | 0.35 | 0.71 | -1.54 | 0.21 | 0.55 | -6.32 | -0.35 | -0.34 | -43.06 |
| $r$ | 0.73 | 0.81 | 0.52 | 0.74 | 0.86 | 0.71 | 0.80 | 0.91 | 0.76 | 0.69 | 0.82 | 0.48 | 0.36 | 0.5 | 0.31 |

However, depending on the time-scale and performance measure of interest, different results arise regarding the model's capability to adequately simulate streamflow under different precipitation forcing.

When using the TRMMv7 precipitation product, the model is able to capture well the timing of the peaks and simulates well the recession limbs of the observed flows (Fig. 5.11). The simulation of rising limbs of the hydrograph is more problematic as often the increase in discharge is delayed compared to observations. Interestingly, to some extent, the results generated from forcing JULES with all different precipitation datasets seem to have similar behaviour, which indicates a model deficiency possibly related to the infiltration excess surface runoff generation mechanism. Clark and Gedney (2008) point out that delayed and lower flow peaks are the outcome of a runoff largely generated by drainage through the bottom of the soil column (i.e. subsurface runoff), as infiltration excess surface runoff occurs less frequently in large grid-scales. Besides, Dingman (2002) suggests that infiltration excess mostly occurs in arid and semi-arid regions where high intensity rainfall is combined with low surface conductivity, or in regions where human activity or frost has made the soil near-impermeable. The peak discharge is often underestimated and in a smoothed hydrograph, of monthly or annual time scales, a clear low bias in the simulated streamflows is observed. This is especially noticeable in Fig. 5.13 that shows seasonally divided flows, where a strong underestimation of flows is observed during the wet summer season. Uncertainties in precipitation forcing datasets and to a lesser extent the runoff routing function might also be responsible for this mismatch. However, the simulations forced with IMD precipitation (Fig. 5.12) show problems in the rising limbs are almost minimised and especially in the monthly time scale, the achieved NSE is the highest of all. This indicates that precipitation is one of the most important factors that introduce uncertainties in the modelling. Unfortunately the time period of available gridded IMD precipitation data overlapping with observed flow data is short (1999–2004), therefore TRMMv7 was chosen as the forcing precipitation product from now on in this study.

#### 5.4.2.2 Sensitivity to parameter perturbation

Results in this section are often presented as Kernel density plots, which is an effective way to visualise the distribution of a variable. Kernel density estimation is a non-parametric method to estimate the probability density function (PDF) of a continuous variable. The PDF values are non-negative and its integral equals to 1.

**Table 5.8:** Annual runoff ratio values for the Bhimgoda catchment under different precipitation datasets

| Year | TRMMv7 | TRMMv6 | IMD | APHRODITE | NCEP |
|---|---|---|---|---|---|
| 1999 | 0.86 | 1.33 | 0.85 | 0.99 | 1.39 |
| 2000 | 0.81 | 1.09 | 0.76 | 0.93 | 1.16 |
| 2001 | 0.86 | 0.93 | 0.75 | 1.11 | 1.72 |
| 2002 | 0.80 | 0.92 | 0.64 | 0.74 | 1.08 |
| 2003 | 0.94 | 1.10 | 0.69 | 0.89 | 1.51 |
| 2004 | 0.84 | 0.85 | 0.78 | 0.76 | 2.11 |
| 2005 | 0.89 | 0.84 | | 1.05 | 1.93 |
| 2006 | 0.76 | 0.84 | | 0.75 | 1.02 |
| 2007 | 0.71 | 0.87 | | 0.92 | 1.39 |
| 2008 | 0.98 | 0.87 | | | 1.40 |

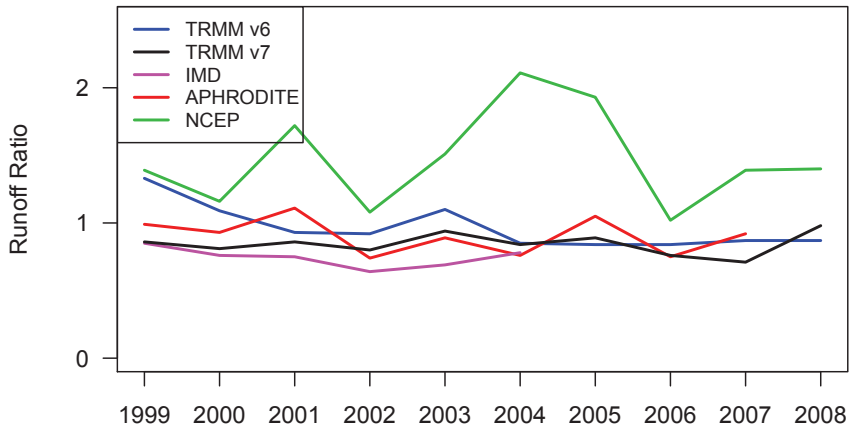


**Figure 5.9:** Annual runoff ratio values for the Bhimgoda catchment under different precipitation datasets

**Table 5.9:** Seasonal Performance scores assessing JULES streamflow-based performance

| Performance scores | DJF | MAM | JJA | SON |
|---|---|---|---|---|
| $ME$ | -19.75 | -72.23 | -750.53 | 10.04 |
| $RMSE$ | 123.01 | 138.06 | 807.24 | 129.07 |
| $PBIAS$ | -8.3 | -22.2 | -44.7 | 1.3 |
| $NSE$ | -2.46 | -4.58 | -10.93 | 0.23 |
| $R^2$ | 0.29 | 0.56 | 0.32 | 0.83 |

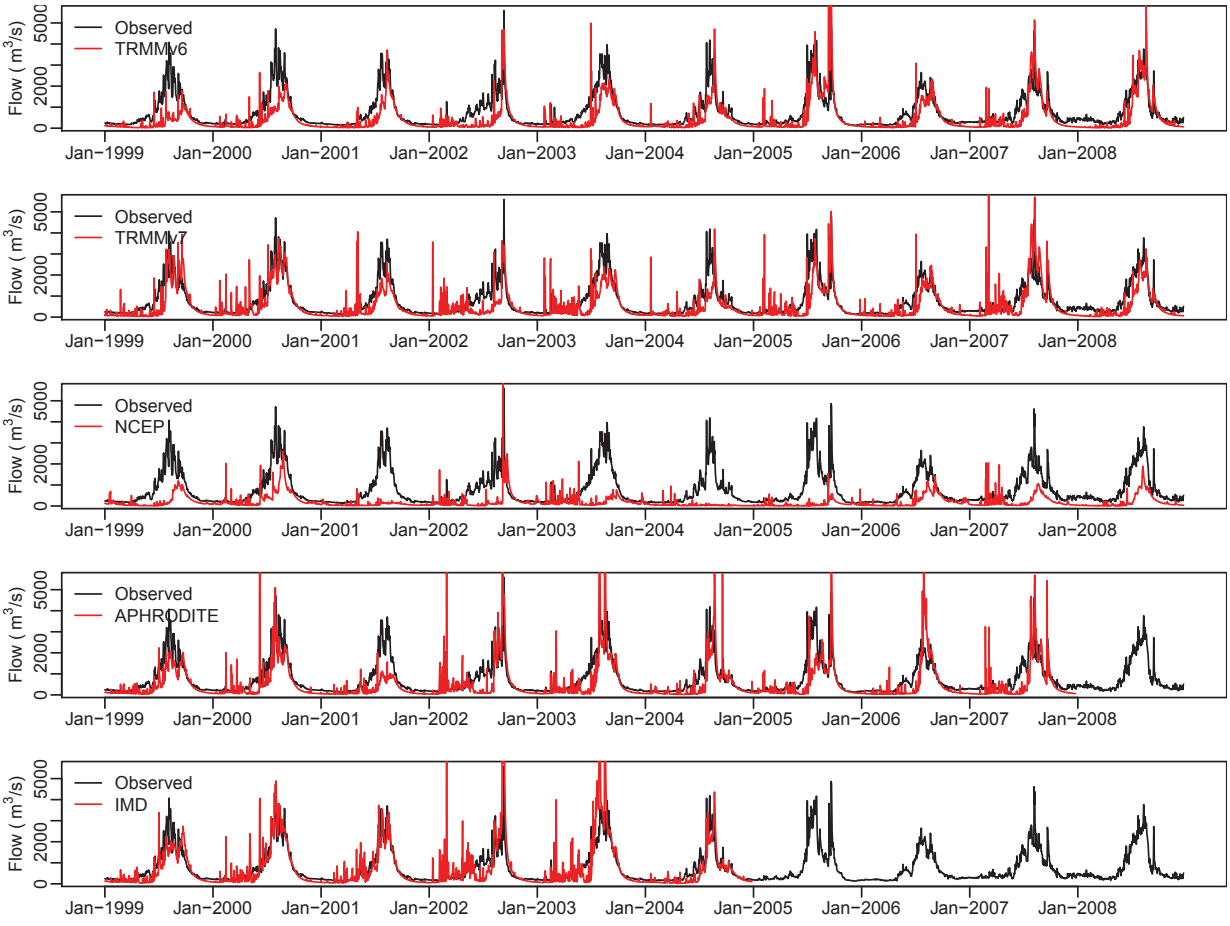


**Figure 5.10:** Streamflow plots comparing observations (black) versus model results (red) under different precipitation forcing

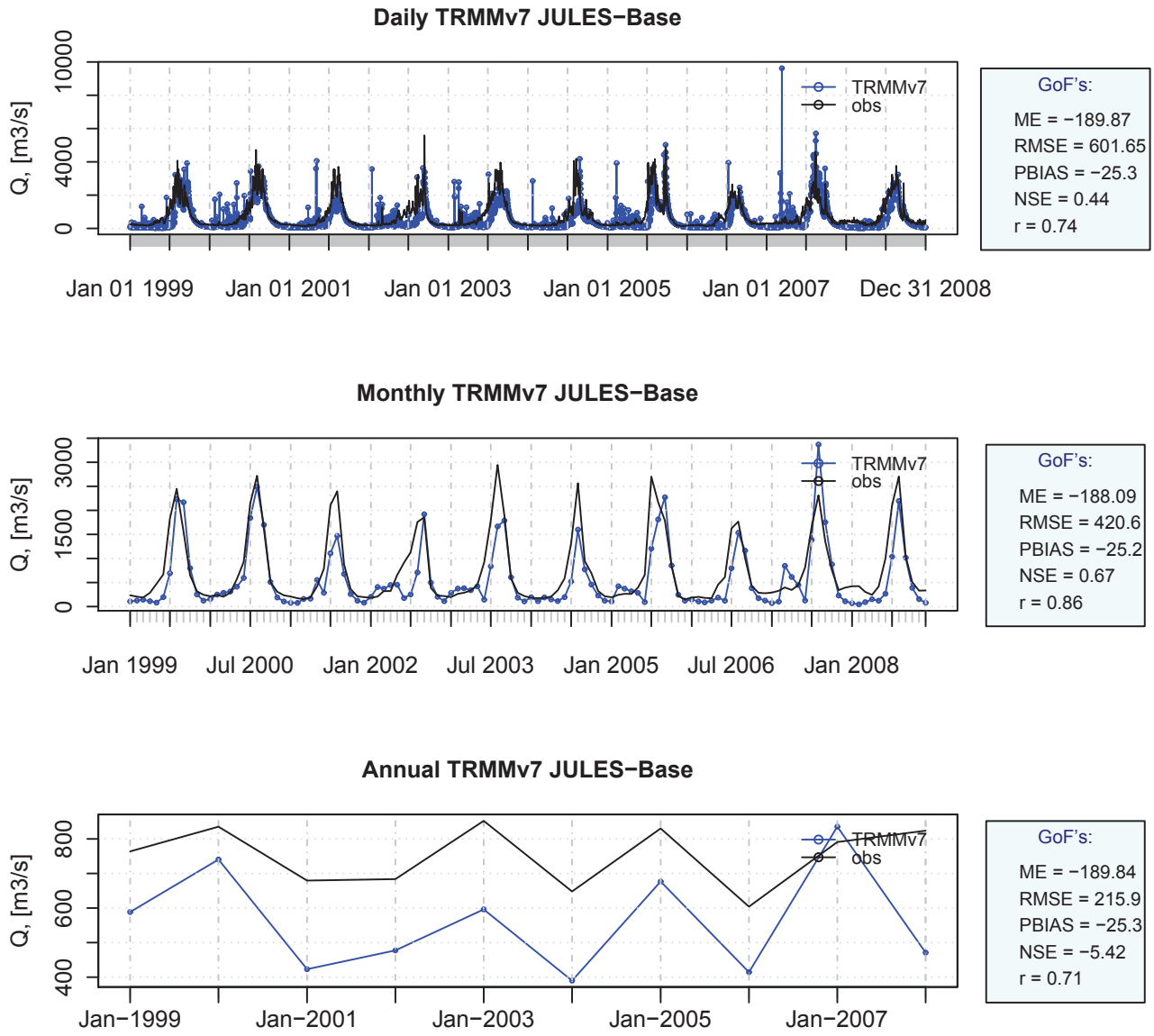


**Figure 5.11:** Daily, monthly and annual streamflow plots, comparing observations to model outputs of JULES with its default parameterisation scheme, under TRMMv7 precipitation forcing. On the right hand side of each plot, various performance scores are indicative of the model's goodness of fit.

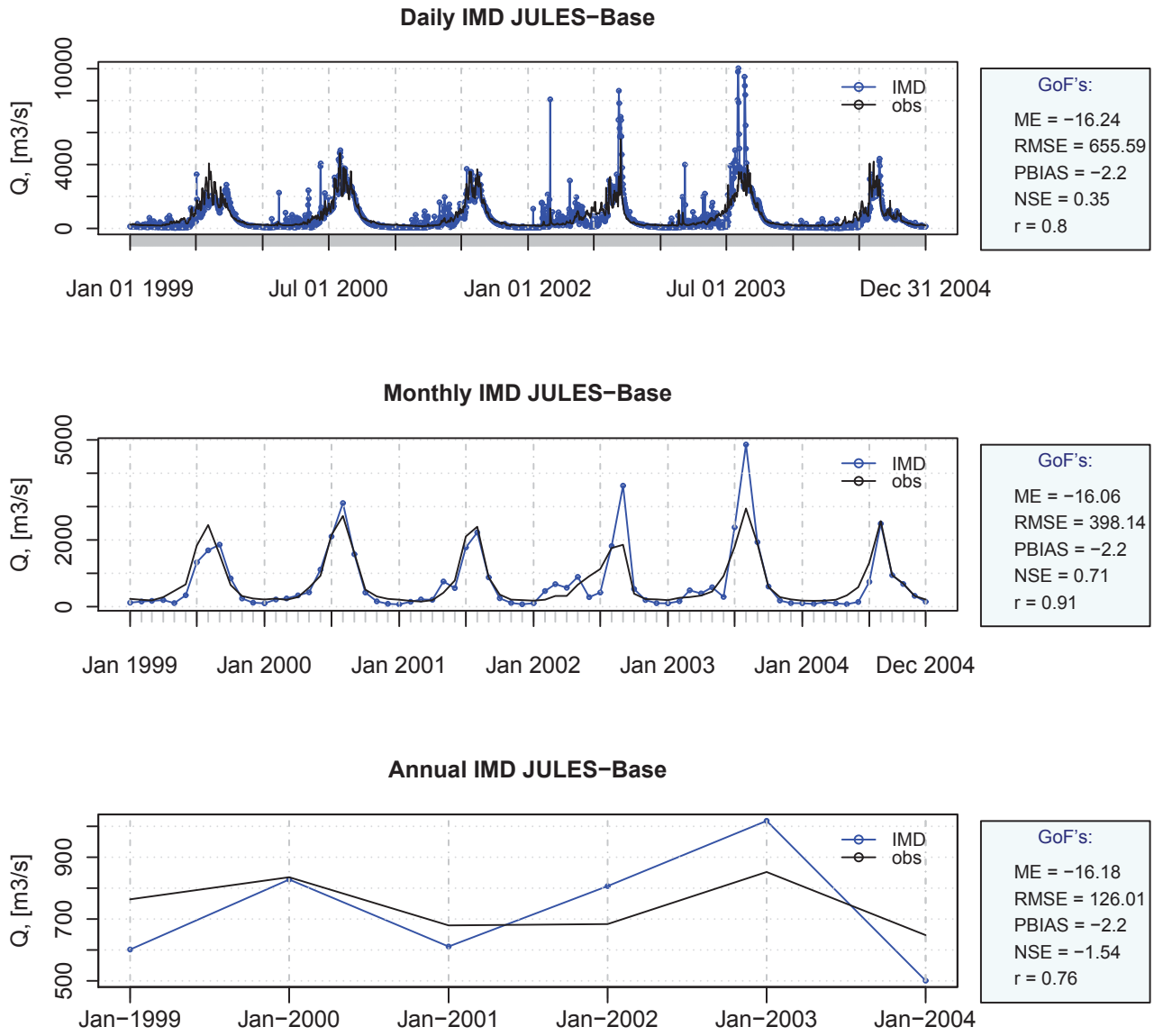


**Figure 5.12:** Daily, monthly and annual streamflow plots, comparing observations to model outputs of JULES with its default parameterisation scheme, under IMD precipitation forcing. On the right hand side of each plot, various performance scores are indicative of the model's goodness of fit.

**Table 5.10:** Seasonal Performance scores assessing JULES-PDM streamflow-based performance

| Function | $B = 0.1$ | | | $B = 0.3$ | | | $B = 0.5$ | | | $B = 0.7$ | | | $B = 1$ | | | $B = 3$ | | |
|---|---|---|---|---|---|---|---|---|---|---|---|---|---|---|---|---|---|---|
| | Daily | Month. | Ann. | Daily | Month. | Ann. | Daily | Month. | Ann. | Daily | Month. | Ann. | Daily | Month. | Ann. | Daily | Month. | Ann |
| $ME$ | -208 | -206 | -208 | -178 | -176 | -178 | -178 | 176 | -178 | -154 | -153 | -154 | -154 | -153 | -154 | -156 | -155 | -156 |
| $RMSE$ | 671 | 429 | 232 | 904 | 383 | 202 | 937 | 380 | 203 | 1079 | 365 | 181 | 1079 | 365 | 181 | 1044 | 369 | 182 |
| $PBIAS$ | -27.7 | -27.6 | -27.7 | -23.7 | -23.5 | -23.6 | -23.7 | -23.6 | -27.3 | -20.5 | -20.5 | -20.5 | -20.5 | -20.5 | -20.5 | -20.8 | -20.7 | -20.8 |
| $NSE$ | 0.3 | 0.66 | -6.4 | -0.26 | 0.72 | -4.63 | -0.35 | 0.73 | -4.68 | -0.8 | 0.75 | -3.49 | -0.8 | -0.75 | -3.49 | -0.68 | 0.74 | -3.57 |
| $r$ | 0.67 | 0.86 | 0.71 | 0.51 | 0.89 | 0.68 | 0.49 | 0.89 | 0.69 | 0.45 | 0.89 | 0.67 | 0.45 | 0.89 | 0.67 | 0.46 | 0.89 | 0.68 |

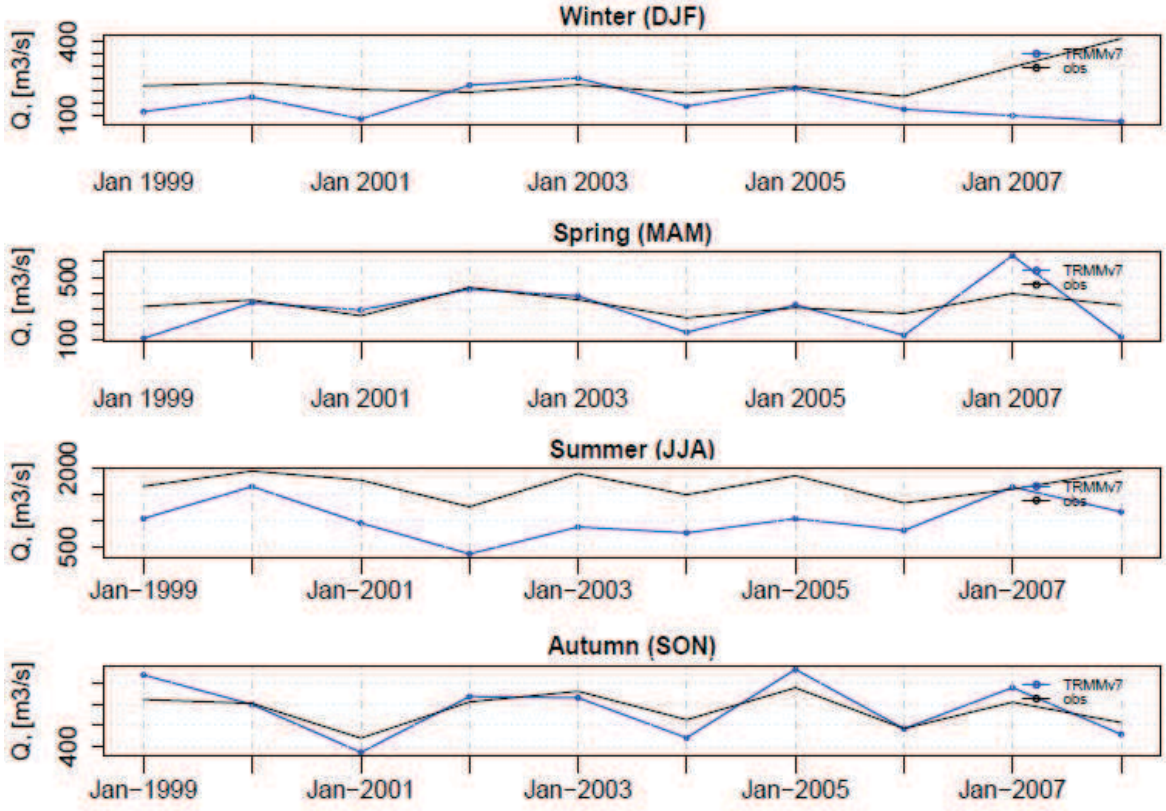


**Figure 5.13:** Seasonally separated streamflow plots comparing observations (black) to model outputs of JULES (blue) with its default parameterisation scheme, under TRMMv7 precipitation forcing.

### Convective rainfall fraction

The impact of different $\epsilon_r$ values ranging from 0.1 to 1 is examined. The highest value of $\epsilon_r = 1$ corresponds to large scale precipitation which has lower intensity and longer duration than convective precipitation.

Figure 5.14 illustrates that as $\epsilon_r$ increases, ET and throughfall are decreased, surface runoff is decreased as well although the frequency of high extremes over crops is increased. Subsurface runoff over crops is increased following the lower intensity precipitation events which allow for more infiltration to the soil. Over forests, subsurface runoff is decreased possibly due to the large decrease in throughfall. ET doesn't vary for $\epsilon_r$ values of 0.3 and 1. Although throughfall is lower for $\epsilon_r = 1$, leading to higher canopy evaporation (via higher canopy interception), this is counterbalanced by lower ET rates as less water ends

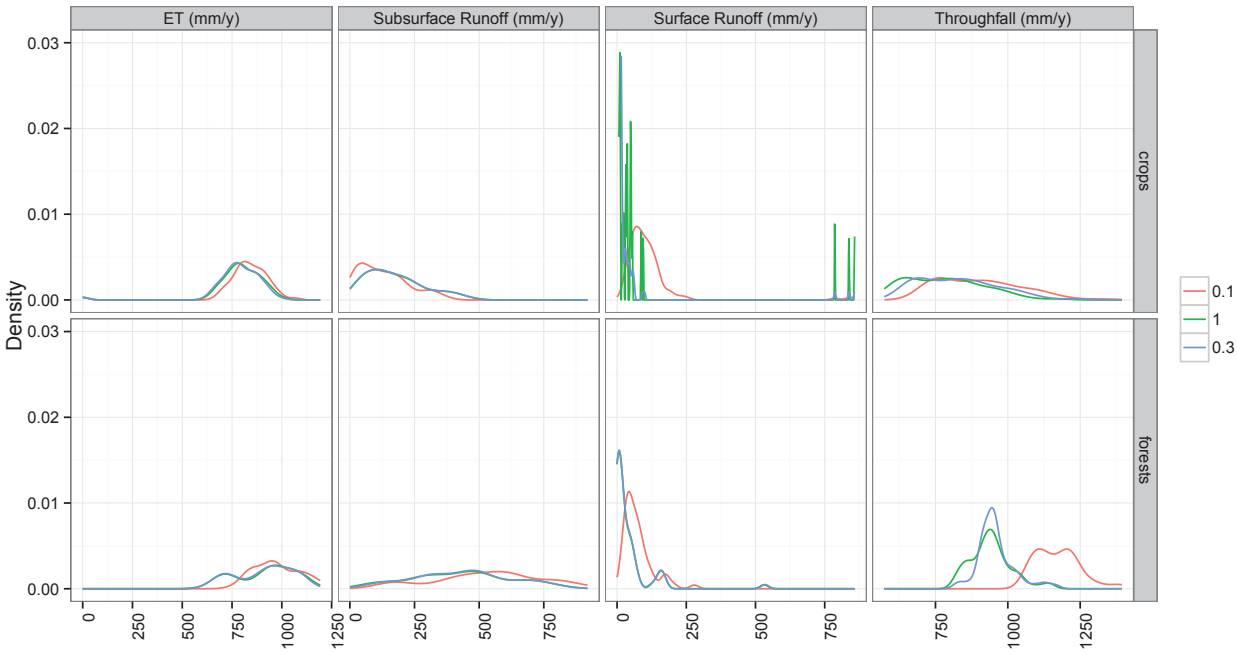


**Figure 5.14:** Kernel density plots, showing distribution of various simulated hydrological fluxes over agricultural and forested areas. Different colours correspond to different convective rainfall fraction ($\epsilon_r$) values, according to the legend.

up in the soil. However, for $\epsilon_r = 0.1$, the high precipitation intensity is associated with higher throughfall values (i.e. less canopy interception and therefore evaporation) which are translated into higher soil evaporation, associated with higher levels of soil moisture, leading to an overall increase in ET.

### Vegetation canopy interception

By modifying the canopy capacity according to Eq. 5.14 interception dependence by LAI is increased. In forests, which have the highest LAI values (7 for broadleef trees), $C_m$ is increased from $0.85$ to $1.80$. This increase of canopy capacity, as expected, is causing decreased throughfall in forests (Fig. 5.15). In croplands however, $C_m$ is reduced slightly from $0.6$ to $0.55$ due to the smaller LAI value (2 for $C_3$ grass) and the impact of this change to throughfall is minimum (Fig. 5.15).

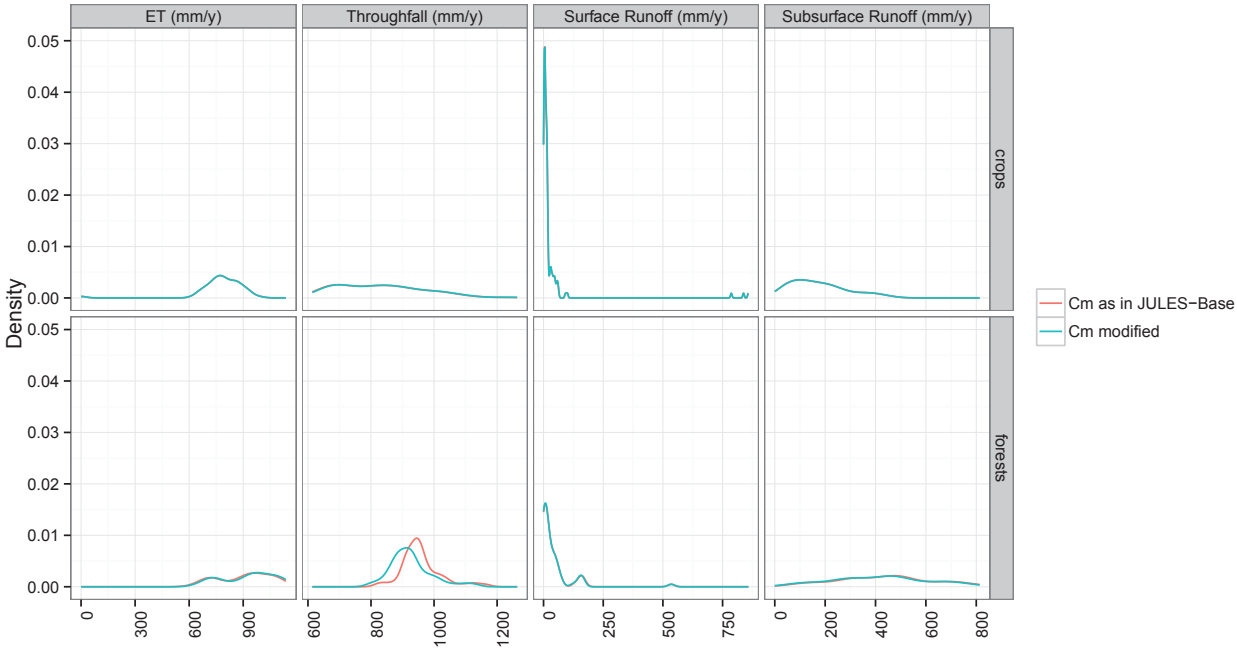


**Figure 5.15:** Kernel density estimates of various simulated hydrological fluxes over agricultural and forested areas. Red colour corresponds to the default JULES canopy capacity ($C_m$) calculated as in Eq. 5.12. Blue colour corresponds to the modified canopy capacity ($C_m$) calculated as in Eq. 5.14.

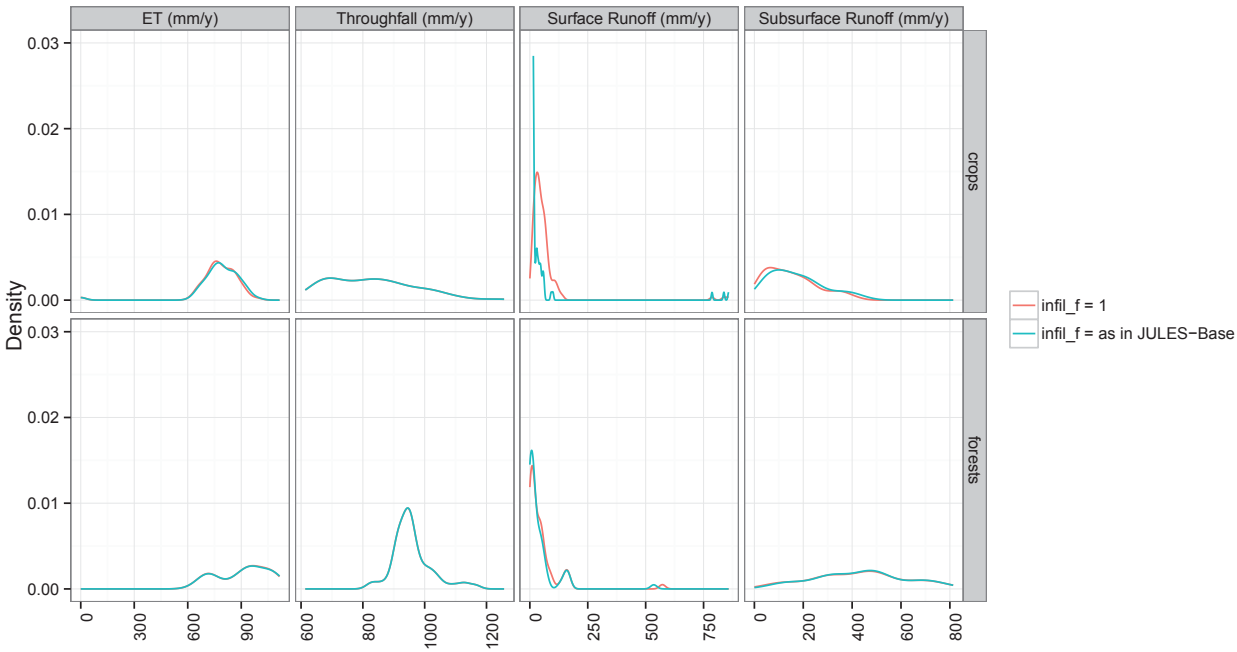


**Figure 5.16:** Kernel density estimates of various simulated hydrological fluxes over agricultural and forested areas. Blue colour corresponds to the default JULES infiltration enhancement factor ($b_s$). Red colour corresponds to the modified infiltration enhancement factor ($b_s$).

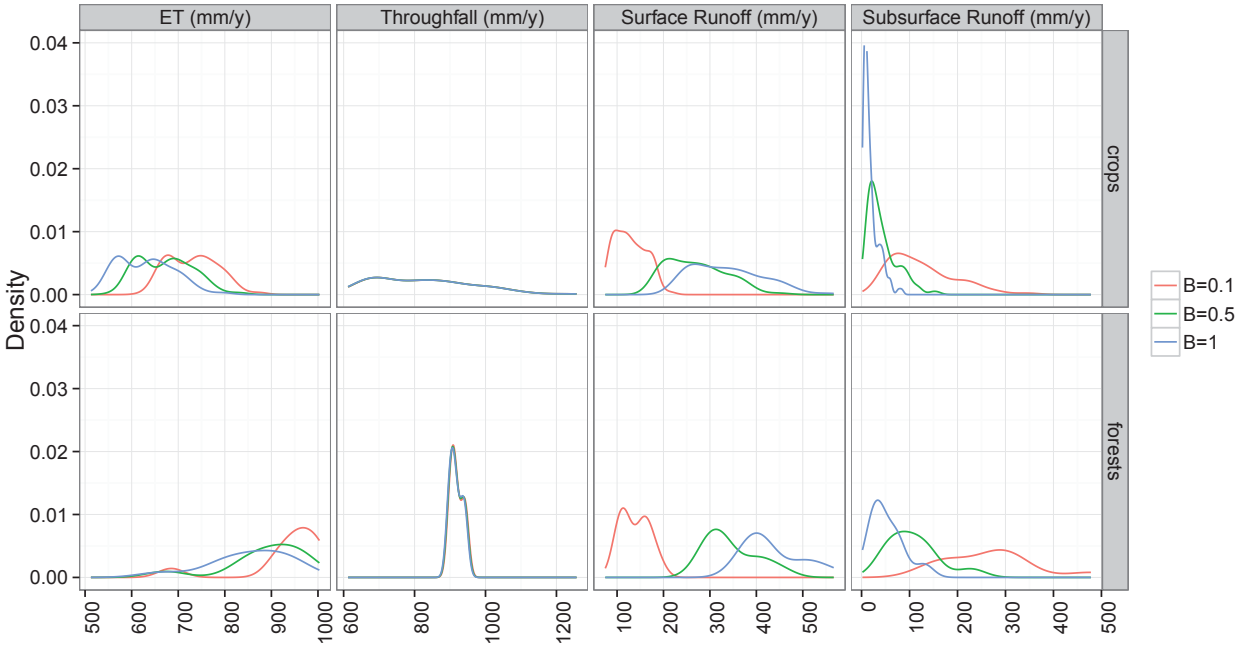


**Figure 5.17:** Kernel density plots, showing distribution of various simulated hydrological fluxes by JULES-PDM, over agricultural and forested areas. Different colours correspond to different $B$ parameter values, according to the legend.

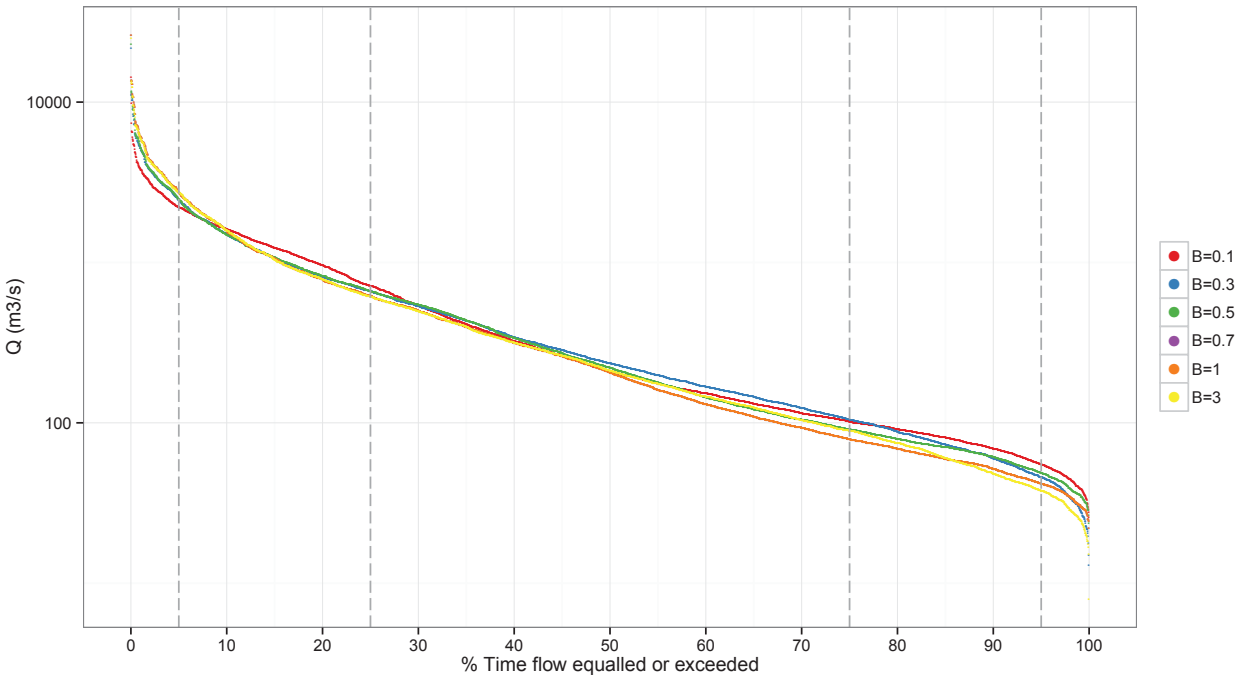


**Figure 5.18:** Flow duration curves of JULES-PDM simulated flows, under different $B$ parameter values, ranging between 0.1 and 3.

**Infiltration enhancement factor**

By decreasing the infiltration enhancement factor, $b_s$, in forests from 4 to 1 and in crops from 2 to 1, the results shown in Figure 5.16 indicate that more surface runoff is generated and less subsurface runoff and this was expected due to the decrease caused in the surface infiltration rate. What is interesting here is that although the reduction of $b_s$ is greater in forests than in crops, the impacts of this reduction are more pronounced in crops. This might be related to other parameters such as rainfall rate which differs from grid to grid, canopy moisture content and/or canopy capacity which is higher in forests.

#### 5.4.2.3 Sensitivity to structural perturbation: TOPMODEL and PDM runoff generation schemes

A sensitivity analysis was performed by testing different $B$ parameter values for JULES-PDM, ranging between 0.1 and 3. As shown in Table 5.10, the best performance scores in terms of NSE are being produced when $B = 0.1$, but in terms of all other performance measures, $B = 1$ (which is the default value in JULES) gives the best scores on average. According to Eq. 5.19, higher $B$ parameter values are associated with higher $f_{sat}$ values, which means that larger faction of the grid area is saturated (lower storage capacity). This is illustrated in Figs. 5.17 & 5.18 as higher $B$ values result in more surface runoff and a corresponding reduction in subsurface runoff. However, higher $B$ values result in lower low flow values (Fig. 5.18), and this is related to the routing and the fact that the subsurface flow component is delayed longer than the surface component. Because more surface runoff is produced now, most of the flow volumes will arrive earlier resulting in less regulated flows and a smaller volume of low flows. In addition, the increase in high flows is balanced by decreased ET fluxes.

For comparison reasons, the default JULES scheme will be hereafter referred to as JULES-Base. In all cases, the JULES-PDM runoff generation scheme produces higher surface runoff and lower subsurface runoff and ET compared to JULES-base (Fig. 5.21). The response is a lot more flashy in JULES-PDM and overall the model's performance in terms of daily streamflow reproduction is poor compared to JULES-base, in the Bhimgoda sub-catchment (Fig. 5.19). However, focusing on monthly time-scales (Fig. 5.23), JULES-PDM is producing the highest achieved NSE value of 0.72.

Similar patterns are observed between JULES-TOPMODEL and JULES-base. Similarly to JULES-PDM (although to a smaller extent) the TOPMODEL runoff generation scheme produces increased sur-

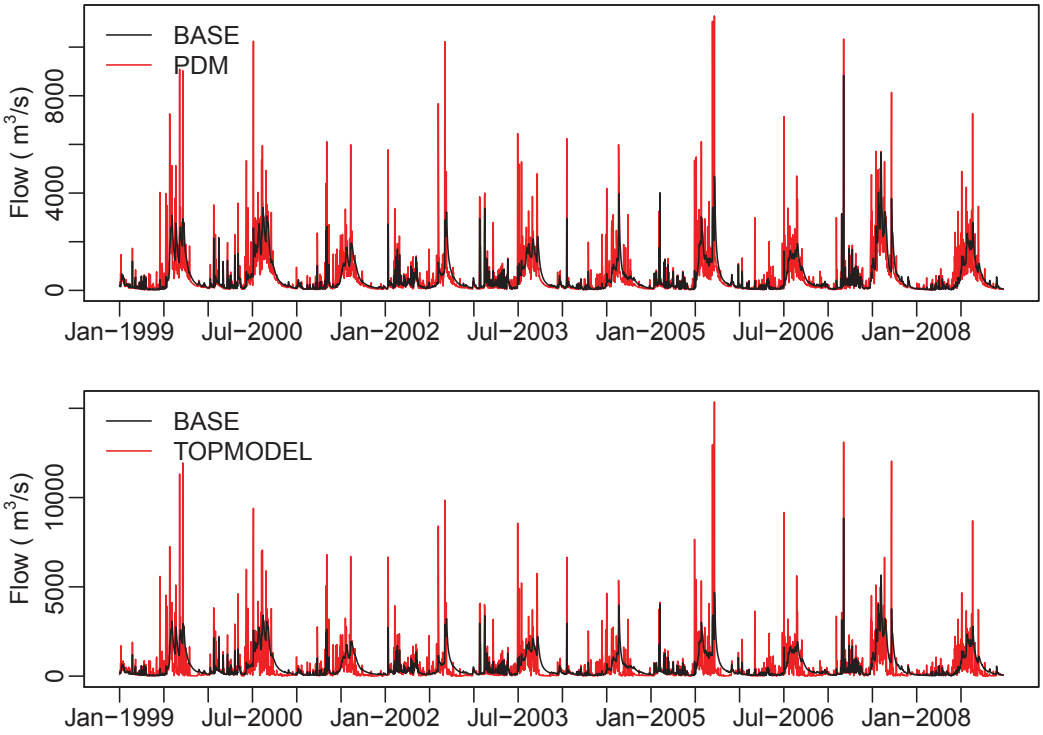


**Figure 5.19:** Daily streamflow simulations of JULES-base (black) versus JULES-PDM (top,red) and JULES-TOPMODEL (bottom,red).

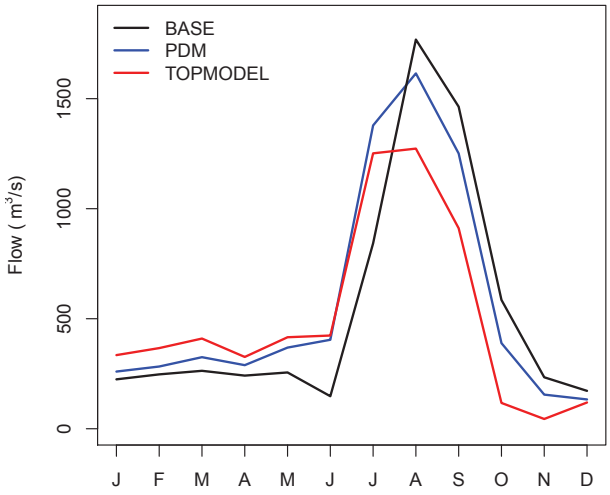


**Figure 5.20:** Inter-annual streamflow variability covering the period 1999–2008, for the Bhimgoda catchment.

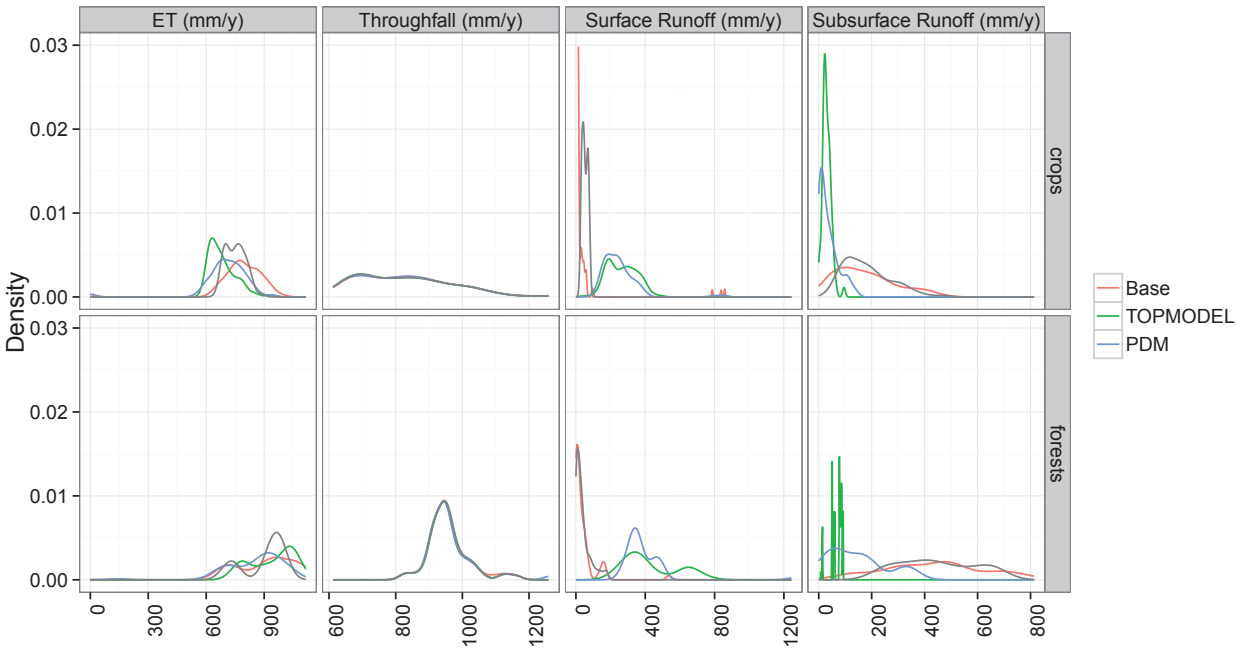


**Figure 5.21:** Kernel density plots, showing distribution of various simulated hydrological fluxes, over agricultural and forested areas. Different colours correspond to different JULES runoff parameterisation schemes (JULES-base, JULES-PDM, JULES-TOPMODEL), according to the legend.

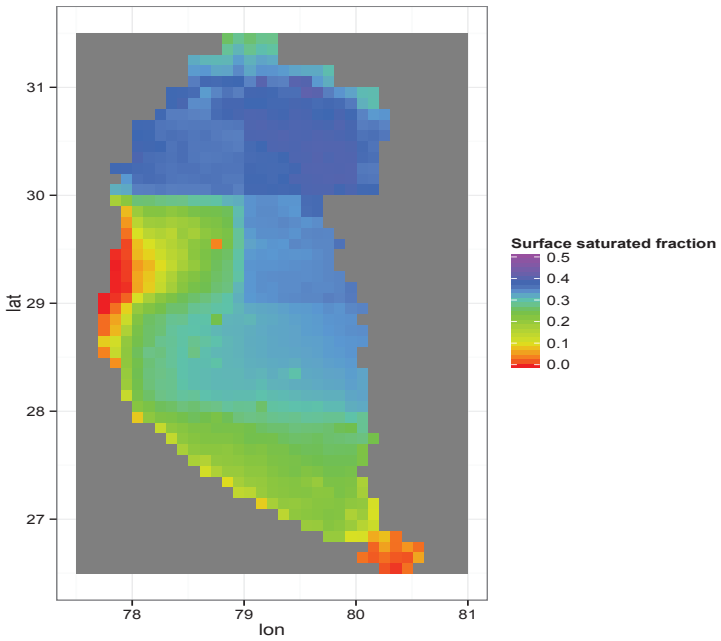


**Figure 5.22:** Average saturated fractions of the grid which are contributing to saturation excess runoff, under the TOPMODEL runoff parameterisation.

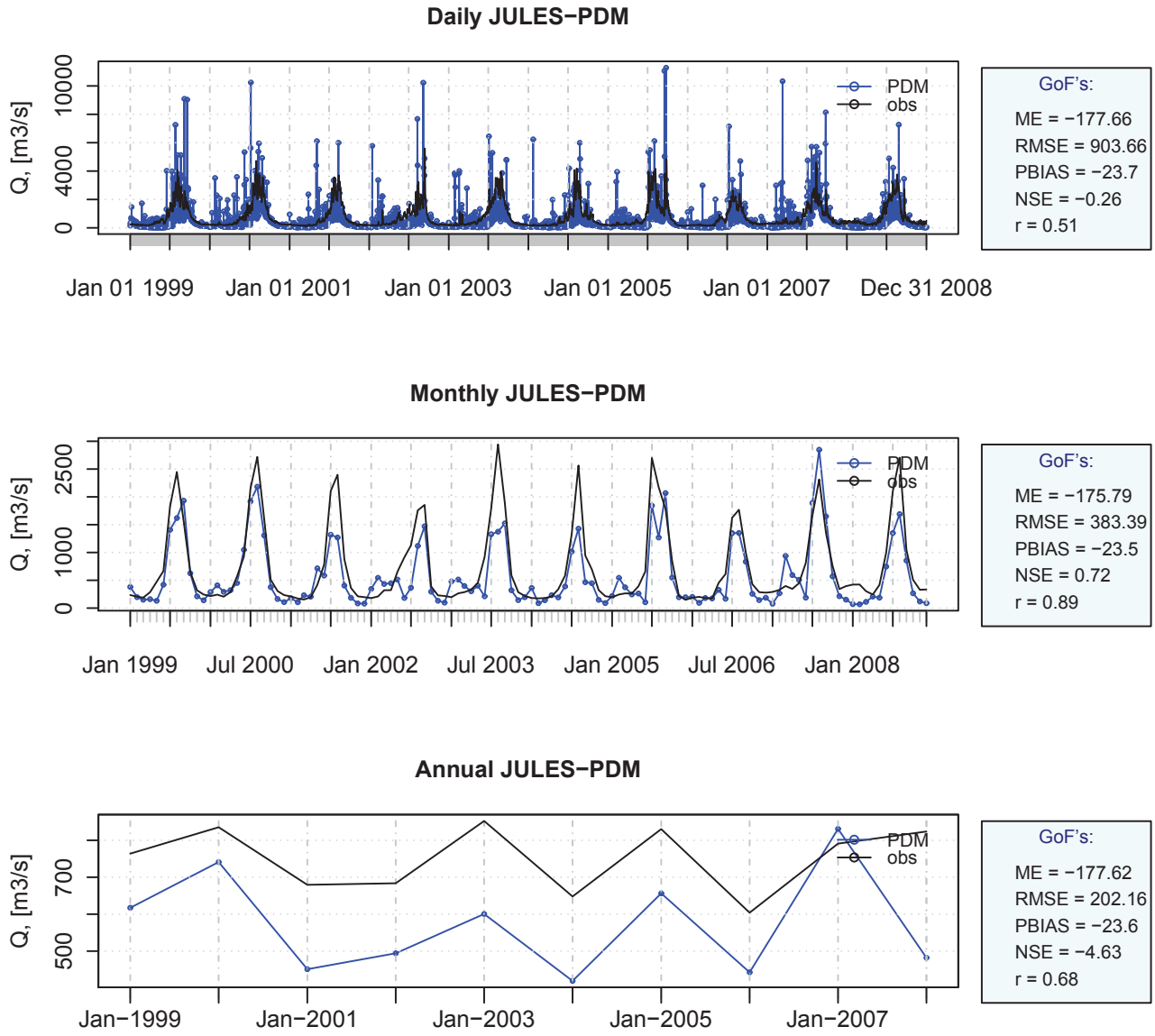


**Figure 5.23:** Daily, monthly and annual streamflow plots, comparing observations to model outputs of JULES-PDM. On the right hand side of each plot, the goodness of fit of the model, based on various performance scores.

face runoff with more flashiness compared to the default JULES parameterisation. JULES-TOPMODEL generates lower ET, especially over crops, whilst subsurface runoff is decreased compared to JULES-base. Figure 5.22 shows that in the north parts of the catchment, 40% of the grid-box surface is saturated

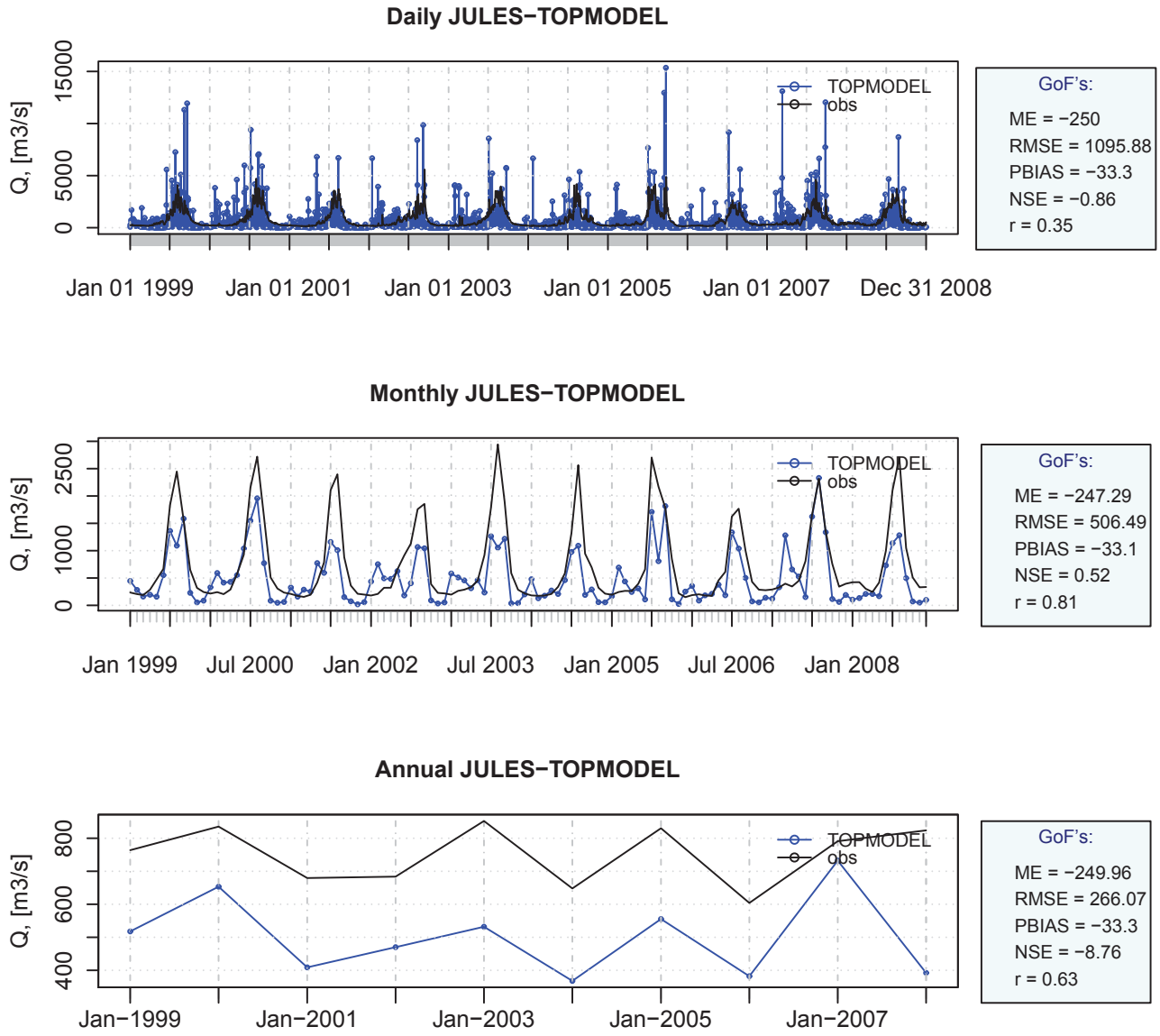


**Figure 5.24:** Daily, monthly and annual streamflow plots, comparing observations to model outputs of JULES-TOPMODEL. On the right hand side of each plot, the goodness of fit of the model, based on various performance scores.

on average, whilst in the mid-catchment areas this proportion is around 30%. It is clear that these numbers are not reasonable, especially for the northern mountainous areas. The model seems to overestimate the saturated fractions of the grid which are contributing to saturation excess runoff and this results in

unreasonably increased surface runoff. As shown in Figure 5.20, JULES-TOPMODEL is over-predicting the dry period flows compared to JULES-base. One of the basic assumptions in the TOPMODEL theory is that the entire basin contributes to streamflow (water table parallel to topography). However, during the dry season and especially in a steep catchment, such as the Bhimgoda catchment is, this assumption is not always valid and might cause overestimation of low flows. Another issue affecting the JULES-TOPMODEL performance is the topographic index grid scale versus the JULES grid scale. Topographic index values that have been aggregated over the coarse grids of the model, shift the topographic index distribution to lower values, leading to increased surface runoff.

#### 5.4.2.4 Sensitivity to temporal resolution of input data

The model's sensitivity to sub-daily meteorological data was investigated. Figure 5.25 shows that the differences between various hydrological variables under daily and sub-daily weather forcing are quite substantial. Throughfall is increased under 3-hourly forcing, which could explain the decrease in ET over crops. However, over forests ET is increased slightly, despite the increase in throughfall. An explanation for that could be that under the 3-hourly forcing, an expected shorter duration of precipitation events is associated with longer periods of dried canopy, which allows for transpiration to occur. The subsequent reduction of surface and subsurface runoff over forests, leads to a poorer streamflow simulation performance under the 3-hourly forcing, in Bhimgoda catchment. On the other hand, surface runoff over croplands is increased, whilst subsurface runoff remains almost the same. The examined performance scores for streamflow generation are in all cases lower when the model was run with 3-hourly meteorological data compared to daily data.

#### 5.4.2.5 Evapotranspiration simulation

When compared to the MODIS and LandFlux ET products, JULES is overestimating ET throughout the simulation period (Figs 5.26–5.29). One could argue that differences between the forcing data of JULES and the data used by the MODIS or LandFlux algorithms to generate the ET products are adding extra noise to this comparison. But the same general picture of JULES overestimating ET appears even when JULES was run with the same forcing data as the ones used by MODIS. This is further discussed in the next Chapter.

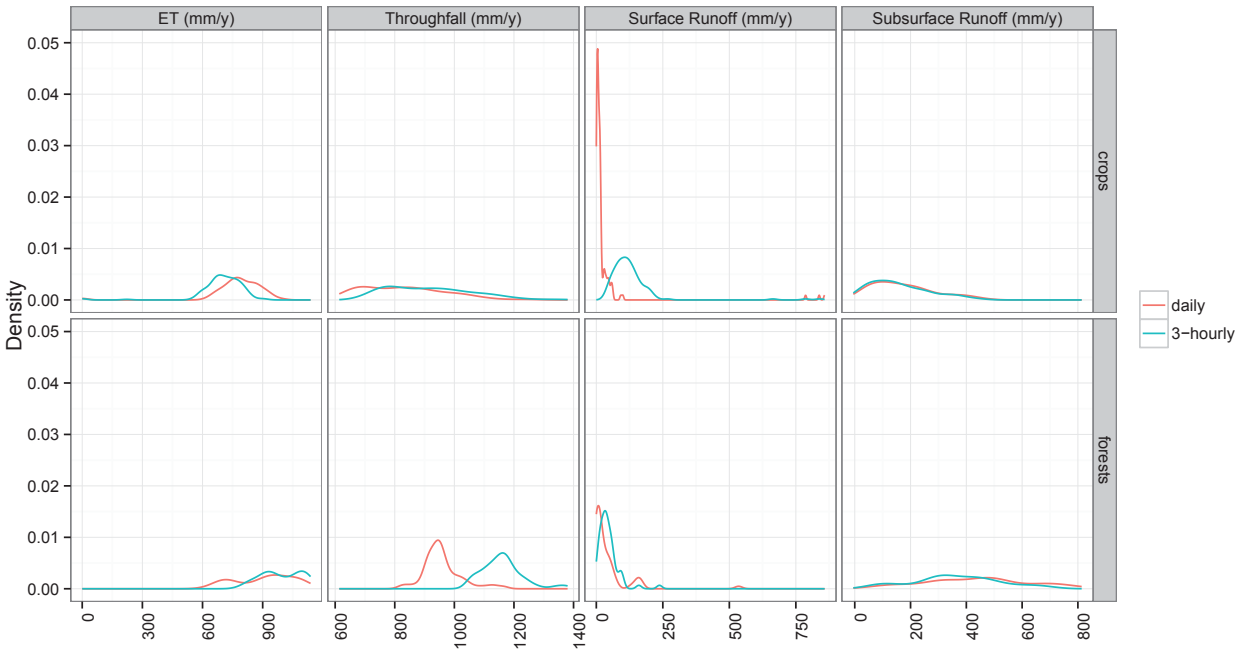


**Figure 5.25:** Kernel density estimates of various simulated hydrological fluxes over agricultural and forested areas. Red colour corresponds to daily meteorological driving data. Blue colour corresponds to 3-hourly meteorological driving data.

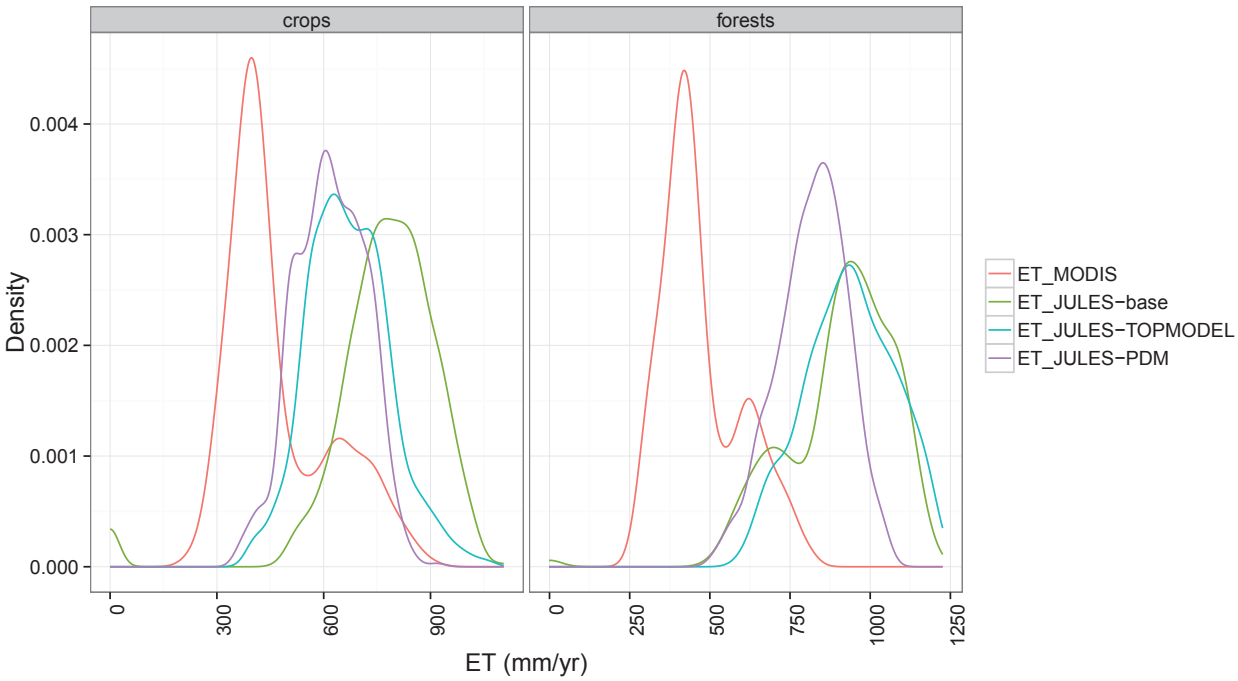


**Figure 5.26:** Kernel density plots, showing distribution of ET values over agricultural and forested areas. Different colours correspond to different runoff parameterisation schemes within JULES (JULES-base, JULES-PDM, JULES-TOPMODEL) and the MODIS ET product, according to the legend.

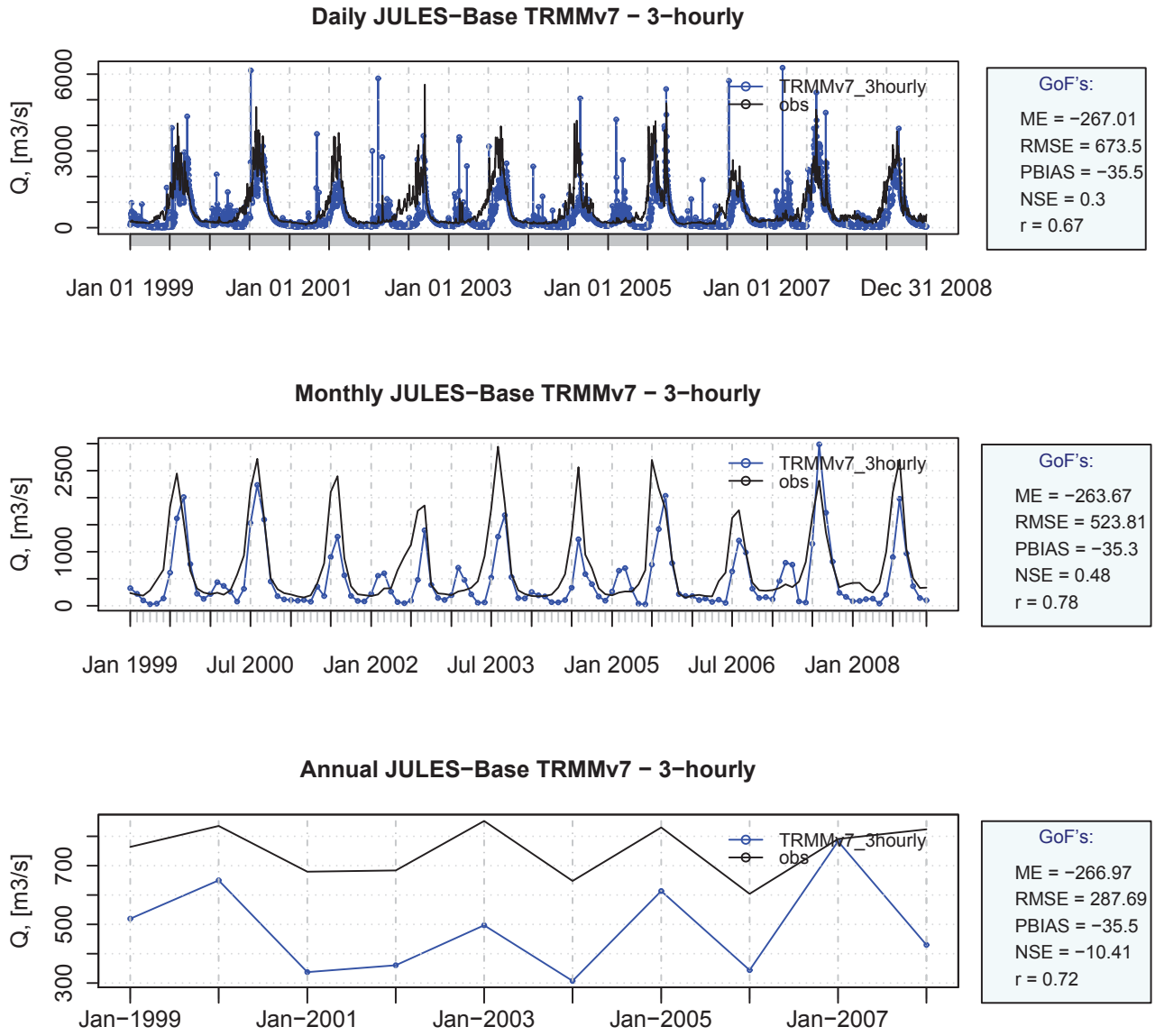


**Figure 5.27:** Daily, monthly and annual streamflow plots, comparing observations to model outputs of JULES-base, when forced with 3-hourly meteorological data. On the right hand side of each plot, the goodness of fit of the model, based on various performance scores.

As shown in Figure 5.28, the highest differences between JULES and MODIS ET occur in the mid-catchment areas and the southern plains. These are densely vegetated areas, mainly occupied by crops and by the moist deciduous forests of the Upper Gangetic plains.

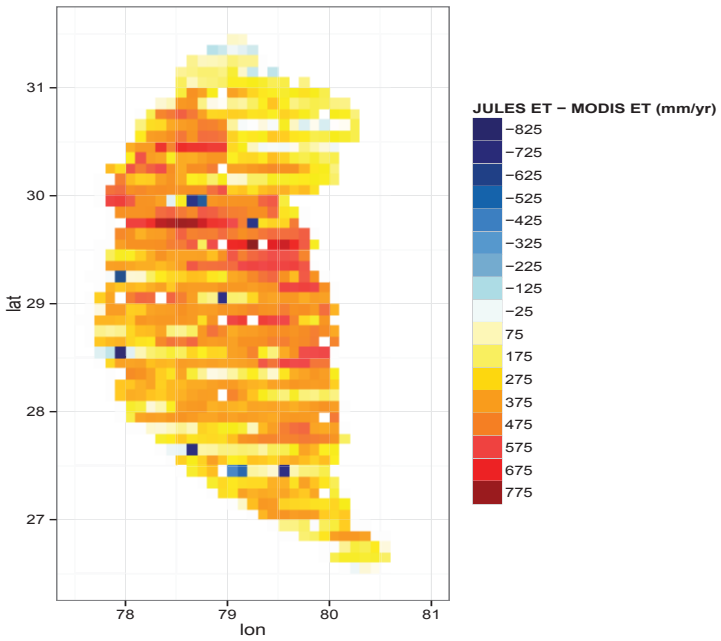


**Figure 5.28:** Differences between JULES-base and MODIS annual ET.

Over the agricultural areas, which cover 60% of the study area, JULES simulates an incorrect land cover with 100% agriculture throughout the entire simulation period, that indeed evaporates more than the bare soil does. The lack of dynamic crop growth routine in the model means that LAI, root depth and canopy height are being kept constant. But this is a poor representation of the actual conditions over the UG basin. In this area, a two-crop rotation system ensures at least 2 cropping seasons per year in between short fallow land periods. The main crops grown in the study area (district of Uttar Pradesh) are rice during the summer months ( July–October) and wheat during the winter months (October–March) (Agropedia, 2013; NFSM, 2013; USDA-I, 2013; FAO, 2013; ICAR, 2013).

JULES tends to overestimate ET mainly during the dry period because then the difference between the default LAI value of 2 and the actual LAI value of the growing crop (wheat) is larger (Fig 5.31, top). This is also clearly illustrated on the bottom plot of Fig. 5.31 that shows the mean seasonal cycle of ET ($\mathrm{mm\,month^{-1}}$) and gives an approximation of the mean bias per month for JULES-base. Similar trends have been observed by Blyth *et al.* (2010), who used surface energy flux measurements from 10 FLUXNET sites around the world, representing a range of climate conditions and biome types, and found that the JULES-base evaporation is higher than that observed. The same results were also found by Van

den Hoof *et al.* (2011), who found that the JULES-base latent heat flux is overestimated over croplands in Europe. One possibility for this bias is an overestimation of canopy interception. Blyth *et al.* (2011), who applied a set of benchmark tests in order to quantify the performance of JULES, found indeed that the model is overestimating evaporation mainly due to the simple approach of using a fixed, predetermined LAI. The fixed annual LAI could explain the overestimation of ET not only over agricultural areas but also over the moist deciduous forests of the study area (that cover most of the Uttarakhand and Uttar Pradesh forested areas), which mainly lose their leaves during the dry winter period.

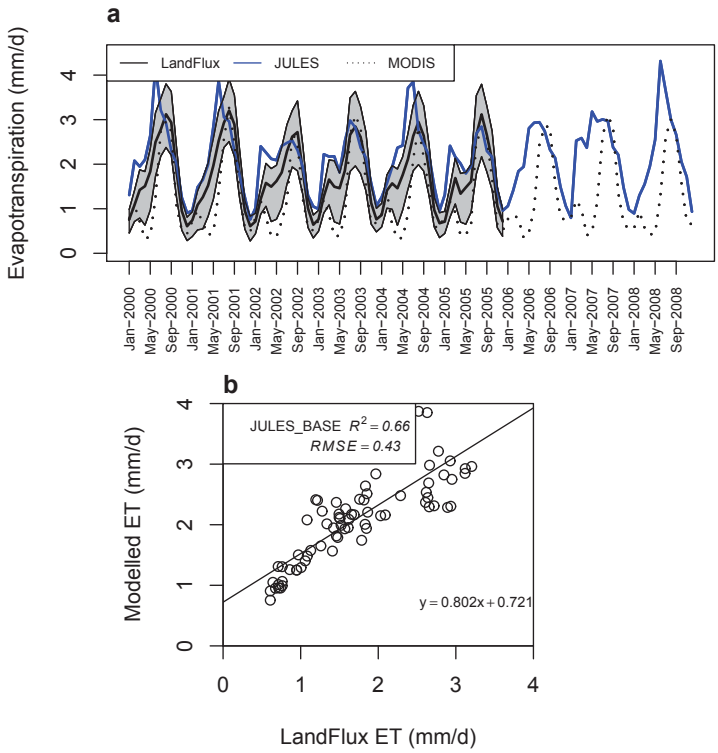


**Figure 5.29:** a: Comparison of the modelled ET with the LandFlux-EVAL product. The shaded area corresponds to the values between the $25^{th}$ and $75^{th}$ percentiles of the distribution. b: Performance scores of JULES in comparison with LandFlux-EVAL ET.

Similar patterns are observed when outputs of JULES-base over agricultural areas are compared to the LandFlux product (Fig. 5.29), although at the end of the dry period (months April–May) JULES produces lower ET values. This underestimation of ET during the dry period could be related to the free drainage lower boundary condition and associated negative soil moisture biases during dry periods.

Since the largest part of the study area is covered by crops, and given the problematic simulation of

ET over agricultural areas, it is important to include dynamic crop growth in the model. The next Chapter describes this new modelling approach for JULES and how it impacts the simulation of ET.

#### 5.4.2.6 Soil moisture simulation

Due to lack of in situ soil moisture measurements, JULES performance, in terms of soil moisture, is evaluated by comparing model outputs to the ESV-SM product (Liu *et al.*, 2012; Wagner *et al.*, 2012) during the simulation period 1999-2008. Figure 5.32 shows that over the crop areas, JULES slightly underestimates top layer soil moisture compared to the ESV-SM product. This could be related to the overestimation of ET over crop land, discussed above. However, over the forested areas, JULES generates higher values of top layer soil moisture compared to the ESV-SM product. Between the different runoff generation mechanisms, the default JULES-base parameterisation gives the best performance, followed by JULES-PDM, in both agricultural and forested areas. The overestimation of soil moisture under the JULES-TOPMODEL scheme in the regions occupied by forest was expected as 40% of the gridbox surface was found to be saturated, as previously mentioned (Fig. 5.22).

### 5.4.3 Uncertainty analysis

The above sensitivity analysis, aims to construct a model that is robust in its predictions. The precipitation input ensemble is used to test the impact of uncertainties in input data, and along with the different parameter combinations explored above (parameter uncertainties), the model's potential to bracket the observations is investigated.

The hydrograph prediction uncertainties shown in Figs. 5.33–5.34, for daily and monthly flows respectively, in the Bhimgoda catchment, indicate that the model is able to reproduce the observed discharge reasonably well. The light shaded areas denote the spread of modelling uncertainty that originates from input data uncertainties (precipitation in this case), whereas the dark shaded areas denote modelling uncertainties resulting from combined input and parameter uncertainty. The simulations manage to bracket the observed discharge throughout most of the time (red line for bracketed values and blue line for non-bracketed values) , although during some periods the prediction uncertainties are quite large, indicating that improvements are required so that the model can function as a proper hydrological tool for

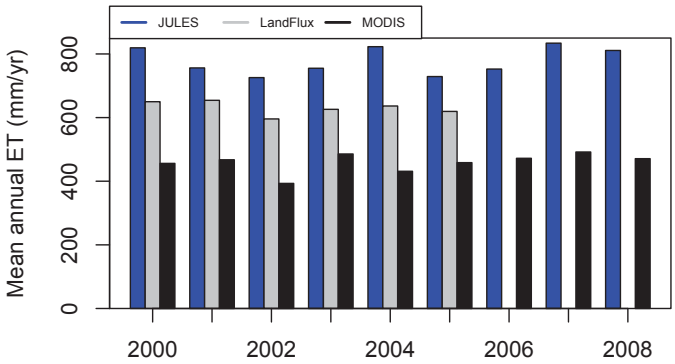


**Figure 5.30:** Mean annual ET estimated by JULES-base versus modelled by the MODIS product.

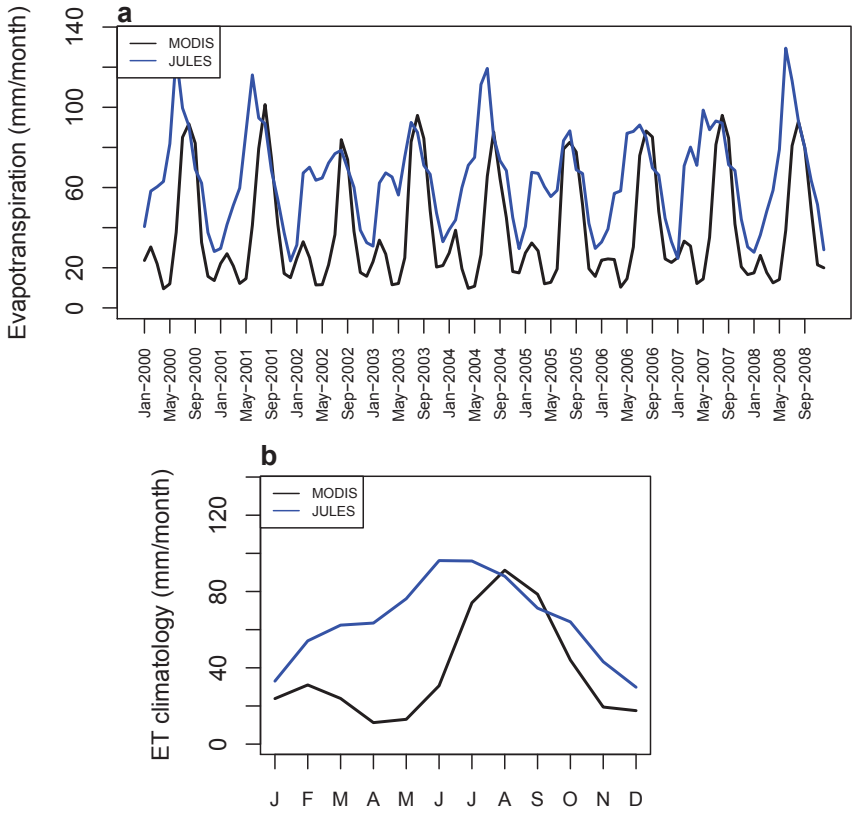


**Figure 5.31:** Top: Comparison between MODIS ET and simulated ET by JULES-base. Bottom: Mean seasonal cycle of ET (mm/m) showing the mean bias per month.

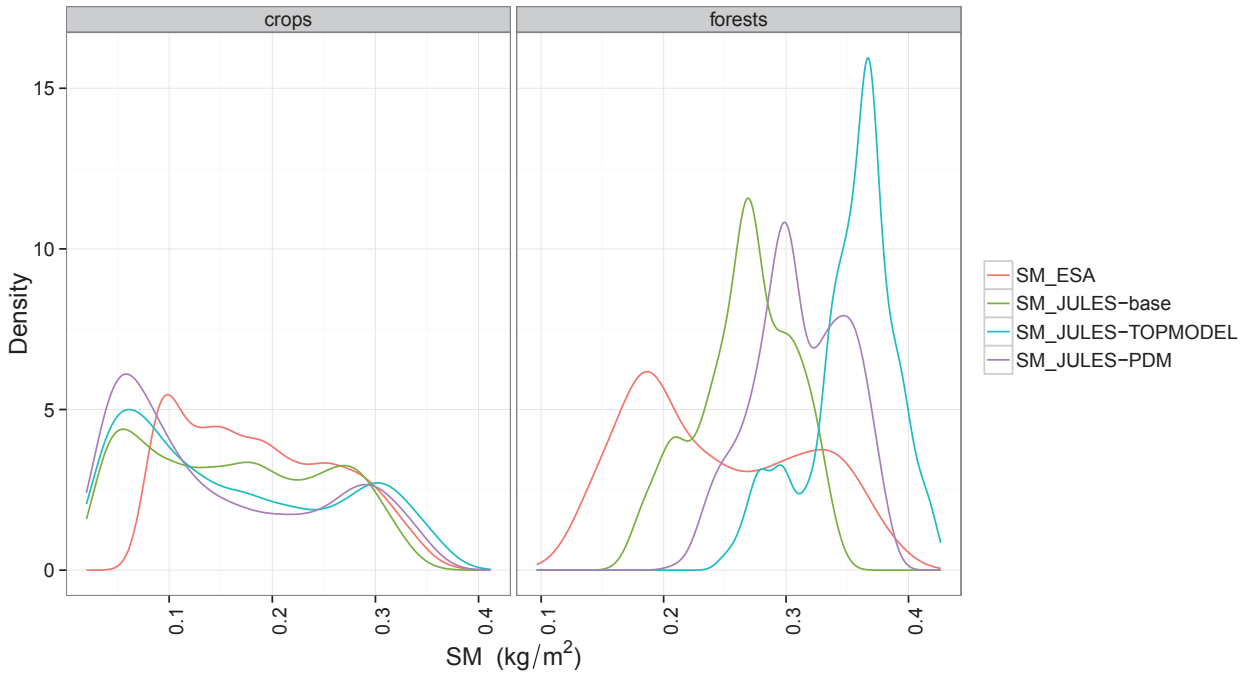


**Figure 5.32:** Kernel density plots, showing distribution of top layer soil moisture values over agricultural and forested areas. Different colours correspond to different runoff parameterisation schemes within JULES (JULES-base, JULES-PDM, JULES-TOPMODEL) and the ESV-SM soil moisture product, according to the legend.

water resources assessments. When uncertainties are examined on a daily basis, the model brackets 76% of the observations (Fig. 5.33), whereas looking into monthly discharge, the model is able to bracket 87% of the observations (Fig. 5.34). Uncertainties in the observations were not considered, although it is possible that they exist as well. The second (and smaller) peak that occurs often in the modelled streamflows, during the dry season (around January), but does not appear in the observations, is due to precipitation events that are translated directly into runoff (Fig. 5.34). The fact that the model does not account for any storage of water in ponds or wetlands (which frequently occurs in the study area), but instead assumes direct runoff into the river, could therefore be responsible for this second peak.

Figure 5.35 illustrates the ET prediction uncertainties and how they compare with the MODIS and LandFlux products. Here, the model was not able to bracket the "observations", as during most of the time ET is overestimated (blue points indicate months that JULES did not encompass the observations). When compared to the MODIS product, JULES is able to bracket only 20% of the values, in comparison

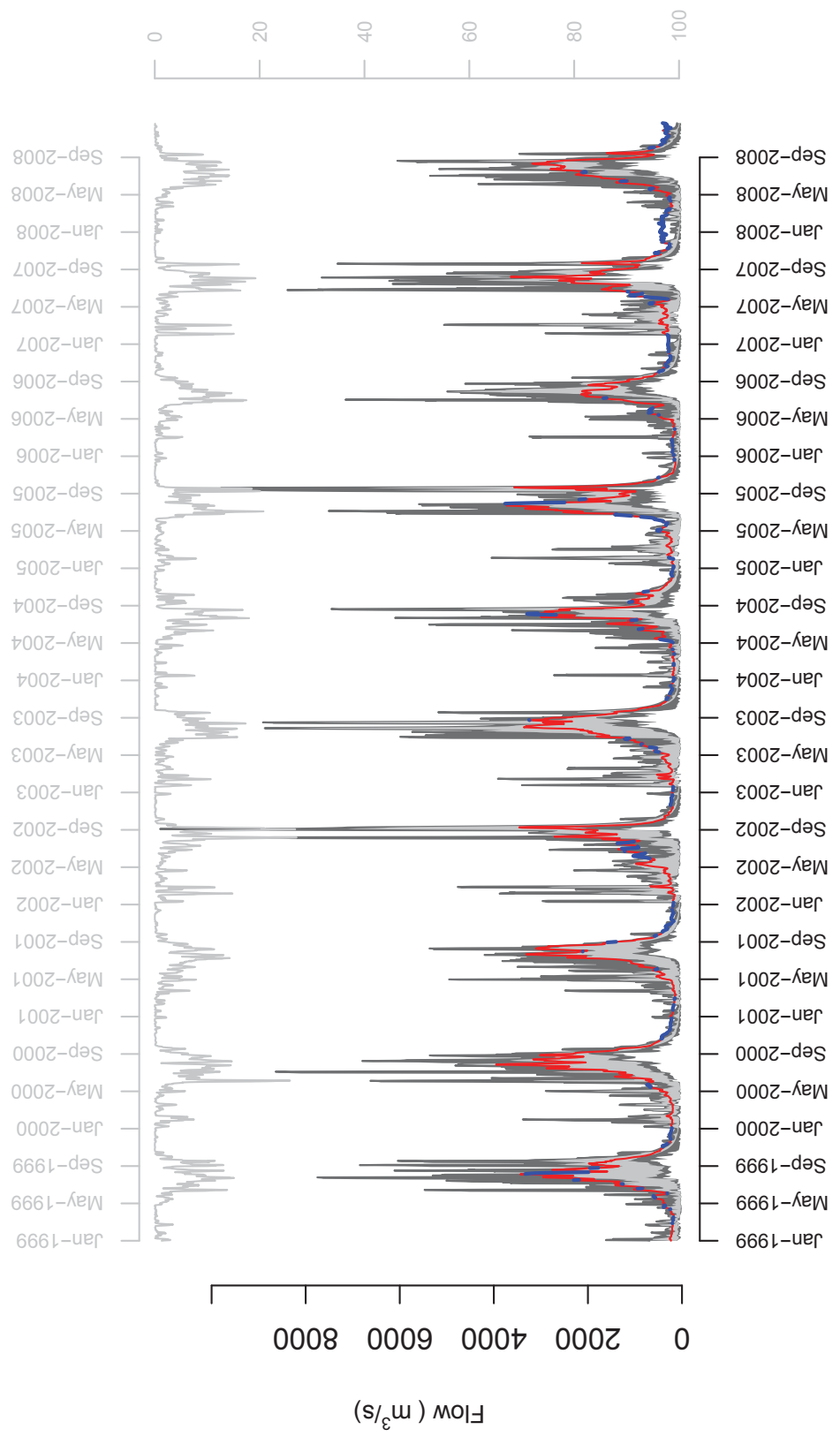


**Figure 5.33:** Daily streamflow uncertainty bands produced after forcing JULES with all different precipitation products, along with all different possible combinations of parameter perturbations explored. The light shaded areas denote modelling uncertainty that originates from input data uncertainties (precipitation in this case), whereas the dark shaded areas denote modelling uncertainties resulting from combined input and parameter uncertainty. With red colour are the observations for Bhimgoda catchment that are bracketed by the model and blue indicates observations that are not bracketed. The top axis shows daily precipitation values, averaged across Bhimgoda basin and across all gridded products explored here.

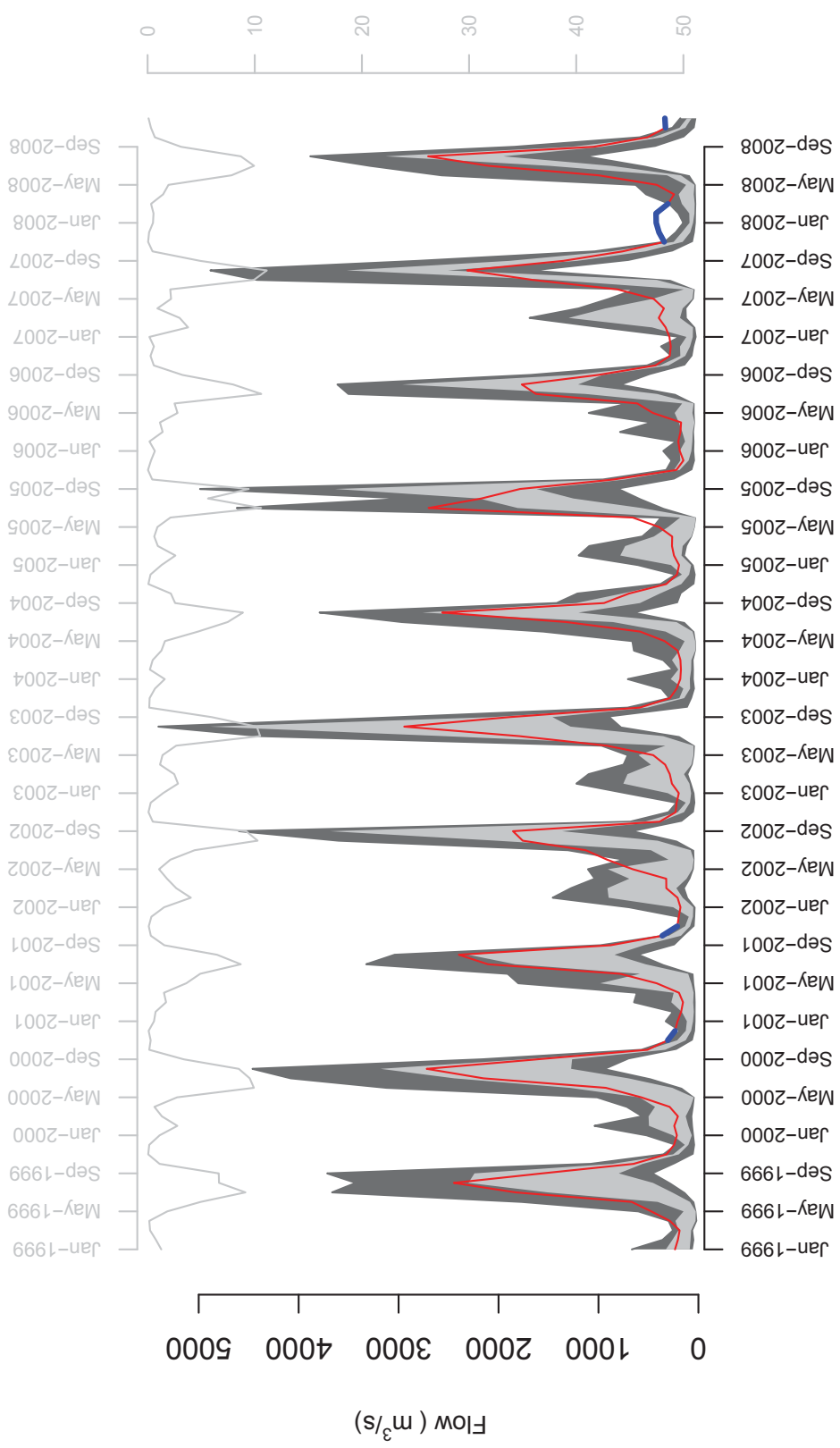


**Figure 5.34:** Monthly streamflow uncertainty bands (grey colour) produced after forcing JULES with all different precipitation products, along with all different possible combinations of parameter perturbations explored. The light shaded areas denote modelling uncertainty that originates from input data uncertainties (precipitation in this case), whereas the dark shaded areas denote modelling uncertainties resulting from combined input and parameter uncertainty. With red colour are the observations for Bhimgoda catchment that are bracketed by the model and blue indicates observations that are not bracketed. The top axis shows monthly mean precipitation values, averaged across Bhimgoda basin and across all gridded products explored here.

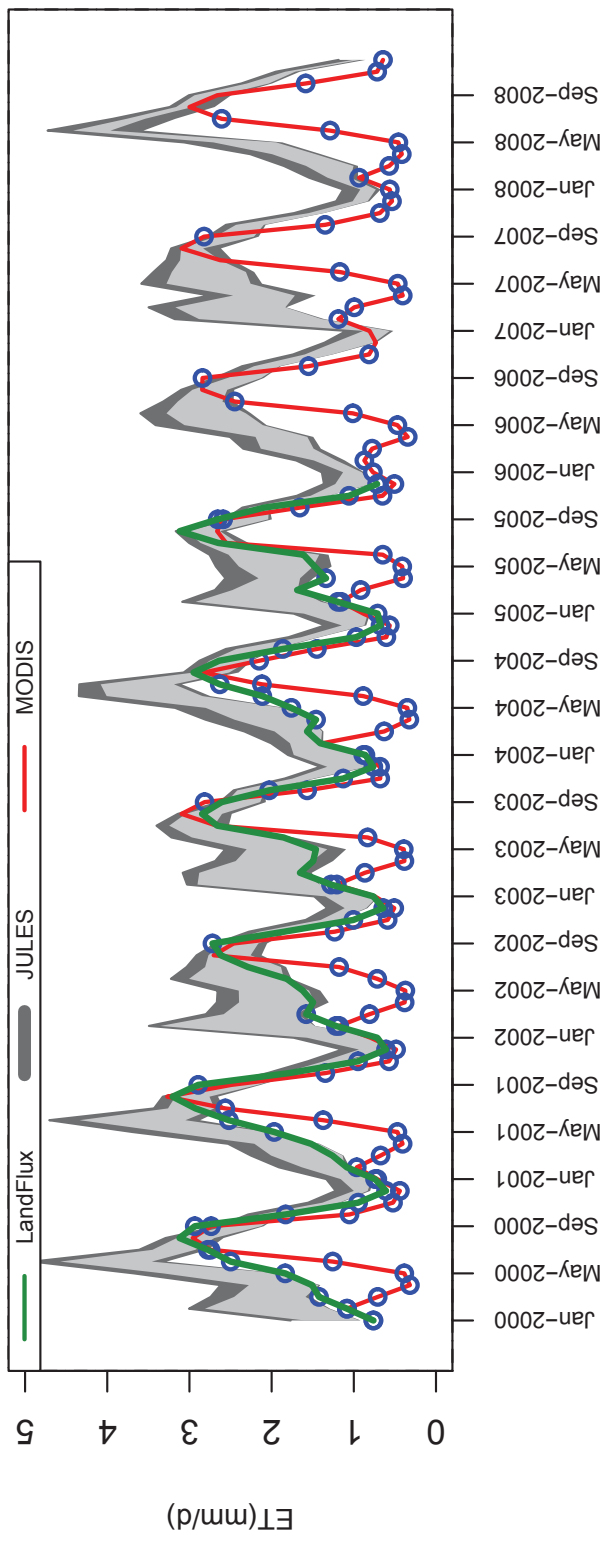


**Figure 5.35:** Monthly ET uncertainty bands (grey colour) produced after forcing JULES with all different precipitation products, along with all different possible combinations of parameter perturbations explored. The light shaded areas denote modelling uncertainty that originates from input data uncertainties (precipitation in this case), whereas the dark shaded areas denote modelling uncertainties resulting from combined input and parameter uncertainty. With red and green colour are the MODIS and LandFlux values, respectively, that are bracketed by the model. Blue points indicate values that are not bracketed. All results shown here are averaged across the UG basin.

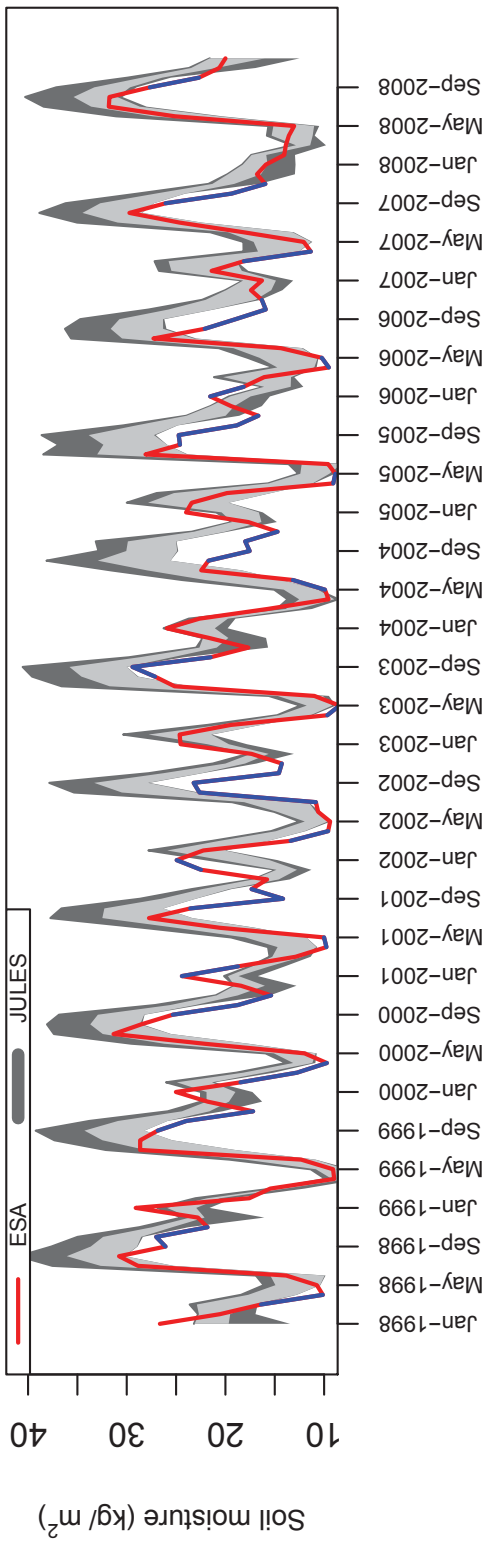


**Figure 5.36:** Monthly top layer soil moisture uncertainty bands (grey colour) produced after forcing JULES with all different precipitation products, along with all different possible combinations of parameter perturbations explored. The light shaded areas denote modelling uncertainty that originates from input data uncertainties (precipitation in this case), whereas the dark shaded areas denote modelling uncertainties resulting from combined input and parameter uncertainty. With red colour are the ESA product values that are bracketed by the model. Blue points indicate values that are not bracketed. All results shown here are averaged across the UG basin.

to bracketing 46% of LandFLux values. As previously discussed, this is likely the outcome of a structural deficiency, mainly caused by the fact that the model is not taking into account the dynamic nature of vegetation. This is further explored in the next Chapter.

In terms of soil moisture, the prediction uncertainties shown in Fig. 5.36 are partially bracketing the observations (ESA product), as the model is able to contain 60% of the observations (red colour, Fig. 5.36). During the dry period the model matches reasonably well the observations but during the wet season the model is over-predicting the top layer soil moisture fluxes, and that is the period with the largest uncertainty bands. During the period 2002–2006, the ESA product does not provide a good coverage over the study area and the missing data do not allow for much interpretation of the results.

## 5.5 Discussion

Based on the sensitivity and uncertainty analysis, several shortcomings of JULES were identified and are further discussed. JULES, which is a global LSM, was not built to operate as a hydrological model, whose results are interpreted in the fine resolutions that water resources applications require for addressing critical water-cycle science questions. Although it is a much more complex model compared to most hydrological models, it does not include some key processes, and this limits its potential to be used in a hydrological and water resources context.

The vertical structure of the model does not allow horizontal water movements, or any horizontal flux exchange in both surface and subsurface levels. This means that overbank flooding is not explicitly represented. In addition, the infiltration excess runoff scheme might not be as appropriate as a saturation excess runoff scheme for soils with high infiltration capacities, and its application leads to lower than in reality values of surface runoff and higher values of soil moisture.

Plant water availability in JULES is described by a factor ($\beta$) that depends on soil moisture content; the factor decreases linearly when soil moisture decreases from its critical point value to its wilting point value. However, this method does not describe the full feedbacks between the plant/soil system. Verhoef and Egea (2014) explore an alternative more sophisticated approach that uses soil water potential, soil hydraulic and chemical effects that could represent more realistically the soil-vegetation-atmosphere interactions. Further, Egea *et al.* (2011) suggested a more adaptable factor ($\beta$) that varies in a curvi-linear

way (and not just linear) to account for the varying sensitivity of stomatal and mesophyllic conductance as well as biochemical capacity to soil moisture deficit. The authors recommended additional ways to describe water stress impacts on canopy exchange processes (i.e. not only via stomatal and biochemical limitations but also through mesophyllic conductance).

At the daily time-scale, additional uncertainty was introduced from the simple runoff routing mechanism. The errors are reduced when looking at the outputs on a monthly basis, where the impact of a simple routing scheme is smoothed. No explicit river channel, wetlands, or ground-water stores are represented in JULES, whilst the model assumes direct runoff into the river without taking into account the water retention time in ditches, ponds or swamps.

The fixed depth of the soil column can affect soil moisture storage, runoff and latent heat fluxes. There is no groundwater component and the lack of its interactions with surface fluxes is crucial for the accurate representation of flux partitioning. Further, the lack of subsurface grid heterogeneity in the default JULES scheme means that soil moisture is distributed uniformly on large scales (11 km in this study), whereas in reality can vary on spatial scales of meters.

The representation of dams and reservoir operations as well as other human interventions, such as irrigation practices, is not included in the current standard JULES version. Besides, the lack of sub-grid heterogeneity means that in this study the model could not simulate irrigation practices, as irrigation would rarely cover an entire gridbox of 0.1°.

The hydrological properties of soils in JULES are constant across each modelling grid. Same for eco-physio-biological properties of plants, which remain constant for each PFT, although studies suggest that 75% of the observed variations in PFT characteristics occur within the same PFT (Kattge *et al.*, 2011). An alternative new approach suggested in the literature (e.g., Van Bodegom *et al.*, 2012), according to which plants should be described by continuous variations of their attributes instead of fixed PFT parameters, yields more robust results.

Further, by generating runoff at a point scale, with a single typical soil profile and without considering the great variations of soil and topographic properties, sharp transitions between high and low flows are expected to occur (Prentice *et al.*, 2014). Given that heterogeneity is present in all land surface properties, down to scales of metres, the tiling approach of JULES cannot solve the heterogeneity problem explicitly, although part of this issue may have been alleviated if JULES were run at a higher resolution.

Other LSMs (e.g. VIC, Liang *et al.*, 1994) use statistical distributions, which is a more promising approach to represent spatial variations of various parameters (such as soil moisture and infiltration rate) in sub-grid scales (Prentice *et al.*, 2014).

Finally, a network of surface flux measurements for the monsoon tropics, would help refine and validate JULES by constraining its parameters. A lack of detailed observations across India is preventing a more thorough understanding of the interactions between land-surface and the atmosphere. Model runs at locations where observed meteorology is available could help develop a more integrated understanding of land-surface dynamics and determine processes responsible for biases in modelled fluxes, at various time scales.

## 5.6 Chapter Summary

In this Chapter, the potential of the LSM JULES was explored, in terms of its ability to simulate hydrological fluxes in the UG river basin. As part of the sensitivity and uncertainty analysis, the model's sensitivity to different processes was explored and its robustness and ability to encompass the observations was quantified.

An analysis of different precipitation datasets revealed large variations between the different products. JULES was found to be very sensitive to precipitation forcing and given the large uncertainties in that forcing, the model's performance can be unreliable. The lack of available flow data for the entire UG catchment limited the study of streamflow simulation to the smaller Bhimgoda sub-catchment.

Overall, JULES performance in terms of reproducing streamflow results at a fine temporal scale, was found to be adequate - given that it is a global LSM, not specifically developed for hydrological modelling. The uncertainty analysis shows that simulations manage to bracket the observed discharge throughout most of the time (87% of observations at monthly time-scales), although prediction uncertainties can be high.

In terms of ET and soil moisture, in the absence of actual measurements, a combination of remote sensing and LSM products were used to validate the model's performance. JULES generates significantly overestimated ET fluxes over both croplands and forested areas, whilst it underestimates top layer soil moisture over croplands. Interestingly, over the forested areas top layer soil moisture is overestimated.

The model was able to encompass a small fraction of ET the observations (only 20% of MODIS values was bracketed), whilst was partially able to encompass soil moisture observations (60% of ESA values were bracketed).

During the structural perturbation of JULES, different runoff generation mechanisms were explored (PDM, TOPMODEL) but the default scheme of the model was found to outperform them. In terms of parameter perturbation, a decreased infiltration enhancement factor, which essentially decreased the surface infiltration rate, achieved the generation of more surface runoff over croplands. By modifying the canopy capacity in order to increase interception dependence by LAI, decreased throughfall in forests was the main achievement. However, this was not followed by surface runoff alteration in forests, which means that the throughfall reduction was mainly translated into a reduction in the soil moisture pool. Through parameter perturbation the high model bias in the estimation of ET was not improved, which is suspected to be related to the lack of a dynamic vegetation cycle in the model. This is further explored in the next chapter.

# Chapter 6

# Introducing dynamic crop growth in JULES

# Introducing dynamic crop growth in JULES

This Chapter is based on the work described on the following publication:
Tsarouchi, G., Buytaert, W., Mijic, A., 2014. Coupling a Land Surface Model with a Crop Growth Model to improve ET flux estimations in the Upper Ganges basin, India. *Hydrology and Earth System Sciences*, 18, 4223-4238.

## 6.1 Introduction

In recent years, much progress has been made in developing sophisticated Land Surface Models (LSMs), which are able to represent biophysical and hydrological processes of the land surface as well as their interaction with the atmosphere. However, one of the significant problems remaining to be addressed is the adequate representation of evapotranspiration (ET), which is the primary source of water transport from the land surface to the atmosphere.

In this study the LSM JULES (Best *et al.*, 2011) is applied, in order to investigate the impact of inter-seasonal land-cover changes in ET fluxes of the Upper Ganges (UG) river basin in India. As previously mentioned in Chapter 5, JULES does not simulate the dynamic growth of vegetation. It follows a more simplified approach, where $C_3$ grass is used as a proxy for annual crops, and which does not allow for constant evolving of parameters such as the LAI, root depth and canopy height. As expected, in a catchment where the dominant land-use type is crops, such a simplistic approach would have negative impacts on the model's performance, as differences in structural and physiological characteristics between natural and agricultural vegetation, are expected to alter the physical land surface properties and the bio-geochemical cycles.

Root depth and density determine the ability of vegetation to access moisture at each level in the soil (Best *et al.*, 2011). LAI, which illustrates the density of the leaves, is an important parameter as it contributes to the latent heat flux calculation by determining the relative fractions of ET and bare soil evaporation in vegetative surfaces (Best *et al.*, 2011). For vegetated surfaces, the maximum amount of

water that can be held by the canopy is a linear function of LAI.

Therefore, a more sophisticated approach that allows for dynamic evolving of those parameters is expected to improve representation of ET fluxes over agricultural areas.

In this Chapter, the dynamic coupling of the LSM JULES with the crop model InfoCrop (Aggarwal *et al.*, 2006a) is presented with the aim to quantify the potential error in ET flux estimations of an LSM without dynamic vegetation. The new coupled system will allow variables to vary consistently with each other along the growing season. The model is parametrised for the two main crops of the UG basin (wheat and rice) to capture well the inter-annual variations in land surface processes with subroutines that represent crop growth using a daily time step from sowing to maturity. A crop calendar based on available data was developed and added to the coupled system, informing it for the crop type, the sowing and harvest dates and the fallow land periods, allowing for 2 cropping seasons per year. In the study area (district of Uttar Pradesh), rice is predominantly rain fed and depends largely on the monsoon-season rains (June to September).

## 6.2 Data

The meteorological datasets used to force the models are summarised in Table 6.1.

**Table 6.1:** Meteorological data used to drive the models.

| Variable | Name | Resolution | Time step | Time domain | Reference |
|---|---|---|---|---|---|
| Precipitation | TRMM 3B42 v7 | $0.25° \times 0.25°$ | 3 hourly | 2000–2008 | Huffman and Bolvin (2013) |
| | MERRA GMAO | $0.50° \times 0.67°$ | 3 hourly | 2000–2008 | GMAO (2004) |
| Surface temperature, | NCEP[a] | $1.00° \times 1.00°$ | 3 hourly | 2000–2008 | Sheffield *et al.* (2006) |
| Wind speed, Radiation, Surface pressure, Specific humidity | MERRA GMAO | $0.50° \times 0.67°$ | 3 hourly | 2000–2008 | GMAO (2004) |

[a] Consist of reanalysis data that have been post-processed and merged with observations (US National Center of Environmental Predictions, Kalnay *et al.*, 1996; Sheffield *et al.*, 2006).

The reanalysis dataset from NASA's Global Modelling and Assimilation Office (MERRA GMAO, GEOS-5) was used for the development of the MODIS ET dataset (Mu *et al.*, 2011) and was chosen in this study to facilitate ET comparison between the models and the MODIS ET product.

The land-cover representation is based on the high-resolution land-cover maps developed and presented in Chapter 4 (Tsarouchi *et al.*, 2014), and based on Landsat satellite imagery.

Soil parameters were created by the UK Met Office Unified Model Central Ancillary Program (UM–CAP) at the model resolution, based on soil texture maps from the HWSD (FAO, 2009) and ISRIC[1] databases, as has already been described in Chapter 5, Section 5.3.2.

The datasets used to evaluate the model's performance are summarized in Table 6.2.

**Table 6.2:** Datasets used to evaluate JULES' performance

| Variable | Name | Resolution | Time step | Time domain | Reference |
|---|---|---|---|---|---|
| Evapotranspiration | MODIS | 1 km | daily | 2000–2008 | Mu *et al.* (2011) |
| | LandFlux-EVAL | 1° | monthly | 2000–2005 | Mueller *et al.* (2013) |
| LAI | MODIS (MOD15A2) | 1km | 8–daily | 2000–2008 | Myneni *et al.* (2002) |

All datasets were transformed to $0.1\,^\circ \times 0.1\,^\circ$ resolution grids, which is the modeling scale.

## 6.3 Study area

The study area, located in northern India, is part of the UG basin, which corresponds to the upper main branch of the river Ganges and covers an area of 87 000 $\mathrm{km}^2$ (Fig. 6.1), as previously mentioned. Because the focus of this study is on improving crop growth simulation, the model is applied only in the areas where the land-use type is agriculture. Hence, in this Chapter as study area I refer to the crop-covered areas of the UG basin, as shown in Figure 6.2 (purple colour).

## 6.4 InfoCrop model description

The functions used to calculate crop development, crop growth, LAI and root depth are based on InfoCrop (Aggarwal *et al.*, 2006a), a crop growth model which has been parametrised for Indian soils and crop systems. The model requires input meteorological time series of solar radiation, maximum and minimum air temperature, precipitation, vapor pressure and wind speed. It simulates crop development, photosynthesis, dry matter production and its partitioning, leaf area growth and ET, in response to the effects of weather, soil properties, sowing dates and crop physiology. Similarly to JULES, the Penman-Monteith

[1]Observations of soil sand, silt and clay fractions are available from the ISRIC world soil information website: www.isric.org

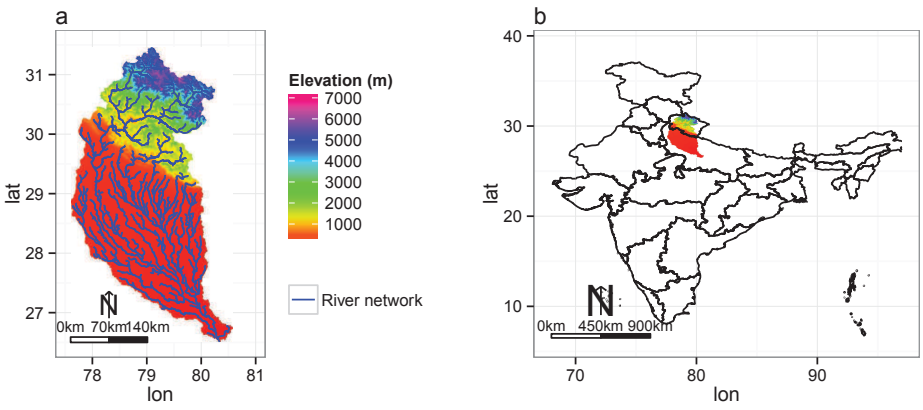


**Figure 6.1: a:** Digital Elevation Model (DEM) of the UG basin showing the ranges of the elevations (m altitude) and the river network. **b:** location map of the study area in north India.

(Monteith, 1965) approach is used to calculate potential evapotranspiration (PET). In the subsurface, the soil column is divided into 3 layers and a *tipping bucket* approach is followed for the soil water balance. Transpiration is calculated as a function of the water availability in the soil, represented by water stress factors for each soil layer. The values of water stress factors range between 0 and 1. The water contents at wilting point, critical point and saturation as well as the water content in each soil layer are required to calculate the water stress factors. Total water uptake is calculated based on the water stress factors of individual soil layers. Photosynthesis is highly sensitive to water stress. Under insufficient water supply conditions, $CO_2$ assimilation rate (photosynthesis) and stomatal conductance decrease rapidly below the potential rates.

The major photosynthesising organs are leafs. The calculation of the photosynthetically active radiation absorbed by the surface area of green leafs is highly dependent on the LAI. This highlights that for optimized crop growth modelling, the most essential requirement is a correct simulation of the time course of LAI. After crop emergence, the main parameters affecting leaf area expansion are temperature and light intensity. In the early stage of juvenile growth, the increase of leaf area over time is approximately exponential. During later development stages, shading from other plant branches might restrict the leaf area expansion. Apart from shading, the senescence of leaves in InfoCrop is also dependent on ageing, nitrogen mobilization, temperature, water stress and death due to pests and diseases (Aggarwal *et al.*, 2006a).

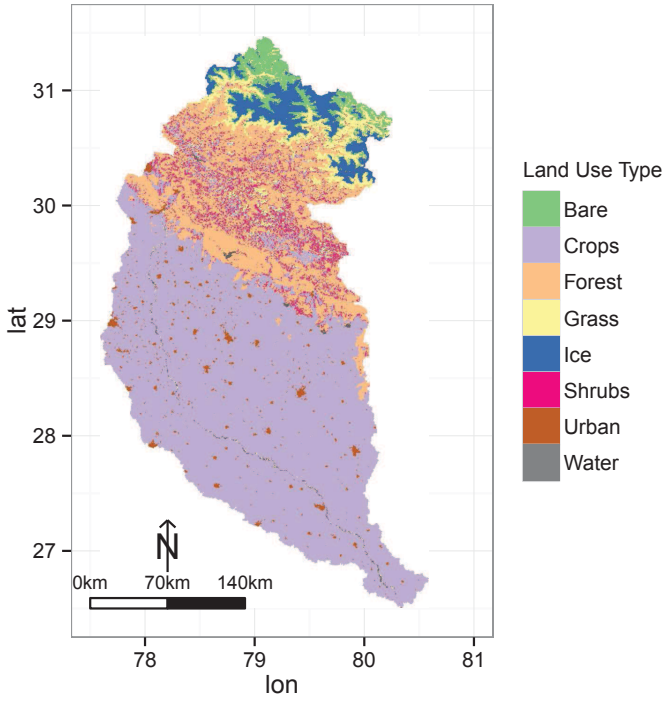


**Figure 6.2:** Land-cover map for year 2000, as developed by Tsarouchi *et al.* (2014).

In InfoCrop, canopy interception is assumed to be equivalent to 25% of the value of LAI at any given time (Penning de Vries *et al.*, 1989).

Root depth extension rate is affected by soil water stress, soil bulk density, potential maximum rooting depth and temperature (low temperatures reduce growth). The maximum rooting depth varies as a function of thermal time to anthesis; the longer the crop duration the deeper the roots would go in the soil. If the roots reach a soil layer with moisture content at or below wilting point, root growth is interrupted. Moisture content near wilting point causes a very low water uptake rate and that leads to insufficient energy production for maintenance respiration by photosynthesis. In such case the crop dies. Otherwise, root growth continues until a crop-specific development stage.

The model separates between 3 development stages: a) seedling emergence, b) anthesis and c) maturity. Under temperate climate conditions, the development rate is mainly affected by temperature.

For a more detailed description of the model see Aggarwal *et al.* (2006a).

## 6.5 Model Coupling

The distributed version of JULES was run with a resolution of $0.1^\circ$ and an hourly time step while InfoCrop was run at a daily time step. To ensure agreement in calculations, the same meteorological and soil datasets were used for both models.

In the coupled version, the full energy balance scheme of JULES was used to calculate water exchange between soil layers, land–atmosphere heat flux exchange, ET etc. in each time step. Every 24 time steps of JULES (i.e. 1 day), the following values (daily averaged) were passed to the crop model: moisture content, ET, volumetric water content at critical point, at saturation and at wilting point, (of each soil layer), and plant net photosynthetic uptake. The crop model then simulated the agricultural practices, processes such as crop growth, dry matter production and partitioning and provided daily values of LAI, root depth and canopy height. These values were returned to JULES, which continued to the next day of the simulation (Fig. 6.3 presents a schematic of the coupled system). In this configuration of JULES the soil carbon content is not varied. The soil column of InfoCrop is transformed into a 4-layer column, to match exactly the equivalent one of JULES. The coupled JULES-InfoCrop model will be hereafter referred to as JULES-Info and the original JULES model will be hereafter referred to as JULES-base.

Based on a crop calendar review (Agropedia, 2013; NFSM, 2013; USDA-I, 2013; FAO, 2013; ICAR, 2013), I concluded that the main crops grown in the study area (district of Uttar Pradesh) are rice during the summer months (July–October) and wheat during the winter months (October–March). Therefore, the JULES-Info model was parametrized for those crops, (following the parameters suggested by the developers of InfoCrop Aggarwal *et al.*, 2006a,b), under a two-crop rotation system and a crop calendar was added to the coupled model. Table 6.3 shows the different parameters used by JULES-Info for rice and wheat.

Canopy height is calculated based on Eq. (61) in Clark *et al.* (2011), where $W$ is the carbon content of the stems, calculated by the crop model.

In JULES-base, the $\mathrm{C}_3$ photosynthesis model (Collatz *et al.*, 1991) is a function of the maximum rate of carboxylation of Rubisco, $V_\mathrm{m}$ (HCTN24, 2001, Eqs. 43, 45 and 51). $V_\mathrm{m}$ is a function of the potential maximum carboxylation rate at 25 °C, $V_\mathrm{max}$. In JULES-base, for $\mathrm{C}_3$, $V_\mathrm{max} = 0.0008 \times n_\mathrm{l}$, where $n_\mathrm{l}$ is the

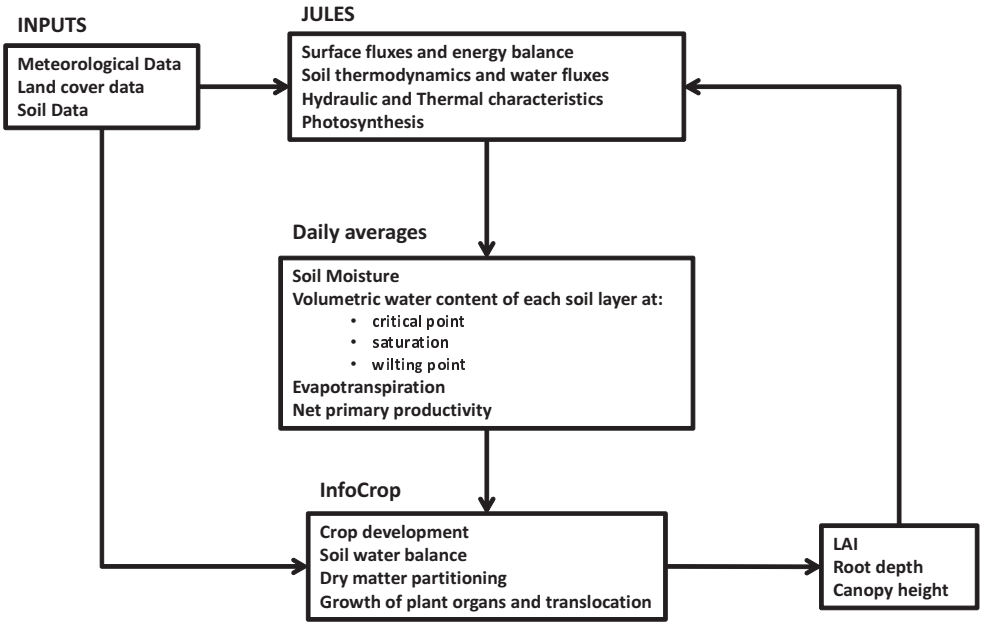


**Figure 6.3:** Flow chart of the coupling system for JULES and InfoCrop models.

leaf nitrogen concentration. In the JULES-Info model the following adaptation was made:

$$V_{max} = \begin{cases} 0.0008 \times n_l, & \text{wheat} \\ 0.00036 \times n_l, & \text{rice} \end{cases} \tag{6.1}$$

since $V_{max}$ of rice is $45\%$ lower than that of wheat (Mitchell and Hardy, 2000).

In JULES-base, the surface infiltration rate $K$ is equal to $\beta_s \times K_s$; Where $K_s$ is the soil saturated hydrological conductivity and $\beta_s$ an enhancement factor (Best *et al.*, 2011). The default value of $\beta_s$ for $C_3$ grass in JULES-base is 2. For the other PFTs, $\beta_s$ is 4 for trees and 2 for $C_4$ grass and shrubs. However, and as also suggested by Van den Hoof *et al.* (2013), no justification can be found for different $\beta_s$ values between different PFTs, therefore, in JULES-Info the value of $\beta_s$ was set equal to 1 for all PFTs.

In JULES-Info, canopy capacity is calculated through an adaptation of the formulas used in JULES-base and InfoCrop, as follows:

$$C_m = 0.05 + 0.25LAI \tag{6.2}$$

**Table 6.3:** JULES-Info parameters for wheat and rice

| Parameters | Wheat | Rice | Units |
|---|---|---|---|
| Optimal temperature | 25 | 30 | °C |
| Maximum temperature | 40 | 42 | °C |
| Base temperature for sowing to germination | 3.6 | 7.6 | °C |
| Thermal time for sowing to germination | 70 | 50 | °C × days |
| Base temperature for germination to 50% flowering | 4.5 | 10 | °C |
| Thermal time for germination to 50% flowering | 800 | 1650 | °C × days |
| Base temperature for 50% flowering to maturity | 7.5 | 10 | °C |
| Thermal time for 50% flowering to maturity | 373 | 430 | °C × days |
| Relative growth rate of leaf area | 0.005 | 0.009 | $\text{days}^{-1}$ |
| Specific leaf area | 0.0020 | 0.0022 | Ha leaf $\text{kg}^{-1}$ leaf |
| Root extension growth rate | 25 | 12 | mm/d |
| Maximum root depth | 2000 | 400 | mm |
| Index of storage organs formation* | 30000 | 56000 | No/kg dry matter |
| Potential weight of the storage organs | 42 | 22 | mg/storage organ |
| Nitrogen content of storage organ | 2 | 1.4 | % |

* Index of storage organs formation: Slope of the relationship between storage organs number $\text{m}^{-2}$ and dry matter accumulated during their formation stage.

This adapted formulation is more in line with the equation suggested by Van den Hoof *et al.* (2013), after taking into account what is used in other LSMs and review papers. The new formula is expected to increase canopy capacity dependence by LAI (Van den Hoof *et al.*, 2013).

InfoCrop calculates dry matter production as a function of the Radiation Use Efficiency (RUE) (Aggarwal *et al.*, 2006a). In contrast, JULES-base follows a biochemical approach, which links the calculation of the leaf level stomatal conductance to the net photosynthetic uptake via a $CO_2$ diffusion equation (Best *et al.*, 2011). Because in the coupled scheme, the ET calculation mechanism of JULES-base is maintained, it is sensible that the photosynthesis is calculated from JULES-base as well. In JULES-Info, the dry matter production is no longer calculated as a function of RUE (according to InfoCrop) but is based on the net primary productivity (structural dry matter) as calculated by the LSM's photosynthesis scheme.

Irrigation in the coupled model has not been included yet and possible impacts of this simplification are discussed in the Results Section.

## 6.6 Model Experiments

The simulations were performed over the study area for a period of 9 years between 2000 and 2008 to coincide with the periods of available data from NCEP, TRMM, GMAO and MODIS.

Four different model simulations were performed: (a) JULES-base driven with the GMAO meteorological dataset; (b) JULES-base driven with TRMM precipitation data and the post-processed NCEP dataset for the rest meteorological variables; (c) JULES-Info driven with the GMAO meteorological dataset; (d) JULES-Info driven with TRMM precipitation data and the post-processed NCEP dataset for the rest meteorological variables.

The JULES-base simulations were run with $\mathrm{C}_3$ crop parameterisation, whilst the JULES-Info simulations were run with dynamic crop growth parameterisation, where its interactions with the environment were simulated.

To quantify the uncertainty in the ET results derived by an LSM with no dynamic vegetation and the impact of the applied changes, LAI and ET output values were validated against the equivalent MODIS and LandFlux-EVAL products. Performance scores tested include the correlation coefficient ($\mathrm{r}$), the coefficient of determination ($\mathrm{R}^2$), the Root Mean Squared Error ($\mathrm{RMSE}$) and the Mean Error.

## 6.7 Results

The sensitivity of JULES was evaluated with respect to the daily and seasonal dynamics of the vegetation cover in the study area. When the model runs without a dynamic vegetation growth scheme, it assumes 100 % agricultural coverage throughout the entire simulation period. There is no information about seedling, emergence or harvesting dates, nor about the duration of fallow land periods between different cropping seasons. In addition, it is assumed that the cultivated crop is a generic $\mathrm{C}_3$ grass. However, when the model is coupled with the crop growth model (and hence dynamic vegetation growth is included), the seedling, emergence and harvesting dates are defined, fallow land periods are included in the simulation and a two crop rotation scheme (wheat vs. rice) is introduced, with different parameterisation for each crop (Table 6.3).

The MODIS LAI is compared with the JULES-Info (forced by the two different meteorological

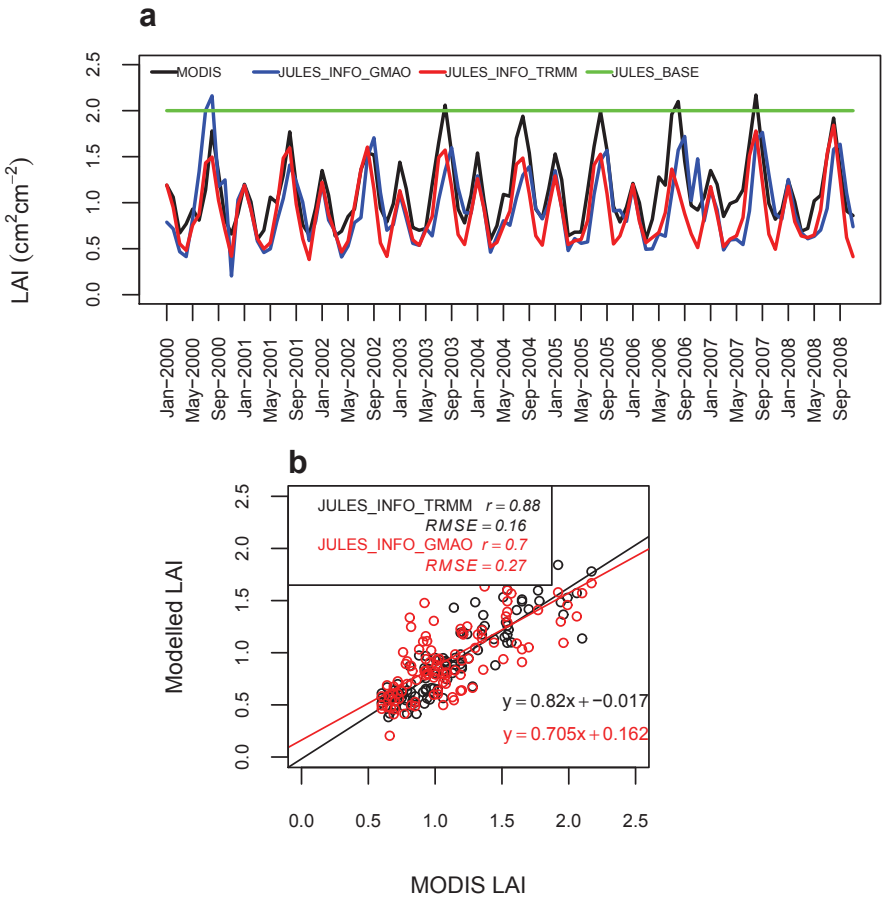


**Figure 6.4: a:** the MODIS LAI is compared with the JULES-Info (forced by the two different meteorological datasets) modelled LAI. JULES-base was run with its default LAI value set to 2 for crops. **b:** performance scores JULES-Info with TRMM and GMAO forcing datasets. The results show that the modelled LAI matches the observed MODIS LAI well. The two peaks per year represent the two cropping seasons as specified by the crop calendar.

datasets) modelled LAI as shown in Fig. 6.4a. JULES-base was run with its default LAI value set to 2 for crops. The results show that the modelled LAI matches the observed MODIS LAI well. The correlation coefficients for TRMM and GMAO forcing datasets are $r = 0.88$ and $r = 0.70$ respectively and the RMSE values are RMSE $= 0.16$ and RMSE $= 0.27$ respectively (Fig. 6.4b). The two peaks per year represent the two cropping seasons as specified by the crop calendar. The reduced LAI values as calculated by the JULES-Info model in comparison to the steady value of LAI $= 2$ used by the JULES-base model are reducing the canopy storage, which is directly translated into a reduced canopy interception. This is expected to cause a decrease in the total ET estimation.

The ET results show that JULES is sensitive to the changes introduced after coupling it with the crop model. In the JULES-base version, ET fluxes are often higher in comparison to the JULES-Info version results (Figs. 6.5, 6.7 & 6.8), as was previously discussed in Chapter 5. There is a significant difference especially when the dry and the fallow land periods are simulated. JULES-base is overestimating ET as it simulates a false land cover with 100 % agriculture that indeed evaporates more than the bare soil does. Figure 6.5 shows that JULES-base, after the wet season peak in ET, reproduces a second lower peak in month October of years 2003–2005. However, JULES-Info in agreement with MODIS and LandFlux-EVAL (Fig. 6.12) does not reproduce that 2nd peak. This behaviour of JULES-base is possibly related to a combination of precipitation and temperature patterns as well as the fact that it operates under a constant LAI of 2. On the other hand, for JULES-Info, October is a month with very low LAI values (near 0.5), as it is the transition period between rice harvesting and wheat planting according to the developed crop calendar (Fig. 6.4a). In addition, JULES-Info matches better the MODIS and LandFlux-EVAL fluctuation and timing of the peak values (Figs. 6.5 and 6.12a). In both plots, the modelled by JULES-base ET is higher than the MODIS ET. JULES-base tends to overestimate ET mainly during the dry period because then the difference between the default LAI value of 2 and the actual LAI value of the growing crop (wheat) is larger. This is also clearly illustrated on Figs. 6.5b and 6.5d which show the mean seasonal cycle of ET($\mathrm{mm\,month^{-1}}$) and give an approximation of the mean bias per month for each of the models. As already discussed in Chapter 5, similar trends of ET overestimation have been observed by Van den Hoof *et al.* (2011) and Blyth *et al.* (2010), who suggest that these errors occur mainly due to the simple approach of using a fixed, predetermined LAI. Therefore and as expected, the more sophisticated approach of JULES-Info, which calculates LAI evolution on a daily basis, offers improved accuracy. The coupled model captures better the seasonal variability of ET. An overall decrease in the modelled ET (Figs. 6.5, 6.7 & 6.8) compared to MODIS ET is observed. $\mathrm{R}^2$ values are significantly improved compared to the JULES-base equivalent values and RMSE values are reduced (Fig. 6.6): $\mathrm{R}^2$ increased from $0.77$ to $0.90$ under GMAO forcing data and from $0.71$ to $0.87$ under TRMM/NCEP data. RMSE decreased from $16.27$ to $10.53$ under GMAO forcing data and from $14.78$ to $11.27$ under TRMM/NCEP data.

Similar information arises from the spatial comparison of the modelled ET with the MODIS product shown in Figs. 6.7 & 6.8, for wet and dry periods respectively (TRMM forcing). Within the JULES-base

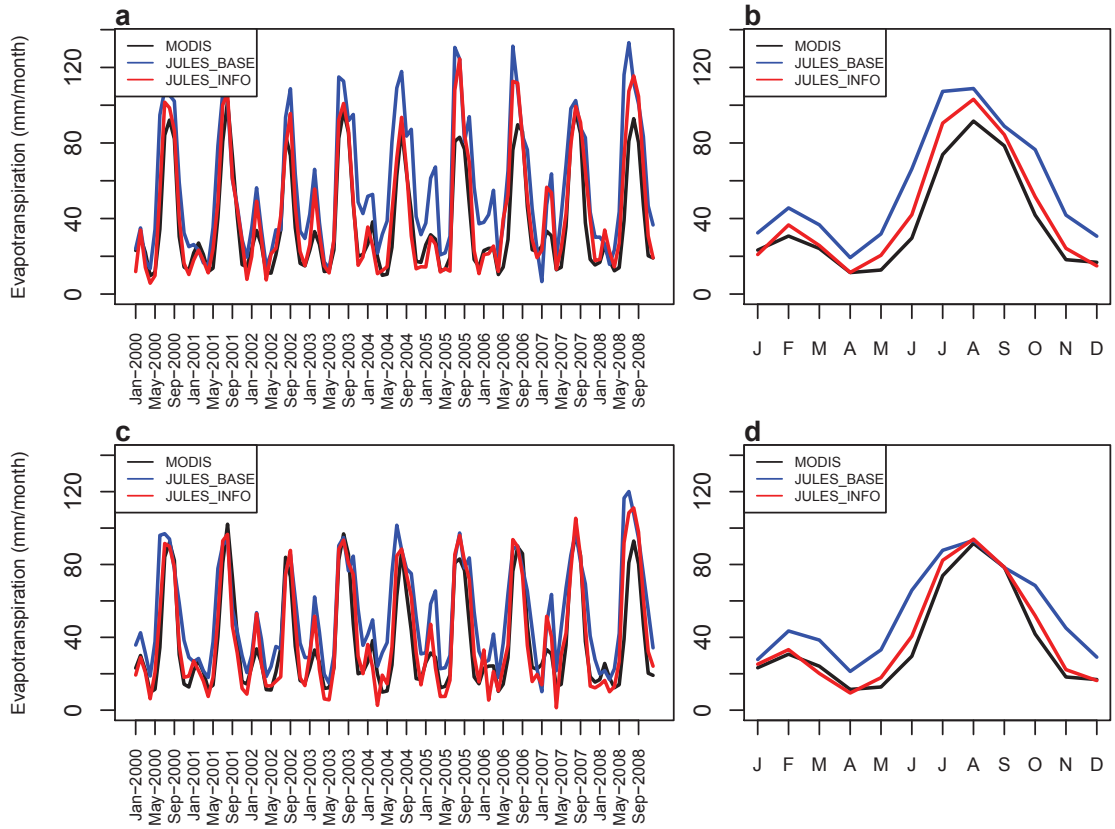


**Figure 6.5:** Comparison between MODIS ET and simulated ET by the two models: JULES-base and JULES-Info. Figs. a & b are with GMAO forcing data and Figs. c & d with TRMM and NCEP forcing data. The right-hand plots (b & d) show the mean seasonal cycle of Evapotranspiration ($\mathrm{mm\,month^{-1}}$) for each of the models, showing the mean bias per month.

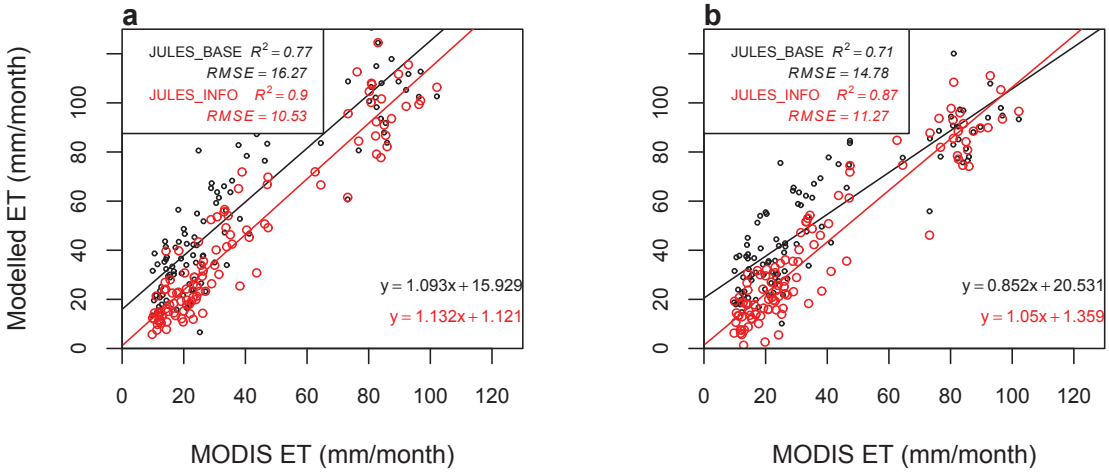


**Figure 6.6:** Performance scores of the two models (JULES-base and JULES-Info) in comparison with MODIS ET. Fig. a is with GMAO forcing data and Fig. b with TRMM and NCEP forcing data.

and JULES-Info models the spatial ET variations are attributable to differences in soil parameters, precipitation and other meteorological variables aside from the vegetation parameters, however it is evident that JULES-Info generates lower ET values that match better the MODIS values, compared to JULES-base.

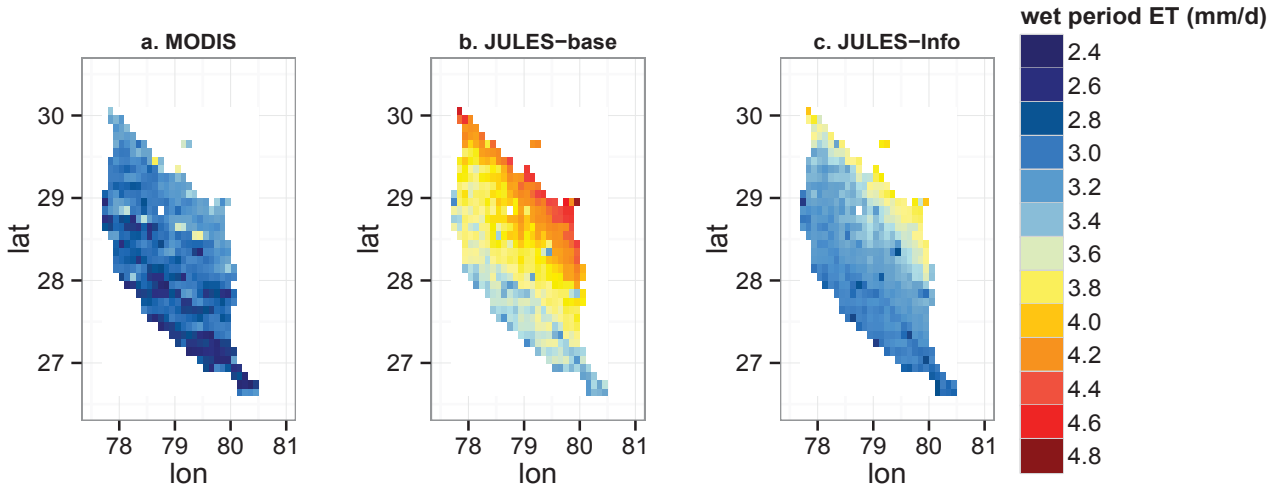


**Figure 6.7:** Spatial comparison of the modelled ET with the MODIS product, for agricultural areas, averaged over the wet (June–September) months of years 2000-2008.

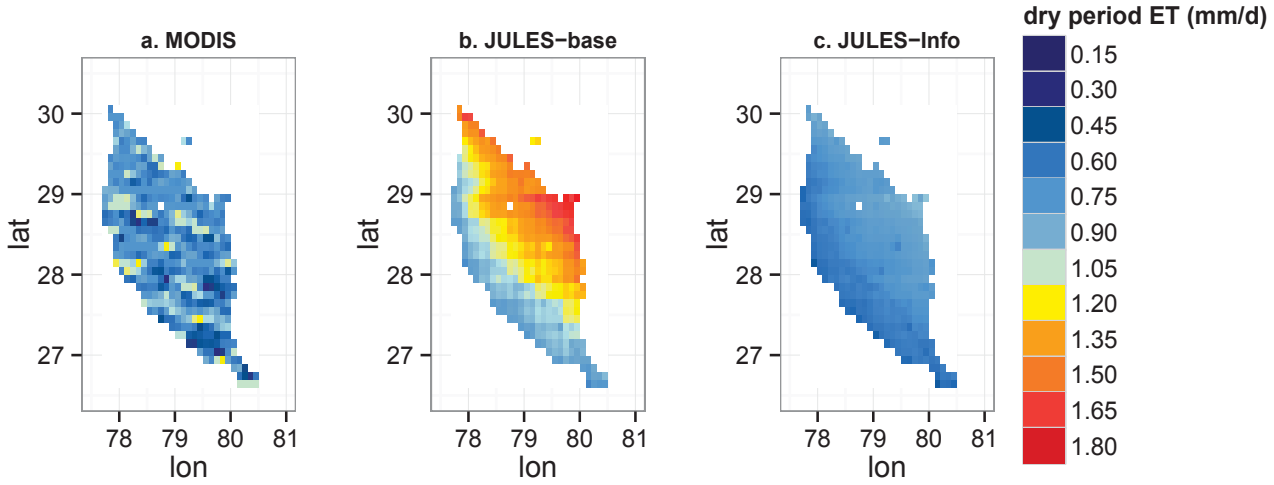


**Figure 6.8:** Spatial comparison of the modelled ET with the MODIS product, for agricultural areas, averaged over the dry (October–May) months of years 2000-2008.

Looking at the mean annual ET in the study area (Fig. 6.9), JULES-Info is matching quite well the equivalent MODIS annual ET, whereas JULES-base constantly appears to generate higher values.

The mean difference in annual ET between JULES-base and JULES-Info is $140\,\mathrm{mm\,yr^{-1}}$ under TRMM precipitation and $160\,\mathrm{mm\,yr^{-1}}$ under GMAO precipitation. The mean difference in annual ET between JULES-base and MODIS is $179\,\mathrm{mm\,yr^{-1}}$ under TRMM precipitation, whereas the equivalent value between JULES-Info and MODIS is $39\,\mathrm{mm\,yr^{-1}}$. The same figures under GMAO precipitation show the same magnitude of difference ($233\,\mathrm{mm\,yr^{-1}}$ difference between JULES-base and MODIS and $73\,\mathrm{mm\,yr^{-1}}$ difference between JULES-Info and MODIS). Those results indicate a high sensitivity of the model with respect to vegetation dynamics.

In Figs. 6.10 and 6.11 the results are partitioned into wet (June–September) and dry (October–May) periods. $\mathrm{R}^2$ and RMSE values are significantly improved during the wet period (Fig. 6.10), when the highest ET rates are being noticed in the study area. However, as shown in Fig. 6.11, which illustrates the magnitude of the Mean Error for both the wet and dry seasons, the main improvement caused by JULES-Info occurs during the dry period, as the model is no longer constantly overestimating ET. In all cases JULES-Info achieves lower Mean Error values than JULES-base does.

Figure 6.12 shows the comparison of the modelled ET with the LandFlux-EVAL product. Similar behaviour is observed here as well. Coefficient of determination with JULES-Info is $\mathrm{R}^2 = 0.82$ and is improved compared to the JULES-base equivalent value ($\mathrm{R}^2 = 0.72$). A noteworthy trend observed here is that during the spring season, both JULES-base and JULES-Info are underestimating ET when compared to the LandFlux-EVAL product. A possible explanation for this could be the fact that irrigation is not accounted for. Different land-cover maps, or forcing meteorology used by the LSMs that contributed in the calculation of LandFlux-EVAL ET could be related as well. However, looking at the wet period ET, JULES-Info provides significantly improved results compared to JULES-base ($\mathrm{R}^2$ increased from $0.61$ to $0.77$).

As shown in Fig. 6.13 (source: USDA-II, 2013) most of the wheat that grows in the study area is rain-fed. In addition, according to USDA-I (2013), rice in the district of Uttar Pradesh is predominantly rain fed and depends largely on the monsoon season rains from June to September. Therefore, the simplification of not accounting for irrigation is not expected to affect significantly the results during the dry period. Furthermore, in JULES transpiration only occurs from the dry fraction of the canopy, which during and after a rain event is a very small part of the canopy. That means that transpiration during the wet season is not expected to change significantly, even if irrigation was applied, since the dry portion of the

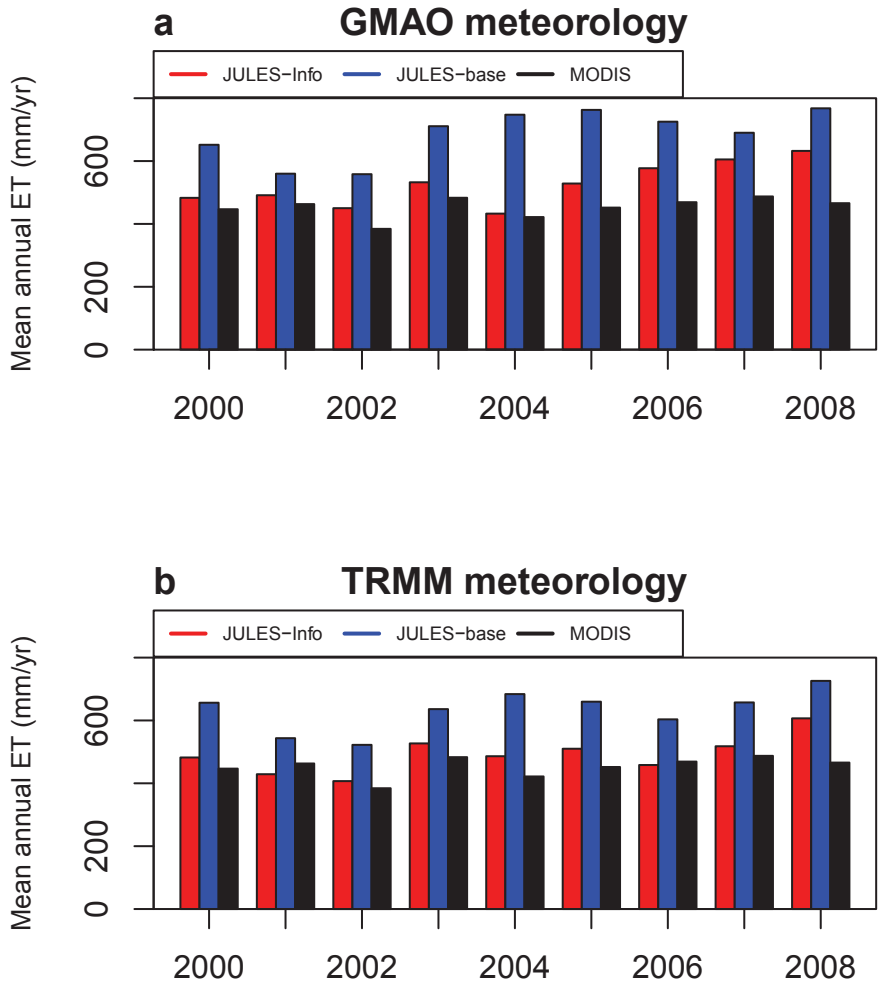


**Figure 6.9:** Comparison of the mean annual ET within the study area, as derived from JULES-base, JULES-Info and MODIS.

canopy that transpires will remain the same. Nevertheless, it is possible that incorporation of irrigation in the coupled model will increase soil evaporation. The application of irrigation in the wet (dry) season could also have an impact in the dry (wet) season ET, as the soil moisture stores could be higher.

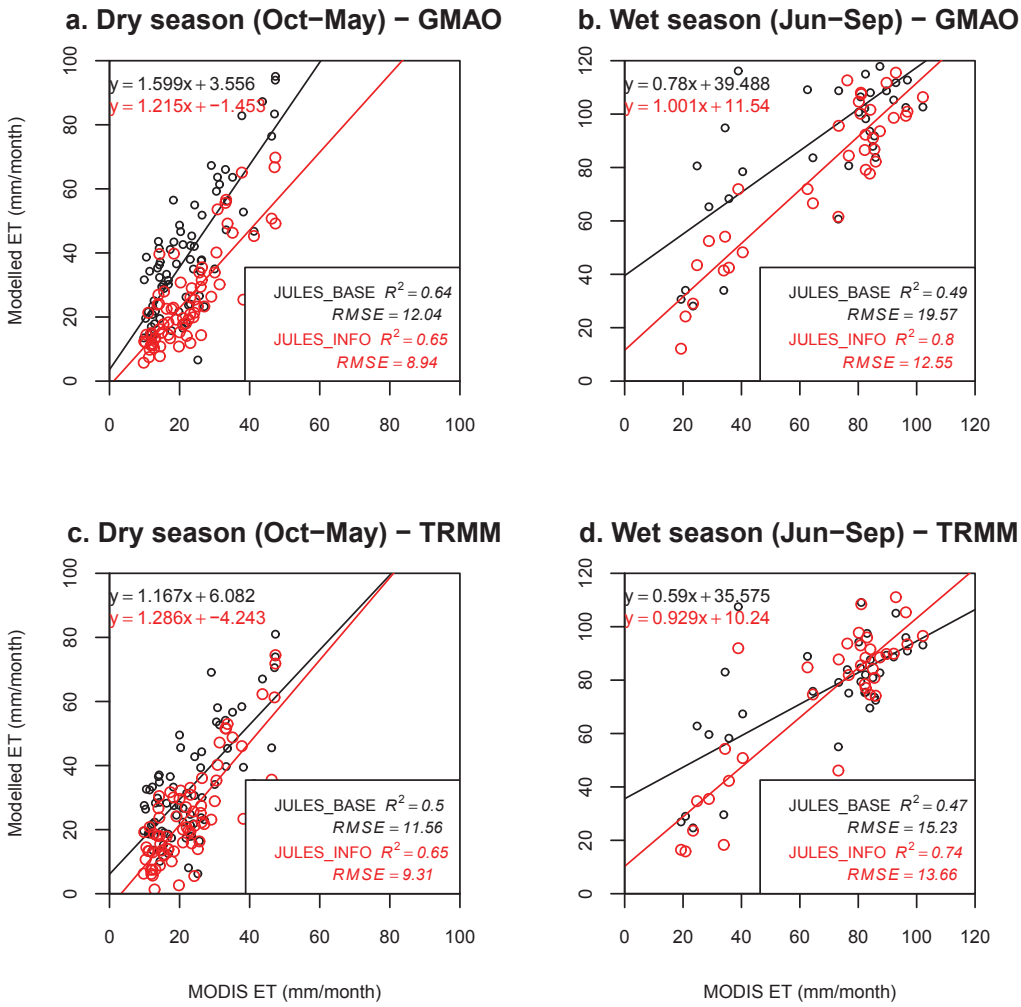


**Figure 6.10:** Results showing coefficient of determination ($R^2$) and RMSE values are partitioned into wet (June–September) and dry (October–May) periods.

## 6.8 Chapter Summary

The objective of this Chapter was to quantify the potential error in ET flux estimations of an LSM without dynamic vegetation. For this reason, the full energy, water and carbon balance scheme of JULES (which describes the exchange between atmosphere - surface - subsurface water fluxes) has been coupled to the crop growth model InfoCrop, which represents the crop development and other physiological processes. The model has been parameterized for wheat and rice, the two main crops of the study area, in a two crop rotating system. A crop calendar was added to the coupled system.

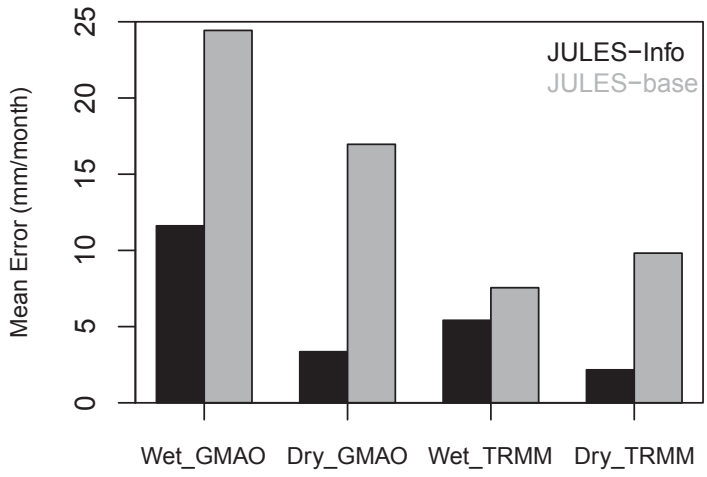


**Figure 6.11:** Mean error showing the discrepancy between both versions of JULES and MODIS ET.

The results show that JULES is sensitive to the changes applied and the incorporation of crop dynamics in the model significantly alters the ET fluxes. An overall reduction is observed in the simulated ET fluxes of the JULES-Info model compared to the original JULES-base model. The seasonal patterns of ET as simulated by JULES-Info match better the MODIS and LandFlux-EVAL ET products than JULES-base does. The difference in mean annual ET between JULES-base and JULES-Info is approximately $150\ \mathrm{mm/yr}$ and can be considered as an indication of the potential error in surface flux estimations of LSMs that do not include vegetation dynamics.

Improving the estimation of energy and water fluxes over croplands through a more accurate description of vegetation dynamics is crucial for projecting potential changes in the hydrological cycle under different climate change scenarios. Increased accuracy of ET estimations is an important step towards a better understanding of the temporal dynamics of climate-surface-groundwater fluxes as a function of agricultural production and inter-seasonal land-cover change; while at the same time is vital for advanced irrigation practices under a water-limited environment.

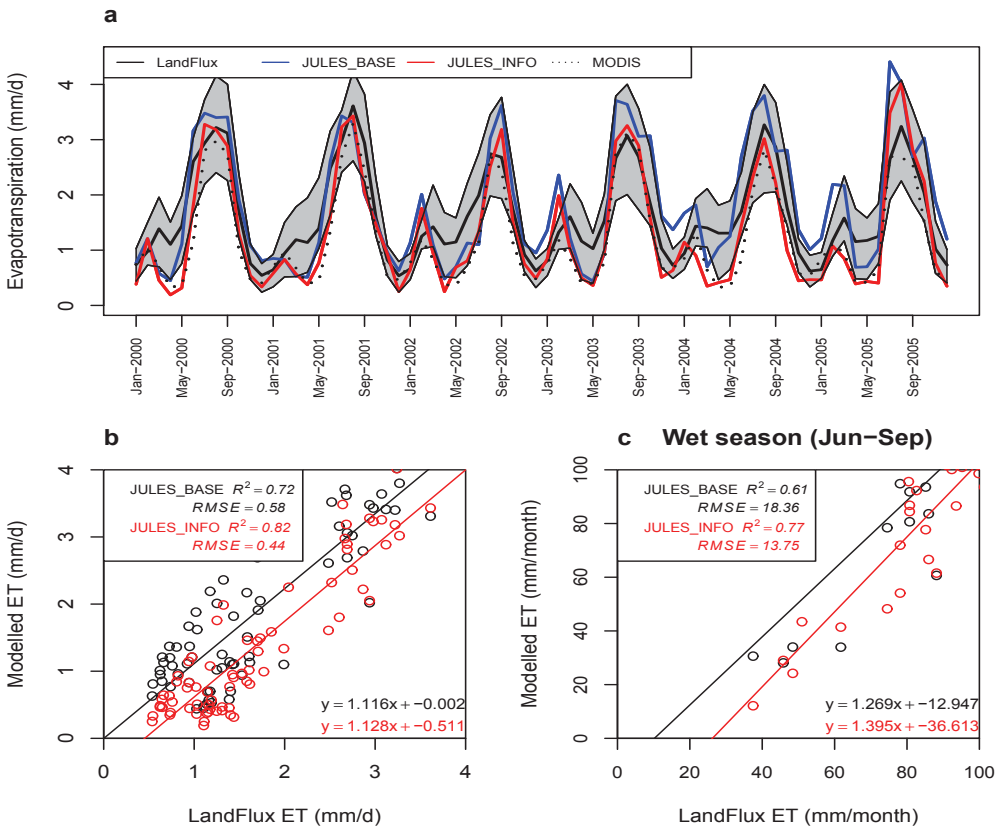


**Figure 6.12: a:** comparison of the modelled ET with the LandFlux-EVAL product. The shaded area corresponds to the values between the 25th and 75th percentiles of the distribution. **b:** performance scores of the two models (JULES-base and JULES-Info) in comparison with LandFlux-EVAL ET. **c:** results and performance scores only for wet (June–September) period.

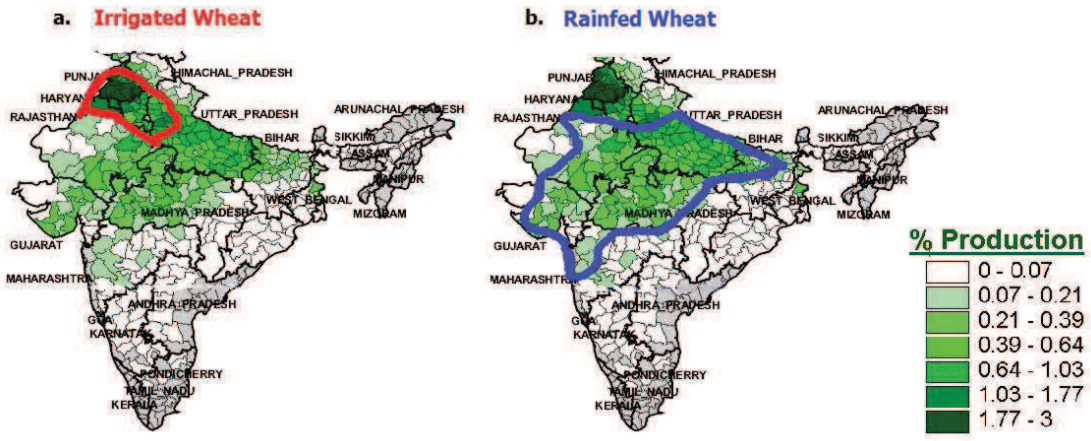


**Figure 6.13:** Map a is showing the irrigated wheat growing areas of India. Map b is showing the rain-fed wheat growing areas. Based on the location of the study area as shown in Fig. 6.1, most of the wheat grown in the UG basin is rain-fed. Source: Adapted from USDA-II (2013).

# Chapter 7

# Comparing Climate change and Land use change as drivers of hydrological change

# Comparing climate change and land-use change as drivers of hydrological change

## 7.1 Introduction

Quantifying how land-use changes and climate change affect hydrological components is a challenge in hydrological science. The Upper Ganges (UG) river basin experiences almost every year monsoon flooding. Studies have shown that there is evidence of strong coupling between the land surface (soil moisture) and atmosphere (precipitation) in north India, which means that regional climate variations and changes in landscape are influencing the temporal dynamics of land-atmosphere interactions. This Chapter aims to quantify how land-use and climate change future projections are affecting the hydrological response of the UG river basin. Future scenarios of land cover were produced for years up to 2035 using Markov chain analysis (as described in Chapter 4). Climate change scenarios were derived from downscaled CMIP5 data from 21 participating models. The LSM JULES was run under different future land-cover and climate change scenarios, to obtain hydrological projections for the UG basin.

Variations in hydrological components (stream flow, evapotranspiration and soil moisture) are calculated during the simulation period. Significant differences on the nearby-future hydrologic fluxes arise under future land-cover and climate change scenarios pointing towards a severe increase in high extremes of flow. The changes in all examined hydrological components are greater in the combined land-use and climate change scenario.

The results are further presented in a water resources context, aiming to address potential implications of climate change from a water demand perspective, discussing whether it is likely that demand thresholds in the UG region will be exceeded in the future.

**Table 7.1:** CMIP5 model output used and data resolution

| Model | Centre | Spatial Resolution (Lon x Lat) | Country |
|---|---|---|---|
| ACCESS1-0 | CSIRO-BOM | 1.88°x 1.25° | Australia |
| ACCESS1-3 | CSIRO-BOM | 1.88°x 1.25° | Australia |
| BCC-CSM1-1-M | BCC | 1.13°x 1.13° | China |
| BNU-ESM | BNU | 2.81°x 2.81° | China |
| CanESM2 | CCCma | 2.81°x 2.81° | Canada |
| CNRM-CM5 | CNRM-CERFACS | 1.41°x 1.41° | France |
| CSIRO-Mk3-6-0 | CSIRO-QCCCE | 1.88°x 1.88° | Australia |
| INM-CM4 | INM | 2.00°x 1.50° | Russia |
| IPSL-CM5A-LR | IPSL | 3.75°x 1.88° | France |
| IPSL-CM5A-MR | IPSL | 2.50°x 1.26° | France |
| IPSL-CM5B-LR | IPSL | 3.75°x 1.88° | France |
| MIROC4h | MIROC | 0.56°x 0.56° | Japan |
| MIROC5 | MIROC | 1.41°x 1.41° | Japan |
| MIROC-ESM | MIROC | 2.81°x 2.81° | Japan |
| MIROC-ESM-CHEM | MIROC | 2.81°x 2.81° | Japan |
| HadGEM2-CC | MOHC | 1.88°x 1.25° | UK |
| HadGEM2-ES | MOHC | 1.88°x 1.25° | UK |
| MRI-CGCM3 | MRI | 1.13°x 1.13° | Japan |
| GFDL-CM3 | NOAA-GFDL | 2.50°x 2.00° | US |
| GFDL-ESM2G | NOAA-GFDL | 2.50°x 2.00° | US |
| GFDL-ESM2M | NOAA-GFDL | 2.50°x 2.00° | US |

## 7.2 Data

Atmosphere-Ocean General Circulation Model (AOGCM) outputs from the fifth phase of the Coupled Model Intercomparison Project (CMIP5) were obtained through the BADC server. All meteorological variables required by JULES were acquired from the historical, RCP4.5 and RCP8.5 experiments of 21 CMIP5 models shown in Table 7.1.

For the future scenarios of land-use change, maps for years up to 2035 were developed following the method described in Chapter 4. Figure 7.1 highlights the uncertainties between these 15 future scenarios for the year 2035 and how their land-cover proportions compare to the historic year 2010. The variations between the different scenarios are not large and the main trends of change identified are forest growth, urbanisation, and on the other hand loss of bare soil, grasslands and shrubs.

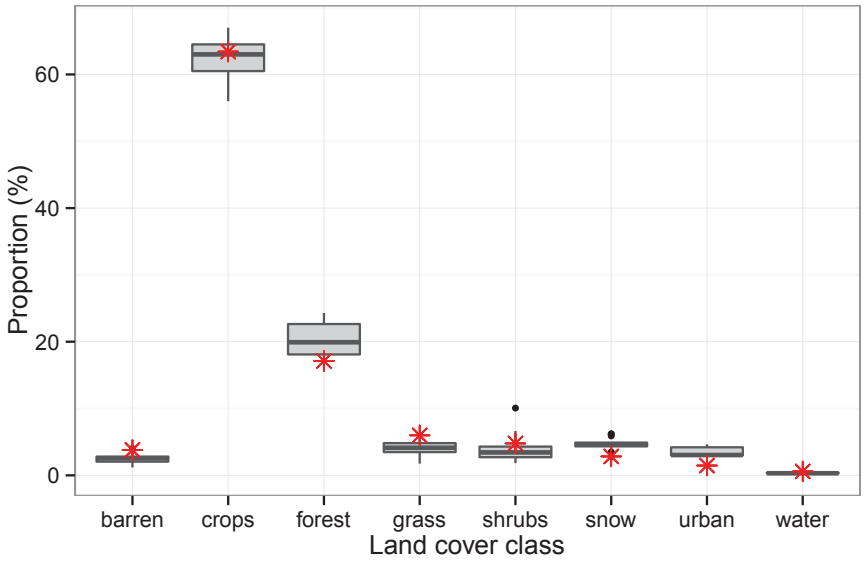


**Figure 7.1:** Box plots indicating land-cover trends with uncertainties for year 2035, as developed by applying Markov chain analysis. With red colour are illustrated the actual land-cover proportions of year 2010, as derived from the Landsat classifications. The middle bar of each box shows the median, while the bottom and top of the box bars show the $25^{\text{th}}$ and $75^{\text{th}}$ percentiles (or first and third quartiles), respectively. The upper and lower whiskers extend to the highest and lowest values that are within $1.5 \times \text{IQR}$ of the box's top and bottom bars, where IQR is the inter-quartile range. Dots show values beyond the end of the whiskers.

## 7.3 Methods

As previously mentioned, the CMIP5 precipitation projections are likely to provide unreliable estimates of the mean values and daily variations of precipitation due to inherent limitations of the GCMs (Raty *et al.*, 2014). Biases have already been identified in simulating the present-day observed Indian summer monsoon climatologies (Sengupta and Rajeevan, 2013). Further, Lutz *et al.* (2014) found large uncertainties and variations between the annually averaged and seasonal precipitation projections over the UG basin. Therefore, a simple bias correction technique, the delta-change method, was applied to diminish the impacts of GCM biases. This is a relatively simple approach that calculates the change in time between the control and future simulations of a variable and applies this change in the baseline (observed) climate by simply adding or scaling the mean climatic change factor (CF) to each day (Fowler *et al.*, 2007). This change is relative change for fluxes in order to avoid negative values, and absolute change

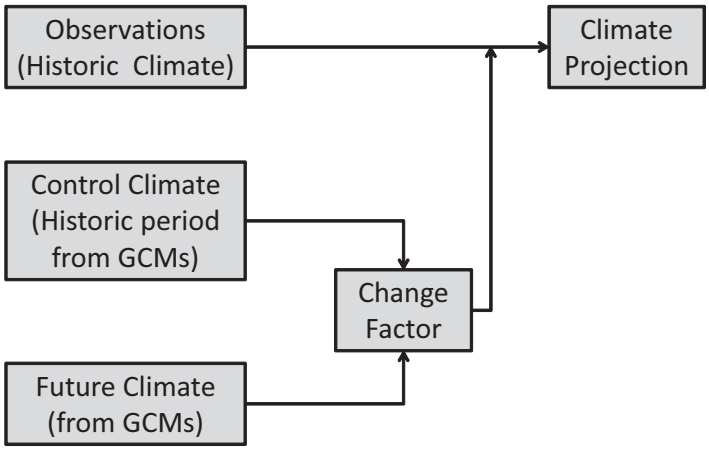


**Figure 7.2:** Flow chart of Delta Change method.

for state meteorological variables. So, for precipitation, radiation and wind speed the monthly CF is calculated as:

$$CF = \frac{\bar{V_{fut}}}{\bar{V_{hist}}} \tag{7.1}$$

Where $\bar{V}$ the monthly climatological mean for a given flux variable. For temperature, pressure, and specific humidity, which are state variables, the CF is calculated as:

$$CF = \bar{V_{fut}} - \bar{V_{hist}} \tag{7.2}$$

As baseline climate, I used the TRMMv7 precipitation product and for the rest meteorological variables the NCEP reanalysis product. The mean climatic CFs were based on monthly-mean climatological conditions over 6-year time slices from 2000 to 2035 and were used to rescale the historical observations at the daily time-scale. For a flow chart describing the method see Figure 7.2. The CFs were further interpolated in the 0.1 degree resolution of the modelling setup.

The next step was to force JULES with the bias corrected GCM model outputs and generate future hydrological projections for the UG basin that go up to year 2035. Two different sets of modelling experiments were run: In the first one, only climate change was taken into account, as JULES was driven by the CMIP5 outputs of 21 models, under two emission scenarios (RCP4.5 & RCP8.5), but land use

was kept constant to historic year 2010. In the second set, both climate change and land-use change were taken into consideration, as apart from the CMIP5 model outputs, JULES was also forced by a time-series of future land-use scenarios.

The impact of both climate change and land-use change on the future hydrological variables of the study area is examined.

## 7.4 Results

### 7.4.1 CMIP5 Projection analysis

A basic analysis of the monthly precipitation climatologies for the UG basin reveals large variations between the different GCM derived precipitation datasets (Fig. 7.3). Interestingly, there are models that are not able to capture at all the seasonal cycle and the summer monsoon precipitation, but instead reproduce a flat annual climatology. This illustrates the large uncertainties that these datasets are accompanied with and questions the ability of some of the models to represent the present-day climate. However, this is no straightforward indicator of their ability to generate reasonable future climate projections.

The spatial patterns of precipitation change between the periods 1975–2005 and 2070–2100 are shown in Figure 7.4. For the summer monsoon period (JJA), the multi-model mean (MMM) pattern of future projections is pointing towards a precipitation increase of around 10-20% throughout India under scenario RCP4.5. As expected, under scenario RCP8.5, which corresponds to stronger radiative forcing, the precipitation increase is stronger (around 50%). However, opposite trends are observed for the dry period (DJF), as the MMM is projecting a decrease in precipitation over areas of northern India (where the study area is located), which again is stronger under RCP8.5. This means that an amplification of the annual cycle is being projected for the end of the century, with stronger wet and dry seasons.

Figure 7.5 shows the spatial patterns of temperature change between the periods 1975–2005 and 2070–2100. The projections indicate a robust signal of temperature increase in all examined periods and under both emission scenarios. The temperature increase ranges from 2 to 4°C under RCP4.5 and from 4 to 6°C under RCP8.5.

A way to compute the relative skill of the CMIP5 models used in this study and estimate which

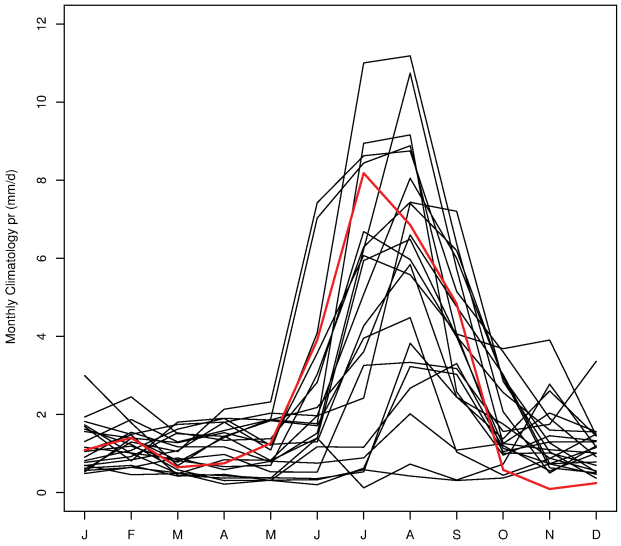


**Figure 7.3:** Monthly precipitation climatologies of the 21 CMIP5 models used in this study (black) and how they compare to the TRMMv7 satellite product (red), over the period 2000–2005.

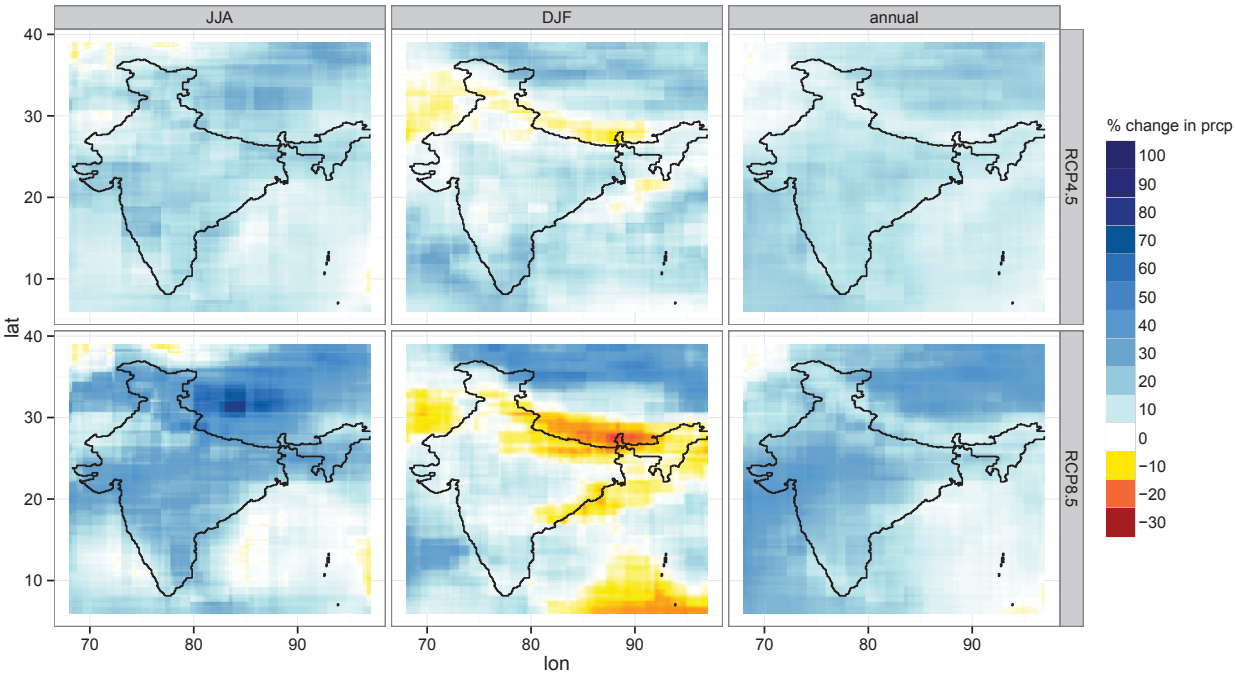


**Figure 7.4:** Multi-model mean % change in precipitation over India between the periods 1975–2005 and 2070–2100. Results are separated under 2 emission scenarios (RCP4.5 & RCP8.5) and three different time-scales: the monsoon period (June-August, JJA), the dry winter period (December-February, DJF) and the annual period.

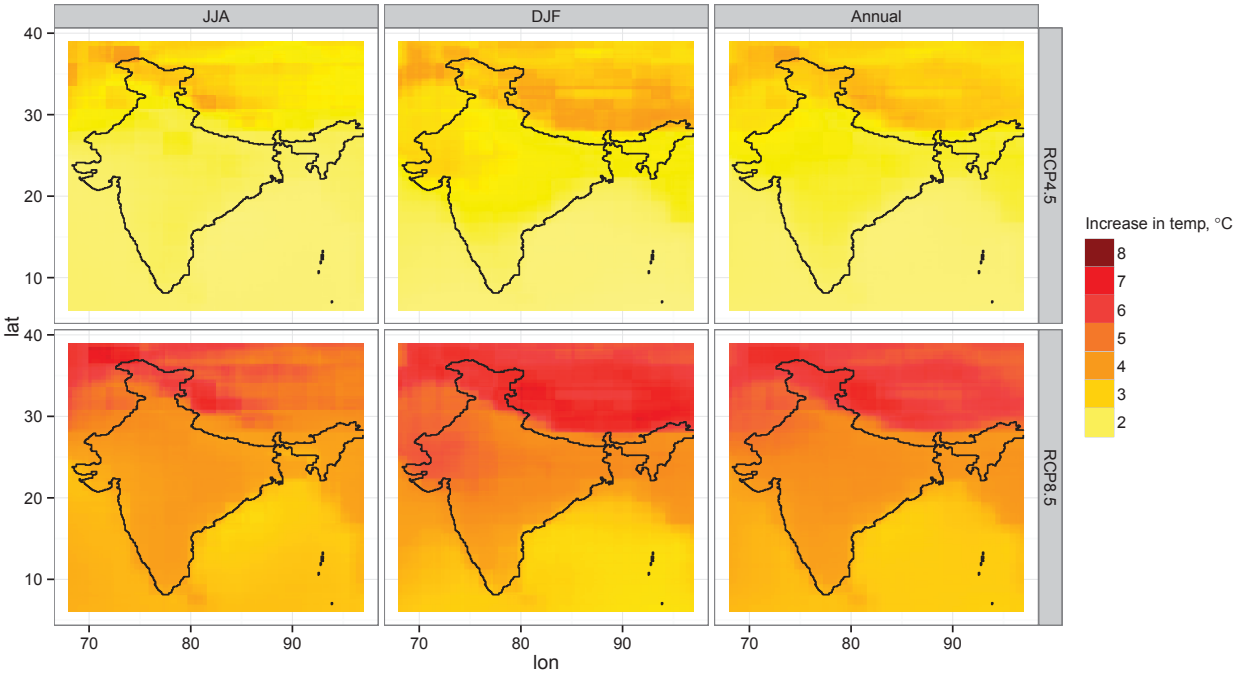


**Figure 7.5:** Multi-model mean change in surface temperature over India between the periods 1975–2005 and 2070–2100. Results are separated under 2 emission scenarios (RCP4.5 & RCP8.5) and three different time-scales: the monsoon period (June-August, JJA), the dry winter period (December-February, DJF) and the annual period.

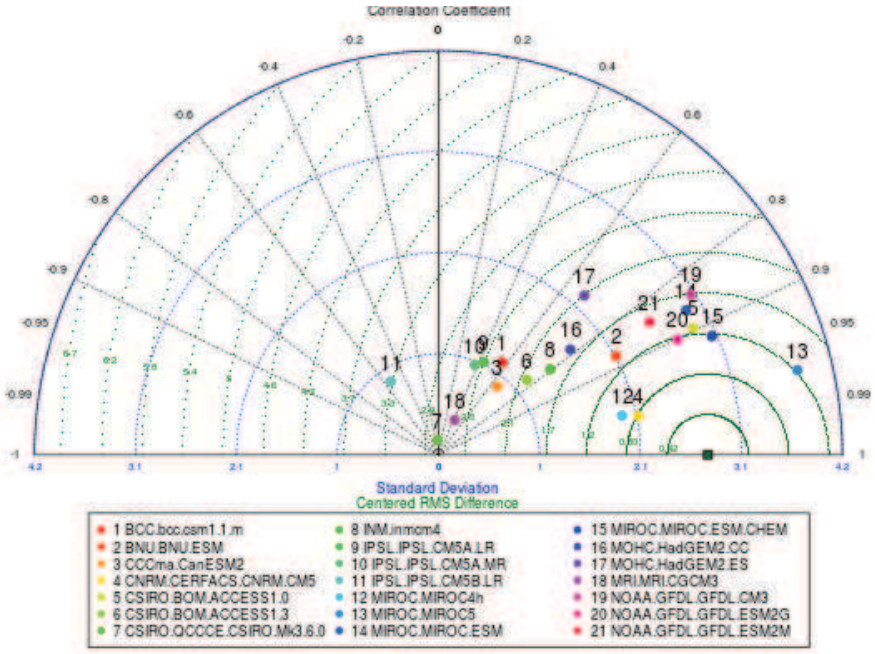


**Figure 7.6:** Taylor diagram that graphically summarises how closely the historic precipitation generated by each of the 21 CMIP5 models used in this study matches TRMMv7 observed precipitation, over the period 2000–2005.

of them perform better, in terms of simulating historical precipitation patterns over the study area, is a Taylor diagram (Fig. 7.6), which quantifies the similarity between modelled and observed precipitation in terms of correlation coefficient, standard deviations and centred root-mean-square (RMS) difference (Taylor, 2001). According to that diagram, the closer a model is to the observation (dark green - squared dot in the bottom right side of graph), the best it performs. Therefore, and based on the Taylor diagram (Fig. 7.6) models such as CNRM-CM5, MIROC4h, MIROC5 are perceived to outperform models like IPSL-CM5B-LR or CSIRO-Mk-3-6-0 in terms of their ability to match historic precipitation well.

Figure 7.7 shows the CFs of precipitation relative to the historic period 2000-2005, averaged in the UG basin. It is evident that the spread of the results is large, and many models show opposite directions of change. Nevertheless, all the mean values (blue lines) point towards an increased precipitation for all months. The uncertainty is higher for the dry months November and December, which have the highest increase in precipitation relative to historic values. On the other hand, the spread seems to be narrower for the wet summer months but nonetheless there are still models with contrasting results.

### 7.4.2 Hydrological Projections

The generated streamflows shown in Figure 7.8 reveal the impact of both climate change and land-use change in the future flows. The spread of the results is indicative of the uncertainties among different GCM forcing data. The spread is large under both emission scenarios, which suggests that the GCM precipitation spread is relatively less sensitive to the level of radiative forcing. Further, it is noticeable that the agreement in projections of low flows is stronger than that of high flows, because the future projections of extreme precipitation events have large uncertainties in the tropical regions as also mentioned in the study by Kharin *et al.* (2013).

Kernel density plots shown in Fig. 7.9 show the distributions of $\mathrm{Q}_5$, $\mathrm{Q}_{25}$, $\mathrm{Q}_{50}$, $\mathrm{Q}_{75}$, $\mathrm{Q}_{95}$, (i.e. flows exceeded 5%, 25%, 50%, 75% and 95% of time respectively), among different GCMs, when only climate change is taken into account ($\mathrm{Q}_{\mathrm{cl}}$) and when both land-use and climate change are taken into account ($\mathrm{Q}_{\mathrm{cl\_lu}}$), for the UG basin. The large variations of flows highlight the large spread among GCM outputs used to force JULES. It is evident that the differences between the two RCPs are greater than the differences between $\mathrm{Q}_{\mathrm{cl}}$ and $\mathrm{Q}_{\mathrm{cl\_lu}}$ of the same RCP. As illustrated by the densities shown in Fig. 7.9,

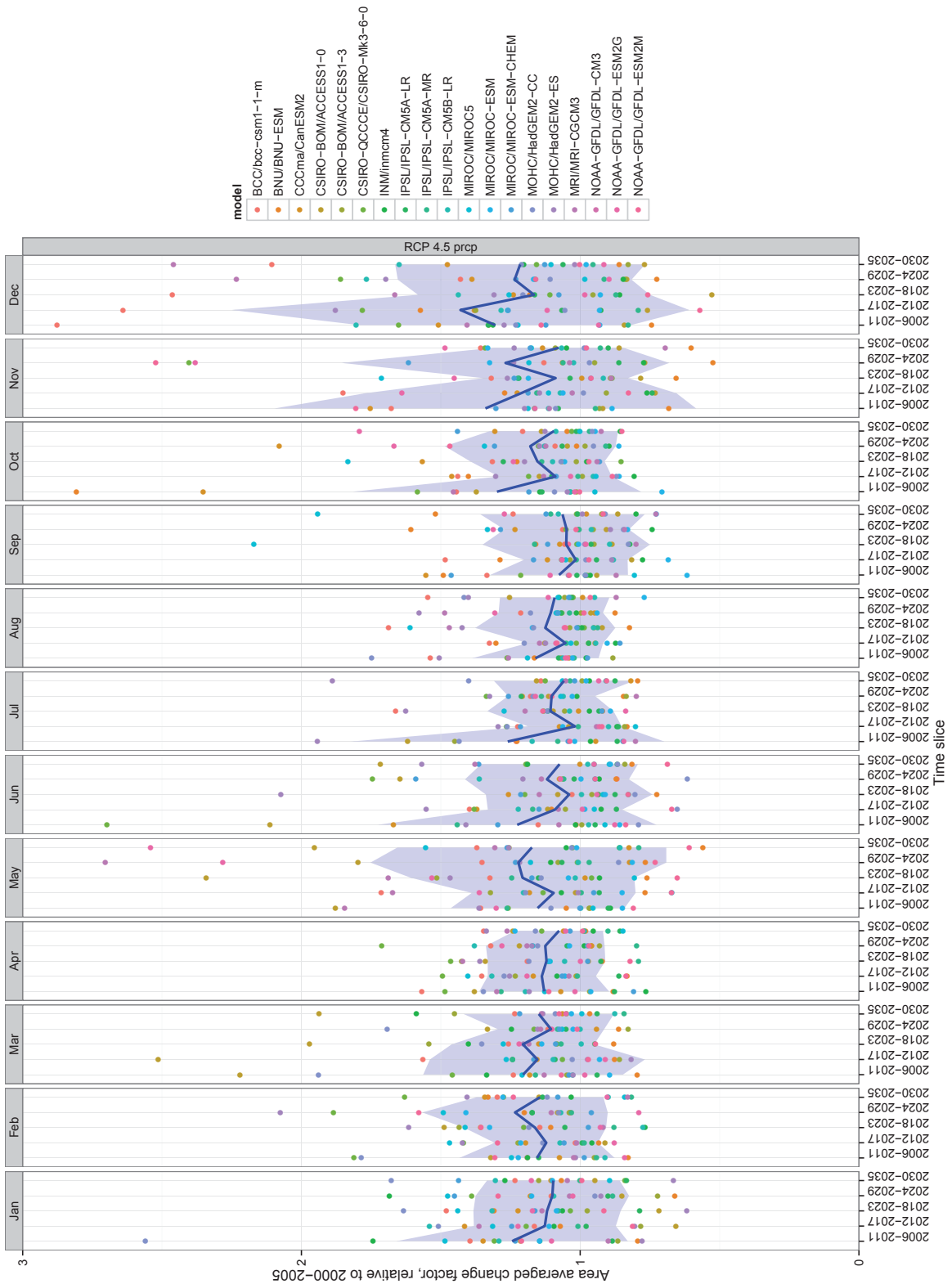


**Figure 7.7:** 6-year CFs of precipitation in the UG basin. Each dot represents the basin's areal average of a particular model. The precipitation anomalies are relative, unit-less values. A higher than 1 value indicates an increase and a smaller than 1 values indicates a decrease of precipitation. The blue line represents the mean value whereas the shading represents the spread of projections from the multi-model ensemble.

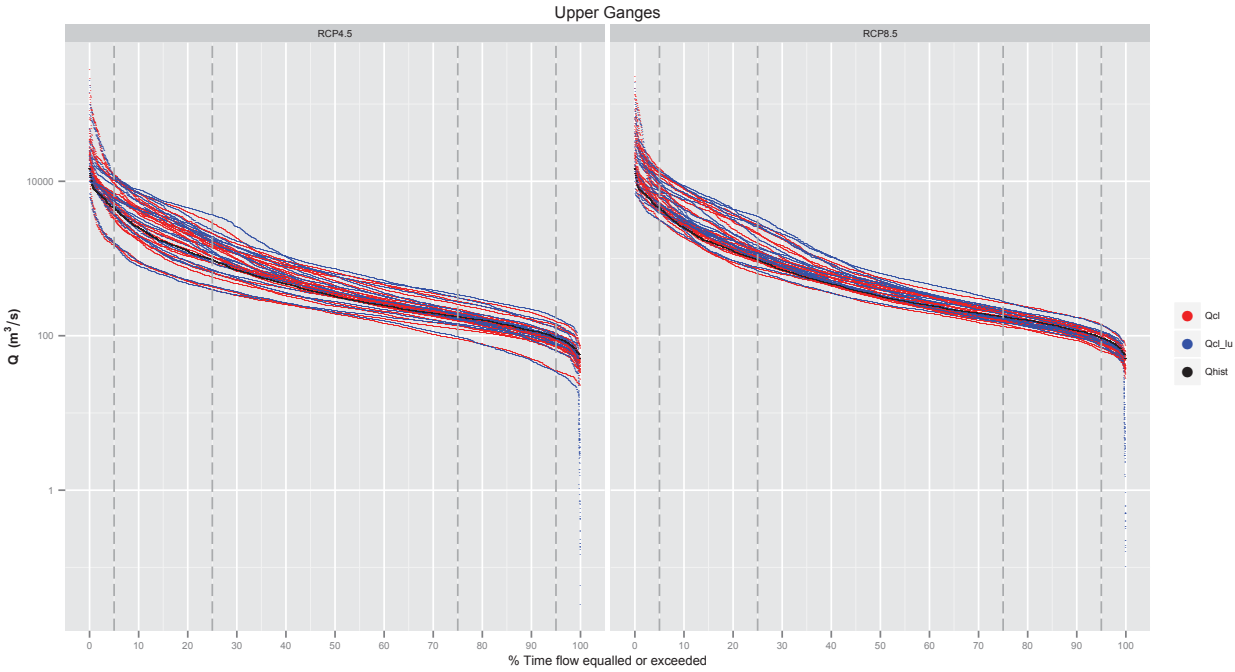


**Figure 7.8:** Flow duration curves of the streamflows simulated by JULES for the UG basin, when forced by CMIP5 model outputs. Red: only climate change is taken into account $(\mathrm{Q_{cl}})$, simulation period 2030-2035, each line represents JULES outputs based on different CMIP5 model forcing. Blue: both climate change and land-use change are taken into account $(\mathrm{Q_{cl\_lu}})$, simulation period 2030-2035, each line represents JULES outputs based on different CMIP5 model forcing. Black: Historical period $(\mathrm{Q_{hist}})$, simulation period 2000-2005.

the agreement in projections of low flows ($\mathrm{Q_{75}}$, $\mathrm{Q_{95}}$) is stronger than that of high flows ($\mathrm{Q_5}$, $\mathrm{Q_{25}}$), as previously discussed.

However, focusing upon the MMM values (Fig. 7.10), for the entire UG basin, when only climate change is taken into consideration (red line), the high flows exceeded only 5% of time ($Q_5$) are projected to increase by 40% compared to historic values, under RCP4.5 and by 59% under RCP8.5 (Table 7.2). When both climate change and land-use change are taken into account (blue line), the increase in the high extremes of flows is slightly higher: 41% increase under RCP4.5 and 62% increase under RCP8.5. In the low flows, the impact of climate change only is not as significant. Low flows exceeded 95% of time ($Q_{95}$) are decreased by 2% under RCP4.5 and by 3% under RCP8.5. When land-use change is also taken into account, $Q_{95}$ is projected to increase by 1% under RCP4.5 and to decrease by 1% under RCP8.5. So there is a clear impact of both climate change and land-use change in the high and low extremes of flows.

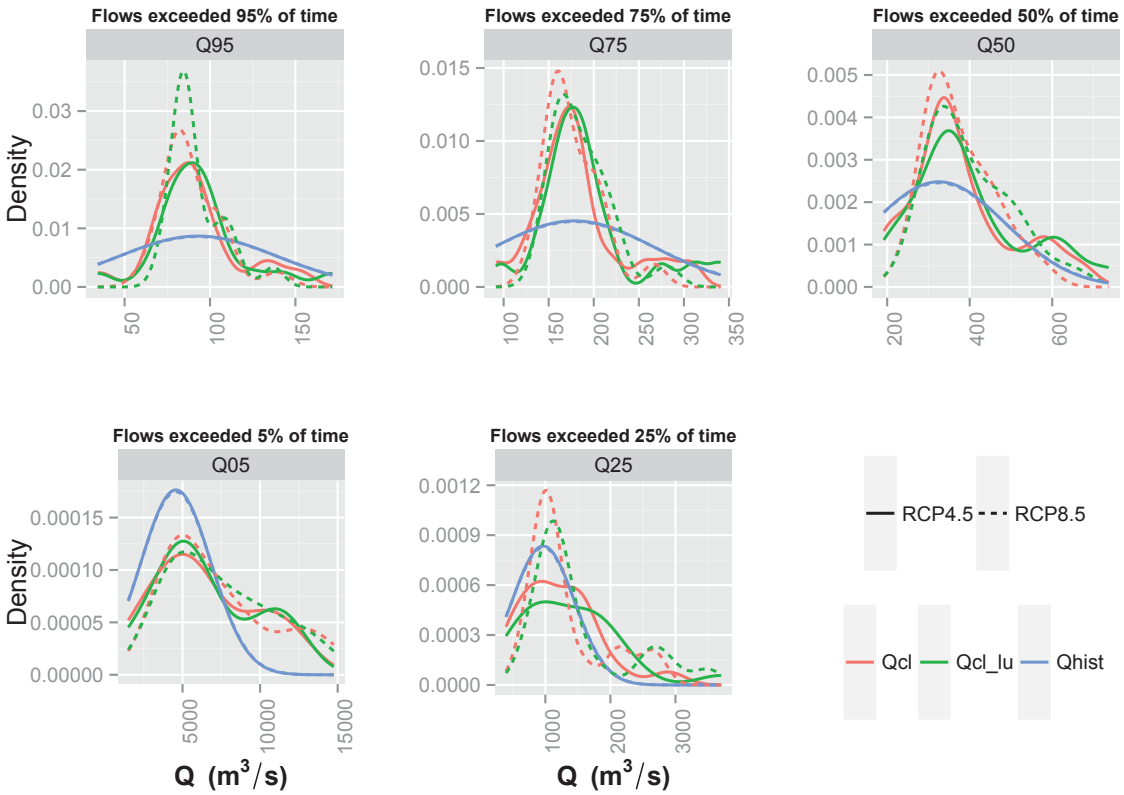


**Figure 7.9:** Kernel density plots showing distribution of $Q_5$, $Q_{25}$, $Q_{50}$, $Q_{75}$, $Q_{95}$ (i.e. flows exceeded 5%, 25%, 50%, 75% and 95% of time respectively), for the UG basin, under both emission scenarios. Pink: Only climate change is taken into account $(Q_{cl})$, simulation period 2030-2035. Green: Both climate change and land-use change are taken into account $(Q_{cl\_lu})$, simulation period 2030-2035.

In the Bhimgoda sub-catchment, when only climate change is taken into account, $Q_5$ is projected to increase by 21% compared to historic values, under RCP4.5 and by 34% under RCP8.5 (Table 7.2). When both climate change and land-use change are taken into account (blue line), the increase in the high extremes of flows is even higher: 22% increase under RCP4.5 and 36% increase under RCP8.5. In the low flows, the impact of climate change only is not as significant. $Q_{95}$ is expected to decrease by 2% under RCP4.5 and by 6% under RCP8.5. When land-use change is also taken into account, $Q_{95}$ is projected to decrease by 5% under RCP4.5 and by 10% under RCP8.5.

The magnitude of increase in the future projections of streamflows might appear unrealistic, and this is partly attributed to the downscaling method used that increased precipitation extremes and partly to the uncertainties of GCM outputs. The mean climatic CFs were calculated from the mean monthly

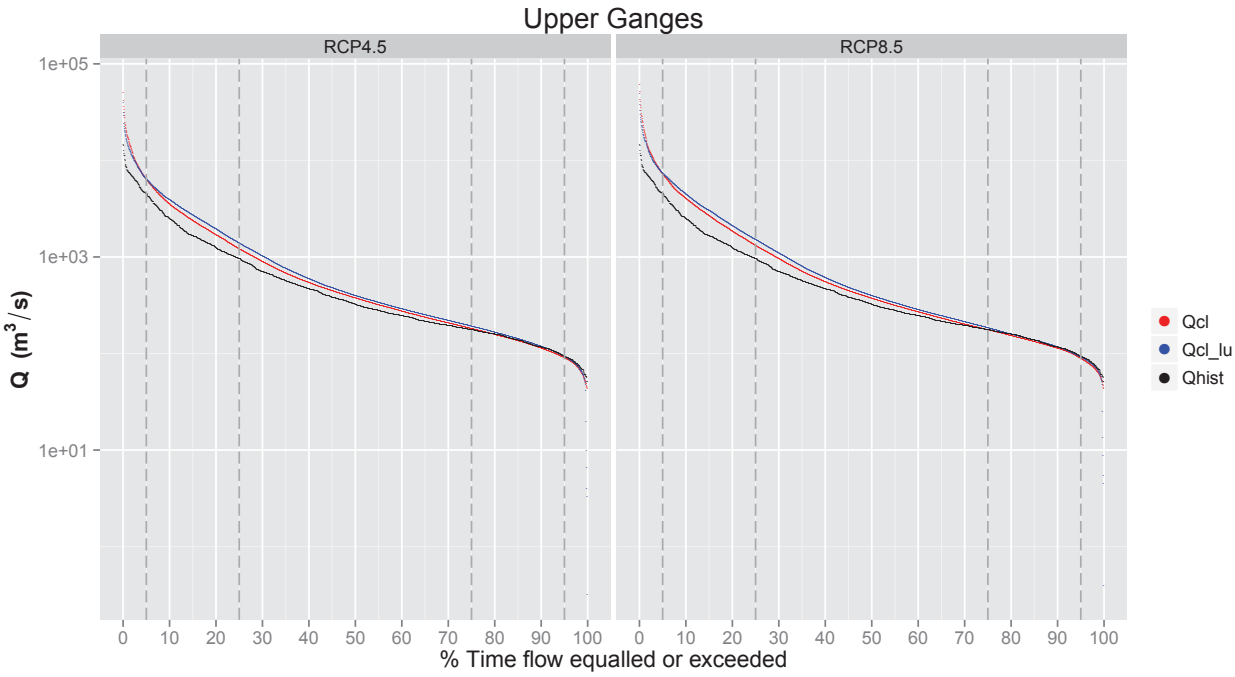


**Figure 7.10:** Flow duration curves of the streamflows simulated by JULES for the UG basin. Red: Multi-model mean values when only climate change is taken into account $(\mathrm{Q_{cl}})$, simulation period 2030-2035. Blue: Multi-model mean values when both climate change and land-use change are taken into account $(\mathrm{Q_{cl\_lu}})$, simulation period 2030-2035. Black: Historical period $(\mathrm{Q_{hist}})$, simulation period 2000-2005.

climatologies over 6-year time slices. However, given the large variability of precipitation on daily time-scales compared to the mean monthly climatology, by scaling the high extremes of precipitation according to the CF, it is inevitable that in some cases precipitation is highly exaggerated in the future projections. In such a large catchment inflated precipitation extremes would be directly translated by JULES into unreasonably high runoff values. Nevertheless, there is qualitative similarity between the results of this thesis and results presented by Lutz *et al.* (2014), who found that for the UG basin, projected precipitation increases during the monsoon period, could lead to increases in total annual runoff up to 10% for RCP4.5 and 27% for RCP8.5, during the period 2041–2050.

Although the general patterns of change in the high and low extremes of flows are similar in both the Bhimgoda and the UG basins, the projected increase in $Q_5$ for the UG basin is almost double the projected increase for the Bhimgoda basin, whereas the projected decrease in $Q_{95}$ for Bhimgoda is almost 5 times higher than the decrease projected for the UG basin. These differences are attributed to climate change

**Table 7.2:** $Q_5$ and $Q_{95}$ flow values $(m^3/s)$ based on the flow duration curves shown in Figure 7.10

| | | Historical | RCP4.5 | | RCP8.5 | |
|---|---|---|---|---|---|---|
| | | $Q_{hist}$ | $Q_{lu}$ | $Q_{cl\_lu}$ | $Q_{lu}$ | $Q_{cl\_lu}$ |
| Upper Ganges | $Q_5$ | 4563 | $6405 = 1.40 \times Q_{5hist}$ | $6446 = 1.41 \times Q_{5hist}$ | $7269 = 1.59 \times Q_{5hist}$ | $7399 = 1.62 \times Q_{5hist}$ |
| | $Q_{95}$ | 93 | $91 = 0.98 \times Q_{95hist}$ | $94 = 1.01 \times Q_{95hist}$ | $90 = 0.97 \times Q_{95hist}$ | $92 = 0.99 \times Q_{95hist}$ |
| Bhimgoda | $Q_5$ | 2070 | $2510 = 1.21 \times Q_{5hist}$ | $2518 = 1.22 \times Q_{5hist}$ | $2770 = 1.34 \times Q_{5hist}$ | $2825 = 1.36 \times Q_{5hist}$ |
| | $Q_{95}$ | 63 | $62 = 0.98 \times Q_{95hist}$ | $60 = 0.95 \times Q_{95hist}$ | $59 = 0.94 \times Q_{95hist}$ | $57 = 0.90 \times Q_{95hist}$ |

mainly (as the magnitudes of change between the climate change only scenarios and the scenarios where both climate change and land-use change are taken into account remain similar). On the other hand, the changes relative to historic period in both high and low flows are lower under RCP4.5 than under RCP8.5.

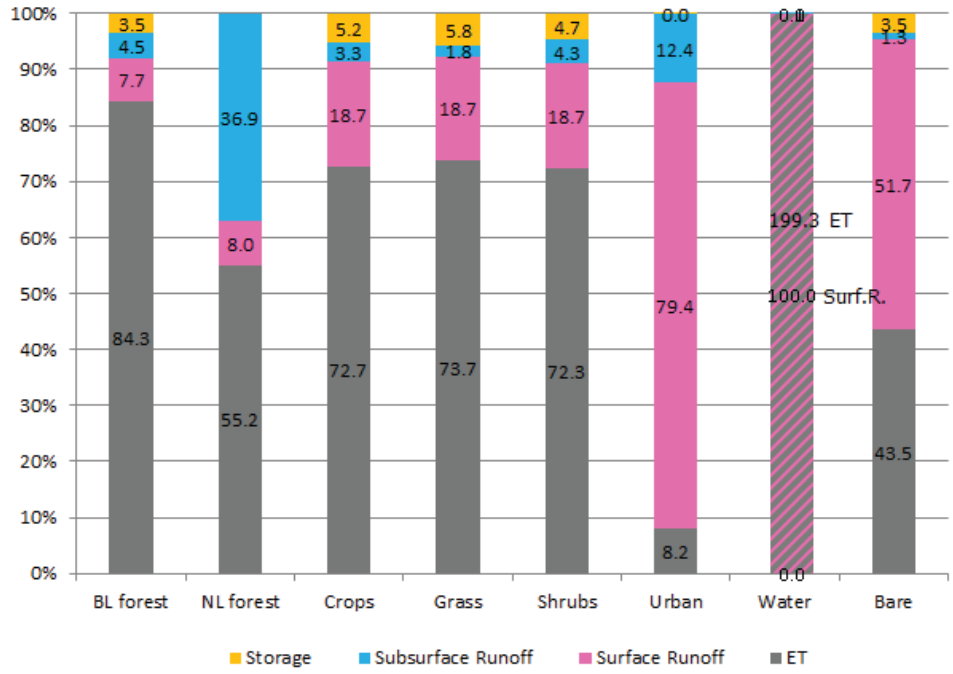


**Figure 7.11:** Flux partitioning in JULES under different land-use types

Useful information regarding the flux partitioning in JULES under different land-use types, is obtained from Figure 7.11. The land-use type water indicates open water (such as lakes). This is not explicitly modelled by JULES (Best *et al.*, 2011), which assumes that there is enough water to ensure maintenance of the lake. The evaporative flux is not removed from any moisture store within the model and also precipitation does not contribute to any water store (there is no infiltration as the lake tile is dis-

connected to the soil moisture column). A large value for the surface heat capacity (equivalent to water of 1 m depth) gives a realistic simulation of the diurnal cycle of a lake's surface temperature (Best *et al.*, 2011). As evaporation from lake surfaces does not draw on the conserved moisture stores, water conservation and water balance are violated. In urban landscapes and to a lesser extent in bare soil conditions, most of the precipitation becomes surface runoff. In bare soils, around 43% of precipitation evaporates whilst in all 5 vegetative land-use types, more than 50% of precipitation becomes ET.

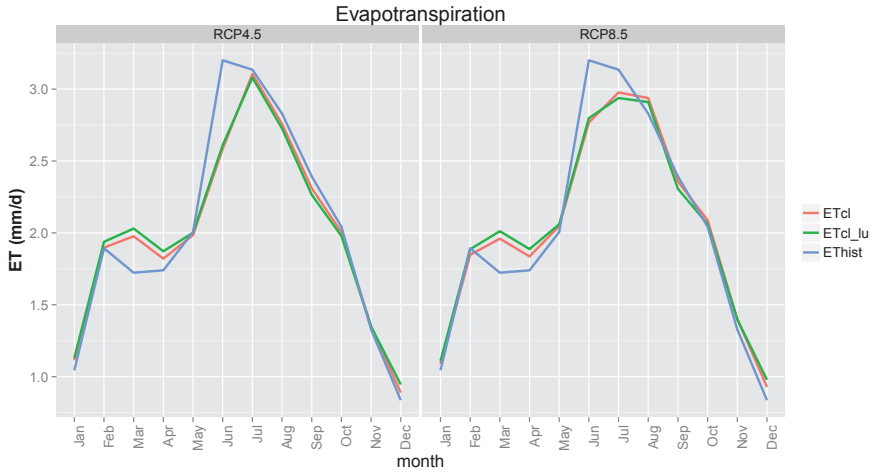


**Figure 7.12:** Multi model mean values of the ET fluxes simulated by JULES, for the UG basin and for each one of the emission scenarios (RCP4.5 & RCP8.5). Blue colour corresponds to the historical simulation period 2000-2005 $(\mathrm{ET_{hist}})$. Pink colour corresponds to the simulation period 2030-2035, when only climate change is taken into account $(\mathrm{ET_{cl}})$. Green colour corresponds to the simulation period 2030-2035, when both climate change and land-use change are taken into account $(\mathrm{ET_{cl\_lu}})$.

The small increase in future streamflows that is attributed to land-use change could be directly related to urbanisation, which is one of the main land-use change trends being projected for the future. On the other hand, it is possible that the impacts of urbanisation are cancelled out by the impacts of forest growth along with bare soil loss, which are less surface runoff and more ET.

In terms of ET fluxes (Fig 7.12), the MMM future projections under RCP4.5 are pointing towards increased ET for the spring months March and April and decreased ET over the summer period (June-September). Under RCP8.5, ET follows similar patterns of change, although in August the projection is pointing towards increased ET compared to historic values. In all cases, it is evident that in the near-term future projections, the inter-model uncertainty is higher than the scenario uncertainty. This is also shown

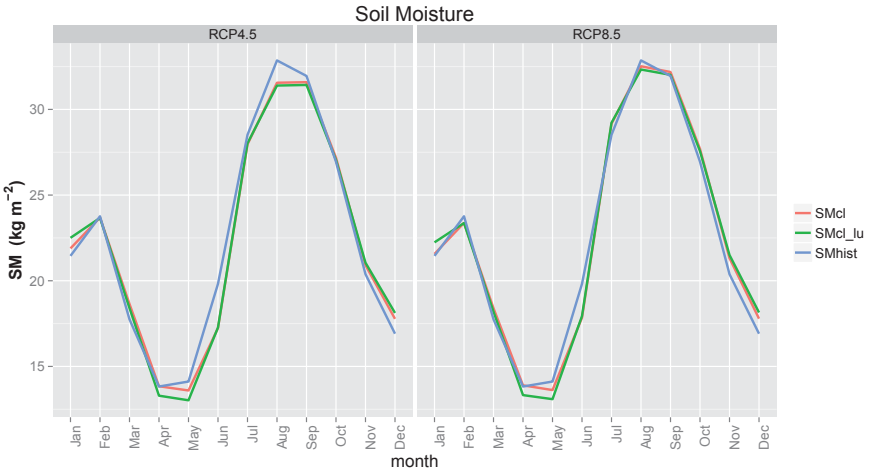


**Figure 7.13:** Multi model mean values of the SM fluxes simulated by JULES, for the UG basin and for each one of the emission scenarios (RCP4.5 & RCP8.5). Blue colour corresponds to the historical simulation period 2000-2005 $(\mathrm{SM_{hist}})$. Pink colour corresponds to the simulation period 2030-2035, when only climate change is taken into account $(\mathrm{SM_{cl}})$. Green colour corresponds to the simulation period 2030-2035, when both climate change and land-use change are taken into account $(\mathrm{SM_{cl\_lu}})$.

in Fig 7.14, which displays monthly percentage changes of ET between historic (2000-2005) and future period (2030-2035), spatially averaged in the UG basin. The spread of results derived by JULES forced with different GCM outputs is large under both RCPs but the MMM changes are never higher than 20%.

Spatial changes of ET between the historical (2000-2005) and future projection period (2030-2035), under both emission scenarios (RCP4.5 & RCP8.5) are shown in Fig. 7.16. Results are split into 3-month period seasonalities for winter (DJF), spring (MAM) and summer (JJA), under the two types of experiments: (a) only climate change is taken into account $(\mathrm{ET_{cl}})$, and (b) both climate change and land-use change are taken into account $(\mathrm{ET_{cl\_lu}})$. The differences between $\mathrm{ET_{cl}}$ and $\mathrm{ET_{cl\_lu}}$ are very small in all seasons examined. The highest increases in ET (100%) are projected to occur during spring in the southern agricultural parts of the catchment. The highest decreases in ET (-40%) are projected to occur during the spring and summer periods, in the mid-north parts of the study area. Nonetheless, those large % changes of ET, are cancelled out when spatially averaged across the catchment results are presented (Figs. 7.12 & 7.14).

On the other hand, the MMM future projections of soil moisture under the same scenario (Fig 7.13) show a decrease in soil moisture from April to September. Interestingly, the changes of soil moisture

relative to the historic period are smaller under RCP8.5 compared to RCP4.5. The overall agreement between historic and both future scenarios seems to be better in the soil moisture results compared to the ET results (see also the spread of results in Figs. 7.14–7.15). Figure 7.15, displays monthly percentage changes of soil moisture between historic (2000-2005) and future projections period (2030-2035), spatially averaged in the UG basin. Is is shown that the spread of results is larger under RCP4.5 compared to RCP8.5. This could be explained by the stronger forcing of the RCP8.5, which leads the GCMs to produce more similar results. In all cases the MMM changes between historic and future projections in soil moisture are never higher than approximately 20%.

Interestingly enough, in terms of spatial changes of soil moisture, it is shown in Fig. 7.17 that the MMM changes reach values of 200%. Similarly to the patterns of ET change, the highest increases in soil moisture (200%) are projected to occur during spring, in the southern agricultural parts of the catchment. The highest decreases in soil moisture (-80%) are projected to occur during the winter and summer periods, in the mid-north parts of the study area. However, it seems that these extreme changes of soil moisture (on the one hand +200% and on the other hand -80%) are cancelled out when spatially averaged results are presented (Figs. 7.13 & 7.15).

As previously mentioned, it seems that the projected for the future increase in precipitation is translated as more intense precipitation events (due to the delta-change approach followed here). Besides, the differences between the two RCP scenarios are not large, especially for the projections of ET and soil moisture fluxes. In the nearby future period examined here (2030-2035), the relative importance of the RCPs is far smaller than the GCM model uncertainties.

Overall, climate change is the main driver of hydrological change in the near term future scenarios explored in this study. If no dramatic land-use changes take place in the nearby future, the main alterations in hydrological fluxes are expected to arise from the change in the meteorology (and mainly precipitation). The relative contribution of land-use change is of an approximate magnitude of 2% compared to historic values. However, the strong inter-model uncertainties of historic and future projections, which were possibly amplified by the delta-change bias correction approach, are posing a limitation to the confidence of these results. Nevertheless, as GCM uncertainties are unlikely to decrease quickly, decisions on the adaptation and mitigation of climate change should not be prevented (Knutti and Sedlacek, 2013).

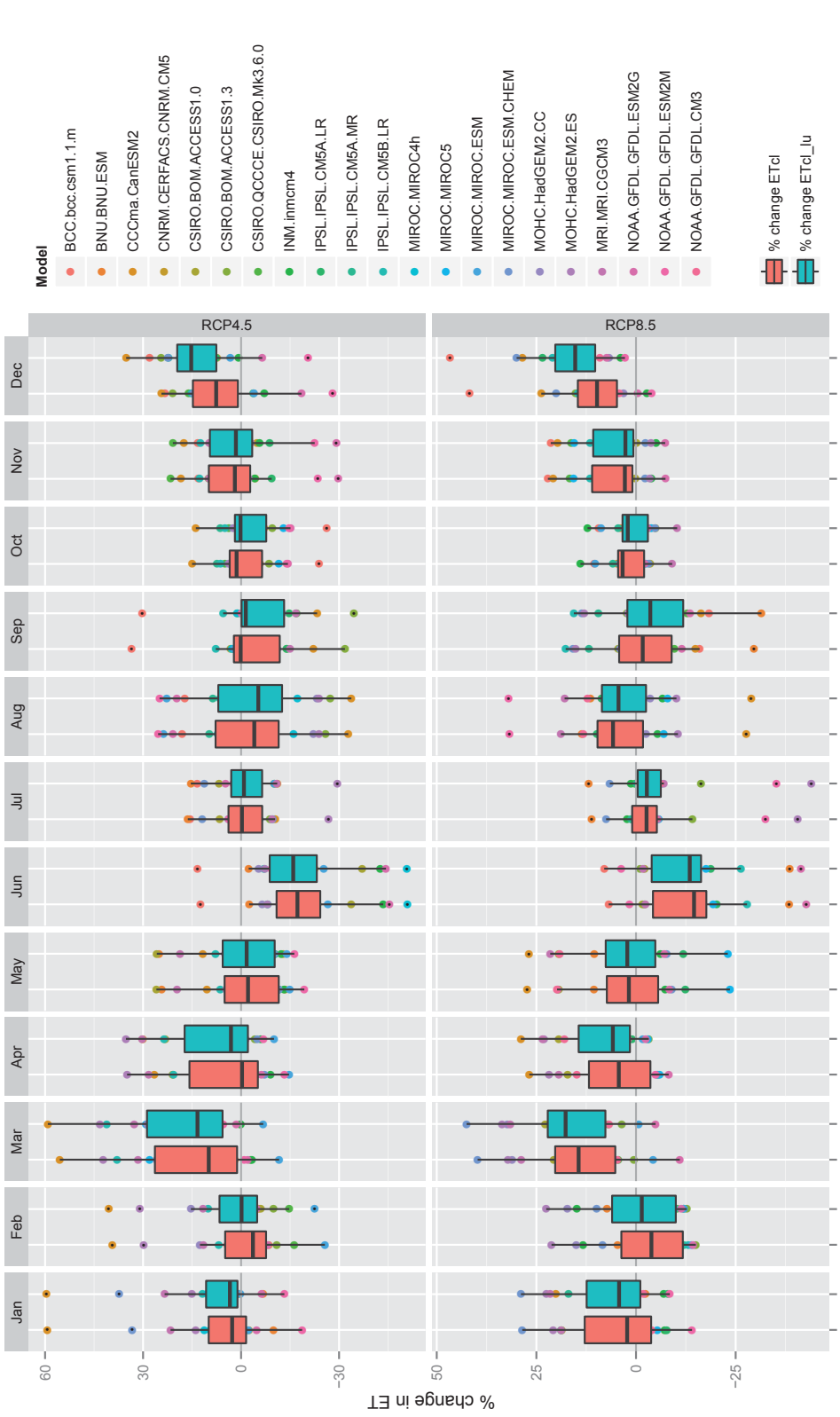


**Figure 7.14:** Percentage changes of evapotranspiration (ET) fluxes between the historical simulation period 2000-2005 and the future projection simulation period 2030-2035, for the UG basin and for each one of the emission scenarios (RCP4.5 & RCP8.5). Pink colour corresponds to the scenarios that only climate change is taken into account. Blue colour corresponds to the scenarios that both climate change and land-use change are taken into account.


**Figure 7.15:** Percentage changes of soil moisture (SM) fluxes between the historical simulation period 2000-2005 and the future projection simulation period 2030-2035, for the UG basin and for each one of the emission scenarios (RCP4.5 & RCP8.5). Pink colour corresponds to the scenarios that only climate change is taken into account. Blue colour corresponds to the scenarios that both climate change and land-use change are taken into account.

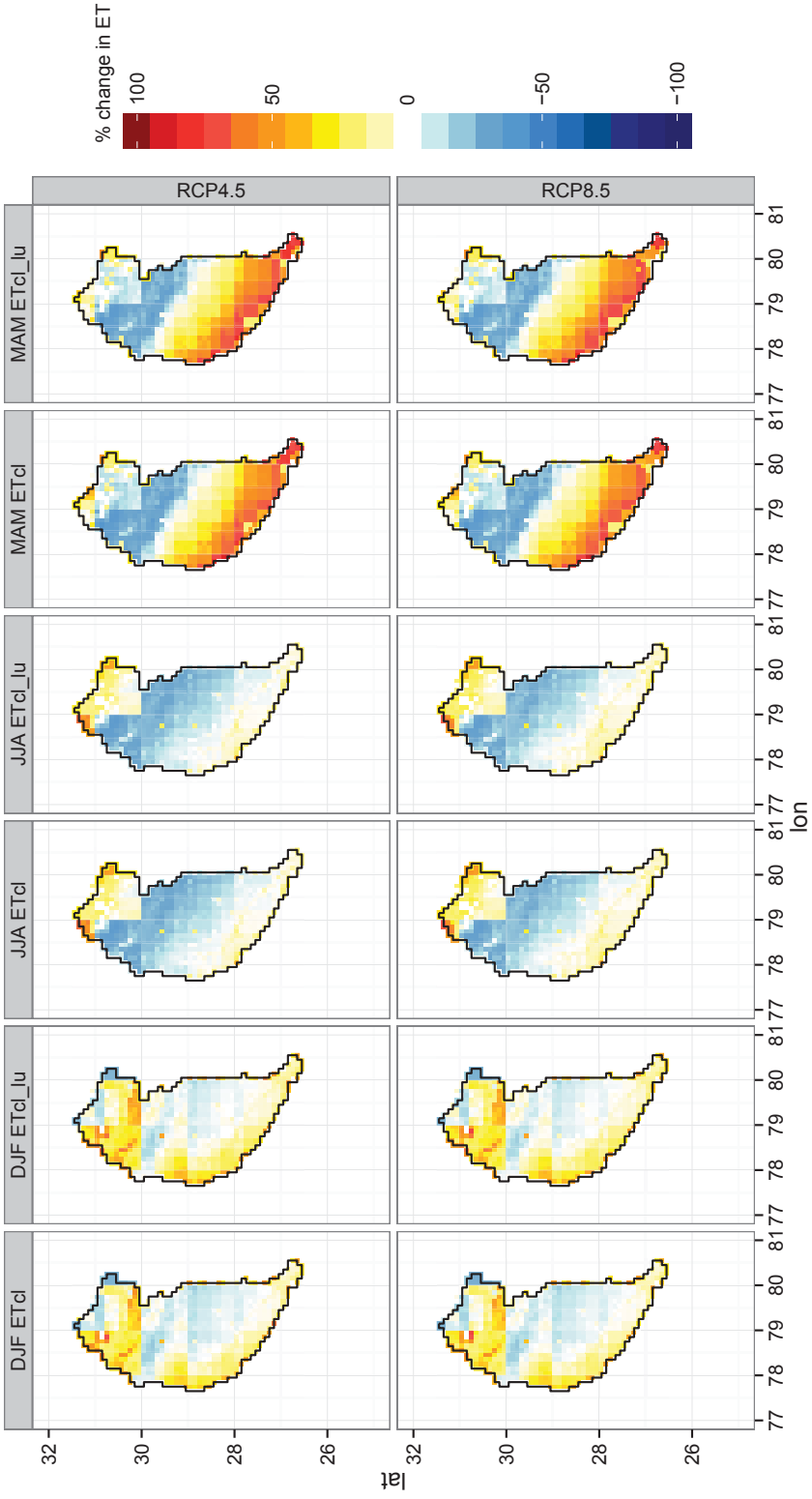


**Figure 7.16:** Percentage changes of spatial evapotranspiration (ET) fluxes between the historical simulation period 2000-2005 and the future projection simulation period 2030-2035, for the UG basin and for each one of the emission scenarios (RCP4.5 & RCP8.5). Results are split into 3-month period seasonalities for winter (DJF), spring (MAM) and summer (JJA), under the two types of experiments: (a) only climate change is taken into account (ETcl), and (b) both climate change and land-use change are taken into account ($\mathrm{ETcl_lu}$).

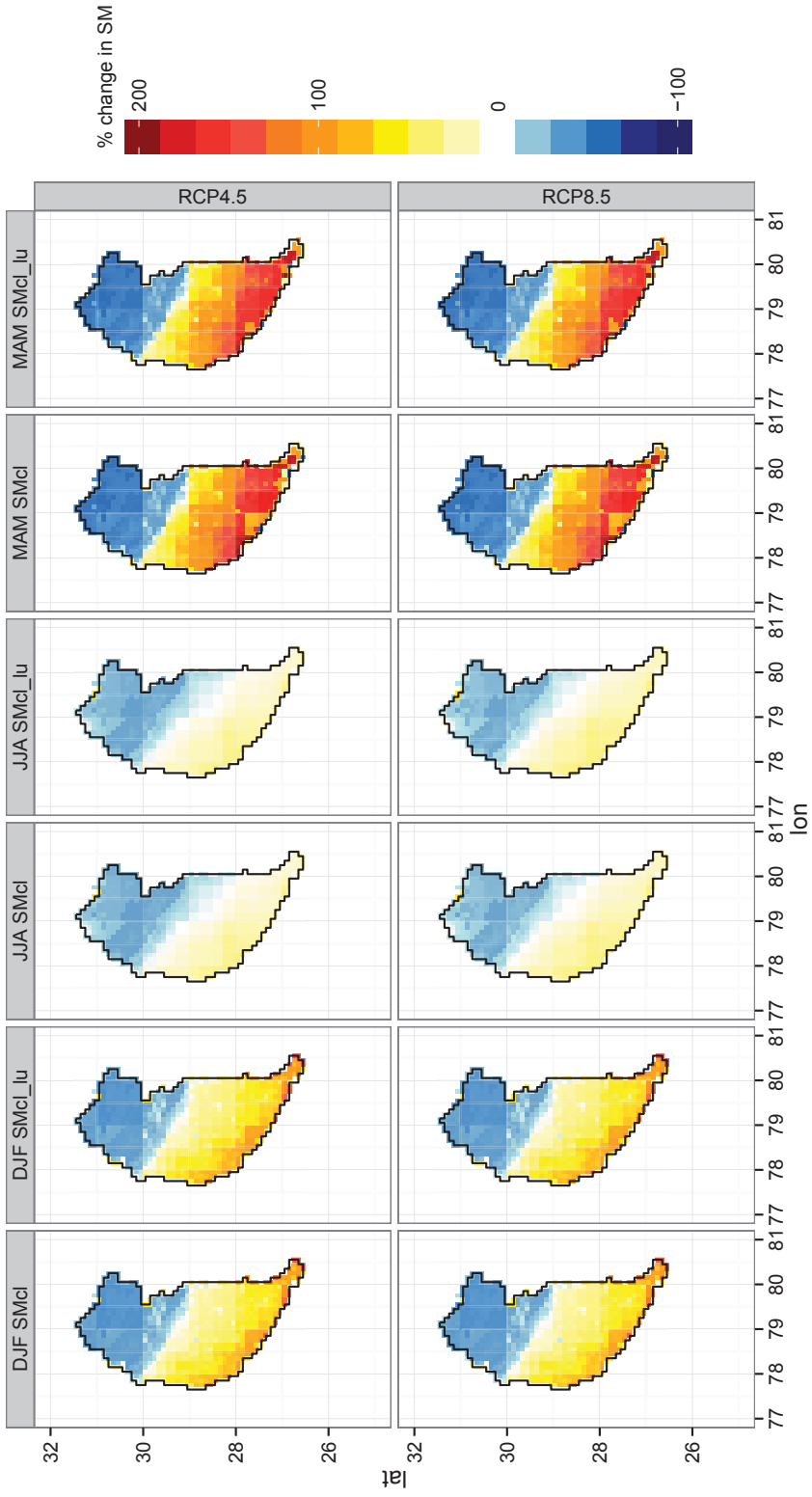


**Figure 7.17:** Percentage changes of spatial soil moisture (SM) fluxes between the historical simulation period 2000-2005 and the future projection simulation period 2030-2035, for the UG basin and for each one of the emission scenarios (RCP4.5 & RCP8.5). Results are split into 3-month period seasonalities for winter (DJF), spring (MAM) and summer (JJA), under the two types of experiments: (a) only climate change is taken into account (SMcl), and (b) both climate change and land-use change are taken into account ($\mathrm{SMcl_{lu}}$).

### 7.4.3 Future projections in relation to water demand

This section places the above results in a water resources context, by discussing what are the implications of climate change on the water resources of the Upper Ganges and whether it is likely that water demand thresholds of the region will be exceeded in the future.

A recent study by Sapkota *et al.* (2013) presents mean monthly water demands for irrigation, industrial and domestic purposes (period 1991-2005), in the UG basin. According to this study, irrigation water demands from canals (which are much higher compared to industrial and domestic ones) are low during the monsoon period from June to September and high from November to February. During the winter months December and January, water demands in the UG basin are already unmet. In recent years pressure has increased on the river canals to maintain flows during the dry season, due to the introduction of high water intensive crops, agricultural expansion and population growth (Sapkota *et al.*, 2013).

Here, the mean monthly water demands shown in Fig.4 of Sapkota *et al.* (2013) are used in combination with future projections of changes in India's water demands, as presented in the study by Amarasinghe *et al.* (2007). This study suggests an expected 8% increase in surface water demand for irrigation, 130% increase in surface water demand for domestic usage and 152% increase in surface water demand for industrial usage, by 2030 under a business as usual scenario, which is mainly extrapolating trends of recent years (calculations after linearly interpolating results presented for years 2025 and 2050).

Based on the two studies mentioned above, future projections of surface water demand for the UG basin are generated, on a monthly basis and for the period 2030-2035. Figure 7.18 shows how the future expected surface water demands compare with the flow volumes as calculated by JULES (period 2030-2035) under the two examined RCP scenarios, when only climate change is taken into account and when both climate change and land-use change are taken into account. Since the main months under water stress are those in the dry season and in order to better visualise the results outside the wet summer period (which is dominated by high flows), the y axis was limited to values lower than 2000 Million $\mathrm{m}^3$ of water.

The future winter months (Dec-Feb) are expected to be the most problematic ones in terms of meeting the surface water demands, with agriculture being the main water user. This poses threats to the river's capability to maintain flows at an acceptable ecological level (environmental flows) during those months.

Sapkota *et al.* (2013) showed that using less water intense crops in the UG basin, is more efficient than reducing the total agricultural area by 40%, in reducing the unmet irrigation water demands. Besides, as previously discussed but also shown in Fig. 7.18, the main driver of future change in water resources is not land-use change. It is climate change but also the changing practices within certain types of land-use (i.e. increased irrigation efficiency, upstream dams) that are expected to drive changes in the future water availability of the UG basin, rather than land-use change per-se.

Understanding the future water availability in India is much more complex than looking from the perspective of climate and land-use change only. For instance, India is one of the greatest hydropower generators in Asia. A potential future increase in hydropower capacity, aside from its large benefits in terms of reducing carbon emissions, brings further environmental concerns regarding river flows, water quality and eco-diversity. Therefore, the impacts of such water management decisions (e.g. hydrowpower dam structures) could also play a major role in the water balance of this region.

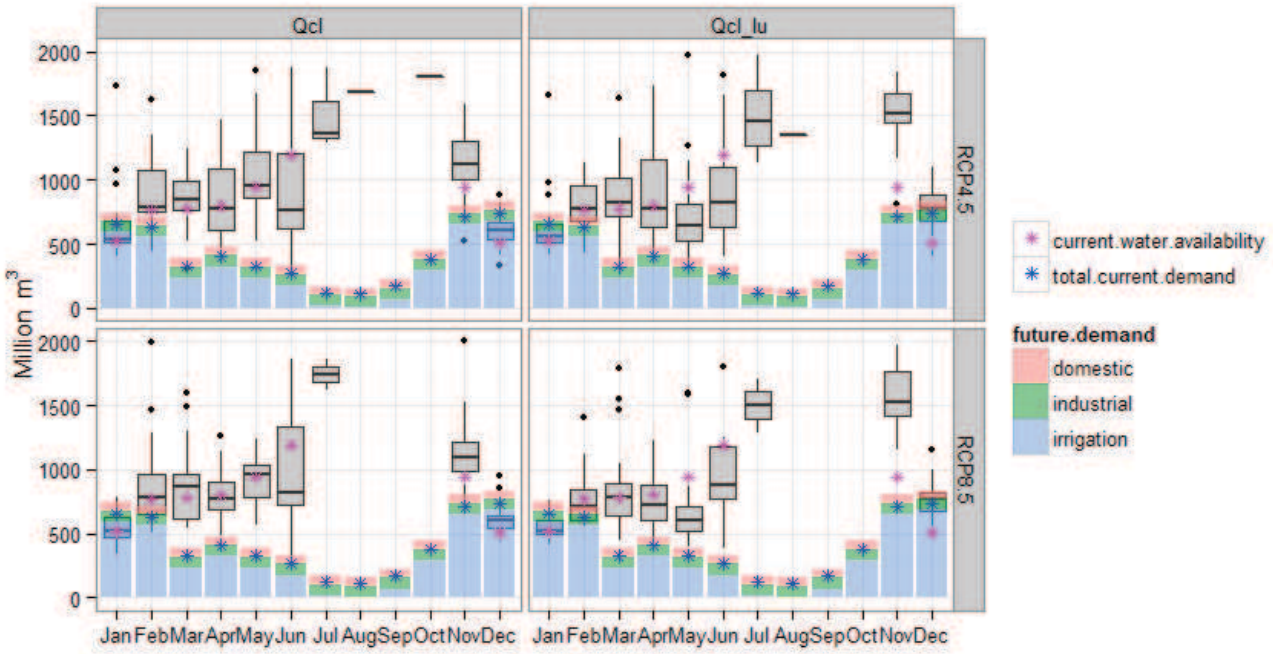


**Figure 7.18:** Bars showing future projections of monthly surface water demand, for irrigation, domestic and industrial usage, during the period 2030-2035, for the UG basin. Box plots indicate monthly flow volumes calculated by JULES under different GCM forcings, for the same period.

## 7.5 Chapter Summary

In this Chapter, the impact of land-use changes and climate change on the future hydrology of the UG basin was assessed by calculating annual variations in hydrological components (stream flow, evapotranspiration and soil moisture).

Large variations between GCM derived precipitation datasets arise from a basic analysis of CMIP5 model outputs. Stronger wet and dry seasons are projected to occur by the end of the century according to MMM values.

Significant differences between the historic and nearby-future hydrologic fluxes arise under future land-cover and climate change scenarios, pointing towards a severe increase in high extremes of flow. During the period 2030–2035, $Q_5$ is projected to increase by 41% under RCP4.5 and by 62% under RCP8.5, compared to historic values of the period 2000–2005. The changes in all examined hydrological components are slightly greater in the combined land-use and climate change scenario compared to the stand-alone climate change scenario. However, the main driver of future hydrological change is climate change.

In terms of spatial changes in ET and SM, the extremely high changes (200% order of magnitude) that occur in various parts of the catchment are cancelled out by changes of the opposite direction, occurring in different parts of the catchment, leading to smaller overall changes in terms of aerial averages.

The large uncertainties in the CMIP5 model outputs were possibly amplified by the delta-change approach followed here and led to a large spread of results for the future hydrological variables. Nonetheless, as GCM uncertainties are unlikely to decrease in the near future, this work could help prioritizing adaptation strategies and regional land-use planning to improve northern India's water resources.

Finally, the results are presented in a water resources context, with the aim of understanding what climate and land-use change mean for the future water resources of the UG basin. When looking into future water availability and demand (period 2030–2035.), the river's capability to maintain ecological flows during the dry season is threatened. It is however important to highlight that under a changing climate, it is not land-use change per se that is expected to drive changes in the water resources availability but changing practices within certain types of land use (i.e. improved crop water productivity), that could significantly impact future water needs.

# Chapter 8

# Conclusions

# Conclusions

## 8.1 Introduction

This thesis sought to explore the effects of large-scale land-use changes and climate change on the water cycle and river flow characteristics by developing a case study in the Upper Ganges (UG) river basin. The three hypotheses that drove the research were: (a) The use of satellite imagery allows for reconstructing historical land-use patterns and projecting them into the future; (b) Accounting for dynamic crop growth in Land Surface Models (LSMs) significantly improves the representation of soil and land-surface processes in the Ganges basin; (c) The combined impacts of land-use and climate change will be greater than the impacts posed by land-use change and climate change individually, on hydrological components.

In the following sections each hypothesis is revisited and the main conclusions of the present research are summarised. The limitation factors of this work are discussed and potential future directions of research are suggested in aspects that have not been covered in the present work.

## 8.2 Hypotheses revisited

**The use of satellite imagery allows for reconstructing historical land-use patterns and projecting them into the future:**

Historical land-cover changes were captured by generating a time-series of land-use maps, after applying supervised classification techniques on historical data sets of satellite images. Subsequently, future spatio-temporal land-cover scenarios were generated based on Markov chain analysis and used to explore changes in water resources.

The main trends of land-use change observed in the study region for the period from 1984 to 2010 are increased areas of forest (+4.7%), agricultural land (+1.3%), and urbanization (+5.8%), at the same time as loss of barren soil (-9.5%), shrubs (-11.6%), and grassland (-9%).

Potential future directions of land-cover change in the UG basin vary and depend on the historic

time period selected by the analyst to project previous changes into the future. In this study, 15 different scenarios based on historic land-cover change produced different future projections. The scenario using land-cover maps for 2008 and 2010 projects future expansion of forest, urban, grass, and shrubland, with a decline in agriculture and bare soil. More confidence can be placed in this result as it is based on analysis of the most recent land-cover changes.

This is the first study attempting to evaluate and understand the dynamics of land-cover change processes in this region by monitoring and analysing the spatial patterns of change at a high resolution, which allows detailed descriptions of land-cover transitions over time. Analysing the patterns of land-cover change is a prerequisite to exploring the sensitivity of the catchment's response to those changes and analysing their impacts on hydrological processes.

**Accounting for dynamic crop growth in LSMs significantly improves the representation of soil and land-surface processes in the Ganges basin:**

The LSM JULES was evaluated in terms of its ability to reproduce hydrological fluxes for the UG basin. Several structural and parameter perturbations were attempted in order to improve the model's performance. Large variations between different precipitation products along with the model's high sensitivity to precipitation input are affecting the model's performance.

Given that JULES is a global LSM, not developed for hydrological purposes, its overall performance was found to be adequate, in terms of its ability to reproduce streamflow, ET and SM fluxes. The uncertainty analysis shows that streamflow observations fall within the uncertainty range of the simulations for 87% of the time, at monthly time-scales.

One of the model's limitations was that it overestimates ET over croplands, and this related to the lack of dynamic crop cycle in the model. To address this issue, JULES is dynamically coupled with the crop model InfoCrop. The aim is to improve the estimation of ET fluxes over croplands, through a more accurate description of vegetation and to quantify the potential error in ET flux estimations of an LSM without dynamic vegetation. An overall improvement is observed in the simulated ET fluxes of the coupled model compared to the original JULES model. The difference in mean annual ET between the original and the coupled model is approximately $150\ \mathrm{mm/yr}$ and is indicative of the potential error in surface flux estimations of LSMs without vegetation dynamics. The proposed modelling scheme offers a

more accurate description of vegetation dynamics over croplands, which is crucial for projecting potential changes in the hydrological cycle under different climate change scenarios.

**The combined impacts of land-use and climate change will be greater than the impacts posed by land-use change and climate change individually, on hydrological components:**

The impact of LUCC and climate change future projections on the hydrological response of the UG river basin is quantified, by calculating annual variations in hydrological components (stream flow, evapotranspiration and soil moisture) during the simulation period (2000–2035).

An analysis of CMIP5 precipitation datasets reveals large variations between different GCM outputs. By the end of the century, the multi-model mean (MMM) future projections of precipitation point towards an intensified seasonal cycle with stronger wet and dry seasons. The CMIP5 meteorological variables were bias corrected and subsequently used to force JULES and generate future hydrological projections for the UG basin (up to year 2035).

Severe increases in the high extremes of flows are being projected for the nearby future (period 2030–2035), under future land-cover and climate change scenarios. The changes in all examined hydrological components are greater in the combined land-use and climate change scenario. During the period 2030–2035, the MMM $Q_5$ is projected to increase by 41% under RCP4.5 and by 62% under RCP8.5, relative to the period 2000-2005. Nevertheless, climate change is the main driver of those changes between the historic and near term future scenarios explored in this study. If no dramatic land-use changes take place in the nearby future, the main alterations in hydrological fluxes are expected to arise from the change in the meteorology. It is not therefore land-use change per se that is expected to drive changes in the near-term future water resources of the UG basin. However, changing practices within certain types of land use could have major impacts on future water demand and availability.

Extremely high changes in ET (100% order of magnitude) and SM fluxes (200% order of magnitude) arising in various parts of the catchment are cancelled out when results are presented in terms of spatially averaged values. The main differences appear between the north and south regions of the catchment.

Despite the strong inter-model uncertainties of historic and future projections, this work is expected to help in prioritizing mitigation and adaptation strategies and regional land-use planning to improve northern India's water resources.

## 8.3 Limitations and future directions of research

A key limitation of the approach followed for the generation of future LUCC scenarios is that historic trend analysis only considers two discrete points in time. Moreover, Markov chain analysis is unable to assimilate ancillary data, which may constrain the rate and direction of change. Land-cover change is driven by socio-economic and biophysical factors (Lambin *et al.*, 2001). Therefore, to make valid predictions about future land-cover change it is necessary to understand the causes of historic land-cover change. For instance, given the observed dependence of the agricultural sector on irrigation, one may hypothesize that an area of land located near an irrigation canal or well is more likely to be converted to cropland than land without a reliable water source. Furthermore, the expansion of cropland may be limited by the presence of the Himalayan mountain range in the north of the basin, where factors such as elevation and slope may impose physical limits on crop growth. Understanding the objectives of national and international policies on afforestation in the region may provide a means to constrain future scenarios of change. These examples demonstrate that land-cover change cannot be modelled unless the underlying driving factors are taken into account.

Future work could improve the prediction of land cover by applying modelling approaches that utilize biophysical and socio-economic datasets. This is a possible way to reduce uncertainty and provide more accurate projections for the future status of land cover in the UG basin. In addition, the development of historic land-use maps in seasonal or even monthly time-scales (if data become available), as opposed to the annual scales presented here, could provide useful insights on the study of past land-use change trends.

The unavailability of historical flow data is one of the main constraints in this work. This limitation severely impacts the historic and future hydrological model simulations, by restricting the streamflow validation in only one sub-catchment of the study area, and over a period of 10 years. Due to strict flow-data sharing policies posed by India, there is a limited number of water resources research studies and the lack of accessible data has been a great challenge for the present research. Ongoing debates about this issue have not managed to reform policies and resolve it yet, and this is something all future studies will have to deal with.

The sensitivity analysis of JULES explored just a few parameter and structural modelling changes,

while the vast majority of parameters was held constant. However, the results showed that there is much room left to improve JULES so that it can function as a proper hydrological model and potential ways of addressing the model's shortcomings were discussed.

At the daily time-scale, the simple runoff routing mechanism introduced uncertainty to the model outputs. The errors were reduced when looking at the outputs on a monthly basis, which smoothed the impact of the simple routing scheme. However, the lack of river channels, wetlands, or groundwater stores in JULES, along with the fact that the model assumes direct runoff into the river, increased the errors in the model outputs. This is related to the vertical structure of the model, which does not allow horizontal water movements, or any horizontal flux exchange in both surface and subsurface levels. The lack of groundwater component and its interactions with surface fluxes is crucial for the accurate representation of flux partitioning and is further affecting the model's performance. The free gravity drainage assumption does not allow for any amount of moisture to be drawn from the soil when the water table in the field drops below the maximum soil depth. Coupling JULES to a groundwater model was not explored during the course of this thesis due to time constraints. It would have been a large project considering the lack of prior experience in the catchment, and the difficulties of parameterising the model with limited data.

The importance of in-situ observational datasets has been recognized across the land-surface modelling community. Specifically for India, where surface fluxes are poorly constrained, new observations could be brought together with historical data, to develop a more integrated understanding of land surface processes. Based on comparisons with new observational datasets, JULES could be evaluated and its parameters further constrained for the monsoon tropics.

The water management (hydropower, irrigation, industrial and domestic usage) and the dam structures play a very significant role in the water balance of this region. The impacts of changing management practices in terms of water usage and storage could be much more important than the impacts posed by climate change or land-use change in terms of future water availability and demand. This has not been taken into account in the modelling work undertaken in the present thesis.

The role of feedbacks between the carbon and the water cycle under climate change conditions has not been extensively discussed in this research. As mentioned earlier, increased $CO_2$ concentrations in the future would mean that leaf stomatal conductance would decrease. Plants would get sufficient $CO_2$

uptake and this would improve their water use efficiency by reduced transpiration rates. On the contrary, the increase in air temperature that is being projected for the future would lead to higher potential evaporation as warmer air can hold more moisture, counteracting the above mentioned effects of increased $CO_2$ concentrations. The importance of these feedbacks between the carbon and the water cycle is significant under rising $CO_2$ and temperature conditions, given that their impacts are likely to affect both food security and water availability. Further, the simulations of future climate scenarios (Chapter 7) took into account future projections of the meteorological variables used to force JULES, but did not account for changes in the $CO_2$ concentrations. It would be interesting for future work to look into the relative effect of changes in precipitation, temperature and $CO_2$ concentration on the water cycle.

Neither JULES nor the new coupled scheme (JULES-Info) account for irrigation. There is lack of available spatial data that separate between rain-fed and irrigated areas of different crops whilst giving timely information regarding the amount of irrigation applied throughout the year, over the study area. Besides, the lack of sub-grid heterogeneity means that in this study the model could not simulate irrigation practices, as irrigation would rarely cover an entire gridbox of $0.1^{\circ}$. However, it is recognised that the impact of irrigation is an extremely important aspect of hydrological modelling in a catchment that is 60% occupied by crops. Work is currently under development, both in respect to more accurate land-use classification of irrigated/rain-fed areas and irrigation representation in JULES. A very interesting future direction of research that would shine light onto water management practices and their feedbacks to the climate would be to compare the behaviour of various hydrological fluxes in irrigated versus rain-fed areas.

The most recent version of JULES (v4.1) includes the JULES-Crop model (currently undocumented) and an interesting suggestion for future work would be the comparison of JULES-Crop and JULES-Info. It is worth exploring how potential differences in the way that crop cycles are represented (global version of JULES-Crop vs locally parameterised JULES-Info), are affecting the model results.

In terms of climate projections, as previously mentioned, the strong inter-model uncertainties of GCM-derived data are attributed to inherent limitations of GCMs (Raty *et al.*, 2014). However, these uncertainties were possibly amplified by the delta-change bias correction approach followed here and are posing a limitation on the confidence of the climate change impacts results. This method assumes a constant GCM bias through time, does not retain the change in variability of climatic variables, and does

not change the temporal sequence of wet/dry days (Fowler *et al.*, 2007).

Alternative directions for future work worthwhile to explore could include utilisation of different bias-correction approaches (e.g. dynamic downscaling based on regional climate models), consideration of additional pathway scenarios (RCP2.6 and RCP6) and usage of data outputs from more GCM models, providing they become available.

Finally, this work has not looked into combining the uncertainties arising from each of the modelling components (historic and future land-use maps, hydrological simulations, climate projections, forcing data), to assess whether they result in compounded uncertainty and what is the contribution of each modelling aspect to the overall uncertainty. Such analysis in the future, could provide useful insights in identifying and tackling the largest sources of uncertainties.

# Bibliography


Agarwal, C., Green, G. M., Grove, J. M., Evans, T. P., and Schweik, C. M. (2002). A review and assessment of land-use change models: Dynamics of space, time, and human choice. Technical Report NE-297, U.S. Department of Agriculture.

Aggarwal, P., Kalra, N., Chander, S., and Pathak, H. (2006a). InfoCrop: A dynamic simulation model for the assessment of crop yields, losses due to pests, and environmental impact of agro-ecosystems in tropical environments. I. model description. *Agricultural Systems*, **89**(1), 1 – 25.

Aggarwal, P., Banerjee, B., Daryaei, M., Bhatia, A., Bala, A., Rani, S., Chander, S., Pathak, H., and Kalra, N. (2006b). InfoCrop: A dynamic simulation model for the assessment of crop yields, losses due to pests, and environmental impact of agro-ecosystems in tropical environments. II. performance of the model. *Agricultural Systems*, **89**(1), 47 – 67.

Agropedia (2013). Agriculture portal of IIT Kanpur. Accessed online Oct 2013.

Alcamo, J., R., L., and Kreileman, E. (1998). *Global change scenarios of the 21st century, results from the IMAGE 2.1 model.* Pergamon, Kidlington, UK.

Amarasinghe, U., A., Shah, T., Anand, B. K., and Hugh, T. (2007). *India's water future to 2025-2050: business-as-usual scenario and deviations*. International Water Management Institute.

Anderson, J. R., Hardy, E. E., and Roach, John T.and Witmer, R. E. (1976). A land use and land cover classification system for use with remote sensor data. *U.S. Geological Survey Professional Paper*, **964**.

Arora, V. K. (2003). Simulating energy and carbon fluxes over winter wheat using coupled land surface and terrestrial ecosystem models. *Agricultural and Forest Meteorology*, **118**, 21 – 47.

Ashrit, R., Douville, H., and Kumar, K. (2003). Response of the Indian Monsoon and ENSO-Monsoon Teleconnection to Enhanced Greenhouse Effect in the CNRM Coupled Model. *Journal of the Meteorological Society of Japan. Ser. II*, **81**(4), 779–803.

Bannari, A., Morin, D., Bonn, F., and Huete, A. (1995). A review of Vegetation Indices. *Remote Sensing Reviews*, **13**, 95–120.

Bell (1974). Markov analysis of land use change – an application of stochastic processes to remotely sensed data. *Socio-economic Planning Sciences*, **8(6)**, 311–316.

Best, M. J., Pryor, M., Clark, D. B., Rooney, G. G., Essery, R. L. H., Menard, C. B., Edwards, J. M., Hendry, M. A., Porson, A., Gedney, N., Mercado, L. M., Sitch, S., Blyth, E., Boucher, O., Cox, P. M., Grimmond, C. S. B., and Harding, R. J. (2011). The Joint UK Land Environment Simulator (JULES), Model description - Part 1: Energy and water fluxes. *Geoscientific Model Development Discussions*, **4**(1), 595–640.

Bhagyanagar, R., Kawal, B. M., Dwarakish, G. S., and Surathkal, S. (2012). Land use/land cover change and urban expansion during 1983-2008 in the coastal area of Dakshina Kannada district, South India. *Journal of Applied Remote Sensing*, **6**(1).

Bharati, L., Lacombe, G., Gurung, P., Jayakody, P., Hoanh, C. T., and Smakhtin, V. (2011). The impact of water infrastructure and climate change on the hydrology of the Upper Ganges River basin. *International Water Management Institute; Colombo; Sri Lanka*.

Bhat, G. S. (2006). The Indian drought of 2002 - a sub-seasonal phenomenon? *Quarterly Journal of the Royal Meteorological Society*, **132**(621), 2583–2602.

Bhatta, B. (2009). Analysis of urban growth pattern using remote sensing and GIS: a case study of Kolkata, India. *International Journal of Remote Sensing*, **30**(18), 4733–4746.

Biggs, T., Gaur, A., Scott, C., Thenkabail, P., Rao, P., Gumma, M., Acharya, S., and Turral, H. (2007). Closing of the Krishna basin: Irrigation, streamflow depletion and macroscale hydrology. *Colombo, Sri Lanka: International Water Management Institute, Research Report 111*, page 24.

Black, E., Vidale, P. L., Verhoef, A., Cuadra, S. V., Osborne, T., and den Hoof, C. V. (2012). Cultivating C4 crops in a changing climate: sugarcane in Ghana. *Environmental Research Letters*, **7**(4), 044027.

Blyth, E., Gash, J., Lloyd, A., Pryor, M., Weedon, G. P., and Shuttleworth, J. (2010). Evaluating the JULES Land Surface Model Energy Fluxes Using FLUXNET Data. *J. Hydrometeor*, **11**(2), 509–519.

Blyth, E., Clark, D. B., Ellis, R., Huntingford, C., Los, S., Pryor, M., Best, M., and Sitch, S. (2011). A comprehensive set of benchmark tests for a land surface model of simultaneous fluxes of water and carbon at both the global and seasonal scale. *Geoscientific Model Development*, **4**(2), 255–269.

Boegh, E., Thorsen, M., Butts, M., Hansen, S., Christiansen, J., Abrahamsen, P., Hasager, C., Jensen, N., van der Keur, P., Refsgaard, J., Schelde, K., Soegaard, H., and Thomsen, A. (2004). Incorporating remote sensing data in physically based distributed agro-hydrological modelling. *Journal of Hydrology*, **287**, 279 – 299.

Bollasina, M. A., Ming, Y., and Ramaswamy, V. (2013). Earlier onset of the Indian monsoon in the late twentieth century: The role of anthropogenic aerosols. *Geophys. Res. Lett.*, **40**(14), 3715–3720.

Bounoua, L., DeFries, R., Collatz, G., Sellers, P., and Khan, H. (2002). Effects of land cover conversion on surface climate. *Climatic Change*, **52**(1-2), 29–64.

Bourne, L. (1976). Monitoring change and evaluating the impact of planning policy on urban structure: a Markov chain experiment. *Plan Canada*, **16**, 5–14.

Bousquet, F. and Page, C. L. (2004). Multi-agent simulations and ecosystem management: a review. *Ecological Modelling*, **176**, 313 – 332.

Bouwman, A., Kram, T., and Goldewijk, K. (2006). *Integrated Modelling of Global Environmental Change: An overview of Image 2.4*. Netherlands Environmental Assessment Agency (MNP), Bilthoven. publication number 500110002/2006.

Breuer, L., Eckhardt, K., and Frede, H.-G. (2003). Plant parameter values for models in temperate climates. *Ecological Modelling*, **169**, 237 – 293.

Briassoulis, H. (2000). Analysis of land use change: theoretical and modeling approaches. In WebBook of Regional Science Ed. S Loveridge.

Briscoe, J. (2005). India's water economy: Bracing for a turbulent future. *World Bank Report No. 34750-IN, viiixi*.

Brooks, R. H. and Corey, A. . (1964). Hydraulic properties of porous media. *Hydrology Papers, Colorado State University*, **3**.

Brown, D., Pijanowski, B., and Duh, J. (2000). Modeling the relationships between land use and land cover on private lands in the Upper Midwest, USA. *Journal of Environmental Management*, **59**(4), 247 – 263.

Brown, D., Walker, R., Manson, S., and Seto, K. (2004). Modeling land use and land cover change. In G. Gutman, A. C. Janetos, C. O. Justice, E. F. Moran, J. F. Mustard, R. R. Rindfuss, D. Skole, I. Turner, Billy Lee, and M. A. Cochrane, editors, *Land Change Science*, volume 6 of *Remote Sensing and Digital Image Processing*, pages 395–409. Springer Netherlands.

Bultot, F., Dupriez, G., and Gellens, D. (1990). Simulation of land use changes and impacts on the water balance – A case study for Belgium. *Journal of Hydrology*, **114**, 327 – 348.

Buytaert, W., Iñiguez, V., Celleri, R., De Bievre, B., Wyseure, G., and Deckers, J. (2006). Analysis of the water balance of small paramo catchments in South Ecuador. In *Environmental Role of Wetlands in Headwaters*, pages 271–281.

Calvet, J.-C. and Soussana, J.-F. (2001). Modelling CO2-enrichment effects using an interactive vegetation SVAT scheme. *Agricultural and Forest Meteorology*, **108**(2), 129 – 152.

Calvet, J.-C., Noilhanm, J., Roujean, J.-L., Bessemoulin, P., Cabelguenne, M., Olioso, A., and Wigneron, J.-P. (1998). An interactive vegetation SVAT-model tested against data from six contrasting sites. *Agricultural and Forest Meteorology*, **92**, 73–95.

Campling, P., Gobin, A., Beven, K., and Feyen, J. (2002). Rainfall-runoff modelling of a humid tropical catchment: the TOPMODEL approach. *Hydrological Processes*, **16**(2), 231–253.

Casanova, J. J. and Judge, J. (2008). Estimation of energy and moisture fluxes for dynamic vegetation using coupled SVAT and crop-growth models. *Water Resources Research*, **44**(7), n/a–n/a.

Chander, G. and Markham, B. (2003). Revised Landsat-5 TM radiometric calibration procedures and postcalibration dynamic ranges. *IEEE Transactions on Geosience and Remote Sensing*, **41**(11, Part 2), 2674–2677.

Chander, G., Markham, B. L., and Barsi, J. A. (2007). Revised Landsat-5 Thematic Mapper radiometric calibration. *IEEE Transactions on Geosience and Remote Sensing*, **4**(3), 490–494.

Charlson, R. J., Schwartz, S. E., Hales, J. M., Cess, R. D., Coakley, J. A., Hansen, J. E., and Hofmann, D. J. (1992). Climate forcing by anthropogenic aerosols. *Science*, **255**(5043), 423–430.

Chaturvedi, R. K., Joshi, J., Jayaraman, M., Bala, G., and Ravindranath, N. (2012). Multi-model climate change projections for India under representative concentration pathways. *Current Science*, **103 , (7)**.

Chavez, P. (1988). An improved dark-object subtraction technique for atmospheric scattering correction of multispectral data. *Remote Sensing of Environment*, **24**(3), 459 – 479.

Chavez, P. (1989). Radiometric calibration of Landsat Thematic Mapper multispectral images. *Photogrammetric Engineering and Remote Sensing*, **55**(9), 1285–1294.

Chavez, P. (1996). Image-based atmospheric corrections revisited and improved. *Photogrammetric Engineering and Remote Sensing*, **62**(9), 1025–1036.

Cherchi, A., Alessandri, A., Masina, S., and Navarra, A. (2011). Effects of increased CO2 levels on monsoons. *Climate Dynamics*, **37**(1-2), 83–101.

Chesworth, W., editor (2008). *Encyclopedia of Soil Science*. Springer.

Christensen, E., Jensen, J., Ramsey, E., and Mackey, H. (1988). Aircraft MSS data registration and vegetation classification for wetland change detection. *International Journal of Remote Sensing*, **9**(1), 23–38.

Chrysoulakis, N., Abrams, M., Feidas, H., and Arai, K. (2010). Comparison of atmospheric correction methods using ASTER data for the area of Crete, Greece. *International Journal of Remote Sensing*, **31**(24), 6347–6385.

Claessens, L., Schoorl, J., Verburg, P., Geraedts, L., and Veldkamp, A. (2009). Modelling interactions and feedback mechanisms between land use change and landscape processes. *Agriculture, Ecosystems & Environment*, **129**(13), 157 – 170.

Clark, D., Harris, P., Pryor, M., and Hendry, M. (2010). Joint UK Land Environment Simulator (JULES) Version 2.2 User Manual. NERC / Centre for Ecology & Hydrology.

Clark, D. B. and Gedney, N. (2008). Representing the effects of subgrid variability of soil moisture on runoff generation in a land surface model. *Journal of Geophysical Research-Atmospheres*, **113**, D10111.

Clark, D. B., Mercado, L. M., Sitch, S., Jones, C. D., Gedney, N., Best, M. J., Pryor, M., Rooney, G. G., Essery, R. L. H., Blyth, E., Boucher, O., Harding, R. J., Huntingford, C., and Cox, P. M. (2011). The Joint UK Land Environment Simulator (JULES), model description - Part 2: Carbon fluxes and vegetation dynamics. *Geoscientific Model Development*, **4**(3), 701–722.

Clarke, K., Hoppen, S., and Gaydos, L. (1997). A self-modifying cellular automaton model of historical urbanization in the San Francisco bay area. *Environment and Planning B: Planning and Design*, **24**(2), 247–261. cited By (since 1996)458.

Cohen, W. and Goward, S. (2004). Landsat's role in ecological applications of remote sensing. *Biosience*, **54**(6), 535–545.

Collatz, Ball, Grivet, C., and Berry, J. A. (1991). Physiological and environmental regulation of stomatal conductance, photosynthesis and transpiration: a model that includes a laminar boundary layer. *Agricultural and Forest Meteorology*, **54**(2-4), 107–136.

Collier, J. C. and Zhang, G. J. (2009). Aerosol direct forcing of the summer Indian monsoon as simulated by the NCAR CAM3. *Climate Dynamics*, **32**(2-3), 313–332.

Congalton, R. G. (1991). A review of assessing the accuracy of classifications of remotely sensed data. *Remote Sensing of Environment*, **37**(1), 35 – 46.

Cox, P., Huntingford, C., and Harding, R. (1998). A canopy conductance and photosynthesis model for use in a GCM land surface scheme. *Journal of Hydrology*, **212**(1-4), 79–94.

Cox, P. M., Betts, R. A., Bunton, C. B., Essery, R. L. H., Rowntree, P. R., and Smith, J. (1999). The impact of new land surface physics on the gcm simulation of climate and climate sensitivity. *Climate Dynamics*, **15**(3), 183–203.

Cox, P. M., Betts, R. A., Jones, C. D., Spall, S. A., and Totterdell, I. J. (2000). Acceleration of global warming due to carbon-cycle feedbacks in a coupled climate model. *Nature*, **408**, 184–187.

Dai, Y. e. a. (2003). The Common Land Model. *Bulletin of the American Meteorological Society*, **84**.

Dash, S. K., Kulkarni, M. A., Mohanty, U. C., and Prasad, K. (2009). Changes in the characteristics of rain events in India. *Journal of Geophysical Research: Atmospheres*, **114**(D10).

de Haan, J., Hovenier, J., Kokke, J., and van Stokkom, H. (1991). Removal of atmospheric influences on satellite-borne imagery: A radiative transfer approach. *Remote Sensing of Environment*, **37**(1), 1 – 21.

de Noblet-Ducoudré, N., Gervois, S., Ciais, P., Viovy, N., Brisson, N., Seguin, B., and Perrier, A. (2004). Coupling the Soil-Vegetation-Atmosphere-Transfer Scheme ORCHIDEE to the agronomy model STICS to study the influence of croplands on the European carbon and water budgets. *Agronomie*, **24**(6-7), 397–407.

Dharssi, I., Vidale, P. L., Verhoef, A., Macpherson, B., Jones, C., and Best, M. (2009). New soil physical properties implemented in the Unified Model at PS18. Technical report, UK Met Office, Exeter.

Dickinson, R. E., Henderson-Sellers, A., and Kennedy, P. (1993). Biosphere/Atmosphere Transfer Scheme (BATS) version 1e as coupled to the NCAR Community Climate Model, Tech. rep., Climate and Global Dynamics Division, National Center for Atmospheric Research, Boulder, Colorado.

Dingman, S. L. (2002). *Physical hydrology*. Upper Saddle River, N.J. : Prentice Hall.

Douglas, E., Beltran-Przekurat, A., Niyogi, D., Sr., R. P., and Vorosmarty, C. (2009). The impact of agricultural intensification and irrigation on land–atmosphere interactions and Indian monsoon precipitation: A mesoscale modeling perspective. *Global and Planetary Change*, **67**, 117 – 128.

Douglas, E. M., Niyogi, D., Frolking, S., Yeluripati, J. B., Pielke, R. A., Niyogi, N., Vorosmarty, C. J., and Mohanty, U. C. (2006). Changes in moisture and energy fluxes due to agricultural land use and irrigation in the Indian Monsoon Belt. *Geophysical Research Letters*, **33**(14).

Drewett, J. (1969). A stochastic model of the land conversion process. *Regional Studies*, **3**, 269–280.

Egea, G., Verhoef, A., and Vidale, P. L. (2011). Towards an improved and more flexible representation of water stress in coupled photosynthesis - stomatal conductance models. *Agricultural and Forest Meteorology*, **151**(10), 1370 – 1384.

Ehlers, M., Jadkowski, M., Howard, R., and Brostuen, D. (1990). Application of SPOT data for regional growth analysis and local-planning. *Photogrammetric Engineering and Remote Sensing*, **56**(2), 175–180.

Encyclopaedia Britannica inc. (2012a). http://www.britannica.com/EBchecked/topic/707931/Lixisol Accessed online Oct 2012.

Encyclopaedia Britannica inc. (2012b). http://www.britannica.com/EBchecked/topic/496182/Regosol Accessed online Oct 2012.

Essery, R., Best, M., Betts, R., and Taylor, C. (2003). Explicit representation of subgrid heterogeneity in a GCM land surface scheme. *Journal of hydrometeorology*, **4**(3), 530–543.

Evenson, R. E. and Gollin, D. (2003). Assessing the impact of the Green Revolution, 1960 to 2000. *Science (New York, N.Y.)*, **300**(5620), 758–62.

Fan, Y. and Miguez-Macho, G. (2011). A simple hydrologic framework for simulating wetlands in climate and earth system models. *Climate Dynamics*, **37**(1-2), 253–278.

FAO (2009). FAO/IIASA/ISRIC/ISSCAS/JRC. Harmonized World Soil Database (version 1.1). FAO, Rome, Italy and IIASA, Laxenburg, Austria.

FAO (2010). *Global Forest Resources Assessment 2010: Main Report*. FAO forestry paper Series. Food and Agriculture Organization of the United Nations.

FAO (2013). AQUASTAT. Information System on Water and Agriculture. Accessed online Oct 2013.

Farouki, O. (1981). Thermal properties of soils in cold regions. *CRREL Monograph.*, **81**, 134.

Fatima, H., Upadhyaya, H. C., and Sharma, O. P. (2010). Impact of carbonaceous aerosols over Indian Monsoon Rainfall. In Krishnamurti, TN and Kim, J and Moriyama, T, editor, *Remote Sensing and Modeling of the Atmosphere, Oceans, and Interactions III*, volume 7856 of *Proceedings of SPIE*. Conference on Remote Sensing and Modeling of the Atmosphere, Oceans, and Interactions III, Incheon, South Korea, Oct 13-14, 2010.

Findell, K. L., Shevliakova, E., Milly, P. C. D., and Stouffer, R. J. (2007). Modeled impact of anthropogenic land cover change on climate. *J. Climate*, **20**(14), 3621–3634.

Finn, M., Reed, M., and Yamamoto, K. (2012). A Straight Forward Guide for Processing Radiance and Reflectance for EO-1 ALI, Landsat 5 TM, Landsat 7 ETM+, and ASTER. Unpublished Report from USGS/Center of Excellence for Geospatial Information Science.

Fischer, G. and Sun, L. (2001). Model based analysis of future land-use development in China . *Agriculture, Ecosystems & Environment*, **85**, 163 – 176. Predicting Land-Use Change.

Foley, J. A., DeFries, R., Asner, G. P., Barford, C., Bonan, G., Carpenter, S. R., Chapin, F. S., Coe, M. T., Daily, G. C., Gibbs, H. K., Helkowski, J. H., Holloway, T., Howard, E. A., Kucharik, C. J., Monfreda, C., Patz, J. A., Prentice, I. C., Ramankutty, N., and Snyder, P. K. (2005). Global consequences of land use. *Science*, **309**(5734), 570–574.

Forest Survey of India (2009). State of forest report. *Ministry of Environment and Forests, Govt. of India*.

Fowler, H. J., Blenkinsop, S., and Tebaldi, C. (2007). Linking climate change modelling to impacts studies: recent advances in downscaling techniques for hydrological modelling. *International Journal of Climatology*, **27**(12), 1547–1578.

Ganguly, D., Rasch, P. J., Wang, H., and Yoon, J.-H. (2012). Climate response of the South Asian monsoon system to anthropogenic aerosols. *Journal of Geophysical Research-Atmospheres*, **117**.

Garcia-Quijano, J. F. and Barros, A. P. (2005). Incorporating canopy physiology into a hydrological model: photosynthesis, dynamic respiration, and stomatal sensitivity. *Ecological Modelling*, **185**(1), 29 – 49.

Geoghegan, J., Villar, S., Klepeis, P., Mendoza, P., Ogneva-Himmelberger, Y., Chowdhury, R., Turner, B., and Vance, C. (2001). Modeling tropical deforestation in the southern Yucatan peninsular region: comparing survey and satellite data. *Agriculture, ecosystems and environment.*, **85**(1/3), 25–46.

GMAO (2004). Global Modeling and Assimilation Office. File Specification for GEOS-DAS Gridded Output Version 5.3. Document No. GMAO-1001v5.3. Technical report.

GOI (2010). Groundwater Scenario of India 2009–10. Technical report, Central Ground Water Board, Ministry of Water Resources.

Goswami, B. N., Venugopal, V., Sengupta, D., Madhusoodanan, M. S., and Xavier, P. K. (2006). Increasing Trend of Extreme Rain Events Over India in a Warming Environment. *Science*, **314**(5804), 1442–1445.

Goward, S., Arvidson, T., and Williams, D. (2006). Historical record of Landsat global coverage: Mission operations, NSLRSDA, and international cooperator stations. *Photogrammetric Engineering & Remote Sensing*, **72**(10), 1155–1169.

Gulati, S. and Sharma, S. (2000). *Population pressure and deforestation in India*. Delhi : Population Research Centre, Institute of Economic Growth, University Enclave.

Guo, Z., Dirmeyer, P. A., Koster, R. D., Sud, Y. C., Bonan, G., Oleson, K. W., Chan, E., Verseghy, D., Cox, P., Gordon, C. T., McGregor, J. L., Kanae, S., Kowalczyk, E., Lawrence, D., Liu, P., Mocko, D., Lu, C.-H., Mitchell, K., Malyshev, S., McAvaney, B., Oki, T., Yamada, T., Pitman, A., Taylor, C. M., Vasic, R., and Xue, Y. (2006). GLACE: The Global Land–Atmosphere Coupling Experiment. Part II: Analysis. *J. Hydrometeor*, **7**(4), 611–625.

Hadjimitsis, D. G., Clayton, C. R. I., and Hope, V. S. (2004). An assessment of the effectiveness of atmospheric correction algorithms through the remote sensing of some reservoirs. *International Journal of Remote Sensing*, **25**(18), 3651–3674.

Hadjimitsis, D. G., Themistocleous, K., Agapiou, A., and Clayton, C. (2009). Monitoring Archaeological Site Landscapes in Cyprus using Multi-temporal Atmospheric Corrected Image Data. *International Journal of Architectural Computing*, **7**, 121138.

Hadjimitsis, D. G., Papadavid, G., Agapiou, A., Themistocleous, K., Hadjimitsis, M. G., Retalis, A., Michaelides, S., Chrysoulakis, N., Toulios, L., and Clayton, C. R. I. (2010). Atmospheric correction for satellite remotely sensed data intended for agricultural applications: impact on vegetation indices. *Natural Hazards and Earth System Sciences*, **10**(1), 89–95.

Hall, F., Strebel, D., Nickeson, J., and Goetz, S. (1991). Radiometric rectification: Toward a common radiometric response among multidate, multisensor images. *Remote Sensing of Environment*, **35**(1), 11 – 27.

Haverkamp, S., Fohrer, N., and Frede, H.-G. (2005). Assessment of the effect of land use patterns on hydrologic landscape functions: a comprehensive GIS-based tool to minimize model uncertainty resulting from spatial aggregation. *Hydrological Processes*, **19**(3), 715–727.

HCTN24 (2001). *Description of the "TRIFFID" Dynamic Global Vegetation Model. Hadley Center Technical Note 24*. Author: Cox, P.M. Hadley Centre, Met Office., London Road, Bracknell, Berks, RG122SY, UK.

Herring, S. C., Hoerling, M. P., Peterson, T. C., and Stott, P. A. (2014). Explaining Extreme Events of 2013 from a Climate Perspective. *Bulletin of the American Meteorological Society*, **95 (5)**, S1–S96.

Hu, C., Muller-Karger, F., Andrefouet, S., and Carder, K. (2001). Atmospheric correction and cross-calibration of LANDSAT-7/ETM+ imagery over aquatic environments: A multiplatform approach using SeaWiFS/MODIS. *Remote Sensing of Environment*, **78(2-Jan)**, 99–107.

Hu, Z.-Z., Latif, M., Roeckner, E., and Bengtsson, L. (2000). Intensified Asian Summer Monsoon and its variability in a coupled model forced by increasing greenhouse gas concentrations. *Geophysical Research Letters*, **27**(17), 2681–2684.

Huffman, G. J. and Bolvin, D. T. (2013). TRMM and other data precipitation data set documentation. Accessed: Nov 2013.

Huffman, G. J., Bolvin, D. T., Nelkin, E. J., Wolff, D. B., Adler, R. F., Gu, G., Hong, Y., Bowman, K. P., and Stocker, E. F. (2007). The TRMM Multisatellite Precipitation Analysis (TMPA): Quasi-Global, Multiyear, Combined-Sensor Precipitation Estimates at Fine Scales. *J. Hydrometeor*, **8**(1), 38–55.

Huguenin, R., Karaska, M., VanBlaricom, D., and Jensen, J. (1997). Subpixel classification of bald cypress and tupelo gum trees in Thematic Mapper imagery. *Photogrammetric Engineering and Remote Sensing*, **63**(6), 717–725.

Hundecha, Y. and Bardossy, A. (2004). Modeling of the effect of land use changes on the runoff generation of a river basin through parameter regionalization of a watershed model. *Journal of Hydrology*, **292**, 281 – 295.

ICAR (2013). Crop calendar of major crops. Accessed online Oct 2013.

IIT Kanpur - Gangapedia (2013). Accessed online Jan 2013.

Immerzeel, W. W., van Beek, L. P. H., and Bierkens, M. F. P. (2010). Climate change will affect the Asian water towers. *Science*, **328**(5984), 1382–1385.

Indian National Science Academy, C. A. o. S. (2001). Growing populations, changing landscapes: Studies from India, China, and the United States. *The National Academies Press.*

IPCC (2007). Climate Change 2007: Impacts, Adaptation, and Vulnerability. Contribution of Working Group II to the Fourth Assessment Report of the Intergovernmental Panel on Climate Change.

IPCC (2013). Climate Change 2013: The Physical Science Basis. Contribution of Working Group I to the Fifth Assessment Report of the Intergovernmental Panel on Climate Change .

IPCC (2014a). Climate Change 2014: Impacts, Adaptation, and Vulnerability. Part A: Global and Sectoral Aspects. Contribution of Working Group II to the Fifth Assessment Report of the Intergovernmental Panel on Climate Change.

IPCC (2014b). Climate Change 2014: Impacts, Adaptation, and Vulnerability. Part B: Regional Aspects. Contribution of Working Group II to the Fifth Assessment Report of the Intergovernmental Panel on Climate Change .

Jain, S. K., Agarwal, P. K., and Singh, V. P. (2007). *Hydrology and Water Resources of India. Series: Water Science and Technology Library, Vol. 57*. Springer.

Jakubauskas, M. E. (1996). Thematic Mapper characterization of lodgepole pine seral stages in Yellowstone National Park, USA. *Remote Sensing of Environment*, **56**(2), 118 – 132.

Jarvis, A., Reuter, H., Nelson, A., and Guevara, E. (2008). Hole-filled SRTM for the globe Version 4, available from the CGIAR-CSI SRTM 90m Database.

Jat, M. K., Garg, P. K., and Khare, D. (2008). Modelling of urban growth using spatial analysis techniques: a case study of Ajmer city (India). *International Journal of Remote Sensing*, **29**(2), 543–567.

Jenson, S. K. and Domingue, J. O. (1988). Extracting Topographic Structure from Digital Elevation Data for Geographic Information System Analysis. *Photogrammetric Engineering and Remote Sensing*, **54**, 15931600.

Joseph, P. V. and Simon, A. (2005). Weakening trend of the southwest monsoon current through peninsular India from 1950 to the present. *Current Science*, **89**, 687694.

Kaimowitz, D. and Angelsen, A. (1998). *Economic models of tropical deforestation: a review*. CIFOR, Bogor, Indonesia.

Kalantari, Z., Lyon, S. W., Folkeson, L., French, H. K., Stolte, J., Jansson, P.-E., and Sassner, M. (2014). Quantifying the hydrological impact of simulated changes in land use on peak discharge in a small catchment. *Science of The Total Environment*, (0), 741 – 754.

Kale, V. (2008). Palaeoflood hydrology in the Indian context. *J. Geol. Soc. India*, **71**, 56–66.

Kalnay, Kanamitsu, Kistler, *et al.* (1996). The NCEP/NCAR 40-Year Reanalysis Project. *Bulletin of the American Meteorological Society*, **77**.

Kalnay, E. and Cai, M. (2003). Impact of urbanization and land-use change on climate. *Nature*, **423**(6939), 528–531.

Kattge, J., Diaz, S., Lavorel, S., *et al.* (2011). TRY – a global of plant traits. *Global Change Biology*, **17**(9), 2905–2935.

Kaufman, Y. (1989). *Theory and Applications of Optical Remote Sensing*, chapter The atmospheric effect on remote sensing and its corrections, pages 336–428. Wiley & Sons, Inc., New York.

Kaufman, Y. J. and Sendra, C. (1988). Algorithm for automatic atmospheric corrections to visible and near-IR satellite imagery. *International Journal of Remote Sensing*, **9**(8), 1357–1381.

Kaushal, N. and Kansal, M. (2011). Overview of water allocation practices in Uttar Pradesh and Uttarakhand with a specific reference to future demands. *SAWAS*, **2**, 27–43.

Kharin, V., Zwiers, F., Zhang, X., and Wehner, M. (2013). Changes in temperature and precipitation extremes in the CMIP5 ensemble. *Climatic Change*, **119**(2), 345–357.

Kneizys, F. e. a. (1988). *Users Guide to LOWTRAN 7*. Air Force Geophysics Laboratory, Hanscom AFB, MA.

Knutson, T. R., Delworth, T. L., Dixon, K. W., Held, I. M., Lu, J., Ramaswamy, V., Schwarzkopf, M. D., Stenchikov, G., and Stouffer, R. J. (2006). Assessment of Twentieth-Century Regional Surface Temperature Trends using the GFDL CM2 Coupled Models. *J. Climate*, **19**(9), 1624–1651.

Knutti, R. and Sedlacek, J. (2013). Robustness and uncertainties in the new CMIP5 climate model projections. *Nature Clim. Change*, **3**(4), 369–373.

Koster, R., Dirmeyer, P., Guo, Z., and Bonan, G. (2004). Regions of strong coupling between soil moisture and precipitation. *Science*, **305**, 1138–1140.

Koster, R. D., Sud, Y. C., Guo, Z., *et al.* (2006). GLACE: The Global Land-Atmosphere Coupling Experiment. Part I: Overview. *J. Hydrometeor*, **7**(4), 590–610.

Kripalani, R. H., Oh, J. H., Kulkarni, A., Sabade, S. S., and Chaudhari, H. S. (2007). South Asian summer monsoon precipitation variability: Coupled climate model simulations and projections under IPCC AR4. *Theoretical and Applied Climatology*, **90**(3-4), 133–159.

Krishnamurthy, V. and Shukla, J. (2000). Intraseasonal and Interannual Variability of Rainfall over India. *J. Climate*, **13**(24), 4366–4377.

Kumar, R., Singh, R. D., and Sharma, K. D. (2005). Water resources of India. *Current Science*, **89**, 794–811.

Lambin, E. and Strahler, A. (1994). Change-vector analysis in multitemporal space - A tool to detect and categorize land-cover change processes using high temporal-resolution satellite data. *Remote Sensing of Environment*, **48**(2), 231–244.

Lambin, E., Rounsevell, M., and Geist, H. (2000). Are agricultural land-use models able to predict changes in land-use intensity? *Agriculture, Ecosystems & Environment*, **82**, 321 – 331.

Lambin, E. F. (1997). Modelling and monitoring land-cover change processes in tropical regions. *Progress in Physical Geography*, **21**(3), 375–393.

Lambin, E. F., Turner, B. L., Geist, H. J., *et al.* (2001). The causes of land-use and land-cover change: moving beyond the myths. *Global Environmental Change*, **11**, 261–269.

Lau, K., Kim, M., and Kim, K. (2006). Asian summer monsoon anomalies induced by aerosol direct forcing: the role of the Tibetan Plateau. *Climate Dynamics*, **26**(7-8), 855–864.

Lau, W., Waliser, D., and Goswami, B. N. (2005). *Intraseasonal Variability in the Atmosphere-Ocean Climate System*, chapter South Asian monsoon, pages 21–72. Springer – Jointly published with Praxis Publishing, UK.

Lau, W. K. M. and Kim, K.-M. (2011). The 2010 Pakistan Flood and Russian Heat Wave: Teleconnection of Hydrometeorological Extremes. *J. Hydrometeor*, **13**(1), 392–403.

Lavender, S. L., Taylor, C. M., and Matthews, A. J. (2010). Coupled Land-Atmosphere Intraseasonal Variability of the West African Monsoon in a GCM. *J. Climate*, **23**(21), 5557–5571.

Legesse, D., Vallet-Coulomb, C., and Gasse, F. (2003). Hydrological response of a catchment to climate and land use changes in Tropical Africa: case study South Central Ethiopia . *Journal of Hydrology*, **275**, 67 – 85.

Lei, H., Yang, D., Lokupitiya, E., and Shen, Y. (2010). Coupling land surface and crop growth models for predicting evapotranspiration and carbon exchange in wheat-maize rotation croplands. *Biogeosciences*, **7**(10), 3363–3375.

Lenney, M., Woodcock, C., Collins, J., and Hamdi, H. (1996). The status of agricultural lands in Egypt: The use of multitemporal NDVI features derived from Landsat TM. *Remote Sensing of Environment*, **56**(1), 8–20.

Lever, W. (1973). A Markov approach to the optimal size of cities in England and Wales. *Urban Studies*, **10**, 353–365.

Li, Y., Kinzelbach, W., Zhou, J., Cheng, G. D., and Li, X. (2011). Modelling irrigated maize with a combination of coupled-model simulation and ensemble forecasting, in the west of China. *Hydrology and Earth System Sciences Discussions*, **8**(2), 3841–3881.

Li, Y., Zhou, J., Kinzelbach, W., Cheng, G., Li, X., and Zhao, W. (2013). Coupling a SVAT heat and water flow model, a stomatal-photosynthesis model and a crop growth model to simulate energy, water and carbon fluxes in an irrigated maize ecosystem . *Agricultural and Forest Meteorology*, **176**(0), 10 – 24.

Liang, S., Fallah-Adl, H., Kalluri, S., JJ, J., Kaufman, Y. J., and Townshend, J. R. G. (1997). An operational atmospheric correction algorithm for Landsat Thematic Mapper imagery over the land. *Journal of Geophysical Research: Atmospheres*, **102**(D14), 17173–17186.

Liang, S., Fang, H., and Chen, M. (2001). Atmospheric correction of Landsat ETM+ land surface imagery. I. Methods. *Geoscience and Remote Sensing, IEEE Transactions on*, **39**(11), 2490–2498.

Liang, S., Fang, H., Morisette, J., Chen, M., Shuey, C., Walthall, C., and Daughtry, C. (2002). Atmospheric correction of Landsat ETM+ land surface imagery. II. Validation and applications. *Geoscience and Remote Sensing, IEEE Transactions on*, **40**(12), 2736–2746.

Liang, X., Lettenmaier, D. P., Wood, E. F., and Burges, S. J. (1994). A simple hydrologically based model of land surface water and energy fluxes for general circulation models. *Journal of Geophysical Research: Atmospheres*, **99**(D7), 14415–14428.

Lin, Y.-P., Hong, N.-M., Wu, P.-J., Wu, C.-F., and Verburg, P. H. (2007). Impacts of land use change scenarios on hydrology and land use patterns in the Wu-Tu watershed in Northern Taiwan . *Landscape and Urban Planning*, **80**(12), 111 – 126.

Liu, X., Ren, L., Yuan, F., Singh, V. P., Fang, X., Yu, Z., and Zhang, W. (2009). Quantifying the effect of land use and land cover changes on green water and blue water in northern part of China. *Hydrology and Earth System Sciences*, **13**(6), 735–747.

Liu, Y., Dorigo, W., Parinussa, R., de Jeu, R., Wagner, W., McCabe, M., Evans, J., and van Dijk, A. (2012). Trend-preserving blending of passive and active microwave soil moisture retrievals . *Remote Sensing of Environment*, **123**(0), 280 – 297.

Lorup, J. K., Refsgaard, J. C., and Mazvimavi, D. (1998). Assessing the effect of land use change on catchment runoff by combined use of statistical tests and hydrological modelling: Case studies from Zimbabwe . *Journal of Hydrology*, **205**, 147 – 163.

Loveland, T. R., Merchant, J. W., Ohlen, D. O., and Brown, J. F. (1991). Development of a land-cover characteristics database for the conterminous U.S. *Photogrammetric Engineering and Remote Sensing*, **57**, 1453–1463.

Lowell, K. (2001). An area-based accuracy assessment methodology for digital change maps. *International Journal of Remote Sensing*, **22**(17), 3571–3596.

Lu, D., Mausel, P., Brondizio, E., and Moran, E. (2002). Assessment of atmospheric correction methods for Landsat TM data applicable to Amazon basin LBA research. *International Journal of Remote Sensing*, **23**(13), 2651–2671.

Lu, D., Mausel, P., Brondizio, E., and Moran, E. (2004). Change detection techniques. *International Journal of Remote Sensing*, **25**(12), 2365–2401.

Luijten, J. (2003). A systematic method for generating land use patterns using stochastic rules and basic landscape characteristics: results for a Colombian hillside watershed. *Agriculture, Ecosystems & Environment*, **95**(23), 427 – 441.

Lutz, A. F., Immerzeel, W. W., Shrestha, A. B., and Bierkens, M. F. P. (2014). Consistent increase in High Asia's runoff due to increasing glacier melt and precipitation. *Nature Clim. Change*, **4**(7), 587–592.

Manoharan, A. and Murugappan, A. (2012). Estimation of runoff in an ungauged rural watershed, Tamil Nadu state, India. *International Journal of Engineering Science and Technology*, **4**.

Maraun, D., Wetterhall, F., Ireson, A. M., Chandler, R. E., Kendon, E. J., Widmann, M., Brienen, S., Rust, H. W., Sauter, T., Themesl, M., Venema, V. K. C., Chun, K. P., Goodess, C. M., Jones, R. G., Onof, C., Vrac, M., and Thiele-Eich, I. (2010). Precipitation downscaling under climate change: Recent developments to bridge the gap between dynamical models and the end user. *Reviews of Geophysics*, **48**(3).

Markham, B. L. and Barker, J. L. (1986). Landsat MSS and TM post-calibration dynamic ranges, exoatmospheric reflectance and at-satellite temperature. *EOSAT Landsat Technical Notes*, **1**, 3–8.

Maruyama, A. and Kuwagata, T. (2010). Coupling land surface and crop growth models to estimate the effects of changes in the growing season on energy balance and water use of rice paddies. *Agricultural and Forest Meteorology*, **150**(7-8), 919–930. cited By (since 1996)7.

Matthews, H. D., Weaver, A. J., Eby, M., and Meissner, K. J. (2003). Radiative forcing of climate by historical land cover change. *Geophysical Research Letters*, **30**(2), n/a–n/a.

May, W. (2002). Simulated changes of the Indian summer monsoon under enhanced greenhouse gas conditions in a global time-slice experiment. *Geophysical Research Letters*, **29**(7), 22–1–22–4.

May, W. (2004). Potential future changes in the Indian summer monsoon due to greenhouse warming: analysis of mechanisms in a global time-slice experiment. *Climate Dynamics*, **22**(4), 389–414.

Meehl, G. A. (1994). Influence of the Land Surface in the Asian Summer Monsoon: External Conditions versus Internal Feedbacks. *J. Climate*, **7**(7), 1033–1049.

Meehl, G. A., Arblaster, J. M., and Tebaldi, C. (2005). Understanding future patterns of increased precipitation intensity in climate model simulations. *Geophys. Res. Lett*, **32**, L18719.

Meehl, G. A., Arblaster, J. M., and Collins, W. D. (2008). Effects of Black Carbon Aerosols on the Indian Monsoon. *J. Climate*, **21**(12), 2869–2882.

Michener, W. and Houhoulis, P. (1997). Detection of vegetation changes associated with extensive flooding in a forested ecosystem. *Photogrammetric Engineering and Remote Sensing*, **63**(12), 1363–1374.

Mitchell and Hardy (2000). *Redesigning Rice Photosynthesis to Increase Yield, 1st Edition*. Elsevier.

Mo, X., Liu, S., Lin, Z., Xu, Y., Xiang, Y., and McVicar, T. (2005). Prediction of crop yield, water consumption and water use efficiency with a SVAT-crop growth model using remotely sensed data on the North China Plain . *Ecological Modelling*, **183**, 301 – 322.

Moghadam, H. S. and Helbich, M. (2013). Spatiotemporal urbanization processes in the megacity of Mumbai, India: A Markov chains-cellular automata urban growth model . *Applied Geography*, **40**(0), 140 – 149.

Monteith, J. (1965). Evaporation and environment. *Symposia of the Society for Experimental Biology*, **19**, 205–234. cited By 1589.

Moore, R. J. (1985). The probability-distributed principle and runoff production at point and basin scales. *Hydrological Sciences Journal*, **30**, 273–297.

Moore, R. J. (2007). The PDM rainfall-runoff model. *Hydrology and Earth System Sciences*, **11**(1), 483–499. Part 3 145JS Times Cited:30 Cited References Count:32.

Moran, M., Jackson, R., Slater, P., and Teillet, P. (1992). Evaluation of simplified procedures for retrieval of land surface reflectance factors from satellite sensor output. *Remote Sensing of Environment*, **41**(2-3), 169–184.

Morisette, J. and Khorram., S. (2000). Accuracy assessment curves for satellite-based change detection. *Photogrammetric Engineering and Remote Sensing*, **66(7)**, 876–880.

Mu, Q., Heinsch, F. A., Zhao, M., and Running, S. W. (2007). Development of a global evapotranspiration algorithm based on MODIS and global meteorology data . *Remote Sensing of Environment*, **111**(4), 519 – 536.

Mu, Q., Zhao, M., and Running, S. W. (2011). Improvements to a MODIS global terrestrial evapotranspiration algorithm . *Remote Sensing of Environment*, **115**(8), 1781 – 1800.

Mueller, B., Hirschi, M., Jimenez, C., Ciais, P., Dirmeyer, P. A., Dolman, A. J., Fisher, J. B., Jung, M., Ludwig, F., Maignan, F., Miralles, D. G., McCabe, M. F., Reichstein, M., Sheffield, J., Wang, K., Wood, E. F., Zhang, Y., and Seneviratne, S. I. (2013). Benchmark products for land evapotranspiration: LandFlux-EVAL multi-data set synthesis. *Hydrology and Earth System Sciences*, **17**(10), 3707–3720.

Muller, M. and Middleton, J. (1994). A Markov model of land-use change dynamics in the Niagara region, Ontario, Canada. *Landscape Ecology*, **9**(2), 151–157.

Myneni, R. B., Hoffman, S., Knyazikhin, Y., Privette, J. L., Glassy, J., Tian, Y., Wang, Y., Song, X., Zhang, Y., Smith, G. R., Lotsch, A., Friedl, M., Morisette, J. T., Votava, P., Nemani, R. R., Running, S. W., Myneni, R. B., Global, G., and Characterization, L. C. (2002). Global products of vegetation leaf area and fraction absorbed PAR from year one of MODIS data.

NFSM (2013). Crop calendar report. Accessd online Nov 2013.

Office of the Registrar General & Census Commissioner, India (2011). Census-2011. http://www.censusindia.gov.in.

O'Keeffe, J., Kaushal, N., Smakhtin, V., and Bharati, L. (2012). Assessment of environmental flows for the Upper Ganga basin. *Technical report, WWF-India, Delhi*.

Osborne, T., Slingo, J., Lawrence, D., and Wheeler, T. (2009). Examining the interaction of growing crops with local climate using a coupled crop-climate model. *J. Climate*, **22**(6), 1393–1411.

Osborne, T. M., Lawrence, D. M., Challinor, A. J., Slingo, J. M., and Wheeler, T. R. (2007). Development and assessment of a coupled crop–climate model. *Global Change Biology*, **13**(1), 169–183.

Overmars, K. P., Verburg, P. H., and Veldkamp, T. A. (2007). Comparison of a deductive and an inductive approach to specify land suitability in a spatially explicit land use model. *Land Use Policy*, **24**(3), 584 – 599.

Parker, D. C., Manson, S. M., Janssen, M. A., Hoffmann, M. J., and Deadman, P. (2003). Multi-agent systems for the simulation of land-use and land-cover change: A review. *Annals of the Association of American Geographers*, **93**(2), 314–337.

Pauwels, V. R. N., Verhoest, N. E. C., De Lannoy, G. J. M., Guissard, V., Lucau, C., and Defourny, P. (2007). Optimization of a coupled hydrology - crop growth model through the assimilation of observed soil moisture and leaf area index values using an ensemble Kalman filter. *Water Resources Research*, **43**(W04421).

Penning de Vries, F., Jansen, D., ten Berge, H., and Bakema, A. (1989). *Simulation of Ecophysiological Processes of Growth in Several Annual Crops*. Simulation Monograph PUDOC, Wageningen, The Netherlands.

Petit, C., Scudder, T., and Lambin, E. (2001). Quantifying processes of land-cover change by remote sensing: resettlement and rapid land-cover changes in south-eastern Zambia. *International Journal of Remote Sensing*, **22**(17), 3435–3456.

Piani, C., Weedon, G., Best, M., Gomes, S., Viterbo, P., Hagemann, S., and Haerter, J. (2010). Statistical bias correction of global simulated daily precipitation and temperature for the application of hydrological models. *Journal of Hydrology*, **395**, 199 – 215.

Pinstrup-Andersen, P. and Hazell, P. B. (1985). The impact of the Green Revolution and prospects for the future. *Food Reviews International*, **1**(1), 1–25.

Pitman, A. J. (2003). The evolution of, and revolution in, land surface schemes designed for climate models. *International Journal of Climatology*, **23**(5), 479–510.

Prakash, S., Mahesh, C., and Gairola, R. M. (2013). Comparison of TRMM Multi-satellite Precipitation Analysis (TMPA)-3B43 version 6 and 7 products with rain gauge data from ocean buoys. *Remote Sensing Letters*, **4**(7), 677–685.

Prentice, I. C., Liang, X., Medlyn, B. E., and Wang, Y.-P. (2014). Reliable, robust and realistic: the three R's of next-generation land surface modelling. *Atmospheric Chemistry and Physics Discussions*, **14**(17), 24811–24861.

Rahman, A., Kumar, S., Fazal, S., and Siddiqui, M. (2012). Assessment of land use/land cover change in the North-West district of Delhi using Remote Sensing and GIS techniques. *Journal of the Indian Society of Remote Sensing*, **40**(4), 689–697.

Rahman, H. and Dedieu, G. (1994). SMAC: a simplified method for the atmospheric correction of satellite measurements in the solar spectrum. *International Journal of Remote Sensing*, **15**(1), 123–143.

Rai, S., Sharma, E., and Sundriyal, R. (1994). Conservation in the Sikkim Himalaya: traditional knowledge and land-use of the Mamlay watershed. *Environmental Conservation*, **21**(1), 30–56.

Raisanen, J. and Raty, O. (2013). Projections of daily mean temperature variability in the future: cross-validation tests with ensembles regional climate simulations. *Climate Dynamics*, **41**(5-6), 1553–1568.

Raja, R., Anand, V., Kumar, A., Maithani, S., and Kumar, V. (2013). Wavelet based post classification change detection technique for urban growth monitoring. *Journal of the Indian Society of Remote Sensing*, **41**(1), 35–43.

Rajeevan, M., Bhate, J., Kale, J., and Lal, B. (2006). High resolution daily gridded rainfall data for the Indian region: Analysis of break and active monsoon spells. *Current Science*, **91**.

Rajeevan, M., Bhate, J., and Jaswal, A. K. (2008). Analysis of variability and trends of extreme rainfall events over India using 104 years of gridded daily rainfall data. *Geophysical Research Letters*, **35**(18), n/a–n/a.

Rajitha, K., Mukherjee, C. K., Vinu Chandran, R., and Prakash Mohan, M. M. (2010). Land-cover change dynamics and coastal aquaculture development: a case study in the East Godavari delta, Andhra Pradesh, India using multi-temporal satellite data. *International Journal of Remote Sensing*, **31**(16), 4423–4442.

Ramanathan, V., Chung, C., Kim, D., Bettge, T., Buja, L., Kiehl, J. T., Washington, W. M., Fu, Q., Sikka, D. R., and Wild, M. (2005). Atmospheric brown clouds: Impacts on South Asian climate and hydrological cycle. *Proceedings of the National Academy of Sciences of the United States of America*, **102**(15), 5326–5333.

Rao, K. and Pant, R. (2001). Land use dynamics and landscape change pattern in a typical micro watershed in the mid elevation zone of central Himalaya, India. *Agriculture Ecosystems & Environment*, **86**(2), 113–123.

Raty, O., Raisanen, J., and Ylhaisi, J. S. (2014). Evaluation of delta change and bias correction methods for future daily precipitation: intermodel cross-validation using ensembles simulations. *Climate Dynamics*, **42**(9-10), 2287–2303.

Ravindranath, N. H., Chaturvedi, R. K., and Murthy, I. K. (2008). Forest conservation, afforestation and reforestation in India: Implications for forest carbon stocks. *Current Science*, **95**(2), 216–222.

Renwick, A., Jansson, T., Verburg, P., Revoredo-Giha, C., Britz, W., Gocht, A., and McCracken, D. (2013). Policy reform and agricultural land abandonment in the EU. *Land Use Policy*, **30**(1), 446–457. cited By (since 1996)14.

Richards, L. A. (1931). Capillary conduction of liquids through porous mediums. *Journal of Applied Physics*, **1**(5), 318–333.

Richter, R. (1996). A spatially adaptive fast atmospheric correction algorithm. *International Journal of Remote Sensing*, **17**(6), 1201–1214.

Rodell, M., Velicogna, I., and Famiglietti, J. S. (2009). Satellite-based estimates of groundwater depletion in India. *Nature*, **460**(7258), 999–1002.

Ropelewski, C. F. and Halpert, M. S. (1996). Quantifying Southern Oscillation-Precipitation Relationships. *J. Climate*, **9**(5), 1043–1059.

Rouchier, J., Bousquet, F., Requier-Desjardins, M., and Antona, M. (2001). A multi-agent model for describing transhumance in North Cameroon: Comparison of different rationality to develop a routine. *Journal of Economic Dynamics and Control*, **25**, 527 – 559. Agent-based Computational Economics (ACE).

Rouse, J., Haas, R., Schell, J., and Deering, D. (1974). Monitoring vegetation systems in the Great Plains with ERTS. *NASA SP-351, Third ERTS-1 Symposium NASA Washington DC*, **1**, 309317.

Sader, S. A. (1987). Digital image classification approach for estimating forest clearing and regrowth rates and trends. *International Geoscience and Remote Sensing Symposium*, **1**, 209213.

Sapkota, P., Bharati, L., Gurung, P., Kaushal, N., and Smakhtin, V. (2013). Environmentally sustainable management of water demands under changing climate conditions in the Upper Ganges Basin, India. *Hydrological Processes*, **27**(15), 2197–2208.

Scanlon, B., R.C., R., Stonestrom, D., D.E., P., and K.F., D. (2005). Impact of land use and land cover change on groundwater recharge and quality in the southwestern US. *Glob Change Biol*, **11**, 15771593.

Schoorl, J. M., Veldkamp, A., and Bouma, J. (2002). Modeling water and soil redistribution in a dynamic landscape context.

Scoccimarro, E., Gualdi, S., Bellucci, A., Zampieri, M., and Navarra, A. (2013). Heavy Precipitation Events in a Warmer Climate: Results from CMIP5 Models. *J. Climate*, **26**(20), 7902–7911.

Scott, C. A., S. B. (2009). Energy supply and the expansion of groundwater irrigation in the Indus-Ganges Basin. *Int. J. River Basin Manage.*

Sellers, P., Randall, D., Collatz, G., Berry, J., Field, C., Dazlich, D., Zhang, C., Collelo, G., and Bounoua, L. (1996). A Revised Land Surface Parameterization (SiB2) for Atmospheric GCMS. Part I: Model Formulation. *J. Climate*, **9**(4), 676–705.

Semwal, R., Nautiyal, S., Sen, K., Rana, U., Maikhuri, R., Rao, K., and Saxena, K. (2004). Patterns and ecological implications of agricultural land-use changes: a case study from central Himalaya, India. *Agriculture Ecosystems & Environment*, **102**(1), 81–92.

Sen Roy, S., Mahmood, R., Niyogi, D., Lei, M., Foster, S. A., Hubbard, K. G., Douglas, E., and Pielke, Sr., R. (2007). Impacts of the agricultural Green Revolution - induced land use changes on air temperatures in India. *Journal of Geophysical Research*, **112**(D21).

Sen Roy, S., Mahmood, R., Quintanar, A. I., and Gonzalez, A. (2010). Impacts of irrigation on dry season precipitation in India. *Theoretical and Applied Climatology*, **104**(1-2), 193–207.

Seneviratne, S. I., Koster, R. D., Guo, Z., Dirmeyer, P. A., Kowalczyk, E., Lawrence, D., Liu, P., Mocko, D., Lu, C.-H., Oleson, K. W., and Verseghy, D. (2006). Soil Moisture Memory in AGCM Simulations: Analysis of Global Land Atmosphere Coupling Experiment (GLACE). *J. Hydrometeor*, **7**(5), 1090–1112.

Sengupta, A. and Rajeevan, M. (2013). Uncertainty quantification and reliability analysis of CMIP5 projections for the Indian summer monsoon. *Current Science*, **105**.

Sheeja, R., Joseph, S., Jaya, D., and Baiju, R. (2011). Land use and land cover changes over a century (1914-2007) in the Neyyar River Basin, Kerala: a remote sensing and GIS approach. *International Journal of Digital Earth*, **4**(3), 258–270.

Sheffield, J., Goteti, G., and Wood, E. (2006). Development of a 50-year high-resolution global dataset of meteorological forcings for land surface modeling. *Journal of Climate*, **19**.

Singh, A. (1989). Digital change detection techniques using remotely-sensed data. *International Journal of Remote Sensing*, **10**(6), 989–1003.

Singh, R. B. (2000). Environmental consequences of agricultural development: a case study from the Green Revolution state of Haryana, India. *Agriculture, Ecosystems & Environment*, **82**, 97–103.

Smakhtin, V. (2013). The ganges water machine: a sexy title or the concept of global relevance? Agriculture and Ecosystems Blog CGIAR Research Program on Water, Land and Ecosystems. Agriculture and Ecosystems Blog.

Sohl, T. L. and Claggett, P. R. (2013). Clarity versus complexity: Land-use modeling as a practical tool for decision-makers . *Journal of Environmental Management*, **129**(0), 235 – 243.

Song, C. and Woodcock, C. (2003). Monitoring forest succession with multitemporal Landsat images: Factors of uncertainty. *IEEE Transactions on Geoscience and Remote Sensing*, **41**, 25572567.

Song, C., Woodcock, C. E., Seto, K. C., Lenney, M. P., and Macomber, S. A. (2001). Classification and change detection using Landsat TM data: When and how to correct atmospheric effects? *Remote Sensing of Environment*, **75**(2), 230 – 244.

Spanner, M. A., Pierce, L. L., Peterson, D. L., and Running, S. W. (1990). Remote sensing of temperate coniferous forest leaf area index: The influence of canopy closure, understory vegetation and background reflectance. *International Journal of Remote Sensing*, **11(1)**, 95111.

Sperber, K., Annamalai, H., Kang, I.-S., Kitoh, A., Moise, A., Turner, A., Wang, B., and Zhou, T. (2013). The Asian summer monsoon: an intercomparison of CMIP5 vs. CMIP3 simulations of the late 20th century. *Climate Dynamics*, **41**(9-10), 2711–2744.

Stephenne, N. and Lambin, E. (2001). A dynamic simulation model of land-use changes in Sudano-Sahelian countries of Africa (SALU) . *Agriculture, Ecosystems & Environment*, **85**, 145 – 161. Predicting Land-Use Change.

Strengers, B., Leemans, R., Eickhout, B., Vries, B., and Bouwman, L. (2004). The land-use projections and resulting emissions in the IPCC SRES scenarios scenarios as simulated by the IMAGE 2.2 model. *GeoJournal*, **61**(4), 381–393.

Sutton, R. T., Dong, B., and Gregory, J. M. (2007). Land/sea warming ratio in response to climate change: IPCC AR4 model results and comparison with observations. *Geophysical Research Letters*, **34**(2), n/a–n/a.

Takada, T., Miyamoto, A., and Hasegawa, S. (2010). Derivation of a yearly transition probability matrix for land-use dynamics and its applications. *Landscape Ecology*, **25**, 561–572.

Takata, K., Saito, K., and Yasunari, T. (2009). Changes in the Asian monsoon climate during 1700–1850 induced by preindustrial cultivation. *Proceedings of the National Academy of Sciences*.

Taub, D. (2010). Effects of rising atmospheric concentrations of carbon dioxide on plants. *Nature Education Knowledge*, **3(10):21**.

Taylor, C. M. and Ellis, R. J. (2006). Satellite detection of soil moisture impacts on convection at the mesoscale. *Geophysical Research Letters*, **33**(L03404).

Taylor, K. E. (2001). Summarizing multiple aspects of model performance in a single diagram. *Journal of Geophysical Research: Atmospheres*, **106**(D7), 7183–7192.

Teillet, P. M. and Fedosejevs, G. (1995). On the dark target approach to atmospheric correction of remotely sensed data. *Canadian Journal of Remote Sensing*, **21**, 373–387.

Tenhunen, S. and Saavala, M. (2012). *An Introduction to Changing India: Culture, Politics and Development*. Anthem Press.

Teutschbein, C. and Seibert, J. (2012). Bias correction of regional climate model simulations for hydrological climate-change impact studies: Review and evaluation of different methods. *Journal of Hydrology*, **456-457**(0), 12 – 29.

Thenkabail, P. S., Schull, M., and Turral, H. (2005). Ganges and Indus river basin land use/land cover (LULC) and irrigated area mapping using continuous streams of MODIS data. *Remote Sensing of Environment*, **95**(3), 317–341.

Trenberth, K. E., Dai, A., Rasmussen, R. M., and Parsons, D. B. (2003). The changing character of precipitation. *Bull. Amer. Meteor. Soc.*, **84**(9), 1205–1217.

Tsarouchi, G., Mijic, A., Moulds, S., and Buytaert, W. (2014). Historical and future land-cover changes in the Upper Ganges basin of India. *International Journal of Remote Sensing*, **35**(9), 3150–3176.

Turner, A. G. (2013). The Indian Monsoon in a Changing Climate. Online, Royal Meteorological Society.

Turner, A. G. and Annamalai, H. (2012). Climate change and the South Asian summer monsoon. *Nature Clim. Change*, **2**(8), 587–595.

Turner, A. G. and Slingo, J. M. (2009). Uncertainties in future projections of extreme precipitation in the indian monsoon region. *Atmospheric Science Letters*, **10**(3), 152–158.

Turner, A. G., Inness, P. M., and Slingo, J. M. (2007). The effect of doubled CO2 and model basic state biases on the monsoon-ENSO system. I: Mean response and interannual variability. *Quarterly Journal of the Royal Meteorological Society*, **133**(626, A), 1143–1157.

Ueda, H., Iwai, A., Kuwako, K., and Hori, M. E. (2006). Impact of anthropogenic forcing on the Asian summer monsoon as simulated by eight GCMs. *Geophysical Research Letters*, **33**(6).

University of Oklahoma (2011). Global geo-referenced field photo library. Online; accessed May-2012.

USDA-I (2013). Crop information - crop descriptions. Accessed online 10/11/2013.

USDA-II (2013). Irrigated and rainfed wheat - India. Accessed online 10/11/2013.

Van Bodegom, P. M., Douma, J. C., Witte, J. P. M., Ordonez, J. C., Bartholomeus, R. P., and Aerts, R. (2012). Going beyond limitations of plant functional types when predicting global ecosystem–atmosphere fluxes: exploring the merits of traits-based approaches. *Global Ecology and Biogeography*, **21**(6), 625–636.

Van den Hoof , C., Hanert, E., and Vidale, P. L. (2011). Simulatind dynamic crop growth with an adapted land surface model JULES-SUCROS: Model development and validation. *Agricultural and Forest Meteorology*, **151**(2), 137 – 153.

Van den Hoof, C., Vidale, P. L., Verhoef, A., and Vincke, C. (2013). Improved evaporative flux partitioning and carbon flux in the land surface model JULES: Impact on the simulation of land surface processes in temperate Europe. *Agricultural and Forest Meteorology*, **181**(0), 108 – 124.

van Genuchten, M. T. (1980). A closed-form equation for predicting the hydraulic conductivity of unsaturated soils. *Soil Sci. Soc. Am. J.*, **44**, 892–898.

Veldkamp, A. and Fresco, L. (1996). CLUE-CR: An integrated multi-scale model to simulate land use change scenarios in Costa Rica . *Ecological Modelling*, **91**(13), 231 – 248.

Veldkamp, A. and Lambin, E. (2001). Predicting land-use change. *Agriculture, Ecosystems and Environment*, **85**.

Verburg, P. and Overmars, K. (2009). Combining top-down and bottom-up dynamics in land use modeling: exploring the future of abandoned farmlands in Europe with the Dyna-CLUE model. *Landscape Ecology*, **24**(9), 1167–1181.

Verburg, P., de Koning, G., Kok, K., Veldkamp, A., and Bouma, J. (1999). A spatial explicit allocation procedure for modelling the pattern of land use change based upon actual land use. *Ecological Modelling*, **116**(1), 45 – 61.

Verburg, P., Kok, K., Pontius, RobertGilmore, J., and Veldkamp, A. (2006). Modeling land-use and land-cover change. In E. Lambin and H. Geist, editors, *Land-Use and Land-Cover Change*, Global Change - The IGBP Series, pages 117–135. Springer Berlin Heidelberg.

Verburg, P., Eickhout, B., and Meijl, H. (2008). A multi-scale, multi-model approach for analyzing the future dynamics of European land use. *The Annals of Regional Science*, **42**(1), 57–77.

Verburg, P., Huajun, T., Wenbin, W., Peng, Y., and Youqi, C. (2009). Recent Progresses of Land Use and Land Cover Change (LUCC) Models. *Acta Geographica Sinica*, **64**, 456–468.

Verburg, P. H., Soepboer, W., Veldkamp, A., Limpiada, R., Espaldon, V., and Mastura, S. S. (2002). Modeling the Spatial Dynamics of Regional Land Use: The CLUE-S Model. *Environmental Management*, **30**(3), 391–405.

Verghese, B. G. (1993). *Harnessing the Eastern Himalayan Rivers : Regional Cooperation In South Asia*. Konark Publishers Pvt. Ltd, Delhi.

Verhoef, A. and Egea, G. (2014). Modeling plant transpiration under limited soil water: Comparison of different plant and soil hydraulic parameterizations and preliminary implications for their use in land surface models. *Agricultural and Forest Meteorology*, **191**(0), 22 – 32.

Vermote, E., Tanre, D., Deuze, J.-L., Herman, M., and Morcette, J.-J. (1997). Second Simulation of the Satellite Signal in the Solar Spectrum, 6S: an overview. *Geoscience and Remote Sensing, IEEE Transactions on*, **35**(3), 675–686.

Wagner, P., Kumar, S., and Schneider, K. (2013). An assessment of land use change impacts on the water resources of the Mula and Mutha Rivers catchment upstream of Pune, India. *Hydrol. Earth Syst. Sci.*, **17**, 2233–2246.

Wagner, W., Dorigo, W., de Jeu, R., Fernandez, D., Benveniste, J., Haas, E., and Ertl, M. (2012). Fusion of active and passive microwave observations to create an Essential Climate Variable data record on soil moisture. *SPRS Annals of the Photogrammetry, Remote Sensing and Spatial Information Sciences XXII ISPRS Congress, 25 August 01 September 2012, Melbourne, Australia*, **I-7**.

Wang, C., Kim, D., Ekman, A. M. L., Barth, M. C., and Rasch, P. J. (2009). Impact of anthropogenic aerosols on Indian summer monsoon. *Geophysical Research Letters*, **36**(21).

Wen, G., Tsay, S.-C., Cahalan, R. F., and Oreopoulos, L. (1999). Path radiance technique for retrieving aerosol optical thickness over land. *Journal of Geophysical Research: Atmospheres*, **104**(D24), 31321–31332.

Weng, Q. (2002). Land use change analysis in the Zhujiang Delta of China using satellite remote sensing, GIS and stochastic modelling. *Journal of Environmental Management*, **64**(3), 273 – 284.

Westhoek, H., van den Berg, M., and Bakkes, J. (2006). Scenario development to explore the future of Europe's rural areas . *Agriculture, Ecosystems & Environment*, **114**(1), 7 – 20.

Westmoreland, S. and Stow, D. (1992). Category identification of changed land-use polygons in an integrated Image Processing/Geographic Information System. *Photogrammetric Engineering and Remote Sensing*, **58**, 15931599.

Whitaker, D. W., Wasimi, S. A., and Islam, S. (2001). The El Niño southern oscillation and long-range forecasting of flows in the Ganges. *International Journal of Climatology*, **21**(1), 77–87.

White, R., Engelen, G., and Uljee, I. (1997). The use of constrained cellular automata for high-resolution modelling of urban land-use dynamics. *Environment and Planning B: Planning and Design*, **24**(3), 323–343.

Wooldridge, S., Kalma, J., and Kuczera, G. (2001). Parameterisation of a simple semi-distributed model for assessing the impact of land-use on hydrologic response. *Journal of Hydrology*, **254**, 16 – 32.

World Bank (2010). Deep Wells and Prudence: Towards Pragmatic Action for Addressing Groundwater Overexploitation in India. Technical report, World Bank.

World Bank (2013). Turn down the heat: Climate extremes, regional impacts and the case for resilience. *A Report for the World Bank by the Potsdam Institute for Climate Impact Research and Climate Analytics*.

Wosten, J., Lilly, A., Nemes, A., and Le Bas, C. (1999). Development and use of a database of hydraulic properties of European soils. *Geoderma*, **90**, 169–185.

Wu, F. (1998). SimLand: a prototype to simulate land conversion through the integrated GIS and CA with AHP-derived transition rules. *International Journal of Geographical Information Science*, **12**(1), 63–82.

Wu, Q., Li, H., Wang, R., Paulussen, J., He, Y., Wang, M., Wang, B., and Wang, Z. (2006). Monitoring and predicting land use change in Beijing using remote sensing and GIS. *Landscape and Urban Planning*, **78**(4), 322 – 333.

Xavier, R., Comin, F., Krishnamurthy, V., and Kinter, J. (2002). *Global Climate -Current Research and Uncertainties in the Climate System*, chapter The Indian Monsoon and its Relation to Global Climate Variability. Springer.

Yamashima, R., Takata, K., Matsumoto, J., and Yasunari, T. (2011). Numerical study of the impacts of land use/cover changes between 1700 and 1850 on the seasonal hydroclimate in monsoon Asia. *Journal of the Meteorological Society of Japan. Ser. II*, **89A**, 291–298.

Yatagai, A., Arakawa, O., Kamiguchi, K., Kawamoto, H., Nodzu, M. I., and Hamada, A. (2009). A 44-year daily gridded precipitation dataset for Asia based on a dense network of rain gauges. *SOLA*, **5**, 137–140.

Yeh, A. and Li, X. (1999). Economic development and agricultural land loss in the Pearl River Delta, China. *Habitat International*, **23**, 373390.

Zaisheng, H., Hao, W., and Rui, C. (2006). Transboundary aquifers in Asia with special emphasis to China. *United Nations Educational, Scientific and Cultural Organization*, pages 10–18.

Zhao, M., Pitman, A. J., and Chase, T. (2001). The impact of land cover change on the atmospheric circulation. *Climate Dynamics*, **17**(5-6), 467–477.

Zulkafli, Z., Buytaert, W., Onof, C., Lavado, W., and Guyot, J. L. (2013). A critical assessment of the JULES land surface model hydrology for humid tropical environments. *Hydrology and Earth System Sciences*, **17**(3), 1113–1132.